Investigating the Impact of Metallic Nanoparticles on Biological Systems and Lysosomal Function.

Sophie Rachel Cook

Cardiff University

School of Biosciences

Ph.D. 2022

Supervised by Dr. Emyr Lloyd-Evans

Abstract

Metallic nanoparticles, including iron oxide nanoparticles (IONPs) are emerging as a component of particulate matter air pollution that is being linked to cellular and organism-level toxicity in experimental studies. While IONPs, in particular superparamagnetic iron oxide nanoparticles (SPIONs), such as magnetite, are also being developed as tools for bioscience-based research, and for these kinds of applications it is important to use nanoparticles with low cytotoxicity and high biocompatibility. IONPs can be endocytosed by cells and trafficked through the endolysosomal system to the lysosome. The acidic and degradative environment of the lysosome can promote degradation of IONPs, releasing free iron, which is linked to production of reactive oxygen species (ROS), mainly through Fenton reactions. The production of ROS is believed to be a main driver of IONP toxicity.

This thesis aimed to develop cellular and *in vivo* (zebrafish) models of iron oxide nanoparticle (IONP) treatment and identify affected pathways, phenotypes and behavioural responses, identifying nanoparticle features associated with greater toxicity or greater biocompatible.

Investigation of the effects of HEPES, and other cell culture buffers, suggested high concentrations of HEPES buffer and common buffer concentrations of PIPES buffer can affect lysosomal phenotypes in CHO H1 cells. This data being used to select cell culture buffers and concentrations for use in further experiments to prevent buffer-related lysosomal phenotypes. This lab has developed a magnetic lysosomal extraction technique using a dextran coated IONP, labelled LRL, that is able to extract high yields of lysosomes from storage disease cells that are difficult to isolate with other extraction methods due to changes in lysosomal density. Comparison of the LRL nanoparticle, with two similar dextran associated IONPs suggested strong differences in toxicity across a range of cellular pathways and phenotypes between the nanoparticles despite similarity in structure, while validating the biocompatibility of LRL nanoparticles. Therefore, the toxicity of LRL nanoparticles was also investigated in an embryonic zebrafish development model (*in vivo*), with zebrafish models being increasingly utilised for investigation of lysosomal storage diseases. These experiments determined that this nanoparticle was also highly biocompatible in the developing zebrafish and could also be used to develop a zebrafish magnetic lysosomal extraction protocol.

Noting the differing toxicities of the similar nanoparticles led to further experiments aiming to compare the effects of composition and size of the nanoparticles with their effects on cellular toxicity. Studies have shown magnetite nanoparticles, a SPION found in particulate matter air pollution, may enter the human brain where these nanoparticles would likely encounter and be endocytosed by microglial cells. Using a human microglial cell line, the cellular toxicity of three different sizes of uncoated magnetite nanoparticles and an uncoated maghemite nanoparticle were compared. This suggested increased cellular toxicity for the uncoated IONPs compared to dextran coated IONPs and indicated that magnetite may have larger toxic impacts on the lysosomes of these cells compared to maghemite, which could be related to nanoparticle size.

This thesis was able to develop several models of nanoparticle toxicity in both cells and developing zebrafish. Together, data in this thesis supports differential lysosomal and cellular toxicity and biocompatibility, between differing IONPs, depending on coating, composition, size and structure of the nanoparticles. This thesis also suggests the lysosome is a primary region of the cell to be affected by IONP-related toxicity, likely due to its role in nanoparticle degradation and as the cellular region initially contending with increased free iron and subsequent ROS production.

Contents Page

Figures List

Table List

Acknowledgements

Firstly, I would like to give a big, big thank you to my supervisor, Dr. Emyr Lloyd-Evans, for providing me with the opportunity to undertake this PhD project and for his continual support and advice throughout. I am very grateful for all the help, guidance, enthusiasm, and ideas from you that have evolved this project into a completed thesis. It has been an honour to work as part of the lab, meeting so many colleagues, watching as many of them completed professional training years, Masters projects and PhDs during my time and making many friends along the way. I would also like to thank Helen for her constant support, even after she set up her own lab group. I would like to add in extra thanks to Dr. Owen Peters who joined as my second supervisor and gave great help and support to the project and thank you to his whole lab for letting me be a part of the group, even though circumstances necessitated mainly virtual contact.

I am grateful to the Medical Research Council GW4 DTP who funded this project and provided a brilliant system for support and meeting other PhD students, and who worked tirelessly to keep projects on track through the difficulties of the Covid-19 pandemic.

A special thanks goes to the other members of the lab who have provided technical help, emotional support and a good laugh, as needed. Thank you to Emily, Brendan, Katie, Hannah, Charlie, Rafa and Abdullah who were all there through most of my PhD, the ups and the downs, and whose support I truly value. A special thanks to Sophie Powell who made my first year so much fun, if only you had been able to stay for more than a year. A big thanks to all my past students who helped work on projects related to mine, the opportunity to teach and pass on my skills was an absolute pleasure.

Thank you to all my family, and especially my parents for their continuing support and patience with my long university education. A special big thanks to Dan for always supporting my work and being there to have a laugh when I needed a break. Thank you for bringing me snacks and drinks as I wrote the thesis and for being patient as we both worked from home in the same room over the Covid lockdowns. Your continuing support throughout my entire PhD has been immeasurable and so greatly appreciated.

There have been many tough days in the last few years, but as we continue to hope we are reaching the other side of Covid, I am also excited to be reaching the end of my thesis and PhD journey, ready for the exciting new journeys that lie ahead.

List of publications

Papers published from thesis data:

Cook, S. R.; Badell-Grau, R. A.; Kirkham, E. D.; Jones, K. M.; Kelly, B. P.; Winston, J.; Waller-Evans, H.; Allen, N. D.; & Lloyd-Evans, E. (2020). Detrimental effect of zwitterionic buffers on lysosomal homeostasis in cell lines and iPSC-derived neurons. *AMRC open research*. 2:21.

Other papers published during PhD:

Cook, S. R.; Bladen, C.; Smith, J.; Maguire, E.; Copner, J.; Fenn, G. D.; Wager, K.; Waller-Evans, H.; & Lloyd-Evans, E. (2020). Visualisation of cholesterol and ganglioside GM1 in zebrafish models of Niemann-Pick type C disease and Smith-Lemli-Opitz syndrome using light sheet microscopy. *Histochem Cell Biol.* 154(5):565-578.

Abbreviations

AM group = Acetoxymethyl

ATP = Adenosine triphosphate

Baf-A1 = Bafilomycin A1

BSA = Bovine Serum Albumin

CC Nanoparticle = Nanoparticle from the company Chemicell

CHO H1 = Chinese Hamster Ovary H1

CMA = Chaperone-Mediated Autophagy

CNS = Central Nervous System

dpf (DPF) = Days Post Fertilisation

DMEM = Dulbecco's Modified Eagle Medium

DMEM/F-12 = Dulbecco's Modified Eagle Medium: Nutrient Mixture F-12

DPBS = Dulbecco's Phosphate Buffered Saline

DMT1 = Divalent metal transporter 1

EM = Electron Microscopy

HBSS = Hanks' Balanced Salt Solution

HMC3 = Human Embryonic Microglia Clone 3

hpf (HPF) = Hours Post Fertilisation

ID Nanoparticle = Iron dextran nanoparticle

IONP = Iron Oxide Nanoparticles

LAMP1 = Lysosomal-associated membrane protein 1

LAMP2 = Lysosomal-associated membrane protein 2

LRL Nanoparticle = Nanoparticle from the company Liquids Research Ltd

MH = Maghemite = Fe_2O_3

MHC protein = Major Histocompatibility Complex Proteins

MLIV = Mucolipidosis Type IV

MN = Magnetite = Fe_3O_4

MRI = Magnetic Resonance Imaging

mTORC = Mammalian Target of Rapamycin Complex

NPC1 = Niemann-Pick Disease Type C1

NRAMP1 =Natural resistance-associated macrophage protein 1

PEG = Poly(ethylene) Glycol

PM = Particulate Matter

PPB = Potassium Phosphate Buffer

ROS = Reactive Oxygen Species

SPION = Superparamagnetic Iron Oxide Nanoparticles

TEM = Transmission Electron Microscopy

TFEB = Transcription factor EB

TPCs = Two pore channels

TRPML1 = Transient receptor potential cation channel, mucolipin subfamily, member 1

TRPML2 = Transient receptor potential cation channel, mucolipin subfamily, member 2

TRPML3 = Transient receptor potential cation channel, mucolipin subfamily, member 3

UT = Untreated

vATPase = Vacuolar ATPase

1 Introduction

1.1 Air pollution

1.1.1 The dangers of air pollution

Air pollution is defined by the World health organisation as 'contamination of the indoor or outdoor environment by any chemical, physical or biological agent that modifies the natural characteristics of the atmosphere'. Humans breathe about 9,000-12,000 litres of air a day, more if exercising or preforming heavy work, and the quality of that air can have a big impact on our health (Todd 2005). In fact, air pollution is one of the great killers of this age, responsible for an estimated 6.4 million deaths world-wide in 2015, compared to 7 million tobacco-related deaths and 0.7 million malaria-related deaths (Landrigan 2017).

Non-communicable diseases account for ~70% of air pollution-related deaths, impacting on cardiovascular disease, stroke, lung cancer and COPD (Forouzanfar et al. 2016). While recent evidence shows air pollution could be an important, yet unquantified risk factor, in neurodevelopmental disorders in children (Grandjean and Landrigan 2014) and neurodegenerative diseases in adults (Kioumourtzoglou et al. 2016). Air pollution can also be considered as having an economic burden, contributed by medical expenditures, lost economic productivity (from inability to work or premature death) and the cost of environmental degradation (Landrigan 2017). One study calculated global annual expenditures for pollution-related health care of between US$240 billion to US$630 billion (Preker et al. 2016).

When the first measurements of carbon monoxide concentrations over tropical Asia, Africa, and South America were made available by the MAPS (Measurement of Air Pollution from Satellite) instrument launched in 1981, it became clear that air pollution was an international issue (Reichle Jr et al. 1986). This showed that industrial air pollution from fossil fuels could affect regional and global air quality and those countries could suffer from air pollution created elsewhere, as well as that produced at home. These findings have been replicated many times in the years since, with a wider and wider range of pollutants being identified (Akimoto 2003).

1.1.2 Composition of ambient air pollution

The nature of air pollution has changed as human activity has changed. Household air pollution (produced mainly through fuel burnt for cooking and heating) has been declining world-wide since the 1990s, however, this is offset by increases in ambient (outdoor) air pollution, the bulk of which is produced by industrial production and vehicular transportation (Landrigan 2017).

The dangers of air pollutants vary depending on their state and composition. Gaseous air pollutants, such as carbon monoxide, sulphur dioxide, nitrogen oxides, volatile organic compounds, and ozone are mostly produced by combustion of fossil fuels and contribute to a great extent to changes in the upper atmosphere and have been shown to be an important driver in climate change (Ramanathan and Feng 2009).

The other main group of air pollutants is particulate matter (PM), which refers to particles of varying size and composition that are suspended in breathing air (Kampa and Castanas 2008). Air pollution PM is formed from a variety of components, commonly consisting of carbon and metal-based particles, with particles sub-classified by size (Hamanaka and Mutlu 2018). Coarse particles (PM10) have a diameter between 2.5-10 µm, fine particles (PM2.5) have a diameter between 0.1-2.5 µm and ultrafine particles (PM0.1) have a diameter <0.1 µm (Hamanaka and Mutlu 2018).

The process of industrialisation has led to a large increase in air pollution in countries across the world, especially in highly urbanised centres. Combustion of traditional fossil fuels (coal, wood, crude oil, lead petrol and high sulphur diesel) 30-40 years ago caused an increase of larger course pollutant particles containing high levels of carbon, lead and sulphur (Valavanidis et al. 2008). Development of cleaner technologies has reduced the release of these types of pollutants, with fine and ultrafine particulate matter becoming more prominent, and consisting of particles composed of a wider range of heavy metals and polycyclic aromatic hydrocarbons.

Iron and iron oxides are often the main heavy metal component of particulate matter air pollution, released by the combustion process, vehicle wear and as a major part of fly ash and industrial dust (Harrison and Jones 1995; Maher et al. 2008; Lovera-Leroux et al. 2015). Analysing pollution levels from tree bark and leaves can act as an effective measure for air

pollution, as trees and plants often act as a reservoir for air pollution particulate matter and are an important natural method for isolating pollution from the air (Kardel et al. 2018). A study of tree bark in Germany found iron was the main heavy metal component of the air pollution accumulated by the bark, with accumulation of lead, copper and nickel also occurring, but to a lesser extent (Huhn et al. 1995). While a study in the UK of leaf leachates, found zinc and iron to be at the highest roadside concentrations, with magnesium, barium and lead at lower levels (Maher et al. 2008). Iron and lead showed the greatest levels of roadside enrichment compared to countryside areas (distant from major roads) suggesting a stronger link between these heavy metals and vehicle-related air pollution (Maher et al. 2008).

1.1.3 Spatial movements of pollution particles

As air pollution particles move away from their source there is often a reduction in their concentration/density in the air, known as dilution (Zhou and Levy 2007). For large particles of particulate matter, more than 1 μm, the main form of movement is turbulent diffusion, a random and chaotic time dependent motion, while gravitational settling of the particles to the ground in a size dependent manner is likely to occur (Zhou and Levy 2007). Coagulation processes are likely to occur with larger aerosol particles, where they collide with and adhere to each other forming even larger particles, slowing down dilution, but increasing settling. For turbulent diffusion, concentration and density gradients are important for determining movement direction and velocity, meaning background concentrations of the pollutants in an area as well as emission concentrations are important for determining movement. Smaller particles of particulate matter, less than 100 nm, are likely to travel further than the larger particles as there is less gravitational settling, and particle movement is more likely to be determined by Brownian diffusion, a random wiggling motion resulting from constant bombardment by surrounding gas molecules (Zhou and Levy 2007).

Of major importance to particle movements are metrological factors, such as wind and moisture levels. Wind speed is integral to determine the extent to which pollutants are initially diluted, with higher wind speeds leading to greater dilution/diffusion of the particulate matter and reducing coagulation, leading to lower particles sizes and reduced gravitational settling (Zhou and Levy 2007).

Height above ground also seems to be important for detecting near road pollution levels; one study of air pollution in roadside tree leaves showed iron particulate was greatest at ~0.3 m above ground, with levels reducing with height apart from a second peak at ~1.5-2 m (Maher et al. 2008). The lower peak may suggest a particular risk to young children walking alongside roads, as they may experience higher levels of particulate matter air pollutants while the second peak suggests a greater risk for walking adults or when driving in cars. As levels of detected PM above roads was found to be significantly lower over 3 m, this may suggest shorter trees and low (~0.3 m) foliage should be planted around roads to provide the greatest protection against PM air pollution.

Rain can act as a natural removal mechanism for some pollutants from the atmosphere (Sharma et al. 1983). Suspended particulate matter can be collected in moisture droplets either during rainout (in clouds) when particles act as a means for the clouds to condense, or washout (below cloud level) when particles are entrapped by raindrops as they fall (Chate et al. 2003). Some studies suggest removal of particulate matter by rain is more common for course PM10 than for fine PM2.5 (Samara and Tsitouridou 2000; Kulshrestha et al. 2009).

Seasonal effects should also be considered in terms of pollution levels. Some studies show a pattern where levels of particulate matter are higher in summer and lower in winter (Sharma et al. 1983; Ali 2015), while other studies find the opposite pattern, suggesting the patterns may be region dependent (Cichowicz et al. 2017; Dėdelė and Miškinytė 2019). The health risks associated with air pollution PM can also often be associated with the changing levels across seasons (Chen et al. 2013b). Patterns of air pollution across a 24-hour period can also be fluctuating, often with pronounced diurnal variation in urbanised areas according to human lifestyle patterns and daylight timings (Liu et al. 2015).

1.1.4 PM2.5 pollution worldwide

In the UK, the air quality standards regulations 2010 require that particulate matter concentrations must not exceed an annual average of 40 μg/m^3 for PM10, a 24-hour average of 50 μg/m^3 more than 35 times in a single year for PM10 and an annual average of 25 μg/m^3 for PM2.5 (National Statistics UK 2021). Meanwhile the world health organisation suggests that to improve health, particulate matter concentrations should be reduced to an annual average of less than 20 μg/m^3 for PM10 and of less than 10 μg/m^3 for PM2.5 (WHO

2018). While there is no proven safe level of air pollution, particularly high levels have been recorded in some countries, often in developing countries where pollution is less well-regulated. For example, roadside 24-hour average PM2.5 levels of between 53–151 $\mu g/m^3$ were recorded during Dec 2007–Jan 2008 in Ho Chi Minh City, Vietnam (Huong Giang and Kim Oanh 2014). Whereas, mean roadside 24-hour average PM10 levels of 98 $\mu g/m^3$ and PM2.5 = 74 $\mu g/m^3$ were recorded during winter 2008-2009 in Chennai city, India (Srimuruganandam and Shiva Nagendra 2012) and of 278 $\mu g/m^3$ and PM2.5 = 90 $\mu g/m^3$ were recorded during April 2010 to June 2010 at sites in Agra, India (Pipal et al. 2011). In Guangzhou, one of the most developed and industrialized cities in South China, high outdoor 24-hour average PM2.5 levels of 123.7 $\mu g/m^3$ were recorded between November 2004 and January 2005 (Huang et al. 2007). While the Ordos region of inner Mongolia recorded average PM2.5 concentrations exceeding 75 $\mu g/m^3$ annually, with peak pollution days in excess of 350 $\mu g/m^3$ (Khuzestani et al. 2017). While countries around the world suffer such high loads of particulate matter air pollution, determining the health impacts of the pollution components must remain a high priority.

1.1.5 Traffic-related air pollution

Air pollution samples for particulate matter taken in urban areas show that motor vehicle related pollution often constitutes the greatest source of PM2.5 (Shah et al. 2004; Shen et al. 2014) and PM0.1 (Zhu et al. 2002).

Zhou and Levy (2007) reviewed literature from 33 studies and estimated that spatial distance of travel for traffic emission is approximately 100-400 m for particulate matter in general, and around 100-300 m for particulate matter less than 100 nm diameter. This could suggest the need for a protective 400 m buffer zones around major roads, such as motorways, to protect the health of people living in the surrounding area, or other pollution reducing mechanisms, such as banks and foliage to protect people living in closer proximity.

Requia and Koutrakis (2018) had a study in Hamilton, Canada that showed residential proximity to a major roadway can be correlated with an increased risk of premature mortality. From their data it was estimated that the premature mortality risk is correlated to buffer zones of 100 m. Within buffer zone 0–100 m the risk was 29.5% higher than for 101–200 m, 179.3% higher than 201–300 m, and 566% higher than 301–400 m. This study also

estimated the percentage of PM2.5 related yearly deaths in Hamilton within each buffer zone, with 41% <100m zone, 32% 101-200 m zone, 14% 201-300 m zone, 6% 301-400m zone and only 3% in the 401-500m zone. Rosenbloom et al. (2012) had a similar estimate from the Onset Study (3547 individuals) in the United States, that 37% of all-cause mortality occurred in individuals living between 0 and 100 m from a major roadway and 33% occurred between 101 and 200 m.

This pattern also appears to be present for specific diseases and not just overall mortality. In a 2003 study for England and Wales, stroke mortality was shown to be 5% higher in people living within 200 m of a main road compared with people living more than 1000 m from the roads (Maheswaran and Elliott 2003). While in a study in LOS Angeles, USA suggested the rate of atherosclerosis progression among people living within 100 m of a major road was found to be two times faster than in the general population (Künzli et al. 2010). Cardiovascular diseases also seem to be particularly impacted by high pollution, for example Valvular heart disease was found to be positively correlated with residential proximity to a major road (up to 300 m) and with increased air pollution, with a stronger correlation in female subjects (Pang et al. 2021). In highly urbanised areas there may be very little housing that is further than 500 m away from a major road, a problem that is only likely to worsen as populations rise and road traffic increases. Economic status may play a role in how near housing is to a main road and in general mortality risk, a second factor that has been considered in many of these studies, with those who are poorer more at risk in both cases. Therefore, it is even more important to reduce air pollution as a public health priority to minimise the risk for increased disease burden in those who may already be more vulnerable.

1.1.6 Air pollution and human disease

Particulate matter in air pollution can become a risk to humans who inhale it depending on its concentration, prevalence, composition and particle size. The size of the particulate matter inhaled from air pollution dictates where it is most likely to deposit in the lungs. PM10 (diameter <10 µm) do not generally penetrate beyond the upper bronchus, as they settle quickly due to gravity and are mostly filtered out by the nose and upper airway (Anderson et al. 2012). While PM2.5 (diameter <2.5 µm) and PM0.1 (diameter <0.1 µm)

can penetrate into the small airways and alveoli. These smaller particles penetrating deeper into the lungs can irritate lung tissue and impact lung health, while small particles reaching the alveoli are potentially able to cross from the lungs into the blood stream, providing passage to nearly all parts of the body (Nemmar et al. 2002b). The size of particulate matter particles also seems to correlate with health risks, with smaller particles that are able to penetrate furthest, being linked to the greatest health risks (Hamanaka and Mutlu 2018). The ESCAPE study investigating data taken from ~300 000 people in 17 cohort studies showed a 22% and 36% increase in lung cancer diagnosis in areas where levels of PM10 and PM2.5, respectively, were increased by 10 $\mu g/m^3$ (Raaschou-Nielsen et al. 2013). With low exposure to pollution, the lungs may be able to clear pollution particles with natural immune measures, but as air pollution levels increase, this will surpass the lungs' ability to counteract the effects.

Long-term exposure to PM2.5 particles has been consistently associated with increased mortality (Krewski et al. 2009), cardiovascular (Puett et al. 2009) and cerebrovascular (Stafoggia et al. 2014) events as well as lung cancer (Hamra et al. 2014). As the lungs are often the bodies primary region of interaction for inhaled air pollution, it makes sense that many lung and respiratory diseases are linked to PM concentrations (Jo et al. 2017). PM air pollution has been repeatedly demonstrated to have significant short- and long-term effects on both the development of asthma and asthma morbidity (Keet et al. 2018). PM air pollution has also been implicated in incidence and mortality of viral respiratory infections, including Covid-19 (Mishra et al. 2020; Baron 2021).

There have been several studies demonstrating a link between PM exposure and decreased cognitive function (Power et al. 2011) as well as accelerated cognitive decline (Weuve et al. 2012). Studies also suggest a close relationship may exist between PM2.5 and neurodegenerative diseases including Alzheimer's disease and Parkinson's disease (Wang et al. 2021a). How PM2.5 particles can enter the brain and the mechanisms behind their link to neurodegenerative diseases has become a quickly growing research field, mostly due to the sensitivity of the brain as an organ and its previously presumed protection from foreign matter extended by the blood brain barrier. One component of PM2.5 air pollution with a particularly strong link to neurodegeneration is iron, often in the form of iron oxides (Maher 2019).

1.2 Iron oxide nanoparticles

1.2.1 Iron is essential to life

Iron is an essential transition metal in all living organisms, including plants, bacteria, animals and humans (Lasocki et al. 2014). It is necessary for energy production (via electron transport), for oxygen transport by haemoglobin in animals, DNA repair and replication, regulation of gene expression and for oxidative metabolism. These functions are mainly based on the ability of iron to easily donate electrons, a function highly utilised in most living organisms, yet this same ability means unregulated iron can be dangerous in the body as its high reactivity with oxygen species can lead to the production of toxic radicals (Lasocki et al. 2014).

Iron is redox-active meaning it can exist in multiple oxidation states by transferring single electrons and switching between ferrous (Fe^{2+}) and ferric (Fe^{3+}) iron through oxidation/reduction reactions (Sander et al. 2015). Due to this property, it can easily form ligands with biomolecules as it is highly and reversibly reactive, so is often utilised as an enzyme co-factor, integral for catalysing certain reactions (Balk and Schaedler 2014). The main forms of iron co-factors are iron-sulphur clusters (involved in the mitochondrial electron transport chain and photosynthesis), heme (involved in oxygen transfer in blood cells), mononuclear iron proteins (such as superoxide dismutase involved in converting harmful oxygen radials back to ordinary molecular oxygen) and diiron-carboxylate proteins which are involved in a range of process including DNA synthesis (Balk and Schaedler 2014; Sander et al. 2015). In mammals low iron levels lead to an iron deficiency condition called anaemia, characterised by low oxygen levels resulting in fatigue, dizziness, shortness of breath and irregular heartbeats (Sander et al. 2015). High iron levels (iron overload) can also be immensely damaging as free iron can react with O_2, creating oxygen radicals that are extremely toxic, primarily leading to DNA damage, protein peroxidation and lipid peroxidation (Toyokuni 1996). Therefore, living organisms have found many ways to safely bind (chelate) iron so that free iron only exists in trace amounts in the body, mainly during transmembrane crossing as Fe^{2+} ions (Mackenzie 2005). Iron overload has been highlighted as a risk factor for development of cancer and Alzheimer's disease (Toyokuni 1996; Connor et al. 2001), while iron accumulation has been identified in several neurodegenerative

disorders including Niemann-Pick disease type C1 (NPC1), Mucolipidosis Type lV (MLIV) (Alshehri 2019) and the neurodegeneration with brain iron accumulation (NBIA) disorders (Hayflick et al. 2003).

1.2.2 Cellular uptake of transferrin bound iron

Non-heme iron can be transported into cells by two different mechanisms: transferrin-bound iron uptake and non-transferrin bound iron uptake (Lane et al. 2015) (**Figure 1-1**). Under normal homeostasis almost all iron in circulation should be bound to transferrin, however, under conditions of iron overload free iron levels may increase as the transferrin becomes saturated.

Transferrin can reversibly bind two atoms Fe^{3+} (ferric) iron, which is normally insoluble at neutral pH, but becomes soluble when bound to transferrin (Morgan et al. 1986). Transferrin-bound iron can attach to the transferrin receptor 1 and transferrin receptor 2 on the cell membrane and be endocytosed by a receptor-mediated endocytic pathway (Graham et al. 2008; Fillebeen et al. 2019). The iron can then travel in a vesicle to endosomes where the decreased pH along with reduction by an endosomal reductase (Fe^{3+} to Fe^{2+}) causes the iron to be released by the transferrin (Halbrooks et al. 2003). The iron, now in the form Fe^{2+}, can then be transported across the endosomal membrane to the cytosol by the action of divalent metal transporter 1 (DMT1) or ZRT/IRT-like proteins 14 (ZIP14) and form part of the labile iron pool (Gunshin et al. 1997; Jenkitkasemwong et al. 2012). Iron in the labile iron pool is then directed for storage as ferritin, for synthesis of heme and iron sulphur clusters in the mitochondria or cytosol, or instead can be exported from the cell by ferroportin 1 (Lane et al. 2015).

In most non-erythroid cells, most of the newly imported iron (~70-80%) is stored as ferritin (Lane et al. 2015). Ferritin is a large multimeric protein with 24 subunits that form a hollow sphere with space for storing up to 4,500 iron atoms within its 8 nm diameter cavity (Chasteen and Harrison 1999). This gives a very high iron: protein ratio, 200x the ratio in haemoglobin, providing highly space efficient iron storage (Chasteen and Harrison 1999). The Fe^{2+} iron entering ferritin is oxidised to Fe^{3+} and then sequestered as ferrihydrite, a less reactive form (Lane et al. 2015). Even within the labile iron pool, Fe^{2+} is likely rarely left unchaperoned due to its highly reactive, ROS producing nature. The poly (rC)-binding

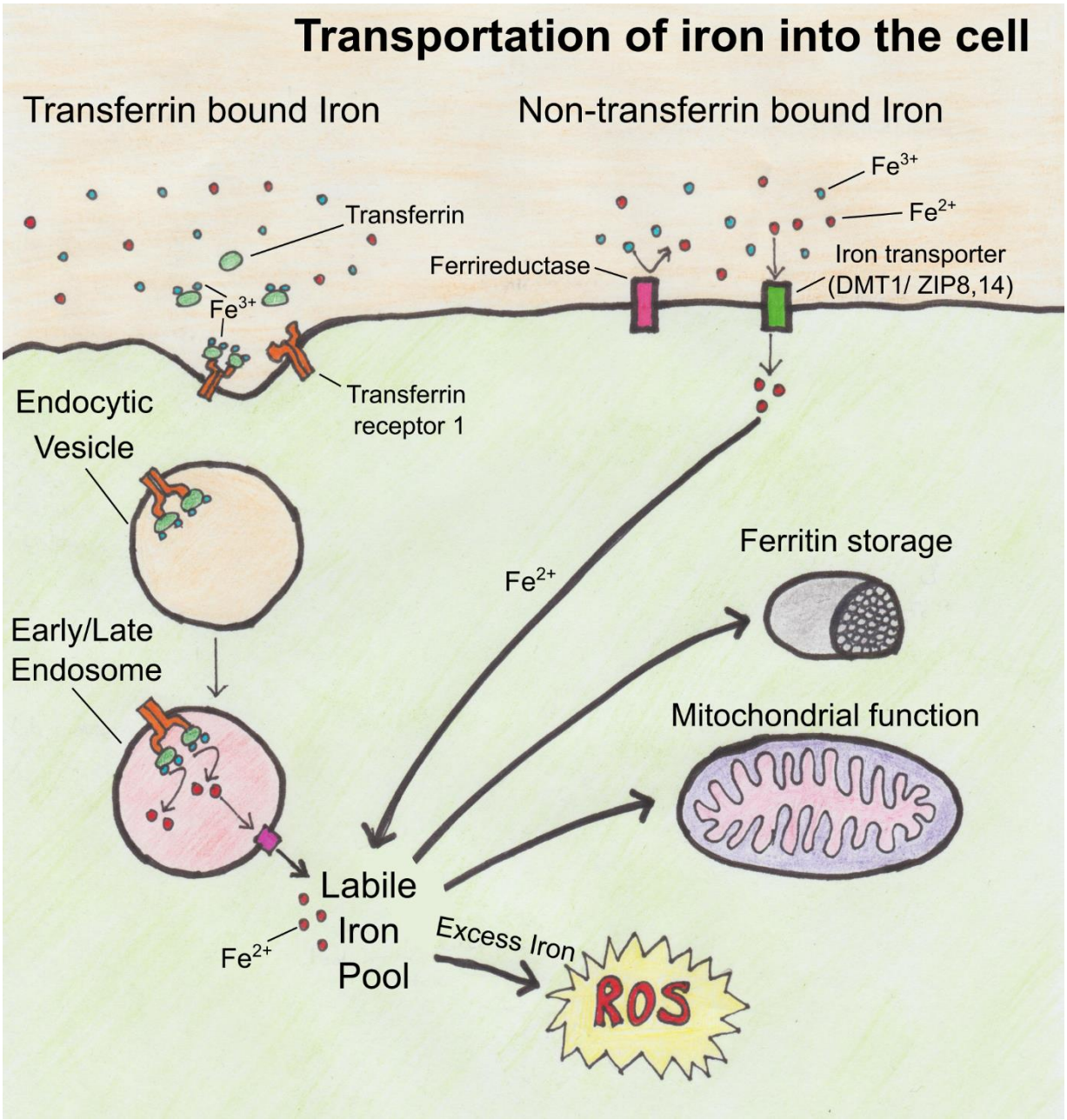

Figure 1-1: The two major iron uptake pathways of the cell. Ferric iron (Fe^{3+}) can bind to transferrin and can be transported into the cell by the binding of transferrin to the transferrin receptor 1 on the cell membrane. The iron is then internalised by receptor-mediated endocytosis of the transferrin receptor and moves through the endocytic pathway until the iron is subsequently released from the transferrin after pH is reduced in the late endosome/lysosomal compartments and the iron is reduced to ferrous iron (Fe^{2+}). The ferrous iron can be transported across the late endosomal/lysosomal membrane by an iron channel, such as divalent metal transporter 1 (DMT1), where it forms part of the labile iron pool (LIP) in the cytosol. Iron in the labile iron pool is then directed for storage as ferritin or used to aid mitochondrial function. In conditions of iron overload non-transferrin bound iron becomes more prevalent with iron transporters on the cell surface able to transport ferrous iron into the cell and ferrireductases able to reduce ferric to ferrous iron. The ferrous iron entering the cell forms part of the labile iron pool, however excess iron in the pool can lead to increased production of reactive oxygen species (ROS) in the cell.

proteins 1-4 are one such set of proteins thought to assist with iron chaperoning in the cell (Shi et al. 2008; Leidgens et al. 2013).

1.2.3 Cellular uptake of non-transferrin bound iron

Non-transferrin bound iron (NTBI) is iron in the body not bound to transferrin, heme or ferritin (or other chelating proteins) (Brissot et al. 2012). NTBI can be present at increased levels during iron overload from chronic disorders, such as hemochromatosis and transfusion iron overload, from conditions that can non-directly affect iron levels, or from high environmental exposure (Brissot et al. 2012). Most of the NTBI circulating in the blood is efficiently taken up by the liver (Brissot et al. 1985). The DMT1 and ZIP14 metal transporters can be a pathway for non-transferrin bound iron uptake into cells (Lane et al. 2015). There is also evidence that the transferrin receptor 2 may mediate uptake of non-transferrin bound iron through a receptor mediated endocytic pathway (Graham et al. 2008). One important factor in cellular uptake of NTBI is the oxidation state of the iron since it cannot cross membranes in the ferric (Fe^{3+}) state unless bound to transferrin (Brissot et al. 2012). The role of NTBI is of particular interest in the brain as transferrin is fully saturated in the CSF under normal conditions and because NTBI appears to be the main source for iron uptake by brain cells, such as astrocytes, oligodendrocytes, and microglia, with *in vivo* experiments in rats suggesting these cell types may not express the transferrin receptor (Moos 1996; Bradbury 1997). This has been suggested to be due to the role of these cell types in scavenging for NTBI in the brain with Bishop et al. (2011) finding that microglia were most efficient at accumulating NTBI, followed by astrocytes.

1.2.4 Iron oxidation and ROS

The main contributor to non-transferrin bound (free) iron toxicity in cells, is the ability of free iron to contribute to the production of free radicals, mainly reactive oxygen species (ROS). The generation of ROS can lead to oxidative stress, believed to be the key mechanism in concentration dependent iron cytotoxicity (Naqvi et al. 2010). The main process through which ROS generation from free iron oxidation is by Fenton and Haber–Weiss chemistries (**Figure 1-2**) (He et al. 2015; Meyerstein 2021). The main ROS product of Fenton chemistries is the hydroxyl radical, a highly reactive and short-lived species (Neyens and Baeyens 2003). Oxidative stress occurs when there is an increase in ROS that overwhelms the biological

systems ability to detoxify the reactive intermediates with antioxidants and repair damage caused (Manke et al. 2013). Oxidative stress induced by ROS can cause cytotoxic changes in cells, including lipid peroxidation, amino acid oxidation in proteins, oxidative loss of enzyme activity and DNA/RNA damage that can ultimately lead to cell death.

Haber Weiss Reaction

$$(1)\ Fe^{3+} + \cdot O_2{}^- \rightarrow Fe^{2+} + O_2$$

Fenton Reactions

$$(2)\ Fe^{2+} + H_2O_2 \rightarrow Fe^{3+} + OH^{\cdot} + OH^-$$

$$(3)\ Fe^{2+} + OH^{\cdot} \rightarrow Fe^{3+} + OH^-$$

Net reaction

$$(4)\ \cdot O_2{}^- + H_20_2 \rightarrow O_2 + OH^{\cdot} + OH^-$$

Further Fenton reaction

$$(5)\ Fe^{3+} + H_20_2 \rightarrow Fe^{2+} + OOH^{\cdot} + H^+$$

Figure 1-2: Iron catalysed production of oxygen radicals. Haber Weiss chemistry **(1-3)** makes use of Fenton reactions **(2,3)** to create net production of oxygen radicals **(4)** with iron catalysing the reaction. The Fe^{3+} produced by the Fenton reaction **(2,3)** can be converted back into Fe^{2+} **(1)** so the process becomes a cycle. Fe^{3+} can also undergo a Fenton reaction **(5)** to produce oxygen radicals and be converted back into Fe^{2+} (Kirschvink et al. 1992; Neyens and Baeyens 2003).

A three-tiered model has been developed for the response of cells to oxidative stress after treatment with transition metal oxide nanoparticles (Huang et al. 2010; Manke et al. 2013). The first tier represents mild oxidative stress and involves transcriptional activation of antioxidant enzymes, such as HO-1, NQO1, superoxide dismutase, catalases and glutathione peroxidases. If the first tier fails to restore a redox equilibrium, the tier two response is initiated, involving activation of pro-inflammatory signalling pathways. If this response is still unable to normalise the redox equilibrium, often the case with high levels or prolonged periods of oxidative stress, then permanent cell changes may take place resulting in

mitochondrial membrane damage and subsequent electron chain dysfunction, leading to cell death.

1.2.5 Iron oxide nanoparticles (IONPs)

IONPs present in a range of different crystalline phases, all with different physical and chemicals properties, such as (FeO), goethite [FeO(OH)], ferrihydrite [$Fe_5HO_8(4H_2O)$], magnetite (Fe_3O_4), hematite (α-Fe_2O_3), and maghemite (γ-Fe_2O_3) (Seabra et al. 2017). The two most common IONPs for use in biological and medical settings are magnetite and maghemite as they can form small nanoparticles with high surface area: volume ratios that have strong magnetic properties and to which a large range of ligands can be attached (Seabra et al. 2017). These two IONP, especially magnetite, are also common forms of iron oxide in PM2.5 and PM0.1 air pollution (Maher 2019).

Conversion of magnetite to maghemite

$$(1)\ Fe_3O_4 + 2H^+ \rightarrow \gamma Fe_2O_3 + Fe^{2+} + H_2O$$

Fenton reactions of magnetite

$$(2)\ Fe_3O_4 + 4H_2O \rightarrow Fe^{2+} + 2Fe^{3+} + 8OH^-$$

$$(3)\ Fe^{2+} + H_2O_2 \rightarrow Fe^{3+} + OH^{\cdot} + OH^-$$

Figure 1-3: Oxidation of Magnetite. (1) Magnetite (Fe_3O_4) can be oxidised to maghemite (γFe_2O_3). **(2** and **3)** Magnetite can also be oxidised to via Fenton reactions to produce oxygen radicals (Kirschvink et al. 1992; He et al. 2015; Schwaminger et al. 2017).

Magnetite and maghemite form specific close-packed cubic lattice structures with iron ions located at interstices between oxygen ions (Seabra et al. 2017). Both iron oxides form a very specific structure called an inverse spinal ferrite consisting of a unit cell of atoms based on a cubic structure of 32 oxygen atoms, that slot together in a repeating pattern (Manjunatha et al. 2019). In magnetite, oxygen ions form a face centred cubic configuration with Fe^{2+} ions and half the Fe^{3+} ions occupying octahedral sites while the other half of the Fe^{3+} ions occupy tetrahedral sites. Magnetite contains a ratio of Fe^{2+} / Fe^{3+} of 0.5, and forms a range of

crystal structures, commonly octahedrons (Seabra et al. 2017). Maghemite also forms a face centred cubic configuration but has some vacant cation sites (normally octahedral sites) to compensate for its greater positive charge. Its structure involves Fe^{3+} ions occupying both octahedral and tetrahedral sites (Machala et al. 2011). Due to their similar structure, magnetite can be oxidised to maghemite (**Figure 1-3**), while both can be degraded under the right conditions to produce iron ions (Fe^{2+}/Fe^{3+}) that can be oxidised via Fenton reactions to produce hydroxyl radicals (**Figure 1-3**) (Schwaminger et al. 2017).

1.2.6 Superparamagnetic iron oxide nanoparticles (SPIONs)

Superparamagnetic iron oxide nanoparticles (SPIONs) refer to IONPs that have superparamagnetic properties, such as magnetite (Fe_3O_4), maghemite (γ-Fe_2O_3), hematite (α-Fe_2O_3) and goethite (FeO(OH)) (Khatami et al. 2019). Superparamagnetism, is a type of magnetism that can occur only in sufficiently small ferrimagnetic or ferromagnetic nanoparticles (<100 nm), that can respond as a single magnetic domain (Hu et al. 2019).

A complete description of this process can be read in the paper by Laurent et al. (2008), but an overview of the process is described here. Paramagnets describes particles that can be magnetised under an external magnetic field, but then lose magnetism when the field is removed. Nanoparticles typically have magnetic anisotropy, a preferred direction for magnetization alignment out of the two stable orientations. Thermal energy can cause the nanoparticle to randomly flip their direction of magnetisation between these two orientations. The average time between two flips is known as the Neel relaxation time. When no external magnetic field is applied, these random flips result in a net magnetisation of zero, as the time spent in both orientations balances out. However, when an external magnetic field is applied paramagnetic materials can align with the direction of the applied field, unlike diamagnetic materials which become repelled by the external field and align in the opposite direction. Unlike ferrimagnets, paramagnets do not retain any magnetisation after the external field is removed. Superparamagnetic materials differ to paramagnetic materials in that they can exhibit this described behaviour below the Curie temperature, while in paramagnetic materials, these properties only occur above the Curie temperature. The Curie temperature can be defined as the temperature at which a ferromagnetic material (constant magnetism) loses its magnetic properties and becomes paramagnetic.

Superparamagnets, therefore, behave as inducible magnets over a much wider range of temperatures than paramagnets and can generate higher-gradient magnetic fields as well as having greater magnetitic susceptibility (stronger magnetism) (Orel et al. 2019). The generation of high-gradient magnetic fields is important for improving the nanoparticle's ability to move towards the source of magnetisation, especially necessary in a liquid solution, where magnetic attraction needs to overcome hydrodynamic drag (Li and Ren 2018). Superparamagnets are preferable in medical or biological applications as they can become highly magnetized when exposed to a magnetic field but have no permanent magnetisation when the field is turned off (Orel et al. 2019). This control for switching the nanoparticles between magnetic and non-magnetic states, has been integral for many of the developed uses of these particles in biological applications, such as the use of SPIONs to promote targeted apoptosis of cancer cells (Subramanian et al. 2018), and for organelle purification (Walker 2015).

1.2.7 Biomedical applications of Iron oxide nanoparticles

Promoted by their superparamagnetic properties together with their high colloidal stability, iron oxide nanoparticles (IONPs) have become a popular choice of nanoparticle in a range of biomedical applications (Nikzamir et al. 2021). Due to the relative abundance of iron utilized in the human body, IONPs have often been considered as biocompatible with low toxicity in humans (Lee et al. 2015b), despite evidence to the contrary for some types of nanoparticles (Alarifi et al. 2014; Abakumov et al. 2018).

SPIONs have been intensely investigated as magnetic resonance imaging (MRI) contrast agents, primarily for detecting tumours and for imaging the central nervous system and gastro-intestinal tract (Nikzamir et al. 2021). In the 1990s, SPION based MRI contrast agents including Feridex and Resovist were developed for imaging the liver and in particular liver macrophages called Kupffer cells (Miller et al. 2017). However, in early 2000s manufacturers ceased commercial production due to lack of sales. A new generation of SPION based MRI contrast agents was then developed with more extensive dextran coating to increase stability and dispersion, including Ferumoxtran which was smaller, more uniform and had a longer circulating half-life than its predecessors (Harisinghani et al. 2003). Ferumoxtran also had greater imaging applications as it facilitated imaging of the lymph node metastasis as

well as liver cells. However, this was also later withdrawn from the market (Miller et al. 2017). This led to the development of Ferumoxytol, an iron oxide nanoparticle for treatment of iron-deficient anaemia and as an MRI contrast agent, FDA-approved since 2009 (Provenzano et al. 2009; Lu et al. 2010). Ferumoxytol is widely available in the US (marketed as Feraheme) along with Canada and Europe (marketed as Rienso). All the above-mentioned iron oxide formulations have been used in humans and in the case of Ferumoxytol, continue to be. While Ferumoxytol is considered much safer than the older type of iron replacement therapy iron dextran (Dexiron) and an improvement on the previous MRI contrast agents, it still carries some risks, including anaphylaxis in a small number of cases.

IONP contrast agents are also being investigated for imaging of amyloid plaques in diagnosis of Alzheimer's disease, due to the ability of iron oxide, in particular magnetite, to bind to these plaques (Azria et al. 2017). IONP tracking agents, detectable by MRI, have been tested for tracking stem cells in the human brain after brain trauma (Zhu et al. 2006), or in patients with melanoma (de Vries et al. 2005). IONP have also been investigated for targeted drug delivery (Lungu et al. 2019; Vangijzegem et al. 2019) especially common as cancer treatments. For example, IONP coated with chitosan and curcumin (Pham et al. 2016) or chitosan and phytic acid (Barahuie et al. 2017) have been shown to be effective in reducing proliferation of certain cancer cells under laboratory conditions. IONP have also been investigated for hypothermia and thermoablative treatment of cancers, due to the superparamagnetic properties of cancer-targeted IONP which can cause heat generation in the surrounding regions, with a temperature increase of 11–12 °C, through the application of alternating magnetic fields (Hernández-Hernández et al. 2020).

1.2.8 Industrial applications and production of IONP

The inherent magnetic properties of iron oxides have been utilized in a broad range of applications including for magnetic seals and inks, magnetic recording media, catalysts, and ferrofluids (Teja and Koh 2009). Ferrofluid solutions produced by the company Liquids Research Ltd (https://liquidsresearch.com/) are being applied for a range of uses including vehicle and exercise suspension systems, for improving loudspeaker efficiency and reducing overheating related failure, and for producing magnetically readable printing ink that can be used for bar coding and document sorting. Magnetite and maghemite are now commonly

used in magnetic storage (Sharrock and Bodnar 1985; Aghazadeh et al. 2018), with the superparamagnetic properties of the metals being the limiting factor for storage capacity of data hard drive disks and so have become integral to technological progress.

Iron oxides, including haematite and magnetite, can be released as air pollution from fuel combustion, engine wear and brake pad wear (Chandra Verma et al. 2015; Pattammattel et al. 2021). It has been estimated that 35% of the break pad wear is emitted as airborne PM, and 86% of these particles are smaller than 2.5 μm, much of which is likely magnetite due to its prevalence in the composition of brake pads (Sanders et al. 2003). Iron oxide nanoparticles can also be added to fuels as it can increase fuel fluidity, reducing resistance and increasing fuel efficiency (Aalam 2015; Suhel et al. 2021). Iron oxide nanoparticles can also be used to enhance heat transfer and reactivity, along with reducing NO_2 production, by binding available oxygen (Mehta et al. 2014; Wen et al. 2019). High levels of magnetite and other iron oxides are found near roads and increased in areas with, and during times of, high air pollution (Mitchell and Maher 2009). Abundant within roadside air pollution are magnetite nanoparticles with a rounded morphology similar to heat treated nanoparticles produced at high-temperatures, therefore, likely combustion- and friction-derived nanoparticles (Chen et al. 2006; Maher 2019).

With the growing variety of present and potential applications for IONPs, and specifically SPIONs, in biomedical and nanotech settings and considering their potential health risks as an air pollutant, it is important to understand their impacts on the health and function of cells. When cells are exposed to IONPs, these are likely first to enter the cell via endocytosis and then be trafficked through the endolysosomal system.

1.3 Cellular trafficking pathways

1.3.1 An overview of endocytosis

Endocytosis is the vital cellular mechanism by which external molecules and macromolecules can be internalised into the cell (Kumari et al. 2010). Endocytosis works as the opposite of exocytosis, which is the mechanism by which unwanted or toxic molecules are ejected from the cell and new lipids and proteins can be delivered to the cell membrane

(Doherty and McMahon 2009). Together the balance of endocytosis to exocytosis maintains precise regulation of interactions between the cell and its surrounding environment. Endocytosis mechanisms are the primary route for uptake of nanoparticles from the cells external environment (Iversen et al. 2011).

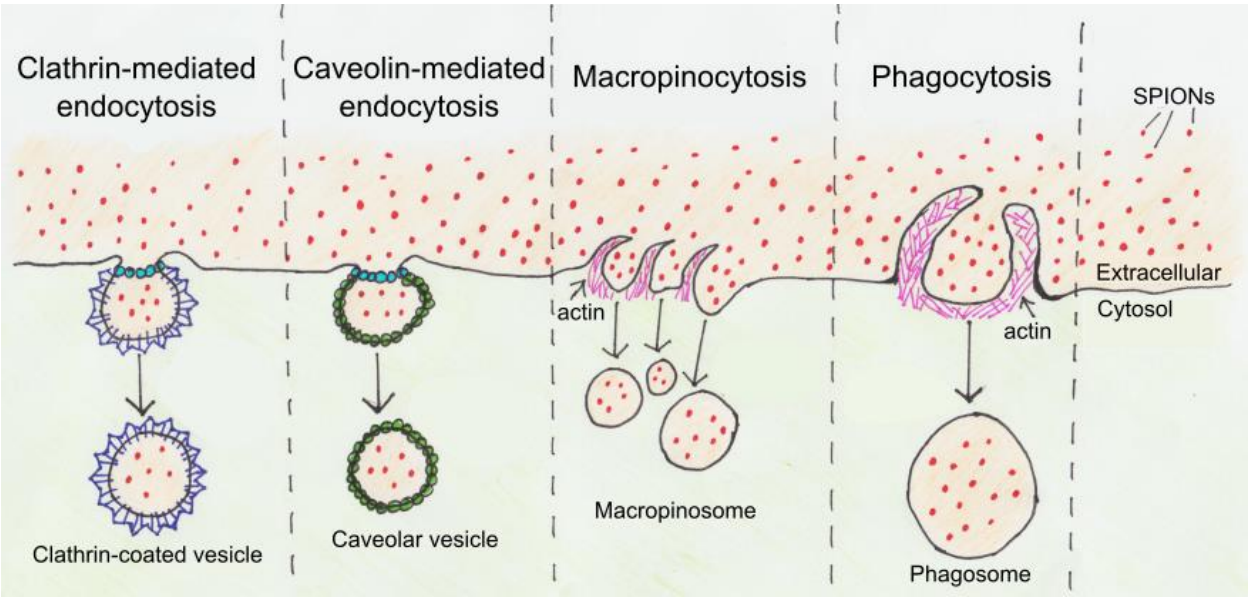

Figure 1-4 : An overview of pathways for cellular endocytosis. Clathrin-mediated endocytosis involves formation of a triskelion cage mediated by clathrin proteins to produce a clathrin-coated vesicle. Caveolin-mediated endocytosis involves initiation from caveolae domains, lipid rafts enriched in cholesterol, sphingolipids and the protein caveolin to produce a caveolar vesicle. Macropinocytosis occurs when ruffles form in the cell membrane due to the creation of lamellipodia by actin disruption and repolymerisation to form large, irregularly shaped macropinosomes. Phagocytosis involves identification of a target particle by phagocytic receptors, which initiates signalling cascades causing remodelling of cell membrane lipids and the actin cytoskeleton, resulting in extension of the cell membrane around the particle and forming a phagosome.

Endocytosis can be split into two main pathways, clathrin mediated endocytosis, and clathrin-independent endocytosis (including caveolae-mediated endocytosis, phagocytosis, and macropinocytosis), see Figure 1-4. Both pathways involve a section of cellular membrane being folded in on itself to form a pouch that once spherical can detach internally from the membrane, engulfing molecules for uptake into an intracellular vesicle. Once formed, endocytic vesicles are then trafficked to the endolyososomal system so the contents of the vesicles can be sorted by the cell.

1.3.2 Clathrin-mediated endocytosis

Clathrin-mediated endocytosis (CME) is by far the best studied of the endocytic mechanisms. It has been observed to be one of the most import routes by which processes including, nutrient uptake, receptor internalisation (Canton and Battaglia 2012), and recycling, as well as synaptic vesical recycling in neurones, (Rizzoli and Betz 2004), can occur. This process of CME can be split into several steps: initiation, cargo selection, coat assembly and stabilization, membrane scission and vesicle uncoating (Kaksonen and Roux 2018). This series of steps is not in reality a linear distinct process, but many of these steps are occurring alongside each other and simultaneously supporting continuation of steps described before and after them (Taylor et al. 2011). Clathrin plays an important role in the vesicles formation, by forming the clathrin triskelion, a three-legged pinwheel-shaped heteropolymer that in the presence of assembly proteins can polymerise into a clathrin cage (Ferguson et al. 2008). As clathrin polymerises the membrane it is bent or curved inwards as this process progresses, forming a curved clathrin cage around the membrane and budding at the endocytosis site, producing the characteristic clathrin-coated pit (Kaksonen and Roux 2018).

1.3.3 Clathrin-independent endocytosis

Several forms of clathrin-independent endocytosis are similar in process to clathrin-mediated endocytosis but lack clathrin coated pits and can instead be mediated by other components including, caveolae, flotilins and Arf6 (Mayor et al. 2014). Of these, caveolae-mediated endocytosis is the best understood and involves initiation of the endocytosis from caveolae domains, lipid rafts enriched in cholesterol and sphingolipids and with the dimeric protein caveolin forming 50-100 nm flask-shaped invaginations in the plasma membrane (Razani et al. 2002). This pathway of endocytosis is specific to uptake of certain molecules including albumin (Schnitzer et al. 1994) and cholera/tetanus toxins (Montesano et al. 1982).

1.3.4 Phagocytosis

Phagocytosis is necessary for ingestion and elimination of microbial pathogens and for tissue homeostasis by clearance of apoptotic cells, so is of particular importance for the

endocytosis of large particles (>0.5 µm), that are too big for endocytosis by other pathways (Aderem and Underhill 1999). Specialist cells that can conduct phagocytosis are called phagocytes. Professional phagocytes are cells that are highly efficient at phagocytosis and include immune cells, such as macrophages and neutrophils (Rabinovitch 1995). While many cells can be non-professional phagocytes playing a role in the clean-up of apoptotic cells, including fibroblasts, epithelial cells, and endothelial cells (Rosales and Uribe-Querol 2017). As it is such a sensitive and complex organ, the brain has its own specialist phagocytes called microglia (Vilhardt 2005).

In mammals, phagocytes recognise material for phagocytosis via a variety of receptors, divided into two categories, nonopsonic or opsonic receptors (Rosales and Uribe-Querol 2017). Nonopsonic receptors directly recognize molecular groups on the surface of the phagocytic targets, while opsonic receptors recognise host-derived opsonins which can bind to foreign particles targeting them for ingestion. After a target particle is identified, phagocytic receptors initiate signalling cascades causing remodelling of cell membrane lipids and the actin cytoskeleton, resulting in extension of the cell membrane with temporary projections of cytoplasm, called pseudopods that surround the particle (May and Machesky 2001; Rosales and Uribe-Querol 2017). At the point of contact a depression in the membrane, called the phagocytic cup, is formed (Rosales and Uribe-Querol 2017). Actin filaments are disrupted at the base of the phagocytic cup, just before the protrusions of the membrane fuse at the opposite end, sealing to produce a new phagosome (Marie-Anaïs et al. 2016).

To detoxify its contents, the phagosome goes through a process called phagosome maturation, consisting first of fusion with early endosomes, with maturation progressing through the endolysosomal system with appearance of late endosomal and lysosomal markers, finally producing a phagolysosome (Rosales and Uribe-Querol 2017). The phagolysosome has an altered membrane composition and highly acidic, degradative environment, promoting breakdown of the phagocytosed material into its constituent components.

1.3.5 Macropinocytosis

Macropinocytosis is different to other forms of endocytosis, such as CME and phagocytosis in the respect that it is not regulated by direct action of cargo and receptor molecules. It was first observed by Warren Lewis (1937), using time lapse microcinematography in rat macrophage cells showing characteristic ruffling on the cell surface that led to fluid engulfment into intracellular vesicles. Lewis first named this process pinocytosis, however, it was then renamed macropinocytosis to differentiate it from processes involving smaller vesicles (Lim and Gleeson 2011). As this then suggests, macropinocytosis produces large (diameter ~0.2-5 µm) heterogenous vesicles, called macropinosomes that have no apparent coat structures (Hewlett et al. 1994).

Macropinocytosis normally occurs in response to activation of receptor tyrosine kinases by growth factors (Haigler et al. 1979; Racoosin and Swanson 1989; Schmees et al. 2012). However, some types of specialised cells are capable of constitutive macropinocytosis, such as antigen-presenting cells (Norbury et al. 1995) and microglia, the macrophage of the CNS (Doodnauth et al. 2019). At the cellular membrane, ruffles form due to the creation of lamellipodia by actin disruption and repolymerisation beneath the membrane at that site. Most of the lamellipodia formed will retract back into the cell, however, some form cup-shaped ruffles, followed by contraction of the actin network at the rim to close the cup and fusion of the membrane to form large, irregularly shaped macropinosomes (Swanson 2008). Owing to the large size of macropinosomes, macropinocytosis acts a non-selective way for cells to internalise large quantities of extracellular fluid and cellular membrane (Mercer and Helenius 2012).

1.3.6 Endocytosis of nanoparticles

The mechanism of endocytosis utilised for uptake of nanoparticles is likely highly dependent on size. While phagocytosis is often associated with large particles, >1 µm, it has also been shown as a viable route of uptake for nanoparticles, including polyethylenimine and polyethylene glycol coated 10 nm iron oxide nanoparticles (Feng et al. 2018), 30-50 nm gold nanoparticles (Krpetić et al. 2010) and of 4 and 20 nm silver nanoparticles (Park et al. 2011).

The other highly relevant mechanism for uptake of larger particles is macropinocytosis. Although this process is cargo unspecific, it can still lead to a high level of nanoparticle

uptake, especially when treatments involve high nanoparticle concentrations (Canton and Battaglia 2012). Macropinocytosis was found in one study to be the dominant pathway for entry into A-549 cells for 6 nm amino-dextran coated magnetite nanoparticles (Cañete et al. 2010). In another study, internalisation of 20 and 60 nm carboxydextran-coated SPIONs into human macrophage occurred by clathrin-mediated endocytosis (Lunov et al. 2011).

Often it is likely uptake in cells occurs simultaneously through multiple pathways. For example, endocytosis of 5-20 nm IONP into microglia was shown to be mediated by both macropinocytosis and clathrin-mediated endocytosis (Luther et al. 2013). Importantly macrophages, such as microglia, are both phagocytic and are capable of constitutive macropinocytosis, meaning uptake of nanoparticles by these pathways is likely to be more common in these cell types. It is likely that the mechanism of nanoparticle uptake is highly dependent on the size, composition and coating of the nanoparticles as well as the cell type into which the nanoparticles are being endocytosed.

There are also suggestions that nanoparticles can induce deformation and complete invagination of the membrane without normal endocytic mechanisms (Lipowsky and Döbereiner 1998; Deserno 2004). These studies have suggested that when phospholipid membranes wrap around spherical particles, then the attraction between the curved nanoparticle surface and the cell membrane produces enough deformation for engulfment. This idea is further corroborated by the uptake of silica particles into live red blood cells, which are incapable of endocytosis (Zhao et al. 2011).

1.3.7 The endolysosomal system

Once external material has been internalised into an intracellular vesicle it is trafficked through the endolysosomal system. This is a multistep process (see **Figure 1-5**), starting with the fusion of internalised vesicles with early endosomes, which mature to late endosomes and then fuse with lysosomes (Mayor et al. 2014). This is a highly dynamic process meaning these organelles are not easily defined as they experience a range of states depending on their progression through these different processes (Elkin et al. 2016).

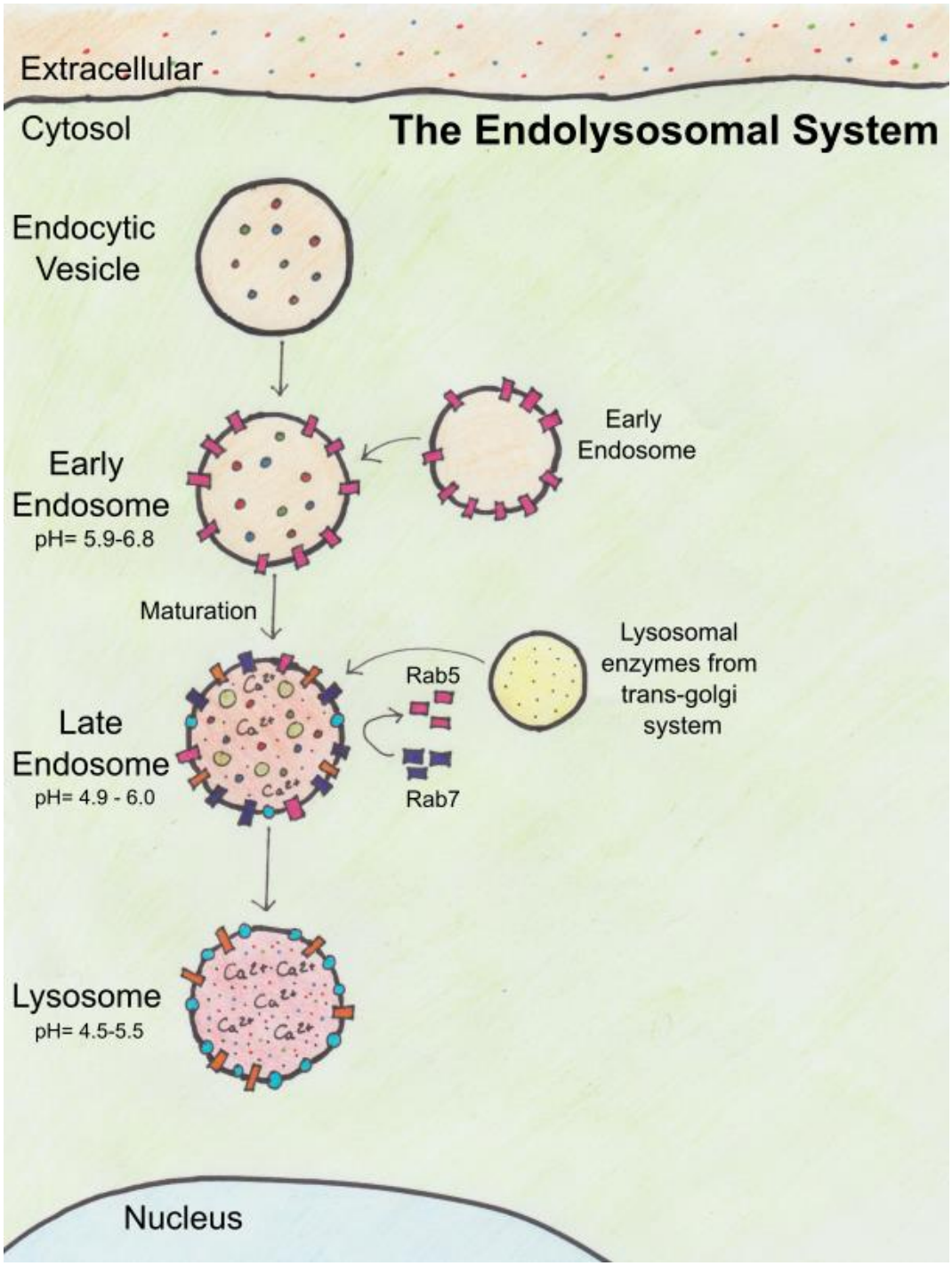

Figure 1-5: An overview of the trafficking pathway through the endolysosomal system. After endocytosis, endocytic vesicles fuse with early endosomes, which act as a sorting hub, recycling receptors and proteins back to the cell membrane, sending nutrients to the trans-Golgi network and selecting targeted molecules for subsequent degradation. Early endosomes can be characterised by the presence of a membrane-associated GTPase, Rab5 and mature to late endosomes characterised by Rab7, with a resultant change in Ca^{2+} concentration, membrane lipids and proteins, and a reduced pH. Vesicles of lysosomal proteins sent from the trans-golgi network are delivered to late endosomes. Late endosomes then either mature into or fuse with lysosomes, creating an acidic lysosomal compartment where the majority of degradative activity occurs.

1.3.8 Early endosomes

In eukaryotes, the endosome is important for regulating whether vesicle components need to be sent for recycling or degradation (Scott et al. 2014). Nearly all the different endocytosis pathways culminate with produced vesicles being delivered to early endosomes often within a few minutes of formation (Canton and Battaglia 2012). The endosome acts as a trafficking hub for incoming cargo. Housekeeping receptors and other reusable proteins are recycled back to the plasma membrane by the recycling endosome, while usable nutrients and other molecules are sent to the trans-Golgi network via retrograde traffic and molecules targeted for degradation are sorted to the lysosome (Scott et al. 2014).

Early endosomes are generally formed in the peripheral cytoplasm with a slightly acidic intraluminal pH (Hu et al. 2015). They can be characterised by the presence of Rab5, a small GTPase with roles in regulating membrane docking and fusion with endocytic vesicles (Christoforidis et al. 1999) as well as regulating interaction with the microtubule network, promoting movement away from the cells periphery and towards the nucleus (Nielsen et al. 1999). The early endosome is only weakly acidic (pH 6.8-5.9) with a progressively reducing pH as it moves away from the cell periphery, mostly through the action of a transmembrane proton pump, the vacuolar ATPase (V-ATPase) (Lafourcade et al. 2008; Huotari and Helenius 2011). The V-ATPase is a rotary nanomotor comprising of multiple subunits with multiple isoforms arranged into two sub-complexes: the V1 subcomplex in the cytoplasmic domain and the V0 subcomplex in the vacuolar domain (Pamarthy et al. 2018). The V1 subcomplex is responsible for ATP hydrolysis to power the pump, while the V0 subcomplex manages the proton translocation across the membrane through hemi-channels.

The early endosome also has an enrichment of the phospholipid, phosphatidylinositol-3-monophosphate, along with a low Ca^{2+} concentration (3-40 μM),which has been suggested to be due to the quick release (within 20 minutes) of internalised extracellular Ca^{2+} from the early endosome via a cation channel (Gerasimenko et al. 1998). There is some evidence this leak could be mediated by TRPML3 (Lelouvier and Puertollano 2011). In early endosomes plaques containing clathrin and components of the endosomal sorting complex required for transport (ESCRT) can start to sort ubiquitinated membrane proteins away into intraluminal vesicles, a few of which may exist per early endosome (Piper et al. 2014).

1.3.9 Late endosomes

Early endosomes mature to late endosomes with a resultant change in pH, Ca^{2+} concentration and membrane lipids and proteins. Through a process of compartment conversion there is a Rab cascade where Rab5 recruits an exchange factor that activates and recruits Rab7 which in turn recruits a GTPase to inactivate the Rab5 (Elkin et al. 2016). In this way a transition is affected between the dominant membrane Rab proteins in early endosomes and late endosomes, changing the membranes' identity and function. Clathrin coated vesicles, containing lysosomal proteins, targeted by the mannose-6-phospahte receptor are released from the trans-Golgi network and bind to late endosomes, where the lysosomal proteins can accumulate ready for digestion when activated by the drop in pH that occurs through the maturation process (Braulke and Bonifacino 2009). Rab7 can recruit the retromer complex to late endosomes to 'rescue' cargo receptors from lysosomal degradation and transport them back to the trans-Golgi network for recycling (Burd and Cullen 2014). Rab7 is also important for continuing the movement started by Rab5 along the microtubule network from cell periphery to a juxtanuclear position (Johansson and Olkkonen 2005).

During maturation, there is a change in lipid enrichment in the endosomal membrane from phosphatidylinositol-3-monophosphate to phosphatidylinositol 3,5-bisphosphate (Michell et al. 2006). Lysosomal proteins, such as LAMP1, also start to accumulate in the late endosomal membrane (Cook et al. 2004) and the number of intraluminal vesicles in each endosome increased (often to >30), each with a diameter of 50-60 nm (Falguières et al. 2008). The pH continues to drop in late endosomes, normally in the pH range of 6-4.9, due to the continued activity of the vATPase (Huotari and Helenius 2011). The concentration of Ca^{2+} in late endosomes/lysosomes also increases from the low early endosome levels. (Lloyd-Evans et al. 2008) .

There have previously been several theories for how cargo was transported between late endosomes and lysosomes, as has been reviewed by Luzio et al. (2007). In the maturation theory endosomes mature to lysosomes, by changes in membrane components and internal composition, similar to how early endosome mature to late endosomes (Luzio et al. 2007). In the vesicular theory, vesicles bud from the late endosome and then deliver their cargo to the lysosome. While a third theory the 'kiss and run' model suggests late endosome and

lysosomes fuse (kiss) to enable content exchange and then separate again (run), similar but not the same as the 'fusion-fission' theory where lysosomes fuse with late endosomes but can then be reformed as sperate organelles.

1.4 The lysosome

1.4.1 Discovery of lysosome

The lysosome was discovered by a British-born, Belgian biochemist, Christian de Duve, in 1955, while he was investigating the action of insulin at a University laboratory in Louvain (Sabatini and Adesnik 2013). His group was studying the distribution of the enzyme glucose-6-phosphatase in rat liver tissue, primarily by using centrifugation to separate cell fractions and enzyme assays to identify which fractions had the highest activity, which they found to be principally in a small granule fraction termed "microsomes" (Beaufay and De Duve 1954). It was at this stage that de Duve's group started studying the activity of a separate enzyme with a low optimum pH of 5, acid phosphatase, initially chosen as a control as it is found in almost all tissues. By serendipity, a member of de Duve's team left a sample in the refrigerator over a long weekend and when subsequently tested it was found the acid phosphatase activity in the sample had increased equal to the combined total of all fresh centrifuge-separated fractions (De Duve et al. 1955; de Duve 1963). Similar outcomes were achieved by freeze-thawing samples and by membrane-destabilising agents. This then led to de Duve's insightful conclusion that the latent enzyme was sequestered in membrane sacs, a theory that would later be proven to be correct, and the newly discovered organelle termed the lysosome (de Duve 1963; De Duve and Wattiaux 1966). For his ground-breaking work towards the identification of the lysosome, de Duve obtained a Nobel prize in 1974, as his early work paved the way for many future scientists to elucidate the inner workings of the cell and improve understanding and develop treatments for a whole range of lysosomal-related diseases.

1.4.2 Lysosomal function

Lysosomes are small, membrane-bound organelles present in all mammalian cells (excluding red blood cells), comprising ~5% of the total intracellular volume (Luzio et al. 2007). Electron

microscopy shows lysosomes to be of heterogeneous size and morphology, often containing electron dense deposits and membrane whorls (Luzio et al. 2007). Lysosomes are necessary for the degradation of intracellular material that is processed through endocytic pathways and through autophagy, a process discussed later in Section 1.5.

Only recently is the scope of roles the lysosome plays really being elucidated: from their primary role in the degradation of macromolecules and recycling of their components, to roles in Ca^{2+} signalling, nutrient sensing, metabolism, cell proliferation and apoptosis (Efeyan et al. 2015; Thelen and Zoncu 2017; Hesketh et al. 2018; Tang et al. 2020). One of main ways the lysosome can act as a regulator in these processes is due to its functional association with master growth regulator mTORC1, named for being the mammalian target of rapamycin complex (Ben-Sahra and Manning 2017). Initiation of mTORC1-driven signalling is led by binding of mTORC1 to the lysosomal surface, requiring both selected growth factors and nutrients (Saxton and Sabatini 2017). At the lysosome, mTORC1 activates S6-kinase by phosphorylation, promoting lipid and nucleotide biosynthesis, ribosome biogenesis, and a switch to glucose metabolism (Lawrence and Zoncu 2019). A major consequence of these changes is the upregulation of protein synthesis, contributing to increased cell growth and proliferation. Also, mTORC1 can regulate TFEB (transcription factor EB), a master transcriptional regulator of lysosomal biogenesis and also implicated in autophagy, endocytosis, exocytosis, lipid metabolism and Ca^{2+} signalling (Peña-Llopis et al. 2011). In a multi-step mechanism, mTORC1 can phosphorylate TFEB creating a high affinity binding site for YWHA regulatory proteins (Tyrosine 3-Monooxygenase/Tryptophan 5-Monooxygenase Activation protein or 14-3-3), which when bound lead to cytosolic retention of TFEB (Vega-Rubin-de-Celis et al. 2017). Inhibition of mTORC1 leads to dephosphorylation of TFEB so it can translocate to the nucleus where it promotes expression of lysosomal biogenesis-related genes (Settembre et al. 2012).

As well as breaking down cellular waste, preventing its build-up is also important, as undegraded material can be directly toxic or cause problems when stored, and for this reason there is a whole range of diseases linked to mutations in lysosomal proteins, known as lysosomal storage disorders (LSDs) (Platt et al. 2012). Presently there are ~70 different LSDs, nearly all of which are characterised by intra-lysosomal accumulation of storage material and neurodegeneration, often leading to early mortality (Cox and Cachón-González

2012). Recently an important role has been uncovered for the lysosome in the degradation of certain cellular proteins that otherwise can aggregate to form plaques. When normal lysosomal homeostasis is dysregulated, this can play roles in the development of Parkinson's disease (aggregation of α-synuclein), Huntington's disease (polyglutamine residues in aggregates of huntingtin) and Alzheimer's disease (aggregates of amyloid and tau) (Cox and Cachón-González 2012). While recent enthusiasm for investigating the genetic basis of complex multifactorial diseases using genome wide association studies (GWAS) has also linked the lysosome to the development of Parkinson's disease (Chang et al. 2017), Huntington's disease (Senkevich and Gan-Or 2020), Alzheimer's disease (Van Acker et al. 2019) and to multiple sclerosis (Sawcer et al. 2011).

1.4.3 Regulation of lysosomal pH

One of the defining features of the lysosome is the acidity of their lumen, with an internal pH ranging from 4.5-5.5 (De Duve and Wattiaux 1966; Wang et al. 2015). This is established by the vacuolar H^+ ATPase (V-ATPase), a proton pump present in the lysosomal membrane (as previously described in Section 1.3.8), and aided by the counterflux of other ions, including Cl^-, Na^+ and K^+ (Ishida et al. 2013). The acidity of lysosomes is key as it provides the optimal pH for the function of a range of hydrolases that facilitate the degradation of macromolecules in the cell (Perera and Zoncu 2016). The degradation of macromolecules is also important for liberation of amino acids, monosaccharides, and free fatty acids for reuse, to prevent wasting resources (Perera and Zoncu 2016).

One of the advantages of the degradative lysosomal enzymes having a low optimal pH is that many then have low activity at the higher pH of the cytosol, reducing their degradative capacity during transport to the lysosome or if released from the lysosome. Another protective method for transport of lysosomal enzymes to the late endosome, is that many of the enzymes, such as the cathepsins, are transported in a precursor form and require the action of proteolytic enzymes and/or low pH to activate (Lutgens et al. 2007). It is also possible that the acidic environment of the lysosome is more favourable for oxidative reactions, important for degradative efficiency (Hu et al. 2015).

Regulation of the V-ATPase could be through several mechanisms: including glucose metabolism, availability of the phospholipid, phosophinositide-3 kinase, and mTORC1

signalling (Cotter et al. 2015). The V-ATPase has also been reported to act as a pH sensor in the lysosome allowing a degree of self-regulation in adjusting lysosomal acidity (Marshansky and Futai 2008). Bafilomycin-A1 acts as a specific and potent V-ATPase inhibitor by binding to the V0 region of the V-ATPase and preventing proton translocation in a concentration-dependent manner (Wang et al. 2021b).

1.4.4 The lysosomal membrane

The membrane of the lysosome is formed by a single phospholipid bilayer with a thickness of ~7-10 nm (Neiss 1984) and is integral for keeping the lysosomes acidic environment, full of highly digestive enzymes, safely contained away from the rest of the cells' components, to avoid inappropriate autolysis. To protect the lysosomal membrane itself from degradation there is a dense layer of glycolipids and glycoproteins, with a thickness ~8 nm, at the inner luminal surface of the lysosome, named the glycocalyx (Neiss 1984). By electron microscopy, the glycocalyx can be visualised as a thin, electron translucent halo between the lysosomal membrane and the electron-dense lysosomal lumen (Neiss 1984).

The glycocalyx is largely composed of heavily glycosylated membrane proteins, of which lysosomal-associated membrane proteins 1 and 2 (LAMP1 and LAMP2) are among the most extensively glycosylated, with glycan chains that weigh more than their protein core (Wilke et al. 2012). LAMP1 and LAMP2 are highly abundant, representing ~0.1-0.2% of the total cell proteins and are enriched in lysosomes and late endosomes (Chen et al. 1985). They are both ubiquitous in human tissues and cell types, with higher expression in more metabolically active cells (Furuta et al. 1999).

The cell has had to evolve mechanisms for efficient transport of metabolites through the glycocalyx. For example, the NPC1 protein, which is enriched on late endosomal/lysosomal membranes, acts as a putative cholesterol/multi lipid transporter (Lloyd-Evans et al. 2008). The lysosome has also had to evolve specific methods for degradation of the lysosomal membrane, as it is being protected by the glycocalyx. This is the presumed role of the intraluminal vesicles seen to accumulate in late endosomes, as a collection of membrane and membrane-bound receptors set for degradation (Schulze et al. 2009). Lipid and protein compositional changes occur between the membrane of the late endosome and lysosome. The main change being the loss of mannose-6-phosphate receptors from the lysosomal

membrane after their retrieval by the retromer complex making this a key mechanism for differentiating late endosomes from lysosomes (Braulke and Bonifacino 2009).

1.4.5 Ca^{2+} signalling

As previously mentioned, the lysosome plays an important role in Ca^{2+} signalling within the cell. Calcium ions or Ca^{2+} are integrally important for cell homeostasis, playing an active role in unicellular organisms, but becoming universally important in multicellular life (Carafoli and Krebs 2016). As the third most abundant metal after iron and magnesium, calcium was readily available to cells, but what really makes calcium such an attractive signalling molecule is its ability to reversibly bind to a range of complex molecules and binding sites of irregular geometry with relative ease (Carafoli and Krebs 2016). Under normal physiological conditions the cytosolic Ca^{2+} concentration is ~100 nM (van der Kant and Neefjes 2014), substantially lower than lysosomal Ca^{2+} stores, estimated to be in the region of 500-600 µM (Christensen et al. 2002; Lloyd-Evans et al. 2008) and endoplasmic reticulum Ca^{2+} stores, estimated at ~0.5-2 mM (Burdakov et al. 2005; Lloyd-Evans et al. 2010; Lloyd-Evans and Platt 2011). Intracellular Ca^{2+} levels are kept substantially lower than extracellular Ca^{2+} concentrations, which are often in the region of 1 mM, (10,000-fold the level of cytosolic Ca^{2+}) to allow rapid increases in Ca^{2+} uptake necessary for tight regulation of signalling (van der Kant and Neefjes 2014). As Ca^{2+} cannot be metabolised, its storage within the cell is of significant importance and its tight regulation paramount (Clapham 1995). Therefore, dysregulation of Ca^{2+} signalling has been linked to a variety of diseases, in particular the LSDs (Lloyd-Evans and Platt 2011), but also Alzheimer's disease (McBrayer and Nixon 2013) and Parkinson's disease (Kilpatrick 2016).

1.4.6 Lysosomal Ca^{2+} signalling

As endocytosis has been shown to contribute only a small amount (~50 µM) to the total content of lysosomal Ca^{2+}, this suggested there was one or more lysosomal membrane Ca^{2+} transporters able to actively pump Ca^{2+} into the lysosome (Lloyd-Evans and Platt 2011). While several lysosomal Ca^{2+} sensors have been proposed, the identity of the lysosomal Ca^{2+} uptake pump still remains elusive (Wu et al. 2021). Lysosomal Ca^{2+} release is regulated by several transmembrane ion transporters, two of the most researched types are the two

pore channels (TPCs) and the transient receptor potential cation channel mucolipins (TRPMLs) .

The TRPML family, consists of three similar members, TRPML1, TRPML2 and TRPML3 (Puertollano and Kiselyov 2009). TRPML1 is mainly localised to late-endosomes-lysosomes and is permeable to Ca^{2+}, K^{+} and Na^{+} ions, with evidence it may also act as a H^{+} leak channel (Waller-Evans and Lloyd-Evans 2015). While it is likely permeable to several ions, under physiological conditions, TRPML1 is thought to act mainly as a transporter of Ca^{2+} from the lysosomal lumen to the cytosol (Kiselyov et al. 2005). Several studies have suggested TRPML1 is most active at low lysosomal pH, but that further reduction in pH below 4.5 decreases channel activity (Dong et al. 2008; Feng et al. 2014). The lysosomal protein, cathepsin B (optimal pH 4.5-5.5), can cleave TRPML1, inactivating it, likely as a regulatory mechanism of TRPML1 activity (Lloyd-Evans and Haslett 2016).

TRPML2 localisations have been difficult to fully explore, due to low expression and difficulty generating specific antibodies, however, evidence suggest its localisation in early-late endosomes and lysosomes, but with highest prevalence in recycling endosomes (Sun et al. 2015). TRPML2 functions as a non-selective cation channel permeable by Ca^{2+}, strongly inhibited by low pH, but not regulated by Ca^{2+} concentrations (Lev et al. 2010). TRPML3 is expressed in mainly in early-late endosomes, but also appears to localise with lysosomes and the plasma membrane; it is believed to act principally to reduce Ca^{2+} concentrations in the early endosome after endocytosis, as it has maximal activity at higher pH (~6-6.5), opposite to TRPML1 (Puertollano and Kiselyov 2009).

1.4.7 Lysosomal Iron regulation

Iron imported into the cell bound to transferrin is released from the transferrin receptor in the early endosome and is then likely exported into the cytosol from the late endosome mainly via DMT1, as described in Section 1.2.2. Yet iron can also be released in the lysosome from degradation of proteins where iron is used as a co-factor and potentially from degradation of extracellular material imported via phagocytosis, in phagocytic cells. Free iron release from endocytosed IONPs is also likely to occur in the lysosome as nanoparticle degradation is correlated with reduced pH, from more neutral cytosolic ~pH7.4 to more acidic lysosomal ~pH4.5-5.5 (Arbab et al. 2005; Lévy et al. 2010; Guzy et al. 2020). DMT1

(NRAMP2) is present in the late endosomal/lysosomal membrane and is likely able to export some of the lysosomal free iron, as Fe^{2+}, released from nanoparticle degradation (Tabuchi et al. 2000). However, when iron levels become high, other channels may be necessary for lysosomal iron export. Genetic evidence in mice suggests the necessity of other Fe^{2+} exporters in the endo-lysosomal membrane of certain cell types, such as in the placenta and in hepatocytes, where DMT1 activity was found not to be essential (Gunshin et al. 2005). TRPML1 has been shown to be permeable to Fe^{2+} in late endosomes and lysosomes, acting as a mechanism for Fe^{2+} release to the cytosol (Dong et al. 2008). Cell type dependent Fe^{2+} transporters also exist, such as NRAMP1 (natural resistance-associated macrophage protein 1, SLC11A1) (Blackwell et al. 2000). NRAMP1 is expressed almost exclusively in macrophages or macrophage-derived cells and neurons and is primarily localised to the late endosome/lysosome and phagosome, rather than the plasma membrane, believed to pump Fe^{2+} out of these organelles (Evans et al. 2001; Forbes and Gros 2003; Wu et al. 2017a). While other lysosomal iron channels may be yet to be discovered.

Free iron released in the lysosome may not be directly exported. The acidic environment of the lysosome has been shown to be an optimal environment for Fenton reactions, which occur more readily at low pH ~3-5 (Arnold et al. 1995). The change in potential for Fenton reactions is caused by increased oxidation potential and enhanced oxidative capacity of ·OH with decreasing pH, alongside increased stability and solubility of ferrous (Fe^{2+}) iron at lower pH (Duesterberg et al. 2008). Fenton reactions produce a highly reactive hydroxyl radical that has a short half-life, meaning if it is produced in the lysosome, it is likely to also have a reactive effect in the lysosome, causing lipid or protein peroxidation.

1.5 Autophagy

1.5.1 Autophagy overview

The term autophagy is derived from Greek meaning “self” and “to eat” and was coined by Christian de Duve to differentiate degradation of intracellular components (autophagy), from degradation of endocytosed extracellular substances, which he termed ‘heterophagy’. As the name suggests, autophagy is the process used by cells for recycling of their own organelles and cellular components to release nutrients (Glick et al. 2010). Autophagy is

crucial for normal cell homeostasis and is involved in multiple cellular processes, including starvation response, cell growth, innate immunity, cellular and tissue remodelling and cell death (Luzio et al. 2007). In virtually all cell types there is a constant low basal level of autophagy occurring to process homeostatic protein and organelle turnover (Levine and Kroemer 2008). When cells have a sudden need for intracellular nutrients/energy then autophagy is rapidly upregulated, such as during starvation, growth factor withdrawal or high energetic demands. Autophagy is also upregulated by cells needing structural remodelling or to rid themselves of damaging components, such as during oxidative stress, infection or accumulation of aggregated proteins. There are three types of autophagy in mammalian cells: micro-autophagy, chaperone-mediated autophagy and macro-autophagy all of which promote lysosomal degradation of cytosolic components (Glick et al. 2010).

Micro-autophagy is the simplest of the three autophagic processes, involving invagination of the lysosomal membrane to capture cytoplasmic contents, followed by internalisation for direct lysosomal degradation (Müller et al. 2000). This creates a non-selective process for autophagy that captures cytoplasmic cargo near the lysosome and acts as a method for recycling of the lysosomal membrane. Like micro-autophagy, chaperone-mediated autophagy provides a direct route for cellular components to be sent to the lysosome for degradation. Cytosolic proteins containing a specific targeting motif are complexed with chaperone proteins that dock at the lysosomal membrane, where the cytosolic proteins are unfolded, internalised into the lysosome, and degraded (Chiang et al. 1989; Bandyopadhyay and Cuervo 2008).

1.5.2 The process of macro-autophagy

Macro-autophagy (**Figure 1-6**) is the most prevalent type of autophagy and the type about which the most is known. Macro-autophagy involves the formation of an isolation membrane, known as a phagophore, derived from the lipid bilayer of the endoplasmic reticulum (ER), trans-Golgi network or endosomes (Glick et al. 2010). Although its exact origin in mammalian cells remains unknown, several studies suggest the phagophore is mainly derived from ER membrane (Hayashi-Nishino et al. 2009; Ylä-Anttila et al. 2009). The phagophore expands to engulf intracellular cargo in what is often considered as an indiscriminate, random selection process, but recent evidence suggests the likelihood of

phagophore receptors that could selectively target the induction of autophagy. Evidence suggests optineurin is an autophagy receptor at the phagophore interacting with adapter molecules and potentiating LC3-II production to induce selective targeting of bacteria, protein aggregates (by detection of polyubiquitination) or damaged mitochondria (known as mitophagy) (Bansal et al. 2018).

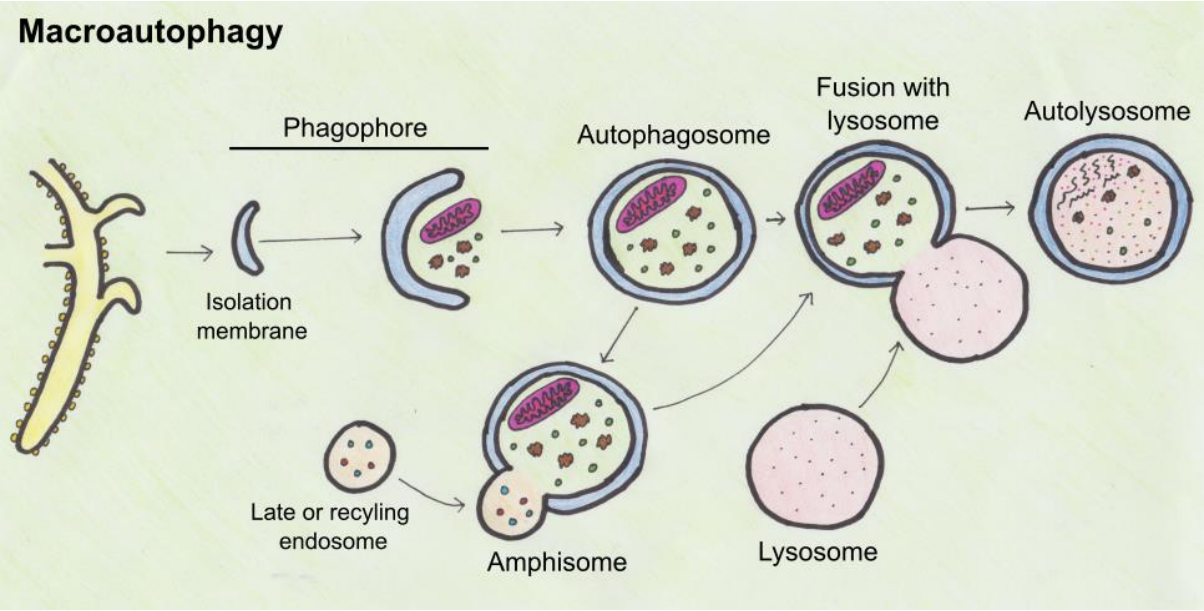

Figure 1-6: An overview of macroautophagy. First an isolation membrane is formed, often derived from the lipid bilayer of the endoplasmic reticulum. This membrane starts to expand forming a phagophore that expands to engulf intracellular cargo. When the edges of the phagophore meet and fuse, this forms a double membrane vesicle, called the autophagosome. The autophagosome then can fuse with a lysosome via the action of Rab7 to form an autolysosome, or it can fuse first to late or recycling endosomes to form amphisomes, which then subsequently fuse lysosomes to produce autolysosomes. In the autolysosome, hydrolytic enzymes can degrade the autophagic cargo, including whole organelles, releasing the liberated nutrients.

The phagophore expands around intracellular cargo, curving the membrane until the edges meet and fuse, sequestering cargo into a double membrane vesicle, called the autophagosome (Glick et al. 2010). At least 16 autophagy-related (ATG) proteins and phosphatidyl-inositol 3-kinase complex are involved in the construction of the autophagosome in a complex, multistep process. (Reggiori and Ungermann 2017). The autophagosome then can fuse with a lysosome via the action of Rab7 to form an intermediate organelle, the autolysosome (Gutierrez et al. 2004). Or it has been shown the autophagosome can fuse first to late or recycling endosomes to form amphisomes, which

then subsequently fuse lysosomes to produce autolysosomes, this process becoming more common under starvation conditions (Berg et al. 1998). In the autolysosome, the lysosomes hydrolytic enzymes can degrade the autophagic cargo, including whole organelles, releasing the liberated nutrients, such as amino acids, back out in the cytoplasm via lysosomal membrane permeases and transporters (Glick et al. 2010).

1.5.3 Regulation of macro-autophagy

One of the key regulators of macro-autophagy is TFEB, the master transcriptional regulator of lysosomal biogenesis. A rise in free cytosolic Ca^{2+}, believed to be regulated by TPML1 mediated Ca^{2+} release, can act as a potent inducer of macro-autophagy by activation of calcineurin (Medina et al. 2015). Calcineurin binds and dephosphorylates TFEB, which can then translocate to the nucleus, where as well as promoting gene expression for lysosomal biogenesis it also upregulates expression of autophagy-related genes (Medina et al. 2015). A rise in free cytosolic Ca^{2+} can also as act an inducer of macro-autophagy by inhibition of mTORC1 activity through a signalling pathway involving AMPK, that then causes increased nuclear translocation of TFEB (Høyer-Hansen et al. 2007).

Starvation has been well studied as a condition for the induction of autophagy, with studies demonstrating regulation of this pathway through a decreased ratio of ATP/AMP that is sensed by AMPK which acts to inhibit mTORC1 and increase autophagy generated ATP production (Hardie 2004). Regulation of starvation-induced autophagy by ROS generation regulating AMPK activation, has also been suggested (Li et al. 2013). Macro-autophagy can be inhibited by protein kinase A binding with cAMP in the presence of glucose to inhibit AMPK and activate mTORC1 (Grisan et al. 2021).

1.5.4 Impact of Iron on autophagy

Iron overload has been shown to impact on regulation of autophagy, with studies suggesting acute short term iron overload stimulates autophagy, likely as a compensatory measure against cellular stress (Chen et al. 2013a; Cen et al. 2018; Jahng et al. 2019). Alongside this rapid activation of autophagy, which can occur within 4-8 hours of iron overload, inhibition of mTORC1 (a potent repressor of autophagy) has been shown to occur (Jahng et al. 2019). While chronic iron overload has been shown to lead to accumulation of autolysosomes, while depleting free lysosomes, by preventing lysosomal reformation from autolysosomes

linked to inhibition of mTORC1 bound to autolysosomes (Jahng et al. 2019). Iron overload, as a result of magnetite nanoparticle treatment, has also been linked to increased autophagosome accumulation both in a human breast cancer cell line and, *in vivo*, in mice (Zhang et al. 2016a).

1.6 Mitochondria

1.6.1 Mitochondria Overview

The mitochondria are the powerhouses of the cell, generating ATP, the cells' energy currency, but also necessitating the high demand of cells for oxygen (Duchen 2004). It is thought that mitochondria evolved from a bacterial progenitor that entered a symbiotic relationship with the ancestor of eukaryotic cells (Leblanc et al. 1997). The primary remaining evidence of mitochondria having an independent bacterial origin, is the presence of mitochondrial DNA, with a circular genome similar to primitive bacteria. However, few of the mitochondrial genes remain on this mitochondrial DNA, with most coded for in nuclear DNA, hence mitochondria have lost independence and are now a cellular organelle.

Mitochondria have a distinctive cylindrical, double membrane structure, ranging from ~0.5-1 µm in diameter (Campbell 2007). The space in between the two membranes is known as the intermembrane space, while the space inside the inner membrane is known as the matrix (Mukhopadhyay and Weiner 2007). The outer mitochondrial membrane has a smooth, tightly stretched structure, while the inner membrane has numerous infoldings or cristae that project into the mitochondrial matrix, dramatically increasing its surface area (Campbell 2007). The outer membrane is similar in composition to the plasma membrane with a 1:1 ratio of lipid to protein (Daum and Vance 1997). It is fairly permeable to ions and has pores and transport proteins, making the composition of the intermembrane space similar to the cytoplasm (Mukhopadhyay and Weiner 2007). In contrast, the inner membrane contains a higher ratio of proteins, due to the inner mitochondrial membrane housing the proteins for the electron transport chain, and differences in phospholipid composition (Daum and Vance 1997). The inner mitochondrial membrane is very selective about what it transports into the matrix, giving the matrix a specific composition, rich in protein, enzymes, and fatty acids.

1.6.2 Mitochondrial function

The primary function of mitochondria is as the producer of energy, in the form of ATP, that is necessary for nearly all cellular functions. Mitochondria produce energy via the process of aerobic respiration, as described thoroughly by Demirel (2002). In brief, pyruvic acid in the mitochondrion reacts with water to produce carbon dioxide and hydrogen atoms, and the hydrogen atoms can then be transported to the cristae by coenzymes. The cristae house the protein components of the electron transport chain, which uses oxidation-reduction reactions to move electrons, extracted from NADH, between protein components down the chain. This produces free energy that is used to pump the hydrogen ions across the inner mitochondrial membrane. The flow of hydrogen ions back across the membrane drives the phosphorylation of adenosine diphosphate (ADP) to adenosine triphosphate (ATP), which acts as an energy store that can be transported around the cell and dephosphorylated to release energy wherever it may be needed.

Although mitochondria have a primary function in ATP production, they also perform a range of other integral functions, such as in heme production, cholesterol biosynthesis, apoptosis and in Ca^{2+} signalling (Audano et al. 2018). These processes performed by mitochondria can lead to the production of reactive oxygen species (ROS) when molecular water is not fully reduced to water (Huang and Manton 2004). Old or damaged mitochondria can produce more ROS, so swift clearance these organelles by mitophagy (the mitochondrial specific pathway of macro-autophagy) is integral to healthy cell functioning. Mitochondria cannot only be a source of ROS in the cell, but are also specifically sensitive to the damaging effects of ROS, with a strong link between oxidative damage in mitochondria and aging (Stefanatos and Sanz 2018). Acute and chronic mitochondrial stress, as can be caused by oxidative damage, activates a signalling pathway that upregulates lysosomal biogenesis in a TFEB-dependent manner (Ivankovic et al. 2016). Also, mTOR (as previously discussed for its roles in lysosomal homeostasis and function) coordinates energy metabolism by regulating the synthesis of nuclear-encoded mitochondrial-related proteins (Morita et al. 2015).

Recent studies suggest links between mitochondria and lysosomes in terms of both function and regulation, as is suggested by the strong involvement of both TFEB and mTOR in both lysosomal and mitochondrial regulation (Audano et al. 2018). Furthermore, electron

microscopy and live cell imaging has identified mitochondrial and lysosomal membrane contacts occurring in healthy cells, that are not related to degradation or bulk transfer of luminal content (Wong et al. 2018). Instead, these contacts were suggested to promote bidirectional regulation between these two organelles. These links could be supportive evidence of why dysfunction of both of these organelles is so closely linked in many neurological diseases, from LSDs, to Alzheimer's and Parkinson's disease (Audano et al. 2018).

Iron plays several key roles in mitochondrial function, where it can function as a cofactor in iron-sulfur cluster-containing proteins, heme-containing proteins, and iron ion-containing proteins (Paul et al. 2017). Some of these iron containing proteins are involved in the electron transport chain with iron being integral for the oxidation-reduction reactions that move electrons along the chain to produce cellular energy as ATP. Synthesis of iron containing heme is dependent on mitochondria, with heme needed to produce a range of important proteins, such as haemoglobin used by the body for oxygen transport. Certain mammalian tissues also express a mitochondrial-specific ferritin, for storage of iron in mitochondria and to sequester free iron to prevent iron-induced ROS generation (Drysdale et al. 2002).

1.7 Experimental aims by chapter

With human exposure to IONPs rising both through environmental exposure from IONPs in air pollution and increasing popularity of IONPs for use in medicine and biological techniques, it is becoming increasingly important to fully elucidate their impact on human cells. As nanoparticle uptake to cells will mainly occur through different routes of endocytosis, the majority of the IONPs will accumulate in lysosomes where the acidic, degradative environment can encourage IONP breakdown to release free iron. Excess free iron can be damaging to cells by facilitating production of ROS through Fenton reactions, with ROS able to cause peroxidation of lipids and proteins which can damage the lysosome. Free iron or subsequently produced ROS may also have effects outside of the lysosome, with mitochondria being a particularly sensitive organelle to both increases in free iron and ROS. Therefore, experiments have been designed in this thesis to investigate the effects of

different structures of IONPs across different cell lines and *in vivo*, in developing zebrafish embryos.

1.7.1 Chapter 3: Investigating the impact of HEPES buffer on lysosomal phenotypes

The role of this first mini chapter is to investigate the cellular toxicity of HEPES buffer on lysosomes, primarily to determine if using HEPES, a zwitterionic buffer used by us and by other labs in superparamagnetic iron oxide nanoparticle mediated lysosomal purification, is sensible in lysosomal studies. With the aim to identify sub-phenotypic concentrations of HEPES that can safely be used in later experiments. Secondarily, a range of other common cell culture buffers will be compared to HEPES to check if they exhibit similar lysosomal effects, in the hopes of identifying alternative buffers for use in lysosomal-related experiments, and any other common buffers that may need to be avoided.

1.7.2 Chapter 4: Comparing cellular toxicity of dextran coated iron oxide nanoparticles

The aim of this chapter is to determine cellular pathways, organelles and phenotypes affected by iron oxide nanoparticle (IONP) treatments using dextran coated nanoparticles. The dextran coating improves nanoparticle stability and biocompatibility by reducing aggregation, sedimentation and, when used as an outer coat, by creating a physical barrier against nanoparticle breakdown and iron ion release. One of the included nanoparticles, LRL, has previously been used by this and by other labs, in a magnetic lysosomal purification method. Therefore, this chapter also investigated whether this nanoparticle and two other nanoparticles with similar compositions would affect nanoparticle toxicity, aiming to further evaluate the validity of LRL for the method, needing strong biocompatibility. This chapter assessed cellular toxicity of each of the nanoparticles comparing their differing characteristics, assessing iron release, lysosomal-related phenotypes, autophagy, lipid peroxidation, release of ROS, mitochondrial phenotypes and general cellular toxicity. As two of these nanoparticles are composed of a mix of magnetite and maghemite, the toxicity of these nanoparticles could also be related to iron oxide nanoparticle air pollution, with magnetite in particular forming a major component.

1.7.3 Chapter 5: Investigating toxicity of LRL and ID nanoparticles in an *in vivo* developmental zebrafish model.

After determining the toxicity of the dextran coated IONP in cells, the toxicity of the LRL nanoparticle, compared to one of the nanoparticles shown to be more toxic in cells, was evaluated in developing zebrafish embryos/larvae. A range of developmental phenotypes were tested, including survival, motor development related phenotypes, heart rate, and movement related phenotypes. If the high biocompatibility of LRL in cells, is equally protective and compatible in developing zebrafish embryos/larvae, then these nanoparticles could also be used to develop a model for *in vivo* magnetic lysosomal purification.

1.7.4 Chapter 6: Comparison of the toxicity of magnetite and maghemite nanoparticles in a human microglial cell line

Magnetite nanoparticles, seemingly from an environmental source, have been found in post-mortem human brains while further studies have provided evidence that inhaled air pollution nanoparticles can be transported to the brain. Our studies in chapter 4-5 indicate that certain IONPs can induce toxic changes mediated from the lysosome. However, the effects of air pollution IONPs, of which magnetite is a major component, have been little studied in brain cells and their lysosomes, despite multiple links between these areas to neurodegenerative diseases, such as Alzheimer's disease. Therefore, this chapter aims to model magnetite nanoparticle treatment in microglial cells, the primary immune cells of the CNS and likely scavengers of nanoparticles entering the brain. This chapter will use superparamagnetic nanoparticles (SPIONs) without a bonded coating, to better compare to air pollution nanoparticles with a focus on magnetite (Fe_3O_4) and using maghemite (γ-Fe_2O_3) for comparison. Initially aiming to identify optimal nanoparticle treatment conditions and evaluate the impacts on lysosomal phenotypes.

2 General Methods

All reagents were purchased from Merck (Sigma-Aldrich), Gillingham, UK unless otherwise stated.

2.2 Cell Culture

It is standard laboratory procedure to maintain cells without antibiotic treatment as this can force readthrough of premature stop codons (Burke and Mogg 1985). Mitigation for infection by mycoplasma is instead by PCR testing. All medium was supplemented with 1% 100X L-glutamine (Lonza, Basel, Switzerland) and 10% heat inactivated foetal bovine serum (HI-FBS) (Pan Biotech) denoted as complete medium. BSA medium can be used to incubate cells during treatments and consists of complete medium with 1% bovine serum albumin (BSA). Hanks' balanced Salt Solution (HBSS) for washing and incubating cells is made up from 10x concentrate (Gibco, Bavaria, Germany) with dH_2O to produce a 1x solution and adding 1 mM HEPES (or for chapter 6 instead using PPB), 1 mM $MgCl_2$, and 1 mM $CaCl_2$.

2.1.1 Maintenance of cells

Chinese hamster ovary H1 (CHO-H1) cell lines were sourced as controls alongside NPC-1 null CHO line and have been maintained in Cardiff since 2010 (Millard et al. 2000). These adherent cells were cultured as monolayers at 37°C/5% CO_2 in Dulbecco's Modified Eagle Medium: Nutrient Mixture F-12 (DMEM/F-12) (Thermofisher, Massachusetts, USA). Cells were subcultured every 2-3 days, washed with Dulbecco's phosphate buffered saline solution (DPBS) and detached with trypsin-EDTA.

The cell line Human Embryonic Microglia Clone 3 (HMC3) was obtained from ATCC (CRL-3304) and is SV40-immortalised from human foetal brain-derived primary microglial culture. These adherent cells were cultured as monolayers at 37°C/5% CO_2 in Dulbecco's Modified Eagle Medium: Nutrient Mixture (DMEM) High Glucose. Cells were subcultured every 2-3 days; washed with DPBS and detached with trypsin-EDTA.

2.1.2 Cell Counting

Cells were counted and set numbers plated and left to set down overnight before treatments, and into wells of plates or chamber slides the day before imaging. This ensured cell density was optimal and consistent for treatments and imaging. Cell counting was also used experimentally in chapter 6, with cell counts normalised to a control treatment group for analysis.

During initial treatment optimisations of nanoparticle treatments in this project a B-hex assay (data not shown) suggested normal cell centrifugation speeds of 133 RCF (800 rpm) for 5 minutes caused increased cell membrane permeabilization/tearing in SPION treated cells, due to the extra density caused by SPION uptake. Therefore, a lower centrifugation speed of 52 RCF (500 rpm) with a longer 10-minute centrifugation time was used for nanoparticle treated cells, which reduced cell membrane permeabilization/tearing in SPION treated cells, increased their yield, and improved cell health post centrifugation.

Cells were washed twice in DPBS, detached with trypsin and centrifuged at either 133 RCF (non-nanoparticle treated) or 52 RCF (nanoparticle treated) for 5 or 10-15 minutes, respectively. The pellets were then resuspended in 1 mL DMEM and vortexed for 1 minute before 10 µL of the solution was immediately transferred to a fast read cell counting slide in duplicate (Immune Systems, Paignton, UK). The counting slides were observed through an Olympus CK2 microscope with a 10x magnification objective and 10x magnification lens, and were counted for each solution, giving a readout of cells/µL solution.

2.2 Nanoparticle treatments

2.2.1 Iron nanoparticles

All iron oxide nanoparticle treatments from each chapter are included in **Table 2-1** with the identifying name given to the nanoparticle in this thesis (thesis name), with the name given to the nanoparticle of the company website (sale name), the company from which the nanoparticle was sold and the thesis chapters in which this nanoparticle was used. Brief details on the main nanoparticles involved in individual chapters are also listed in the specific method sections of those chapters.

Table 2-1: List of nanoparticles used in this thesis. Including for each nanoparticle, the thesis/sale name, company of sale and chapters in which this nanoparticle is used.

Thesis Name	Sale Name	Company	Chapters
LRL	DexoMAG® 40	Liquids Research Ltd.	4, 5, 6
CC	FluidMAG-DX	Chemicell	4
ID	Iron-dextran	Sigma Aldrich (Merck)	4, 5
3 nm MN	Fe_3O_4 in Water, 15 wt%, 3 nm	US Research Nanomaterials	6
8 nm MN	Fe_3O_4 in Water, 15 wt%, 8 nm	US Research Nanomaterials	6
20 nm MN	Fe_3O_4 in Water, 20 wt%, 15-20 nm	US Research Nanomaterials	6
5 nm MH	Fe_2O_3 in Water, gamma, 15wt %, 5 nm	US Research Nanomaterials	6

2.2.2 Electron microscopy (EM) for nanoparticle characterisation

Nanoparticle samples were prepared and imaged by the Electron Microscopy officer (Tom Davies) of the Cardiff Catalysis Institute in the School of Chemistry for analysis.

Nanoparticle samples were diluted to equal concentrations in double distilled H_2O and for chapter 4 nanoparticles sonicated for 30 seconds, or for chapter 6 nanoparticles were vortex resuspended for 30 seconds prior to 6 µL being dropped onto a 300 mesh copper grid with holey carbon film. Once samples had dried on the grids, they were imaged on a JEM 2100 transmission electron microscope (TEM) (JEOL) operating at 200 kV.

2.3 Statistics and analysis

2.3.1 Image Analysis

Analysis of fluorescence microscopy images used ImageJ 1.52n software, with the 'analyse particles' function to analyse fluorescence area/cell and particle count. Analysis of fluorescence intensity across the cell used ImageJ 1.52n software with the 'plot profile' function. For plot profile analysis each plot profile data column was averaged, and, where necessary, background was then subtracted from the averaged data in each image to provide an overall plot profile value used in the bar graphs. Plot profile data from multiple

cells was averaged across rows to create the relative intensity plot profile line graphs with background averaged for inclusion where necessary.

Representative microscopy images were processed for presentation (including false colouring and merging images) on Adobe Photoshop CS6 Extended software and figures compiled on Inkscape 1.0 software.

2.3.2 Statistical Analysis

All statistical analyses were performed in GraphPad Prism 8 software (www.graphpad.com) to test for statistical significance. For measuring a variable with three or more separate treatment groups (e.g. control vs nanoparticle 1 vs nanoparticle 2) a one-way ANOVA was used. When two different factors were involved in comparing a response (e.g. incubation time and nanoparticle treatment) a two-way ANOVA was used.

Data was checked for normality and a parametric (normally distributed) or non-parametric (not normally distributed) post-hoc test chosen accordingly. For all statistical tests, significance data is presented from values of post-hoc tests if primary ANOVA showed significance. The degree of significance was denoted on the graphs in each chapter in p-value groupings (*p<0.05, **p<0.01, ***p<0.001, ****p<0.0001) and described in the figure legends along with the type of statistical and post-hoc tests performed. For parametric tests Tukey's or Dunnett's multiple comparison post-hoc tests were used, dependent on the initial experimental hypothesis. Tukey's test compared the mean of each group to the mean of all other groups (comparing all variables to each other), while Dunnett's test compare the mean of each group back to that of a chosen control (comparing each variable to a control). For data that is not normally distributed then an applicable alternative post-hoc tests was used, normally Kruskal-Wallis test, which does not rely on a normal distribution of data.

Only significant differences are shown on the graphs and non-significant comparisons can be inferred where left blank. Where all comparisons on a graph were non-significant, then this was also stated in the figure legend. Statistical analysis was only completed on data with at least 3 technical replicates (n) or biological replicates (as stated), described in the figure legend for each experiment. To demonstrate where a potential change could exist (either as a preliminary experiment or in an unfinished section) some data presented has less than 3 repeats so will not have been statically analysed.

2.4 Microscopy

A Zeiss Axio Observer inverted microscope fitted with a Colibri LED light source and a Zeiss Axiocam Mrm CCD camera and using Axiovision 4.7.1 software was used for microscopy imaging, unless otherwise stated.

Where stated, probes were co-stained for nuclei with 2 µg/ml Hoechst 33341 trihydrochloride trihydrate (Invitrogen, California, USA) *nuclear stain (hereon named Hoechst). Hoechst excitation/emission maxima 350/461.*

2.4.1 Acridine Orange Lysosomal Stability Assay

Acridine orange can be used as a live cell stain to identify acidic vesicles, primarily lysosomes and late endosomes and can be adapted as a test for lysosomal membrane stability (Pierzyńska-Mach et al. 2014). In live cells acridine orange diffusely binds cytoplasmic RNA and nuclear DNA when in its monomer form (low energy state) and emits green fluorescence. In low pH environments (such as the lysosome) acridine orange becomes protonated, converting to a dimer form that stacks (high energy state) causing an emission shift and orange/red fluorescence to be emitted. Acridine orange sensitizes the lysosomal membrane to photo-oxidation by blue (UV) light (365 nm). Exposure to UV can cause rupture of the lysosomal membrane, deacidifying the lysosome and causing Acridine orange to leak into the less acidic cytosol changing its conformation back to the low energy state. Loss of lysosomal integrity can be measured as a 'loss of red puncta' (acidic vesicles at 590 nm) or as a rise in 470 nm (green) fluorescence. If the lysosomal membrane is partly destabilized by treatments before acridine orange staining, rupture of the lysosomal membrane will occur faster, so in this way Acridine orange acts as an indicator for lysosomal membrane stability. Acridine orange excitation wavelength and emission range: 470 nm excitation and 480-560 nm (monomers- green), 590-660 nm (dimers/stacks - red).

Acridine orange powder (Invitrogen) was serial diluted in HBSS to 2 µg/mL. Cells either pre-incubated with or without the addition of an overnight 2 µg/mL U18666A treatment were washed twice in HBSS, loaded with 2 µg/mL acridine orange for 15 minutes at 37°C, washed twice with DPBS and left in HBSS for imaging. For each well an area of representative cells was selected, and images recorded automatically once a minute for 9 minutes. At time 0

minutes and at each minute interval images were taken in the 470 nm and 590 nm channels to detect DNA/RNA staining (non-lysosomal, 470 nm) and acidic vesical staining (lysosomal, 590 nm), respectively. From time 0 minutes the 365 nm fluorescence channel was turned on at 100% intensity throughout the experiment as this sensitises the metachromatic protonated acridine orange dimers (orange emission) to photo-oxidation.

2.4.2 Calcein-AM (quenched by free iron)

Calcein-AM can cross the cells plasma membrane and then reacts with unspecific cytosolic esterases to produce calcein as a fluorescent product (Tenopoulou et al. 2007). Calcein is not membrane permeant so is retained in the cytosol where its fluorescence is quenched following its chelation of free iron. While some Calcein-AM may enter lysosomes and be cleaved to produce calcein there, its fluorescence and iron chelating potential is strongly reduced at low pH of <5.

Cells were washed twice with HBSS and incubated with 5 µM Calcein-AM (Biotium, California, USA) in HBSS for 30 minutes at 37°C. Then cells were washed twice in HBSS and imaged in HBSS at 380 nm excitation.

2.4.3 Cellular autofluorescence

Cells were washed twice with HBSS and left in HBSS for imaging. Cells were imaged at 365 nm, 380 nm, 470 nm and 590 nm excitation without staining to determine autofluorescence.

2.4.4 Cyto-ID (autophagy stain)

Cyto-ID measures autophagic vacuoles and monitors autophagic flux in live cells and is optimized to allow for minimal staining of lysosomes while selecting for fluorescence upon incorporation into pre-autophagosomes, autophagosomes, and autolysosomes (Chan et al. 2012). Cyto-ID: excitation/emission maxima 490/520 nm.

Autophagy was measured using the Cyto-ID Autophagy detection kit (Enzo, Exeter, UK). Cells were washed twice with HBSS and incubated with a 1/500 dilution of Cyto-ID Green detection reagent in 1x assay buffer with Hoechst for 30 minutes at 37°C. Then cells were

washed twice with HBSS and imaged in HBSS at 470 nm (Cyto-ID) and 380 nm (Hoechst) excitations.

2.4.5 DPPP (lipid peroxidation stain)

DPPP stains lipid peroxidation in cell membranes. DPPP molecules are incorporated into cell membranes where they can be oxidized to a fluorescent product, DPPP oxide, by lipid hydroperoxides also located in the cell membranes (Takahashi et al. 2001). DPPP: excitation/emission maxima 351/380 nm.

Cells were washed twice with HBSS and incubated with 10 µM DPPP (TCI, Zwijndrecht, Belgium) in HBSS for 15 minutes at 37°C. Then cells were washed twice with HBSS and imaged in HBSS at 365 nm excitation. As a positive control untreated cells were incubated with 150 µM hydrogen peroxide (H_2O_2 – Pierce, Massachusetts, USA) for 60 minutes prior to DPPP staining.

2.4.6 Fura-2, AM staining of resting cells

The Fura-2,AM probe includes an AM group which neutralises the probes negative charge and enables the probe to cross the cell membrane where the AM group is cleaved from the probe by the activity of cytosolic esterases, trapping the probe in the cell as Fura-2 (Roe et al. 1990). Fura-2 can fluoresce when excited at 340 nm and 380 nm. When Fura-2 binds Ca^{2+}, the fluorescence at 340 nm increases, but the fluorescence at 380 nm is Ca^{2+} independent and is not affected by Ca^{2+} binding. This provides a basis for ratiometric imaging, which considerably reduces the effects of uneven dye loading, leakage of dye, photobleaching, unequal cell thickness and background noise. A ratio of fluorescence at both excitation wavelengths can be calculated to indicate Ca^{2+} levels. Free iron has been reported to quench Fura-2,AM staining in cells, making it a potential indicator for the presence of Fe^{2+} and Fe^{3+}, with a suggested 1000-fold higher affinity to Fe^{2+} than Fe^{3+} (Kress et al. 2002). Fura-2, AM: excitation maxima 340/380 nm, emission maxima 505 nm.

Cells were washed twice with DPBS and loaded with Fura staining solution (5 µM Fura-2,AM (Abcam, Cambridge, UK) in complete DMEM with 0.0025% Pluronic F127) for 1 hour at 37°C. Then cells were washed twice with HBSS and imaged in HBSS at 365 nm and 380 nm excitations. To control wells, 10 mM of Iron(II)ethylenediammonium sulphate (Alfa Aesar,

Lutterworth, UK - Fe2+ release) or Iron(III) oxide (Sigma - Fe3+) was added and preincubated for 30 minutes prior to Fura-2,AM staining as controls for the two species of iron ions.

2.4.7 Light Microscopy

Cells were washed twice with HBSS and left in HBSS for imaging under visible light.

2.4.8 Lysosomal Ca2+ Signalling

While the lysosome is only 1-3% of cellular volume it's Ca^{2+} store of ~600 µM is comparatively large, yet in terms of global cellular Ca^{2+} release, the lysosomal Ca^{2+} store is quite small. There are many differing methods in the literature for measuring lysosomal Ca^{2+} content, mainly utilising Gly-Phe β-naphthylamide (GPN), which when cleaved by cathepsin C produces a product that induces lysosomal swelling and rupture (Lloyd-Evans et al. 2008; Morgan et al. 2011a). However, GPN alone cannot be used to determine lysosomal Ca^{2+} content, as this can also trigger ER Ca^{2+} release, which is a much bigger Ca^{2+} store than in the lysosome (Lloyd-Evans and Waller-Evans 2020). This ER Ca^{2+} release can prevent accurate determine of the initial, smaller GPN-induced lysosomal Ca^{2+} release. Therefore, it is more accurate to first clamp other intracellular stores before addition of GPN, using the Ca^{2+} ionophore ionomycin, which releases intracellular Ca^{2+} stores except from the lysosome, which is protected by the glycocalyx (Alshehri 2019). It was also necessary to conduct all experiments in a low 10 µM $CaCl_2$ containing buffer to prevent an influx of extracellular Ca^{2+} from regenerating Ionomycin-released stores.

Cells were washed twice with chilled BSA medium (1% BSA in DMEM/F-12) and loaded with Fura staining solution (5 µM Fura-2,AM (Abcam) in DMEM with 1% BSA and 0.0025% Pluronic F127) for 1 hour in a dark cool box at ~16°C, to prevent compartmentalisation of the probe (Bootman et al. 1994). Cells were then washed with and left in HBSS for 10 minutes to allow de-esterification of the calcium dye, before washing and imaging cells in low Ca^{2+} HBSS (1× HBSS with 1 mM HEPES, 1 mM $MgCl_2$, and 0.05 mM $CaCl_2$). Fura-2, AM: excitation maxima 340/380 nm, emission maxima 505 nm.

Intracellular Ca^{2+} responses were recorded using a Zeiss Axiovert 35 microscope with a Cairn Optospin filter exchanger, Orca Flash 4.0 sCMOS camera and MetaFluor 7.10 software, with the additional physiology module for live cell Ca^{2+} imaging. Cytoplasmic regions of interest

(ROIs) were drawn around whole cells in the field of view before imaging of each treatment, with a further region drawn containing no cells to act as measurement of background. Changes in fluorescence emission (510 nm) were recorded at both excitations of 340 nm and 380 nm over the course of each experiment. The ratio of 340 nm to 380 nm fluorescence was calculated, after subtraction of background fluorescence. Peak height then related to Ca^{2+} release, calculated by 340/380 ratio above baseline and measured in relative fluorescent units (RFU). Imaging of cells was started to form an initial baseline, then 2 µM ionomycin (Calbiochem, Gillingham, UK) was added to wells to release all intracellular non-lysosomal Ca^{2+} stores, creating a large peak on the traces. As the 380 nm channel is Ca^{2+} insensitive, this allows detection of a peak in comparison to Ca^{2+} sensitive 340 nm channel. When traces have returned to baseline, 500 µM Glycyl-L-phenylalanine 2-napthylamide (GPN, Abcam) was added, leading to a secondary Ca^{2+} release and hence peak on the traces. GPN is a lysomotrophic peptide that when cleaved in the lysosome by the lysosomal enzyme cathepsin C produces a product that induces osmotic lysis of the lysosome and consequent release of lysosomal Ca^{2+} stores (Lloyd-Evans et al. 2008).

2.4.9 LysoTracker Green (lysosomal stain)

LysoTracker Green is a fluorescent dye that loads into acidic compartments in live cells due to its protonation at low pH preventing it from crossing membranes (Pierzyńska-Mach et al. 2014). LysoTracker predominantly stains lysosomes, but it will also stain any acidic endosomes with a pH<5.4. LysoTracker Green: excitation/emission maxima 504/511 nm.

Cells were washed twice with HBSS and incubated with 300 nM LysoTracker Green DND-26 (Invitrogen) and Hoechst in HBSS for 15 minutes at 37°C. Then cells were washed twice with HBSS and imaged in HBSS at 470 nm (LysoTracker Green) and 380 nm (Hoechst) excitations.

2.4.10 Magic Red (cathepsin B activity)

Magic red stains whole, live cells for cathepsin B activity, an endo-lysosomal enzyme (Creasy et al. 2007). Magic red consists of a cathepsin B target sequence peptide linked to a red (Cresyl Violet) fluorescent probe, that fluoresces when excited after the target peptide has been cleaved by active cathepsin B. Magic red cathepsin B: excitation/emission maxima 570/630 nm.

Cells were stained with the Magic Red Cathepsin B kit (Bio-Rad, Watford, UK) according to the kit instructions for 1 hour at 37°C in darkness, with Hoechst then added for 5 minutes at 37°C. Cells were imaged at 590 nm (Magic Red) and 380 nm (Hoechst) excitations.

2.4.11 Micronuclei

Micronuclei are extra-nuclear bodies containing damaged fragments of/whole chromosomes and an increase of micronuclei in cells can be a sign of genotoxicity (Luzhna et al. 2013). Micronuclei per total number of cells was counted from images of Hoechst DNA staining (**Figure 2.1**).

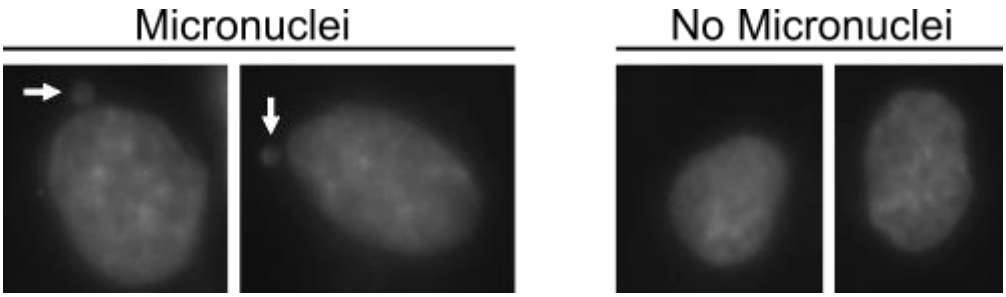

Figure 2.1: Identification of micronuclei in images of Hoechst staining. Presence of extranuclear micronuclei in the two left images are indicated by white arrows. Two images of nuclei without visible micronuclei are shown on the right for comparison.

2.4.12 MitoTracker Green (mitochondrial stain)

MitoTracker Green is a mitochondrial stain which localises to mitochondria regardless of mitochondrial membrane potential (Doherty and Perl 2017). MitoTracker Green: excitation/emission maxima 490/516 nm.

Cells were washed twice with HBSS and incubated with 200 nM MitoTracker green FM (Invitrogen) and Hoechst) in HBSS for 15 minutes at 37°C. Then cells were washed twice with HBSS and imaged in HBSS at 470 nm (MitoTracker Green) and 380 nm (Hoechst) excitations.

2.4.13 NucView® 488 Caspase-3 Assay

The NucView® 488 Caspase-3 Assay involves a Caspase-3 substrate bound to a DNA dye that is released after substrate cleavage allowing it to bind DNA which causes it to fluoresce (Sztiller-Sikorska et al. 2009). Caspase-3, needed to cleave the substrate, is activated in

apoptotic cells, hence fluorescence is an indicator of apoptosis. Nucview 488: excitation/emission maxima 500/530 nm.

A NucView® 488 Caspase-3 Assay kit (Biotium) was used. Cells were washed twice with HBSS and incubated with 5 µM Nucview substrate solution in complete medium and co-stained with Hoechst for 30 minutes at room temperature in darkness. Then cells were washed twice with HBSS and imaged in HBSS at 470 nm (Nucview) and 380 nm (Hoechst) excitations. Camptothecin (Fluorochem, Hadfield, UK) was added to control wells at 20 µg/mL for overnight treatment as a positive control, inducing caspase-3-mediated apoptosis.

2.4.14 Phagocytosis Assay

Where necessary cells were pre-treated overnight with 25 nM Bafilomycin A1. To each well of cells in normal cell culture medium, one drop per well of Fluoresbrite Plain YG 3.0 Microspheres (Polysciences, Germany) was added (spheres approximately 3.0 µm in diameter) and incubated with the cells at 37°C/5% CO_2 for 60, 30, 15 or 5 minutes consecutively to be ready to image together (treatment of a well with and without Bafilomycin-A1 at each time point). In the last 5 minutes of treatment, concentrated Hoechst (working concentration 2 µg/mL) was added to the nanosphere medium in HBSS and incubated for 5 minutes before the cells were then washed thrice in HBSS. The cells were imaged in HBSS at 470 nm (nanospheres), 380 nm (Hoechst) excitations, and under visible light, to visualise the large nanospheres in context of the cells. Fluoresbrite Plain YG 3.0 Microspheres: excitation/emission maxima ~441/486 nm.

2.4.15 Wheat germ agglutinin and Phalloidin (cell membrane and cytoskeleton stains)

Wheat germ agglutinin (WGA) stains cell membranes by selectively binding to sialic acid residues; when live cells are stained cold this should ensure only the cell membrane is stained as endocytosis is inhibited. Phalloidin toxin stains the cytoskeleton by selectively labelling F-actin. Rhodamine wheat germ agglutinin: excitation/emission maxima 545-555/570-580 nm. Alexa Fluor 488 phalloidin: excitation/emission maxima 495/518 nm.

Cells were washed twice in chilled complete medium (4°C). Cells were stained in the dark for 30 minutes at 4°C with 10 µg/mL rhodamine wheat germ agglutinin (Vector Laboratories, Oxfordshire, UK) in chilled complete medium. Then cells were washed twice in chilled

complete medium and twice in HBSS before PFA fixation (chilled 4% w/v in PBS, pH 7.4 for 8 minutes). Cells were treated with 0.1% triton (100x) in HBSS for 15 minutes at room temperature to permeabilise the membranes, then washed twice with HBSS. Cells were treated with 1x Alexa Fluor 488 phalloidin stain (Invitrogen) in HBSS with 1% BSA in the dark at room temperature for 30 minutes and then washed twice with HBSS. For nuclear staining, cells were then treated with Hoechst in HBSS for 10 minutes at room temperature, washed twice with HBSS and left in HBSS for imaging. Cells were imaged on a Zeiss Axiovert 35 microscope fitted with Cairn Optospin filter wheels at excitation and emission ports, an Orca Flash 4.0 sCMOS camera, an Exfo xCite multiband lightsource with Micromanager software, using a 550 nm filter for WGA, a 470 filter for phalloidin and a 340 nm filter for Hoechst.

2.4.16 Phen Green (quenched by metal ions)

Phen Green stain is quenched by the presence of several ions and is particularly responsive to Fe(II), Cu(I), somewhat less responsive to Fe(III), Cu(II) and only slightly responsive to a range of other metal ions including Cd(II), Ni(II), Co(II), Mn(II) and Zn(II) (Petrat et al. 1999; Shingles et al. 2004). Phen Green SK: excitation/emission maxima 506/520 nm.

Phen green SK, diacetate (Invitrogen) solution (5 µM) was made by vortexing 2 µL of 5 mM Phen green solution with 10 µL 5% pluronic F-127 (Sigma) for 30 seconds and then mixing this with 2 mL warmed BSA medium. Cells were washed twice with warmed BSA medium and incubated with 5 µM Phen green solution for 1 hour at 37°C. Then cells were washed once in HBSS and stained with Hoechst for 5 minutes, washed twice with HBSS and imaged in HBSS at 470 nm (Phen green) and 380 nm (Hoechst) excitations.

2.4.17 Super oxide staining (SO-ID)

Super oxide was measured with the ROS-ID Superoxide detection kit (Enzo) hereon named SO-ID. The superoxide detection reagent is a cell-permeable probe that reacts specifically with superoxide, but not with reactive peroxide, hydroxyl or peroxynitrite species (Ding et al. 2015). ROS-ID Superoxide detection reagent: excitation/emission maxima 490/525 nm.

Cells were washed twice with HBSS and incubated with an appropriate volume of staining solution (2 µL superoxide detection reagent in 10 mL HBSS) for 1 hour at 37°C. Then 20 minutes before staining was ready, a ROS inducer (400 µM Pyocyanin) was added to a well

of control cells as a positive control, with Hoechst added to all wells for the last 5 minutes of staining. When staining was complete, cells were washed twice with HBSS and imaged in HBSS at 470 nm (SO-ID) and 340 nm (Hoechst) excitations.

2.5 Cell plate assays and spectrophotometry

2.5.1 CellTiter-Glo (ATP luminescence assay)

The CellTiter-Glo Luminescent Viability assay kit (Promega, Wisconsin, USA) was used to quantify ATP, indicating the presence of metabolically active cells and mitochondrial health when cell survival remains constant or cell survival and proliferation when cell numbers are not consistent between treatments. When added to a well of cells the CellTiter-Glo solution lyses cells to release ATP and then an UltraGlo rLuciferase can convert luciferin to Oxyluciferin by utilising the ATP from the cells, producing a luminescence output proportional to the ATP in the well.

Cells, plated in a collagen-coated 96-well plate (Gibco) were acclimatised to room temperature for 30 minutes, then 100 µL CellTiter-Glo reagent was added per well and the contents mixed for 2 minutes on a shaker to induce cell lysis, then the plate was incubated at room temperature for 10 minutes to stabilise the luminescent signal and the luminescence output recorded with multi-scan cross pattern (5 reading/well) on a SPECTRAmax GEMINI EM microplate reader (PMT 600; bottom read). Triplicate data was averaged for each replicate.

2.5.2 Ferrozine assays (free iron assay)

Nanoparticles were added to citrate-phosphate buffer (pH 3/5/7) to produce 0.1 mg/mL (chapter 4) or 40 µg/mL (chapter 6) nanoparticle solutions and incubated on a shaker at 37°C for 24 hours or 2 hours, with a non-incubated sample (0 hours) prepared just before plating to act as a control for pre-existing Fe^{2+} in the nanoparticle solutions. A standard curve for Fe^{2+} was generated from Iron(II)ethylenediammonium sulphate (Alfa Aesar) for normalisation and run on every plate of the same experiment for accurate comparison. Ferrozine assays were conducted in 96-well, clear, F-bottom microplates (Greiner Bio-one). To sample wells 5 µL of 16 mM Neocuproine hydrochloride (Acros organics, Geel, Belgium) was added with 40/10 µL of each the nanoparticle-buffer solutions and 35/55 µL mQ H_2O for calculation of Fe^{2+} only/ Fe^{3+} (calculated by Fe^{2+} subtracted from total Iron - Fe^{2+} and

Fe^{3+}) respectively. Different volumes of nanoparticle solution had to be added for Fe^{2+} only or total iron wells to keep results in the assay range. To correct for interference in the assay output by the absorption of the NPs themselves equivalent blank wells lacking ferrozine were prepared. To 'total iron' wells 10 µL of 5 mM L-Ascorbic acid (vitamin C- Sigma) was added and the whole plate incubated for 10 minutes at room temperature for the vitamin C to convert free Fe^{3+} to Fe^{2+} allowing detection of total free iron. Finally, 20 µL of 25 mg/mL FerroZine, iron reagent, hydrate (Acros Organics) made up in mQ H_2O was added to every sample and standard well to start the assay. Ferrozine binds ferrous iron, but not ferric iron, into a complex that absorbs strongly at 550-570 nm with an associated colour change. After initial optimisations a 20-minute incubation with ferrozine, at room temperature, was determined to be optimal for readout. After incubation, the plate was scanned on a Tecan Infinite F50 absorbance reader at 570 nm using software Magellan for F50. Each nanoparticle was run on its own plate, due to well constraints from the large number of variables, controls and standards. To process data, blanks were subtracted, values normalised to standards, adjusted to sample volume and converted to calculate iron content in 100 µL of 0.1 mg/mL nanoparticle solution.

2.5.3 Ferrozine assay with nanoparticles pre-incubated with BSA

Bovine serum albumin (BSA) was added to nanoparticle solutions to test if nanoparticle breakdown occurs differently in the presence of protein, as would occur in the intra-lysosomal environment. Nanoparticle solutions (3 nm Fe_3O_4 or LRL nanoparticles) were either pre-treated with 2 mg/mL BSA (+BSA) or mQ H_2O (-BSA) and incubated at room temperature for 10 minutes before addition to pH 5 citrate-phosphate buffer resulting in a 0.1 mg/mL nanoparticle solution, that was either incubated at 37°C for 24 hours (24h) or not pre-incubated (0 hours - 0h) and then scanned for absorbance readings (same as ferrozine assays), to measure colour change (absorbance units - AU). Ferrozine assays were initially run on BSA-incubated nanoparticle solutions, but the BSA caused sedimentation in the wells and impacted absorbances in an Fe^{2+} independent manner. Instead, colour change of the nanoparticle solutions themselves was used as a surrogate reading. Absorbance colour change of the nanoparticle solution is also an established method for detecting nanoparticle breakdown (Lévy et al. 2010).

2.5.4 Live cell plate assay: LysoTracker Green

Cells were washed once in HBSS and scanned in HBSS in the plate reader to obtain blank (unstained) readings for each well; a control for autofluorescence. Wells were then treated with 300 nM LysoTracker Green DND-26 (Invitrogen) in HBSS for 15 minutes at 37°C, washed twice in DPBS and scanned again in HBSS to obtain LysoTracker fluorescence readings. Fluorescence was measured using a SPECTRAmax GEMINI EM microplate reader (Molecular Devices) with multi-scan (9 readings/well), bottom read (excitation: 485nm; auto cut-off: 515 nm; emission: 525 nm), manual PMT (600), with 6 flashes/read settings.

2.5.5 Live cell plate assay: MitoTracker Green

Fluorescence was measured using a SPECTRAmax GEMINI EM microplate reader with multi-scan (9 readings/well), bottom read (excitation: 485nm; auto cut-off: 515 nm; emission: 525 nm), manual PMT (400), with 6 flashes/read settings.

Cells were washed once in HBSS and scanned in HBSS in the plate reader to obtain blank (unstained) readings for each well; a control for autofluorescence. Wells were then treated with 200 nM MitoTracker green FM (Invitrogen) in HBSS for 15 minutes at 37°C, washed twice in HBSS and scanned again in HBSS in the plate reader to obtain MitoTracker fluorescence readings.

2.5.6 Fluorimetry of Fura-2,AM

Fluorimetry was used to quantify potential quenching of the Fura probe after addition of iron ion releasing compounds, and to check if this occurs equally at both 340 nm and 380 nm excitations.

Fura-2,AM solution at 5 µM was prepared in cuvettes at room temperature. The solutions were scanned on a RF-5301PC spectrophotometer (Shimadzu) at two excitation wavelengths (340 and 380 nm) over a time course denoted by t (time) followed by the number of minutes. A baseline was recorded (t0) just before addition of 10 mM iron solutions, either Iron(II)ethylenediammonium sulphate (Alfa Aesar - Fe^{2+} release) or Iron(III) oxide (Sigma - Fe^{3+}) for each experiment, then every subsequent time point (t1, t2, t4, t6, t8, t10, t15, t20, t25, t30, t60) referred to the number of minutes past addition of iron for that recorded time point. Fluorescence output was recorded in relative fluorescent units for a spectrum scan of 400 nm to 600 nm emission wavelength (speed: medium; sampling

interval: 1.0; slit width: 5/5; sensitivity: high; response time: auto). The area under the curve was calculated for results at both excitation wavelengths, for each iron species. From these values a final ratio was calculated for 340/380, for each iron species.

2.5.7 Resazurin (cell metabolism assay)

Cell viability was measured using resazurin, a purple compound that is reduced to a pink and fluorescent product, resorufin, when metabolised by cells. This requires cell numbers/well to remain consistent between treatments, so cell counts were done before plating to ensure consistency and there was no major difference in cell growth rate between treatments. Resazurin: excitation/emission maxima 530-570/585-590 nm.

Cells were treated with 100 µg/mL Resazurin in complete cell medium, incubated at 37°C and scanned live in a plate reader SPECTRAmax GEMINI EM microplate reader (Molecular devices) to detect fluorescence at 570 nm excitation and 590 nm emission after 4- and 22-hours of incubation. Optimisations in CHO H1 cells, showed the earlier time point of 4 hours to be optimal for a strong linear fluorescence readout in healthy, untreated cells, while the 22-hour time point showed metabolic saturation.

2.6 Zebrafish maintenance

2.6.1 Animal Welfare Statement

This study only used wild-type adult zebrafish for breeding; all larvae were used prior to 5 days post fertilization and were euthanised using tricaine at the end of all experiments. All animal experiments were carried out in accordance with EU directive 2010/63/EU and the UK Animal Welfare Act, 2006.

2.6.2 Maintenance of Zebrafish

Wild-type AB/TL zebrafish were sourced from the Division of Biosciences, University College London and were housed in a multi-rack aquarium system in the School of Biosciences aquarium, Cardiff University. The adult zebrafish were maintained in aerated, 28 °C water according to standard protocols. Fish were kept under a 12 h light/dark cycle.

2.6.3 Breeding and egg collection

For mating, a single male and female were transferred to a breeding tank in the late afternoon and started courtship after the light was switched on the next morning, which ended with egg deposition and fertilization. Specialist breeding tanks with plastic inserts allowed eggs to fall though to a lower area once laid where they could not consequently be eaten by the adults. To improve chances of breeding, tanks were placed on top of printed images of stones and rocks alongside marbles placed in the tanks above the inserts to mimic rocks, as the fish only like to lay eggs over rocky areas for protection.

Eggs were collected by gently pouring tank water over a thin-holed sieve and then transferring eggs to a petri dish. Then the eggs were washed with E3 fish medium (5 mM NaCl, 0.17 mM KCl, 0.33 mM $CaCl_2$, 0.33 mM $MgSO_4$, 0.00001% (w/v) methylene blue (King British), to remove debris, waste, and unfertilised embryos, and were subsequently maintained in E3 fish medium in a 28°C incubator.

3 Chapter Three: Investigating the impact of HEPES buffer on lysosomal phenotypes

3.1 Introduction

3.1.1 Identifying effective biological buffers

Buffering agents are solutions formed from a mixture of weak acids and their conjugate bases that can maintain their pH within a specific range. For biological buffers, this is the neutral range of pH 6-8 to cover the physiological pH of 7.4 (Good et al. 1966). The identification of effective biological buffers is important because maintaining the pH of aqueous solutions while the concentration of hydrogen ions (H^+) is changing is critical as pH changes can alter biological phenotypes and processes.

In 1966, Dr. Norman Good described a series of buffers considered to have great characteristics for biology and biochemistry known as 'Good's buffers' (Good et al. 1966). These buffers typically have high water-solubility, low cell membrane permeability, high chemical stability, pKa values near physiological pH (solutions have greater buffering capacity at a pH near their pKa value), low absorption spectra in UV and visible regions and are non-toxic to cells. Since Good first described these buffers, many additional buffers have been found to fit these characteristics and even improve upon the original buffers for certain applications (Ferguson et al. 1980; Brooke et al. 2015; Taha et al. 2017).

3.1.2 Zwitterionic Buffers

The majority of Good's buffers are zwitterionic, as these often have particularly strong buffering capacity (Good et al. 1966). A zwitterionic molecule consists of at least one functional group that can be positively charged and at least one that can be negatively charged with the charged atoms linked by one or more covalent bonds, while the net charge of the molecule remains zero (**Figure 3-1**). Changes in pH, and therefore, the availability of hydrogen ions, causes the neutral zwitterionic molecule to change form to either an anion (low pH) or cation (high pH).

Zwitterionic buffers also often exhibit less interference in biological processes than buffers made from inorganic or organic salts, as their anionic and cationic sites are on non-

interacting groups. Their zwitterionic nature also gives these buffers greater solubility in water, another highly desirable characteristic of biological buffers (Good et al. 1966).

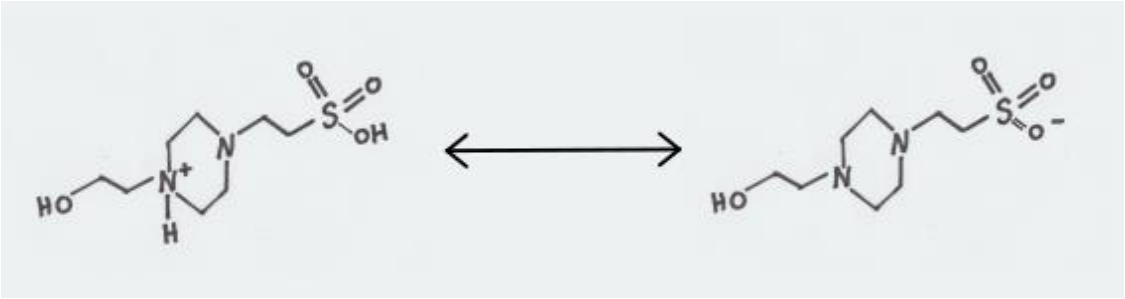

Figure 3-1: HEPES is a zwitterionic molecule. HEPES is zwitterionic as it has both a sulphonate group that can become negatively charged (acidic) and an amine group that can become positively charged (basic). This allows strong buffering potential with only this molecule present, rather than requiring sperate positively and negatively charged molecules.

When choosing which buffer would best suit an experiment it is important not only to choose a biological buffer with all the desirable characteristics identified for Good's buffers, but also to consider which buffers may have relevant off-target effects. For example, when protein concentration will be measured, it is pertinent to consider which buffer to use as quite a few biological buffers interfere with the Lowry protein assay (Lleu and Rebel 1991). In particular HEPES buffer has been shown to increase the rate of the colour change reaction in the Lowry protein assay, according to the degree of amino group protonation in the buffer, but does not affect the BCA protein assay (Lleu and Rebel 1991).

3.1.3 Changes of pH in cell culture medium

The pH of cell culture medium, even when buffered, will not remain stable under all conditions. Changes in temperature can affect the pH of culture medium, as can CO_2 concentration, and as cells grow, release metabolites and respire, these can also affect culture medium pH (Michl et al. 2019). Therefore, it is integral to grow cells in tightly temperature and CO_2 controlled environments and to change medium regularly. However, this also explains why it is common to add extra buffers to medium to help maintain physiological pH, especially when using cell treatments that may cause changes to medium pH.

Cytoplasmic pH is tightly regulated by ion transport proteins on the plasma membrane to keep it in the near neutral range, although optimal intracellular pH can vary dramatically between cell lines (Srivastava et al. 2007). Even fairly small changes in pH of the culture medium can affect intracellular pH, impacting cell health and function (Michl et al. 2019).

Changes in medium pH and medium buffering capacity can have major effects on cell metabolism. Lactate/lactic acid is produced physiologically by cells, largely from glycolytic metabolism, which can reduce the pH of medium by reacting with the HCO_3^- ions in the buffering medium (Michl et al. 2019). In one study, the addition of 10 mM HEPES and MES (zwitterionic Good's buffers) was used to reduce medium acidification from lactic acid, but addition of these buffers significantly increased lactate production, in turn increasing lactic acid, so they gave no overall benefit to maintaining medium pH (Michl et al. 2019). However, this does suggest addition of the buffers led to a higher rate of glycolytic metabolism, likely because acidity causes inhibitory feedback on metabolic rate (Erecinska et al. 1995; Wilmes et al. 2017).

Changes in extracellular pH have been linked to changes in cell behaviour, growth rate and contact inhibition (Taylor 1962; Ceccarini and Eagle 1971b,a). In one early experiment, as pH was raised, between pH 7.4 and 8, cell motility increased, but increasing pH further, to between 8 and 8.3, caused contraction and detachment of the cells (Taylor 1962). Extended exposure to these changes in medium pH caused irreversible damage to the cells; above pH 8.5 this occurred within just 10-15 minutes. Reduction of pH from 7.3 to 5.6 led to an immobilization of all cell components, with cell processes being withdrawn and impeded movement of intracellular vesicles, although cell morphology was not dramatically affected. While most cells kept at pH 6.5 for 1 hour recovered without visible damage, cells maintained at low pH for long periods would lyse. More recent studies have built upon these finding to show intracellular acidification can inhibit protein synthesis and G0/G1 cell cycle progression, suggesting a mechanism for the effect on cell growth (Flinck et al. 2018).

3.1.4 Experimental use of HEPES Buffer

After it was first described as part of the original list of Good's buffers, a wide range of applications was found for HEPES buffer in biological experiments (Good et al. 1966). Also known as N-2-hydroxyethylpiperazine-N'-2-ethanesulfonic acid, HEPES is a zwitterionic

buffer with a piperazine ring; it has a pH range of 6.0 to 8.5, and is commonly used as a buffer for cell culture medium since it was shown in the 1960s not to be cytotoxic at buffering concentrations (Williamson and Cox 1968).

HEPES had advantages over conventional $NaHCO_3$ buffered medium as it has a better physiological pKa of 7.31 (37°C) compared to 6.1 pKa (37°C) for $NaHCO_3$ (Good et al. 1966; Itagaki and Kimura 1974). Being zwitterionic, HEPES also benefits from less interference in biological processes and high water solubility (Good et al. 1966). Furthermore, HEPES has low metal binding and did not negatively impact cell viability and maximum cell density across a range of cell lines (Williamson and Cox 1968; Shipman 1969).

3.1.5 Off-target effects of HEPES buffer

After many years of use, it has become apparent that there are quite a few downsides to the use of HEPES in certain applications. These effects can be difficult to compare between laboratories as many different concentrations of HEPES are utilised. Most processes/protocols use HEPES concentrations between a broad range of concentrations, often from 5 mM to 50 mM (Mattson et al. 1995; Gutiérrez et al. 1997; Craver and Knoll 2007). There is evidence that HEPES can accumulate in the cytoplasm and only slowly reduces in concentration after HEPES is removed from cell culture medium taking more than 48 hours before it is undetectable by NMR spectrophotometry (Depping and Seeger 2019).

It has long been known that phototoxic effects are seen in certain cell culture medium that has been exposed to near ultraviolet or visible radiation and that this process is exacerbated by the presence of 25 mM HEPES in the medium (Zigler et al. 1985). This is a common concentration of HEPES buffer added to culture medium for maintaining pH, yet it led to a 10-fold increase in the generation of phototoxic H_2O_2 relative to HEPES-free medium. It was subsequently found that in the presence of HEPES buffer, production of H_2O_2 was greatly increased when oxidants such as peroxynitrite were present (Kirsch et al. 1998). When provided with an appropriate oxidant, 20 mM HEPES concentrations caused consistent H_2O_2 production, while incubation with potassium phosphate buffer led to low H_2O_2 production.

HEPES has also been suggested to block chloride (Cl^-) channels in *Drosophila* neurones affecting phenotypes in a concentration dependent manner (Yamamoto and Suzuki 1987). Also, in *Drosophila*, HEPES has been shown to cause tissue artifacts in the retina when used

during fixation (Nie et al. 2015). Severe lumen and cell morphological defects were seen in pupal and adult retina, not present when fixed in PBS, suggesting HEPES may need to be avoided during some fixation processes.

Furthermore, HEPES buffer has been shown to stimulate ATP production in cells, affecting ATP-dependent cellular processes and cellular metabolism (Luo et al. 2010). Addition of HEPES buffer has been shown to reduce P-glycoprotein (ATP-dependent efflux pump) uptake of substrates in a concentration-dependent manner (Luo et al. 2010). As the P-glycoprotein efflux pump transports a wide range of compounds including many pharmaceutical drugs (Hochman et al. 2002), these effects of HEPES could be important to a large number of studies.

With HEPES buffer linked to a range of side effects in a cell type-dependent manner and variable use of buffering concentrations between laboratories/protocols, the potential of this buffer in altering, creating, or masking phenotypes and processes could be very widespread. This could add a possible explanation for the numerous issues in replicating phenotypes between laboratories and experiments when buffers are not kept consistent.

3.1.6 Impact of HEPES buffer on lysosomes and vacuoles

Of particular importance to the culture of mammalian cells in our laboratory, are the findings that HEPES buffer has been shown to be a potent inducer of lysosome biogenesis and autophagy (Tol et al. 2018). Treatment of macrophages with 20-25 mM HEPES leads to dramatic nuclear translocation of the microphthalmia family (MiT/TFE) of transcription factors, which act as key players in cellular response to internal and external cell stress (Tol et al. 2018). This included nuclear translocation of TFEB (the master regulator of lysosomal biogenesis and autophagy), which promotes lysosomal-autophagic gene expression, leading to an increase in lysosomes/autophagosomes. It is not yet fully clear how HEPES causes MiT/TFE nuclear translocation. The master regulator of cell growth, mTORC1, can control the subcellular localisation of MiT/TFE, but the HEPES-dependent nuclear translocation was shown to be mTORC-1 independent, while also leading to an increase in lysosomal pH (Tol et al. 2018). This could be a mechanism for MiT/TFE translocation similar to that seen with use of v-ATPase inhibitors, where a lysosomal proton pump triggers increased lysosomal pH by blocking v-ATPase action (Roczniak-Ferguson et al. 2012; Settembre et al. 2012). There is

still relatively little known about the effects of HEPES on lysosomes, despite evidence that HEPES impacts lysosomal homeostasis.

As shown when imaging cells by transmission electron microscopy (TEM), the addition of HEPES buffer can cause a vacuolation phenotype, similar to that seen in sucrose-driven vacuolisation, which is also driven by TFEB nuclear translocation (Tol et al. 2018). This builds on data from as early as 1982 (Poole et al. 1982), which suggested addition of HEPES buffer caused a vacuolation phenotype in chick embryo chondrocytes, increasing the production of vacuoles filled with proteoglycan aggregates and calcium deposits. However, HEPES-driven vacuolisation appears morphologically different to sucrose-driven vacuolation which is led by endocytosis, intracellular accumulation of sucrose as a non-metabolizable sugar and hyperosmolarity (Poole et al. 1982). Yet the full mechanism behind HEPES-driven vacuolisation, which has been seen across many cell types including foetal mouse myocardial cells (Goshima 1973), mouse macrophages (Brune 1980) and human fibroblasts (Verdery et al. 1981) is still to be fully elucidated.

3.1.7 Alternative buffering solutions

A range of other common cell culture buffers are included in **Table 3-1** below to compare to HEPES buffer, including PIPES, MES, MOPS, Tris and potassium phosphate buffer (PPB).

Table 3-1: Comparing HEPES and other common cell culture buffers.

Buffer	Good's Buffer?	pH range	pKa
HEPES	Y	6.0-8.5	7.31 (37°C)
PIPES	Y	6.1-7.5	6.7 (37°C)
MES	Y	5.5-6.7	5.98 (37°C)
MOPS	Y	6.5-7.9	7.04 (37°C)
Tris	N	7.0–9.0	7.9 (37°C)
PPB	N	5.8 – 8.0	7.21 (20°C)

PIPES buffer is a zwitterionic buffer with a piperazine ring, also known as Piperazine-N,N'-bis(2-ethanesulfonic acid) (Good et al. 1966; Ferreira et al. 2015). PIPES has become particularly popular for buffering solutions while prepping and fixing samples for electron microscopy (Baur and Stacey 1977; Schiff and Gennaro 1979) as it can improve retention of lipids in membranes, helping to maintain the samples structural integrity, producing superior ultrastructural detail in imaging (Schiff and Gennaro 1979).

MES is a zwitterionic buffer containing a morpholine ring and is also known as 2-(N-Morpholino)ethanesulfonic acid (Good et al. 1966; Ferreira et al. 2015). MES is often used in metal binding experiments as many agree it forms no significant complexation with Cd, Pb, Cu nor Zn and only light complexation with Mg, Co, Ni (Ferreira et al. 2015). It is also commonly used in redox studies, as unlike HEPES and PIPES, it does not appear to produce radical species (Grady et al. 1988).

MOPS is an analogue of MES and likewise contains a morpholine ring; it is also known as 3-(N-Morpholino)propane sulfonic acid (Good and Izawa 1972; Roy 1998; Ferreira et al. 2015). MOPS is commonly used for maintaining pH in denaturing gel electrophoresis of RNA to prevent pH changes cause by decomposition of denaturing agents (Ferreira et al. 2015), and in antibody production (Nagira et al. 1995).

Tris (Tris(hydroxymethyl)aminomethane) is a non-zwitterionic organic compound that has been used as a biological buffer for a long time due to its physiological pH range and pKa, and because it is cheap and easy to make (Good et al. 1966; Williamson and Cox 1968; Ferreira et al. 2015). Due to its common availability in labs a range of uses have been found for Tris buffer, mostly as a component for mixed buffer formulations, such as for electrophoresis, SDS-PAGE and cell lysis solutions (Ferreira et al. 2015) and for standardising acid solutions and measuring pH (Tishchenko 2000). However, its use in cell culture experiments has become less widespread since it has been found to inhibit several enzymes and complexes with a high number of metal ions and because it's buffering capacity becomes less efficient below pH 7.5, which is the important range for most biological experiments (Ferreira et al. 2015).

Finally, potassium phosphate buffers (PPB), also known as Gomori buffers, are a traditional non-zwitterionic biological buffer consisting of a mixture of monobasic dihydrogen

phosphate (KH_2PO_4) and dibasic monohydrogen phosphate (K_2HPO_4) (Bates 1945). PPB has long been used as a biological buffer, as it is cheap and easy to produce (Gorman and Levine 1965; Ridnour et al. 2000).

The aims of this chapter are firstly, to elucidate to what extent HEPES buffer can interfere with LysoTracker green staining and if this phenotype is concentration dependent. Secondly, this chapter aims to review a range of buffers, including several Good's buffers, to see if other common cell culture buffers can effect lysosomal phenotypes.

3.2 Materials and Methods

3.2.1 Buffer preparation

Cell culture buffers, including MES, MOPS, PIPES, potassium phosphate buffer (PPB) and Tris (Roche, St Albans, UK) were made as 1 M stock solutions in mQH_2O (or 1 M NaOH in mQH_2O for PIPES) from powders. All buffers were adjusted to pH 7.4 and filter sterilised through a 0.22 µm filter. PPB was produced by combining 1 M monobasic dihydrogen phosphate (80.2%) and 1 M dibasic monohydrogen phosphate (19.8%) to produce a pH 7.4 solution. HEPES buffer (Thermofisher/Lonza) was purchased as a pre-made 1 M, pH 7.4 solution.

3.2.2 Cell culture and buffer treatments

CHO H1 cells were seeded at a normal cell number (~4000-5000) or high cell number (~7000-8000) in IbiTreat 8-well µ-slides (Thistle Scientific, Glasgow, UK) and grown overnight before treatment. The lower number of seeded cells produced normal confluency (~70-80%) cells after 3-day treatments, while the higher seeded number produced overconfluent (~90-100%) cells after 3-day treatments. CHO-H1 cells at normal and high confluency were either treated with HEPES buffer at concentrations between 0 and 100 mM for 3 days, or with 10 mM of various zwitterionic buffers (MES, MOPs, PIPES, PPB, Tris or HEPES) for 3 days.

3.2.3 Methods for determining buffer toxicity on lysosomes

Lysotracker green staining (refer to methods Section 2.4.9) was used to investigate lysosomal area after buffer treatments. Micronuclei were counted (refer to methods Section 2.4.11) to indicate genotoxicity levels after buffer treatments.

3.3 Results

3.3.1 HEPES buffer can cause increased lysosomal area

Buffers, such as HEPES, are added to culture medium in which cells are incubated to maintain pH, often especially useful during treatments that can change the pH of cell culture medium. To investigate if HEPES effects lysosomal phenotypes, HEPES treated CHO H1 cells were stained with LysoTracker Green across a HEPES concentration curve to measure changes in lysosomal area per cell (area^2/cell).

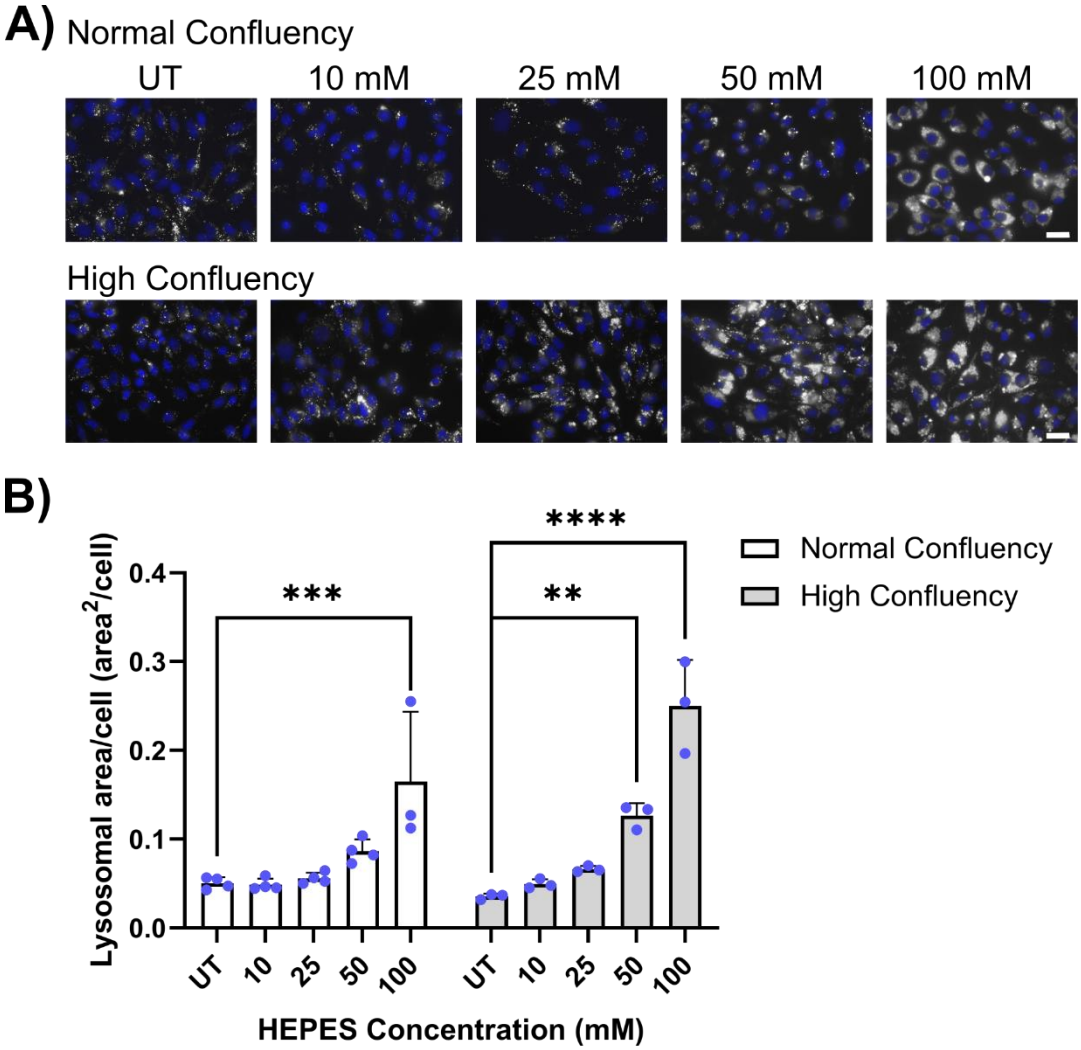

Figure 3-2: Changes in lysosomal area in CHO-H1 cells grown in various concentrations of HEPES buffered media. A) Representative images of CHO-H1 cells loaded with LysoTracker green (grey scale) and counterstained with Hoechst nuclear stain (blue), following 3-day treatment of medium buffered with various concentrations of HEPES. Scale bars = 10 µm. UT = Untreated control cells. **B)** Quantitative analysis of LysoTracker fluorescence in normal confluency and high confluency CHO-H1 cells as lysosomal area per cell, n=3–4 (data points averaged from analysis of cells in 9 images). Data presented as average bars ± SD with plotted data points and analysed using a two-way Anova test with post hoc Tukey's. ** p<0.01, *** p<0.001, **** p<0.0001.

When growing CHO H1 cells at a normal confluency, a 3-day incubation with lower concentrations of HEPES buffer, such as 10 mM, have no effect on lysosomal area^2/cell (**Figure 3-2A and 3-2B)**. While a 10x higher concentration of 100 mM caused a greater area of LysoTracker staining in the cells with a significant 226% increase in lysotracker staining analysed by area^2/cell. Still high concentrations of 50 mM cause a 71% increase in area^2/cell,

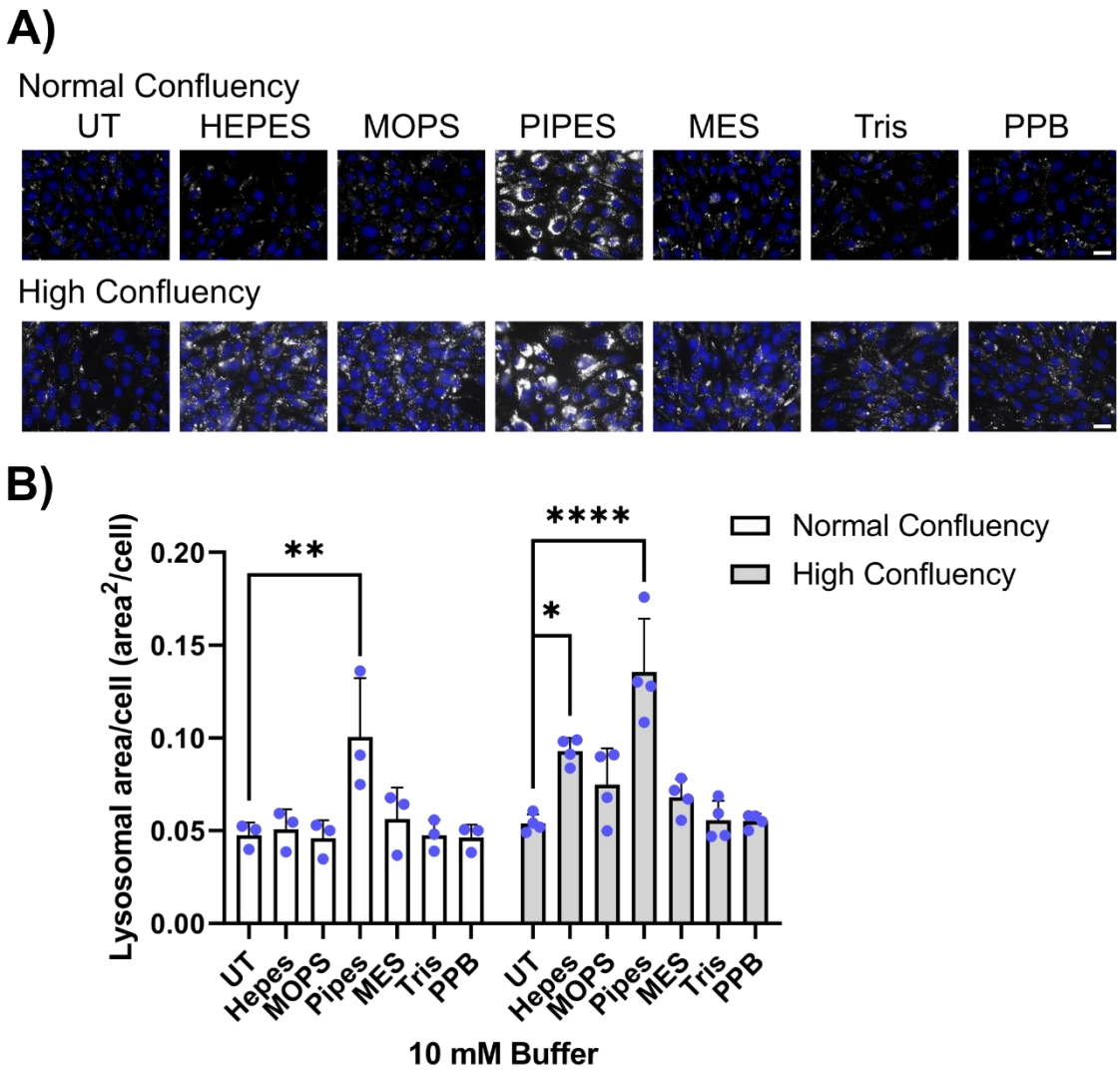

Figure 3-3: Changes in lysosomal area in CHO-H1 cells grown in zwitterionic buffered media. A) Representative images of CHO-H1 cells loaded with LysoTracker green (grey scale) and counterstained with Hoechst nuclear stain (blue), following treatment for 3-days with medium buffered with 10 mM of various zwitterionic buffers. PPB = potassium phosphate buffer and UT = untreated control cells. Scale bars = 10 µm. **B)** Quantitative analysis of LysoTracker fluorescence in normal confluency and high confluency CHO-H1 cells as lysosomal area per cell, n=3–4 (data points averaged from analysis of cells in 9 images). Data presented as average bars ± SD with plotted data

points and analysed using a two-way Anova test with post hoc Tukey's. *p<0.05, **p<0.01, ****p<0.0001.

but in normal confluency cells this change is not significantly different to untreated control cells. Cell confluency appears to affect the response of the cells to the buffer, as a stronger phenotype of increased LysoTracker area staining is seen in very high confluency CHO H1 cells after a 3-day incubation with HEPES buffer (**Figure 3.2A and 3.2B**) with both concentrations of 50 mM and 100 mM in the high confluency cells causing significant 256% and 605% increases in area^2/cell, respectively.

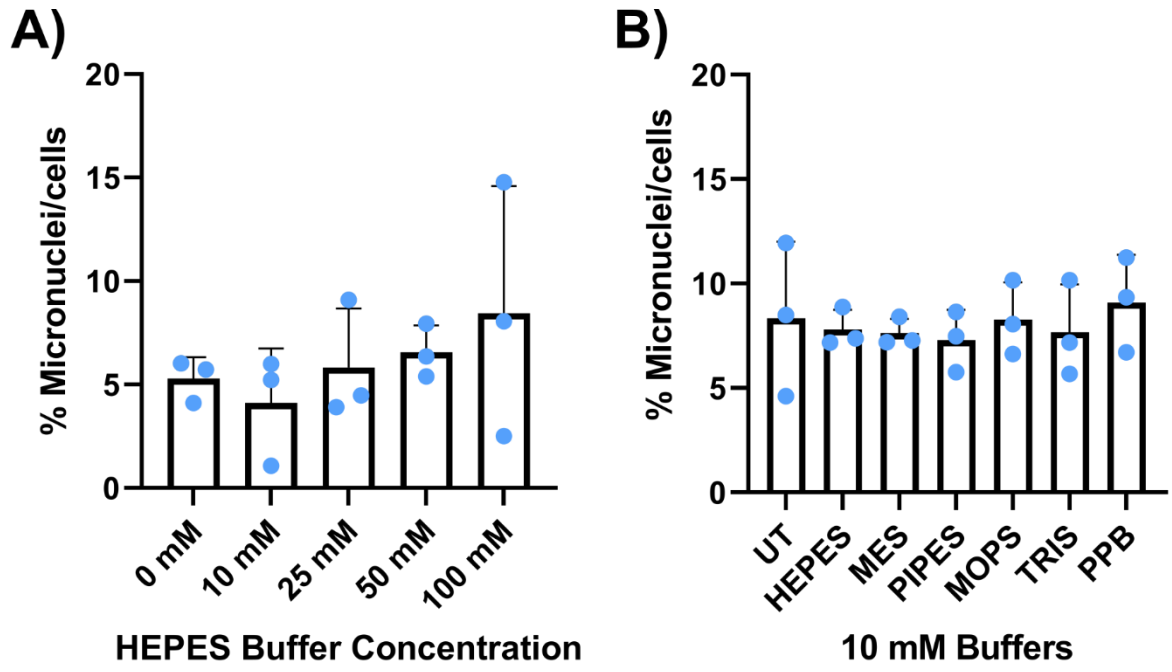

Figure 3-4: At the selected concentrations none of the zwitterionic buffers caused an increase in genotoxicity-induced micronuclei production in CHO H1 cells. Number of micronuclei were counted and divided by the number of cells, from images of Hoechst staining. For each repeat (values shown as blue dots) 9 representative images were analysed per treatment to give a percentage average. **A)** Percentage micronuclei per total cells at increasing concentrations of HEPES buffer in cell culture medium. **B)** Percentage micronuclei per total cells with 10 mM of a range of common buffer's added to cell culture medium. UT = untreated control cells and PPB = Potassium phosphate buffer. All data n=3. Data presented as averages ± SD and analysed using one-way Anova tests, post hoc Tukey's test (no significances).

3.3.2 Alternative buffers for lysosomal studies

In order to check what buffers could be used as effective replacements for HEPES, a range of common cell culture buffers were tested at 10 mM to check if they caused changes in

LysoTracker Green staining and therefore, lysosomal area per cell (area^2/cell). Tris and potassium phosphate buffer (PPB) are traditional cell culture buffers, while HEPES, MOPS, PIPES and MES are all zwitterionic Good's buffers. In cells at normal confluency only 10 mM PIPES caused a significant change in LysoTracker green staining with a 119% increase compared to the untreated control (**Figure 3-3A and 3-3B**). While at high confluency, the HEPES treated cells also have significantly increased LysoTracker Green staining compared to controls, with a 72% increase, however, the PIPES treatment still causes the biggest change in LysoTracker Green staining with a strongly significant 151% increase compared to the untreated control (**Figure 3-3A and 3-3B**). While no significant differences were found in LysoTracker staining area between cells treated with MOPS, MES, Tris or potassium phosphate buffer (PPB) compared to untreated control cells.

3.3.3 Impact of HEPES buffer on genotoxicity

After determining there were lysosomal defects after treatment of cells with certain concentrations of HEPES and other buffers, it was also briefly investigated if signs of genotoxicity might be present by counting micronuclei. Micronuclei are small extranuclear bodies that stain positive for Hoechst nuclear stain as they contain damaged chromosome fragments or chromosomes not incorporated after cell division and are indicative of genotoxicity from DNA damage.

None of the concentrations of HEPES buffer tested (10-100 mM) caused a significant change in micronuclei production, measured by calculating a percentage of micronuclei per total number of cells (**Figure 3-4A**). Similarly, none of the other buffers, when added to the cell culture medium at 10 mM, had any effect on the percentage of micronuclei (**Figure 3-4B**).

3.4 Discussion

3.4.1 HEPES buffer can cause increased lysosomal area

This study provides novel evidence of how addition of HEPES buffer to cell culture medium can affect lysosomal phenotypes in a concentration-dependent manner, work that has been published in a peer reviewed journal (Cook et al. 2020a). Also, this is the first study to show the lysosomal effects of HEPES buffer on Chinese hamster ovary H1 (CHO H1) cells. HEPES concentrations of 10-25 mM are common for buffering medium during experiments or as an addition to cell culture medium, while for some experiments even higher concentrations have been used (Mulder et al. ; Medzon and Gedies 1971; Hoyle et al. 1992; Kannan et al. 2017). It is also common for HEPES to be included in commercially available cell culture mediums, where cells would be consistently cultured in the presence of the buffer, so it is important to account for this if extra buffers are added during experimental conditions (for example with addition of drug treatments).

A major breakthrough in understanding some of the potential negative effects of HEPES buffer on lysosomal studies came from a paper in 2018 (Tol et al.). In this paper it was first demonstrated how HEPES buffer can lead to lysosomal expansion in cultured cells, using RAW macrophages. Our data here corroborates the findings in this work to show that in a different and non-phagocytic cell line, CHO H1, HEPES buffer can also trigger concentration-dependent lysosomal expansion as seen by observing LysoTracker Green staining. In this study, in normal confluency cells only 100 mM concentrations of HEPES in the culture medium for 3 days caused a significant increase in LysoTracker Green staining area. This suggests that CHO H1 cells may actually be more resilient to the lysosomal expansion effects of HEPES buffer than other cells lines, as RAW cells in the Tol et al. (2018) study showed significantly increased LysoTracker Green staining after just 7 hours of incubation with just 25 mM HEPES (Tol et al. 2018). As CHO H1 cells are non-phagocytic, it is likely they would have slower uptake of HEPES buffer, which could explain differences in comparison to phagocytic RAW cells. In this study, at neither confluency did a 3-day incubation with 25 mM HEPES cause significantly increased lysosomal expansion, however, Tol et. al (2018) used flow cytometry analysis in comparison to ImageJ analysis used in this study and so were analysing fluorescence rather than area, which may lead to differing detection sensitivity for

lysosomal expansion. Therefore, in analysing lysosomal area, this study also adds a new layer of analysis to the lysosomal expansion phenotypes.

Alterations in lysosomal expansion can be a particularly important cellular phenotype, especially in the context of lysosomal storage diseases, where this is often a primary phenotype (Platt and Lachmann 2009). In relation to these diseases, the presence of HEPES buffer could mask or accentuate lysosomal phenotypes inconsistently. However, considering the lysosome plays important roles in regulation of many cellular processes, including stress adaption and nutrient metabolic processing, HEPES-induced lysosomal changes could have implications in a multitude of diseases, including cancer, immunology, and neurodegeneration, where the use of cell culture models is prominent.

In CHO H1 cells, confluency of the cells affected the impact of HEPES buffer on lysosomal area, with a lower concentration of HEPES buffer needed to cause lysosomal expansion. This is an important new finding as it indicates that when using HEPES buffer in experiments to determine lysosomal phenotypes, maintaining cell confluency across experiments may be of importance to observe similar phenotypes and ensure consistency. Not only this, but it also indicates that when growing cells at a higher confluency or with additional stressors, the accentuated effect of HEPES buffer may need additional consideration. This could be of greater importance when studying lysosomal phenotypes in cultured lysosomal storage disease cell lines, where cell growth rate is often affected making it harder to keep confluency consistent when comparing between untreated and diseased cell lines (Kacher and Futerman 2006; Schulz et al. 2006; Rusyn et al. 2008).

Furthermore, 10 mM HEPES did cause a significant increase in lysosomal staining when compared to control cells in the overconfluent cohort in comparison to all the 10 mM buffers, enforcing the impact confluency can have and demonstrating that even at low doses HEPES may cause negative lysosomal changes in CHO H1 cells. Indeed, long-term growth of NPC1 null and control CHO H1 cells in HEPES containing media, showed significantly exacerbated phenotypes in the control cells, that were not similarly replicated in NPC1 null, which could have effects in turn on the outcome of potential drug treatments (Cook et al. 2020a).

3.4.2 Alternative buffers for lysosomal studies

While HEPES appeared not to caused significant lysosomal expansion at low concentrations over 3 days in CHO H1 cells, other similar zwitterionic buffers may have similar or worse lysosomal effects. For many studies, 10-25 mM concentrations of HEPES are used, so a range of common cell culture buffers were tested at 10 mM to ascertain whether any would cause similar lysosomal changes to HEPES. Under conditions of normal confluency (cells not overgrown), 10 mM HEPES does not cause significant change in LysoTracker Green staining, yet 10 mM PIPES led to a significant increase in LysoTracker area. It is, therefore, likely that PIPES has an even more profound effect on lysosomal expansion/swelling than HEPES. In agreement with this finding, Tol at al. (2018) also found 10 mM PIPES caused a significant increase in LysoTracker staining, yet in their RAW cells this increase was similar to that seen with addition of 20 mM HEPES. This could suggest that either, HEPES or PIPES causes greater lysosomal expansion in RAW or CHO H1 cells, respectively.

There is evidence to suggest that HEPES causes differential effects in different cell types and that HEPES may have stronger effects in immune cells, such as macrophages. In RAW macrophages HEPES has been shown to trigger an inflammatory phenotype that resembles an M1-like activation state (Tol et al. 2018). When M1-activated, macrophages undergo lysosomal biogenesis and have increased phagocytic activity (Daigneault et al. 2010), which could partially explain why these cells are more sensitive to lower concentrations of HEPES buffer if the HEPES related and M1-activated lysosomal expansions/biogenesis have a synergistic or additive effect. While the side-effects of PIPES have not been studied as much as HEPES, it is likely PIPES also has several underlying, currently unknown effects. Certainly, the strong phenotype PIPES induces in lysosomal expansion/biogenesis is worth further study and suggests PIPES buffer should be strongly avoided in any work that may be affected by changes in the lysosomal (or likely also the autophagic) system.

None of the other buffers used in this study caused significant negative changes in lysosomal area over 3 days in these CHO H1 cells, however, MES at 20 mM (double the concentration used here) has been shown in other studies to cause increased lysosomal staining (Tol et al. 2018). Furthermore, it is difficult to determine whether the benefits of many of the zwitterionic buffers may outweigh their known and potentially unknown side effects. As always, it may be best to make a choice of the right buffer for the right

experiments. Regarding the chosen selection, potassium phosphate buffer may be a desirable choice for lysosomal-based experiments as it had very little impact on LysoTracker staining even with the added stressor of high cell confluency.

3.4.3 Impact of HEPES buffer on genotoxicity

HEPES has been shown to be highly compatible with cell growth and proliferation in many studies (Williamson and Cox 1968; Shipman 1969; Depping and Seeger 2019; Michl et al. 2019) and indeed this was one of the prime reasons it was so favoured by Good et. al. (1966) in their original paper. It was identified that the CHO H1 cells used in this study produced micronuclei that could be easily detected with Hoechst staining. Increased production of micronuclei can act as an indicator for genotoxicity and identification of micronuclei is commonly used *in vivo* as a method for measuring chromosomal damage caused by genotoxic agents (Fenech and Morley 1985; Luzhna et al. 2013).

As the micronuclei frequency test is an easily available test not previously used in conjunction with HEPES to the best of the authors knowledge, micronuclei were also counted from the nuclear staining images of each of the treatments. Consistent with previous studies, the micronuclei test also suggested that there is not increased genotoxicity from any of the concentrations of HEPES buffer tested, nor from any of the other buffers at 10 mM. While on its own this test is in no way conclusive, it can be a useful addition to the other methods already published demonstrating HEPES has little effect on genotoxicity, despite its many other side effects.

4 Chapter Four: Comparing cellular toxicity of dextran coated iron oxide nanoparticles

4.1 Introduction

4.1.1 Application of IONP coatings

Nanoparticles can be tailored to specific physical, optical, electronic, chemical or biomedical properties by coating a thin film of material on their surface (Wang et al. 2004). Coatings can be applied to nanoparticles to make them more stable or degrade less fast, to disperse them in solution and prevent aggregation/sedimentation, to prevent the core compound affecting the environment, to gain the active effect of a coating polymer, or to allow attachment of further ligands to the nanoparticle (Tassa et al. 2011). In terms of increased biocompatibility, the polysaccharide dextran, or the polymer polyethylene glycol (PEG) are two of the most common IONP coatings used in biomedical applications (Yu et al. 2012).

4.1.2 Benefits of dextran coating

Dextran is composed of a complex branched polysaccharide polymer chain of various lengths, generally ~1 kDa to 2000 kDa (Predescu et al.). Dextran has the advantage of being biocompatible, biodegradable and water soluble and is commonly used to coat nanoparticles in biomedical applications. The main benefit of attaching dextran to nanoparticles is far greater stability at physiological pH, meaning the particles degrade to release Fe^{2+}/Fe^{3+} more slowly, have greater biocompatibility and lower cytotoxicity than uncoated nanoparticles (Saraswathy et al. 2014; Shaterabadi et al. 2017). The dextran coating reduces aggregation and settling of the nanoparticles (Shaterabadi et al. 2017), which is especially important when using these nanoparticles as treatments where maintaining an even distribution and dosing is important to consistent results. Uncoated nanoparticles tend to exhibit strong magnetic dipole-dipole interactions between individual nanoparticles and as their magnetic moments line up this can lead to agglomeration (Ciftja 2009). In fact, dextran coated ferrite nanoparticles possess negative charge under physiological conditions (pH 7; ionic strength 0.15 M NaCl) maintaining repulsive forces between the nanoparticles through electrostatic interactions and steric repulsion keeping them from agglomerating and maintaining their stability in suspension (Latorre-Esteves et

al. 2009; Shaterabadi et al. 2017). This laboratory has previously found that coating IONP with a 40 kDa dextran provides better stability of the particles than a 10 kDa dextran (Walker 2015). A thicker dextran coat likely provides greater protection to the core from degradative effects of the lysosomal environment, including acidic pH and enzymes, with the rate of dextran metabolism in the lysosome being a key indicator for the rate of nanoparticle degradation and free iron release.

4.1.3 Methods for lysosomal purification

When de Duve first identified lysosomes as an organelle, it was through separating components of the cell via differential centrifugation (De Duve et al. 1955). Differential centrifugation is a method for isolating fractions, groups of cellular components of a similar size and weight reliant on density-dependent sedimentation. Fractions can be separated successively by this method, with the supernatant removed and the pellet resuspended, then centrifuged again at greater speed after each step until the fraction of interest is purified. The necessary centrifugation speed - determined by relative centrifugal force (RCF or g) – and duration required is particular to the fraction of interest. When de Duve first isolated lysosomes, he also purified mitochondria and peroxisomes due to their similar densities (Appelmans et al. 1955; De Duve et al. 1955).

A new method was then developed known as density gradient centrifugation, which was similar to differential centrifugation, except the cellular components are centrifuged across a sucrose gradient. This provides far more precise separation of organelles and for decades was the primary method for separating lysosomes, peroxisomes and mitochondria (Graham 2001). One main disadvantage of this technique was its inability to purify lysosomes effectively from cells exhibiting lipid accumulation phenotypes associated with lysosomal dysfunction and storage diseases. Lipids can accumulate as either primary or secondary storage material in the lysosomes of storage disease cells, and a plethora of other conditions, leading to a reduction in their buoyant density (Cox and Cachón-González 2012; Yang et al. 2014; Fineran et al. 2016). The density of storage disease lysosomes varies depending on the degree of storage and so is more variable than for non-diseased lysosomes. When these lysosomes are then separated by density gradient centrifugation, they present a wide band that does not match non-diseased cell lysosomes, and are often

contaminated by other organelles (Walker and Lloyd-Evans 2015). Some storage disease lysosomes may also be lost into other fractions reducing the lysosomal yield and excluding a selection of phenotypic lysosomes.

In an attempt to circumvent this problem, loading of lysosomes with different heavy molecules (including dextran, gold and iron) was trialled, to increase their density and allow them to separate from other similar density organelles (Arborgh et al. 1973; Henning and Plattner 1974; Arai et al. 1991). However, this method is time-consuming requiring many centrifugations and sample cleaning steps to produce a fairly low yield of lysosomes due to the high risk of membrane damage from separating the densely loaded organelles at high centrifugal force. This technique does not resolve the issue of the higher buoyancy of storage disease lysosomes and their differential separation compared to non-diseased lysosomes. This problem is often compounded by defective endocytic trafficking that is a major phenotype of many of the lysosomal storage diseases (te Vruchte et al. 2004). Slower endocytosis and trafficking in diseased cells can mean loading molecules take longer to reach the lysosome, so a longer incubation period post removal of loading molecule may be required to ensure lysosomal localisation compared to non-diseased cells. An incubation period is required after the treatment period, to make sure the majority of endocytosed material reaches the lysosomes, and that endocytic vesicles and early/late endosomes are not also being purified. Longer incubations with heavy molecules, such as iron, may also increase the risk of degradation of the added material and related toxicity to the cells.

4.1.4 Magnetic separation of lysosomes

IONP may present a novel technique to purify lysosomes, including storage disease lysosomes, that can avoid the issues faced by density gradient centrifugation. The first attempt at this method was documented in the early 1990s in *Dictyostelium discoideum*, a soil-dwelling social amoeba, using iron oxide (FeO) coated dextran nanoparticles purified with a 0.8 tesla magnet (Rodriguez-Paris et al. 1993). This study found that ~76% of ingested iron was located in the purified lysosomal fraction, indicating most of the particles were retained in the endocytic system and in particular lysosomes.

This method was then adapted by Diettrich et al. (1998) to use an overnight treatment of iron oxide (FeO) coated dextran nanoparticles to attempt purification of lysosomes from

infantile free sialic acid storage disease (ISSD) patient fibroblasts. Lysosomes from homogenised cells were isolated in a column using a magnet, then eluted with either hypotonic solution or buffers with low concentrations of non-ionic detergents. Enzyme assays preformed on the eluted fractions suggested ~50% enrichment of lysosomes was achieved, but with high lysosomal activity in the post nucleic supernatant (elute not retained magnetically in column) it was clear the yield of purified lysosomes was low (Diettrich et al. 1998). Likely reasons for this include the low magnetic properties of FeO, potential cytotoxicity and a short treatment time.

A few years later a mouse study investigating NPC (Niemann-Pick type C) disease by injecting iron dextran particles into the liver, found they were able to isolate different separated fractions of organelles from the endocytic system (Chen et al. 2005). By avoiding the use of detergents to elute lysosomes from the column, they were able to purify the lysosomes structurally intact, but yields were very low. Acridine orange staining showed the extracted lysosomes were still functional and could be reacidified after, however, due to low yields it took an entire fraction (100 µg of vesicles) to run the one assay.

Another attempt in the same year managed greater lysosomal yields from HL-60 cells by addition of hypotonic and isotonic buffers as well as detergents for elution (Duvvuri and Krise 2005). The hypotonic buffers were useful for swelling the cells and bursting the cellular membrane for homogenisation, while the addition of an isotonic buffer after homogenisation helped maintain organelle integrity. Although maintaining lysosomal integrity after homogenisation increased the lysosomal fraction yield, the use of detergents meant the lysosomes were not intact post elution.

The next step was the successful magnetic extraction of a purified early endosome fraction by Glebov et al. (2006) using a short and precise 10-minute pulse (incubation with nanoparticles) followed by a 10-minute chase (incubation without nanoparticles). The short pulse meant nanoparticles would not yet have travelled further down the endocytic system, yet despite the short treatment time a fairly high early endosome yield was eluted due to the use of a more highly magnetic iron oxide nanoparticle, provided by Liquids Research Ltd (LRL).

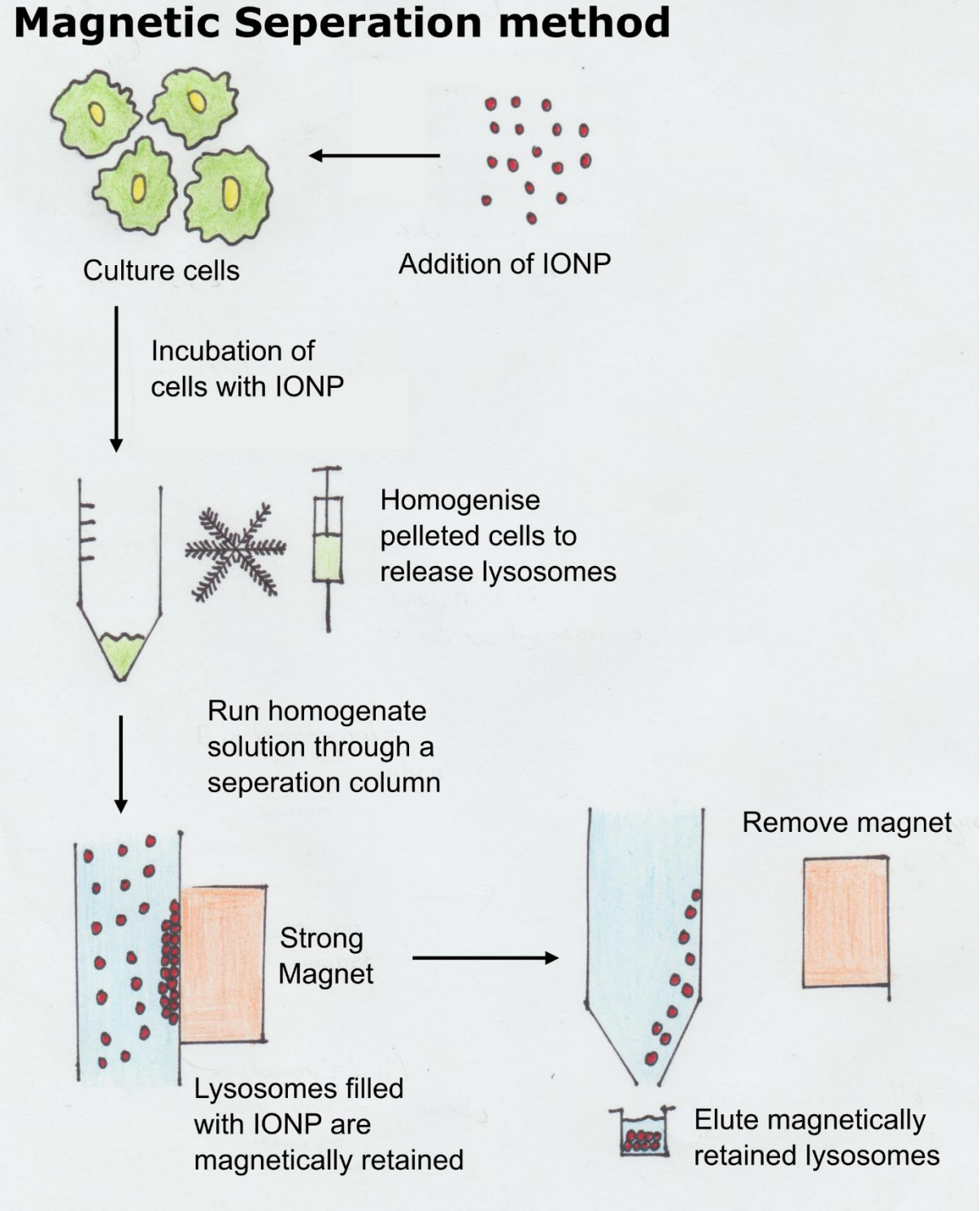

Figure 4-1: A simplified overview of the magnetic lysosomal separation method. Cultured cells are treated with IONP for a pulse and chase period, so IONP are endocytosed are trafficked to lysosomes. IONP treated cells are then homogenised to release lysosomes and the homogenate run through a separation column with a strong magnet that retains IONP filled lysosomes. Then lysosomes can be eluted in a purified solution by removal of the magnet.

This led to work in our laboratory using the LRL nanoparticle, a dextran coated SPION (superparamagnetic iron oxide nanoparticle) with strong inducible magnetic properties for lysosomal purification by magnetic extraction (Walker and Lloyd-Evans 2015). This method was optimised in the lab for extracting lysosomes with a 24-hour pulse and 24-hour chase to extract a high purity lysosomal fraction from CHO H1 cells (**Figure 4-1**), a non-phagocytic cell line and with a longer 36-hour chase to extract a high purity lysosomal fraction from a NPC1 diseased CHO cells (CHO M12) (Walker 2015). Toxicity of the LRL nanoparticle was then compared to a similar dextran coated SPION from Chemicell (CC) and an iron dextran nanoparticle (ID) similar to the nanoparticle used in most of the previous lysosomal extraction experiments just discussed. This comparison led to preliminary data suggesting differences in cytotoxicity of the three different nanoparticles despite their similar compositions (Walker 2015). The LRL nanoparticle was shown to be the least cytotoxic and was used for the magnetic lysosomal extraction technique, proving to be an effective tool for purifying lysosomes from both non-diseased and lysosomal storage disease cells (Walker and Lloyd-Evans 2015). Further investigation of the phenotypic responses of cells to LRL treatment was still needed to fully validate its biocompatibility and suitability for the magnetic lysosomal extraction method. While, this work also exposed unanswered questions about how the differences in structure, size and iron species of three iron oxide and dextran nanoparticles could affect their cytotoxicity and behaviour within the cell. These two experimental questions then becoming the premise for this thesis chapter.

4.1.5 Aims of Chapter 4

The focus of this chapter is on iron oxide nanoparticles (IONPs) as these are widely used in industrial and biomedical applications and are often assumed to have low cellular toxicity, despite evidence to the contrary. Compared to the uncoated nanoparticles, IONP coated with a surface ligand, such as dextran, are often more stably suspended in solution, have reduced aggregation, making particle size less variable and, dependent on the ligand, have lower cytotoxicity (Section 4.1.2), so are often a more desirable candidate for use in cell culture experiments. The use of a dextran coated nanoparticle for the magnetic lysosomal purification method is a prime example of how the desirable properties of an IONP can be utilised in a biomedical environment, in this case to aid the study of lysosomal phenotypes in cells exhibiting lysosomal storage disease phenotypes. For these experiments utilising an

IONP, it is also integral to rationalise whether the nanoparticle treatments themselves are associated with cellular impairment as this would impact the use of this method in phenotyping diseased cells. A comparison of the cellular impact of differing types of dextran-coated nanoparticles is, therefore, an ideal starting point that is highly relevant to their utility in cell culture experiments and is also a starting point for eventual comparison of uncoated nanoparticles.

In producing the nanoparticle toxicity model, a range of iron oxide and dextran nanoparticles were used (**Figure 4-2**): LRL are 80% magnetite/20% maghemite nanoparticles with a 40 kDa dextran-coat, CC are 50% magnetite/ 50% maghemite nanoparticles with a 40 kDa dextran-coat and ID are nanoparticles with a dextran core, instead of coat, then coated with ferric hydroxide (FeO). A CHO H1 cell line was chosen for use in these experiments as the cells are quick to grow and divide, with a good lysosomal to cell ratio, are well characterized as a cell line, are capable of a high level of nanoparticle uptake through endocytosis (especially for a non-phagocytic cell line) and were previously utilised for IONP mediated lysosomal purification which allows for comparison with historic data in the lab. Groups of phenotypes were assessed including: ability of IONPs to release free iron, the impact of IONP treatment on lysosomes and autophagy, investigation of reactive oxygen species (ROS) production, mitochondrial effects, cell morphology changes, and two basic cell death/toxicity markers. The identification of phenotypes in this chapter was to identify pathways in the cell affected by nanoparticle treatment, rather than to fully elucidate the individual significance of any particular phenotypes, to both find common IONP-induced changes/toxicity and also to compare the effect on toxicity between the three different structures and compositions of the chosen IONP. The aim was also to further investigate the cytotoxicity of LRL nanoparticles, used for the magnetic lysosomal extraction technique, as high compatibility would further validate the use of these nanoparticles in this method.

4.2 Materials and Methods

4.2.1 Cell culture and nanoparticle treatment

Three different dextran-complexed iron oxide nanoparticles (IONPs) were used in this chapter, as briefly described below (**Figure 4-2**):

- **LRL** – 40 kDa dextran-coated magnetite/maghemite (80%/20%) nanoparticle (DexoMAG-40) from Liquids Research Ltd (Bangor, UK).
- **CC** – 40 kDa dextran-coated 50 nm magnetite/maghemite (50%/50%) nanoparticles (FluidMAG-DX) from Chemicell (Berlin, Germany).
- **ID** - Iron-dextran, a ferric hydroxide (FeO) coated complex with a 40 kDa dextran core (D8517) from Sigma Aldrich (Merck).

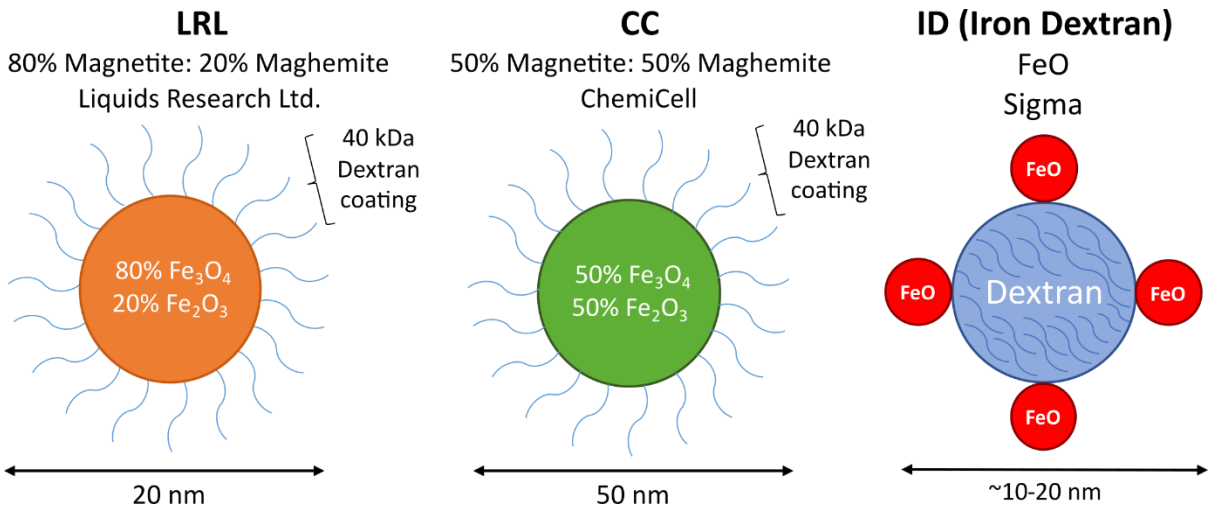

Figure 4-2: Compositions and structures of Chapter 4 IONPs. From top, details of nanoparticle name, iron oxide composition and manufacturing company. Dextran (in blue) coats the LRL and CC nanoparticles and forms a core for ID nanoparticles.

In this chapter the cells were treated with nanoparticles in the same manner as an established method for magnetic lysosomal purification that maximises lysosomal yield (Walker and Lloyd-Evans 2015). CHO H1 cells (general cell culture described in methods Section 2.1.1) grown in 6-well plates, were treated with IONPs at 1 mg/mL in cell culture medium with 10 mM HEPES buffer for a 24-hour pulse, optimal for nanoparticle endocytosis. After treatment the cells were then washed twice with PBS to remove

nanoparticle solutions, detached from the plate with trypsin, spun down, and replated after cell counting into an IbiTreat 8-well μ-slide (Thistle Scientific). After the 24-hour pulse (P), cells were then incubated for a 24-hour or 36-hour chase (CH) period (denoted as 24hP:24hCH or 24hP:36hCH, respectively), providing time for nanoparticles that have been endocytosed (in the pulse period) to move through the endocytic system (in the chase period) and collect predominantly in the lysosomes (Pagano et al. 2000; Pagano 2003).

For every experiment, a non-nanoparticle treated control was present; other controls were included as necessary, commonly 25 nM Bafilomycin-A1 (Baf-A1; Tocris, Bristol, UK) and 2 μg/mL U18666A (Calbiotech) drug treatments for an overnight incubation with untreated control cells. Baf-A1 is an inhibitor of vacuolar type H^+-ATPase (V-ATPase) so causes lysosomal deacidification and inhibits autophagy. U18666A is an inhibitor of the lysosomal membrane transporter, NPC1, and induces phenotypes similar to Niemann–Pick type C disease that include lysosomal expansion and impaired endocytosis.

Electron microscopy (refer to method Section 2.2.2) was used to visually characterise the nanoparticles.

4.2.2 Degradation of IONP to release free iron

Phen green fluorescent staining (refer to method Section 2.4.16) and Calcein-AM (refer to methods Section 2.4.2) were used to detect the presence of heavy metal ions in cells. Ferrozine assays (refer to method Section 2.5.2) were used to investigate if nanoparticle degradation is pH dependent.

4.2.3 Impacts of IONPs on lysosomal function and autophagy

Acridine Orange fluorescent staining in a lysosomal stability assay (refer to method Section 2.4.1) was used to indicate membrane stability of acidic vesicles. LysoTracker Green fluorescent staining (refer to method Section 2.4.9) was used to indicate lysosomal area. Cyto-ID fluorescence staining (refer to method Section 2.4.4) was used to measure autophagic vesicles and monitor autophagic flux.

4.2.4 Lysosomal-related IONP phenotypes

Imaging of unstained cells by fluorescence microscopy indicated levels of cellular autofluorescence (refer to method Section 2.4.3). DPPP fluorescence staining (refer to method Section 2.4.5) was used to indicate lipid peroxidation levels. Superoxide levels were detected by So-ID fluorescence staining (refer to method Section 2.4.17).

4.2.5 Fura-2,AM as a Ca2+ probe and free iron indicator

The Fura-2,AM probe was used in measuring lysosomal Ca^{2+} release after addition of ionomycin and GPN (refer to method Section 2.4.8). The Fura-2, AM probe was also used to indicate the presence of free iron through quenching of the probe (refer to method Section 2.4.6). Fluorimetry of Fura-2,AM in the presence of Fe^{2+} and Fe^{3+} (refer to method Section 2.5.6) was used to investigate whether the probe is radiometric between 340 nm and 380 nm excitation wavelengths in terms of quenching.

4.2.6 Mitochondrial-related phenotypes

MitoTracker Green fluorescence staining (refer to method Section 2.4.12) was used to indicate mitochondrial area. CellTiter-Glo Luminescent Viability assay (refer to method Section 2.5.1) was used to quantify ATP. Metabolism of resazurin (refer to method Section 2.5.7) and the consequent colour change was used to measure cell metabolism.

4.2.7 Cellular Toxicity of IONP

Light Microscopy (refer to method Section 2.4.7) was used to investigate cell morphology. Phalloidin and Wheat germ agglutinin fluorescent staining (refer to method Section 2.4.15) was used to visualise the cell membrane and cytoskeleton, respectively. Nucview fluorescent staining (refer to method Section 2.4.13) was used to investigate caspase-3-mediatated apoptosis. Micronuclei/cell were counted (refer to method Section 2.4.11) to indicate genotoxicity levels.

4.3 Results

This chapter aims to identify which cellular pathways are being affected by IONP treatments and to evaluate the range of different responses from three different dextran coated IONPs (LRL, CC and ID).

4.3.1 Electron microscopy (EM) for IONP characterisation

The first aim was to evaluate the shape and size of each of the nanoparticles by electron microscopy to confirm these characteristics did match those stated by each nanoparticle manufacturer. The LRL nanoparticles are composed of an iron oxide core with a magnetite: maghemite ratio of 80%:20% and coated in a 40 kDa dextran, giving the nanoparticles a

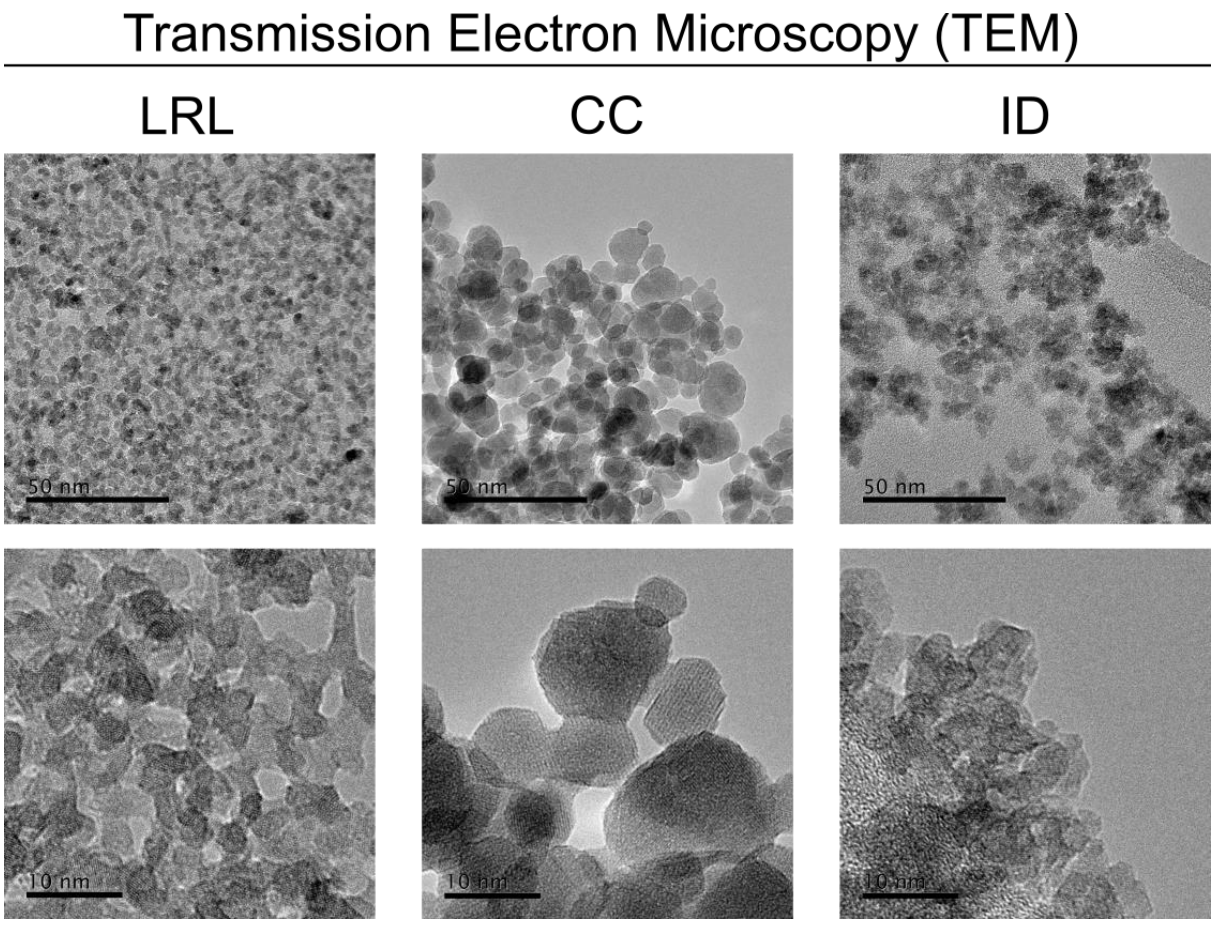

Figure 4-3: Characterisation of IONPs structures under electron microscopy. Images were taken by TEM with representative images of LRL nanoparticles in the left column, CC nanoparticles in the middle column and ID nanoparticles in the right column. The top row of images has 50 nm scale bars and the bottom row are at higher magnification with 10 nm scale bars.

hydrodynamic diameter of 20 nm. The TEM images show the iron oxide core of LRL nanoparticles to be less than 10 nm in diameter with a consistent size and spherical shape (**Figure 4-3**). The CC nanoparticles are composed of an iron oxide core with a magnetite: maghemite ratio of 50%:50% and coated in a 40 kDa dextran, giving the nanoparticles a hydrodynamic diameter around 50 nm. From the TEM images the CC nanoparticles have an iron oxide core that is a more crystalline polygon shape, many forming hexagons, most with a core more than 10 nm in diameter with a wide range of core sizes (**Figure 4-3**). The ID nanoparticles have a 40 kDa dextran core coated in FeO, with an unknown hydrodynamic diameter. The TEM images of the ID nanoparticles show small, less than 10 nm diameter, rounded and consistently sized FeO coated nanoparticles (**Figure 4-3**).

4.3.2 Degradation of IONP to release free iron.

As IONPs can be degraded in the acidic environment of the lysosome releasing free iron (Fe^{2+} and Fe^{3+}), the first step was to assess if free iron levels in the cell were raised and to evaluate how important a low pH is to IONP degradation.

The cellular stability of the nanoparticles was first assessed to determine if they are degraded in cells to release free iron (Fe^{2+} and Fe^{3+}). The fluorescent signal of Phen green staining is quenched by a range of metal ions but is most strongly quenched by Fe^{2+} and Cu^{+}. Two of the IONP treatments caused increased Phen green quenching in CHO H1 cells compared to the untreated control cells after a 24h pulse:24h chase (**Figure 4-4A**). Quantification of Phen green staining area showed significantly quenched fluorescence after CC and ID treatment, with 45% and 56% decreased fluorescence, respectively, and no significant difference after LRL treatment compared to untreated control cells (**Figure 4-4C**).

The probe Calcein-AM can chelate, and be fluorescently quenched by intracellular free iron, so acted as a second determinant of cellular free iron concentrations, focused on cytosolic free iron concentrations. Two of the IONP treatments caused increased quenching of calcein in CHO H1 cells compared to the untreated control cells after a 24h pulse:24h chase (**Figure 4-4B**). Quantification of Calcein-AM fluorescence intensity showed significantly quenched fluorescence after CC and ID treatment, with 75% and 60% decreased fluorescence, respectively, and no significant difference after LRL treatment compared to untreated control cells (**Figure 4-4D**).

To determine how breakdown of the IONPs is affected by pH, ferrozine assays were run as cell free experiments, calculating free Fe^{2+} and Fe^{3+} after nanoparticles were incubated in citrate phosphate buffer (pH 3/5/7) at 37°C (representing human body temperature) for 0, 2 and 24 hours (**Figure 4-5C-H**). A range of pH was chosen to determine pH dependency of the degradation effects, pH5 buffer was selected to represent the general pH of the lysosome, with comparison of pH5 and pH7 being the most relatable to cell conditions. While ferrozine reagent detects Fe^{2+}, addition of vitamin C to the samples also allowed calculation of Fe^{3+}.

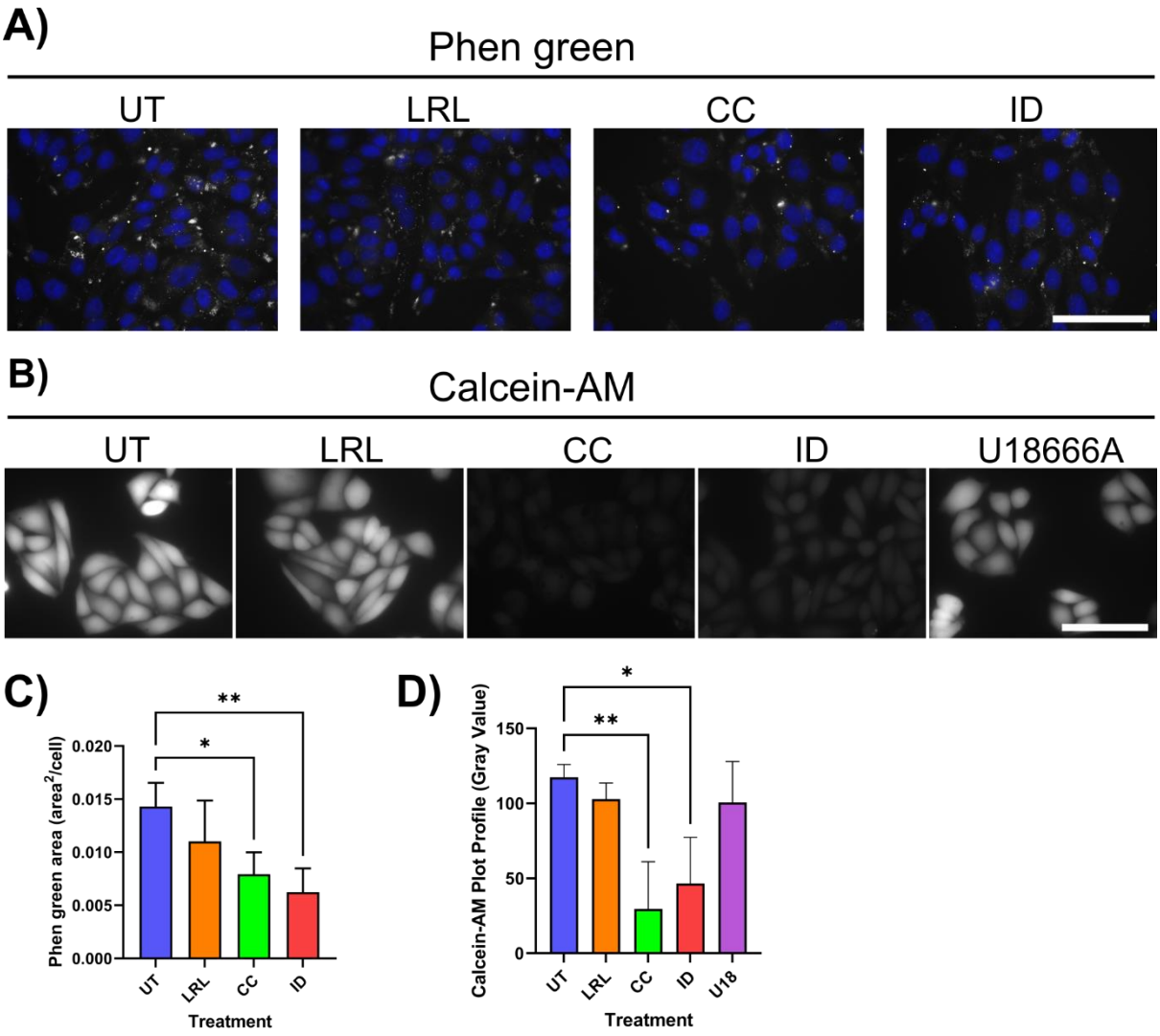

Figure 4-4: In cells IONPs can breakdown to release free iron. Phen green and Calcein-AM staining can be quenched by free iron as an indicator of nanoparticle degradation. Representative images of A) Phen green staining (grey scale), counterstained with Hoechst nuclear stain (blue) and **B)** Calcein-AM staining (grey scale), in CHO H1 cells treated with IONP (24hP:24hCH). Scale bars = 40 µm. Area analysis (9 images/treatment/repeat) for C) Phen green (n=4) and D) Calcein-AM (n=3). Data presented as average bars ± SD and analysed using a one-way Anova test with Dunnett's post-hoc test. UT=untreated control cells. *p<0.05, **p<0.01

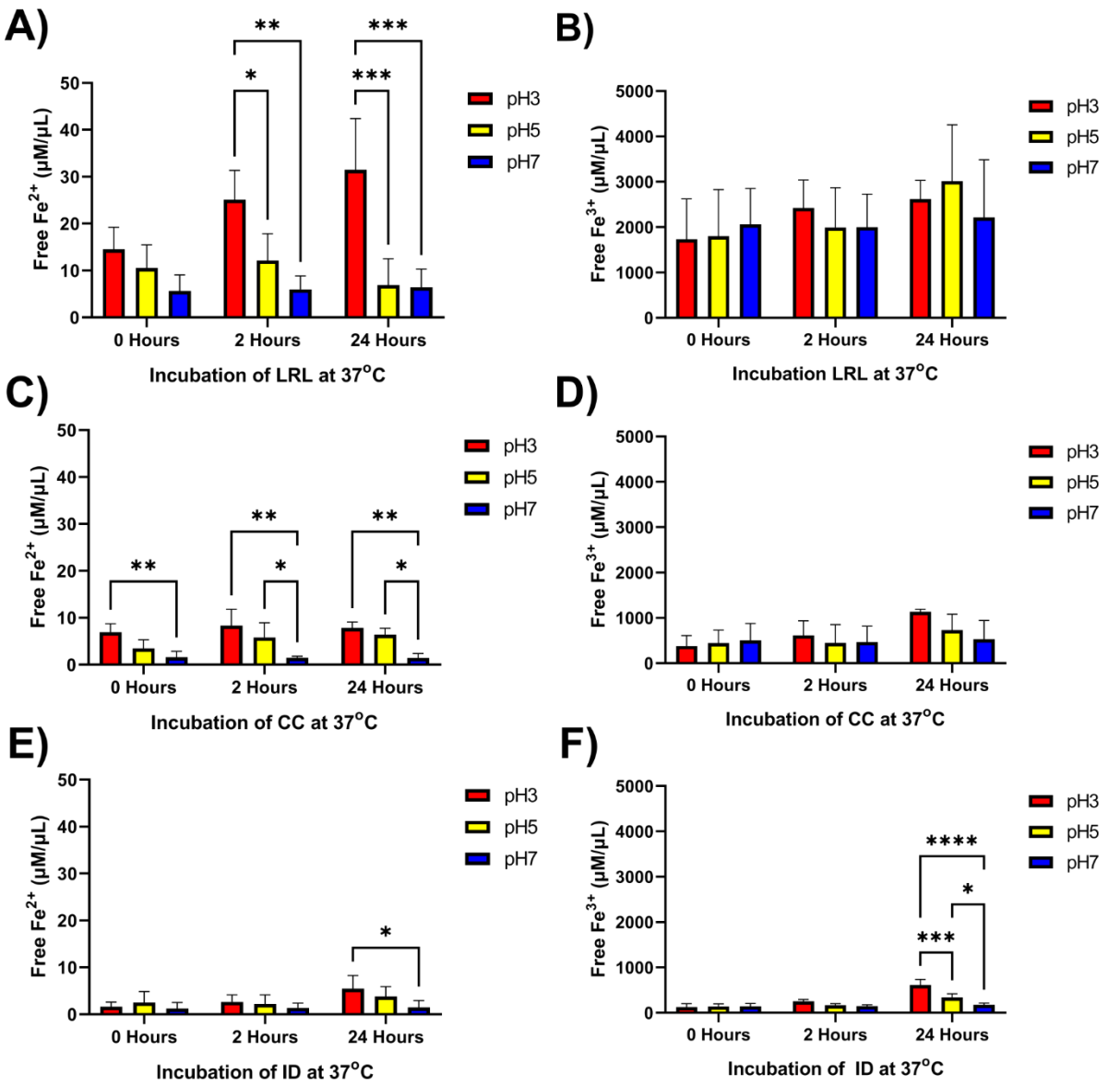

Figure 4-5: Degradation of IONPs to release Fe^{2+} or Fe^{3+} is pH dependent. Ferrozine assays were run with IONP solutions in pH3 (red), pH5 (yellow) pH7 (blue) citrate-phosphate buffer incubated at 37°C for 0, 2 or 24 hours. Ferrozine assays were normalised to an iron standard for quantification of Fe^{2+} and, by addition of vitamin C, Fe^{3+} was calculated. Analysis of iron release for **A)** LRL Fe^{2+} or **B)** LRL Fe^{3+}, **C)** CC Fe^{2+} or **D)** CC Fe^{3+}, **E)** ID Fe^{2+} or **F)** ID Fe^{3+}. Data presented as average bars ± SD and analysed using a two-way Anova test with Tukey's post-hoc test comparing within each incubation time grouping. n=3. *p<0.05, **p<0.01, ***p<0.001, ****p<0.0001.

LRL nanoparticles had the largest basal (0-hour) recorded Fe^{2+} concentrations (**Figure 4-5C**) with Fe^{2+} concentrations at pH3 significantly higher than at pH5 or pH7 after both 2-hour and 24-hour incubations and with greater Fe^{2+} concentrations after 24 hours than after 2 hours for all repeats. LRL nanoparticles also produced the greatest basal (0-hour) Fe^{3+} concentrations, however, there was no significant differences between any pH groups or

any differences between time points for Fe^{3+} concentrations after LRL treatment (**Figure 4-5D**). No significant difference was seen in Fe^{2+} or Fe^{3+} release from LRL degradation between pH5 and pH7 buffers for any incubation time point.

Differences in Fe^{2+} concentrations were seen between pH3 and pH7 buffers at all time points for CC nanoparticles (**Figure 4-5E**). Significantly greater Fe^{2+} concentrations also seen between pH5 buffer compared to pH7 after 2-hour and 24-hour incubations with 290% and 344% increases, respectively. No significant differences between any pH groups were seen for Fe^{3+} concentrations with CC nanoparticles (**Figure 4-5F**). Despite pH3 and pH5 values for CC Fe^{3+} concentrations not being significantly different to pH7 within any incubation time group, the pH3 value at 24-hours was significantly different (*p=0.0402) to the 0-hour pH3 value for CC Fe^{3+} concentrations (analysis not shown on graph).

In contrast to the previous two IONP, ID nanoparticles showed significant Fe^{2+} concentrations only after 24-hour incubation between pH3 and pH7 (**Figure 4-5G**) while being the only IONP to show significant differences in Fe^{3+} concentrations between different pH buffers (**Figure 4-5H**). In ID nanoparticle solutions after 24-hour incubation all three pH buffers had significantly different Fe^{3+} concentrations negatively correlated with pH. This change in Fe^{3+} concentrations at 24-hours was the only significant difference between pH7 and pH5 buffers for ID nanoparticles, with a 94% increase at pH5, compared to a 348% increase for pH3 compared to pH7.

Pre-incubation of the LRL nanoparticles with 2 mg/mL bovine serum albumin (BSA) protein, led to a reduction in IONP breakdown compared to samples free of additional protein (**Supplementary Figure 4-1**).

4.3.3 Impacts of IONPs on lysosomal function and autophagy

Having observed the release of free Fe^{2+} and Fe^{3+} *in vitro* by ferrozine assays and quenching of Phen green *in cellulo,* it was next investigated whether the presence of higher lysosomal free iron could alter lysosomal membrane integrity.

The protocol for acridine orange staining with exposure to UV (365 nm) light can act as an indicator for comparing lysosomal membrane stability between treatments. In the CHO H1 cells, the acridine orange accumulated in acidic vesicles in a dimerised form (red, 590 nm

excitation fluorescence), and in the cytosol and nucleus as a monomer form (green, 470 nm excitation fluorescence) (**Figure 4-6A**), with a similar baseline fluorescence for all treatments (**Figure 4-6B**). When the cells were continuously exposed to UV light, over a short period of time (minutes) increased 470 nm fluorescence (monomer form), accompanied by a less clear decrease in 590 nm fluorescence (dimer form), was seen in all treatment groups (**Figure 4-6C**). After optimisation, analysis of the 2-minute time point in comparison to the initial 0-minute baseline was chosen as it presented a point where differences became clear between treatment groups, but before 470 nm fluorescence reached a saturated level of intensity. Data from the 470 nm excitation channel alone was used for analysis as bleed-through was observed in the 590 nm excitation channel.

After 2 minutes exposure to UV light, only CC treatment showed a significant difference to untreated cells with a large 208% increase (**Figure 4-6G**), suggesting CC treatment led to an increased level of lysosomal membrane instability. In contrast, when the nanoparticle cells were all pre-treated with U18666A, the significant difference from CC treatment was lost (**Figure 4-6D-F,H**).

The lysosome is where most nanoparticles taken up by endocytosis will be trafficked to in the cell and where the majority of nanoparticle degradation is likely to occur, so checking for changes in the degradative pathways of the cell is a primary step for investigation, especially after having observed that some nanoparticles can impact on the integrity of the lysosomal membrane. A significant reduction in LysoTracker area (staining for acidic vesicles) was seen after CC and ID treatment (24hP:24hCH) with 40% and 66% reductions, respectively, compared to untreated control cells (**Figure 4-7A and C**). ID treatment caused the greatest reduction in LysoTracker area of all the IONP treatments, with staining area reduced to around one third of untreated controls. Yet none of the IONP treatments completely abolished staining of acidic vesicles, as is demonstrated by the negative control, overnight treatment of 25 nM Bafilomycin A1 (BafA-1), which deacidifies lysosomes. In comparison, LRL treatment led to no change in LysoTracker area compared to untreated controls. Particle count was also calculated to indicate whether the change in area was from fewer or smaller acidic organelles. In contrast to LysoTracker area analysis, no significant effects were observed on particle count (**Figure 4-7D**).

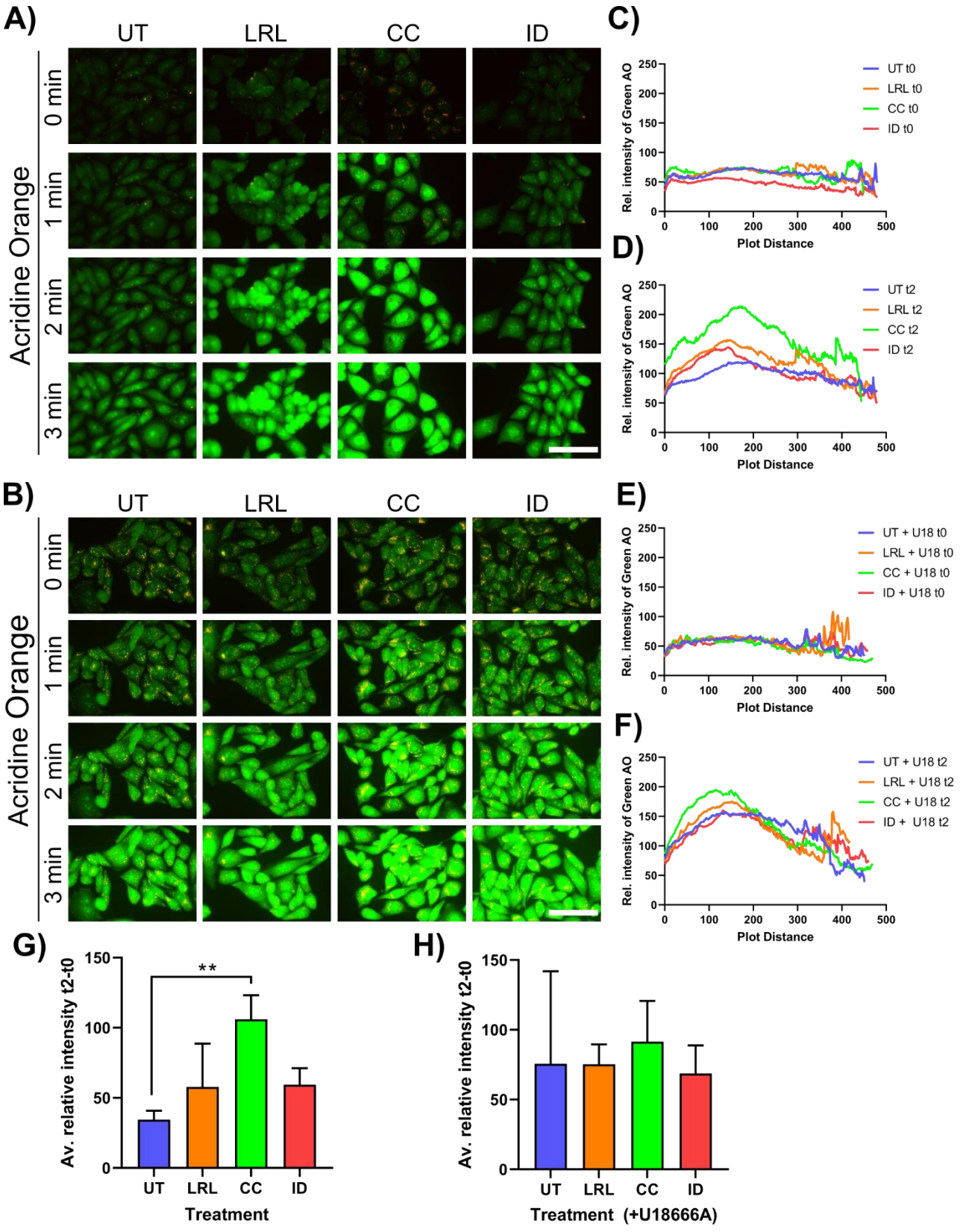
A)
UT
LRL
CC
ID
Acridine Orange
0 min
1 min
2 min
3 min
B)
C)
UT t0
LRL t0
CC t0
ID t0
Rel. intensity of Green AO
Plot Distance
D)
UT t2
LRL t2
CC t2
ID t2
E)
UT + U18 t0
LRL + U18 t0
CC + U18 t0
ID + U18 t0
F)
UT + U18 t2
LRL + U18 t2
CC + U18 t2
ID + U18 t2
G)
Av. relative intensity t2-t0
**
Treatment
H)
Treatment (+U18666A)

Figure 4-6: Lysosomal membrane stability was affected by CC nanoparticle treatment. Acridine orange (AO) is protonated in acidic vesicles (red) in contrast to the cytosol (green). Photo-oxidation by UV light causes rupture of the lysosomal membrane and shifting of red AO fluorescence back to green. Representative images of AO staining in **A)** IONP treated CHO H1 cells (24hP:24hCH) and **B)** IONP + U18666A (2 µg/mL overnight) treated CHO H1 cells to demonstrate lysosomal membrane stability based on the length of time before rupture. Analysis of relative staining intensity across cells (9 images/treatment/repeat), for the IONP treated cells **C) and D)** at 0 minutes and 2 minutes, respectively and for the IONP + U18666A (U18) treated cells **E) and F)** at 0 minutes and 2 minutes, respectively. Average of the change in intensity across plot from 0 minutes (t0) to 2 minutes (t2) for **G)** IONP and **H)** IONP + U18666A treated cells. UT=untreated control cells. Scale bars = 40 µm. Analysis by One-way ANOVA with Dunnett's post hoc test. Data represents mean ± SD; ** $p<0.01$. All n=3.

LysoTracker staining was also measured by live cell plate assay to provide quantitative experimental data, yet no significant changes in the fluorescence between the IONP treatments was detected (**Supplementary Figure 4-2**). It is likely the plate reader is more sensitive to the fluorescence of LysoTracker Green than the CCD camera on the microscope used for imaging the stain. Bafilomycin-A1 treatment (25nM overnight), the negative control, deacidifies lysosomes, with very low staining quantified from microscopy images, yet by plate assay there was still fairly high levels of fluorescence. Results in the plate assay may also be strongly affected by random scanning of dense regions of cells, as CHO H1 do not have contact inhibition and can grow on top of each other in these regions. Although cell counting and adequate re-suspension of cell solutions before seeding was preformed to minimise this occurrence. Therefore, microscopy imaging and analysis was chosen as a focus for quantifying the stains rather than using the plate assays, as this method proved sensitive and effective for discerning the changes in fluorescence after IONP treatments.

Changes in autophagy regulation often occur when organelle dysfunction is detected by the cell, with this process able to be regulated by lysosome dysfunction or dysfunction of other cellular organelles. Therefore, autophagy was investigated as an indicator for organelle dysfunction caused by the nanoparticle treatments. Autophagy can be measured by Cyto-ID staining for autophagic vacuoles. Cyto-ID staining was significantly increased (41%) only in CC treated cells compared to untreated control cells (**Figure 4-7B and E**). In contrast, neither LRL nor ID treatments significantly altered Cyto-ID staining.

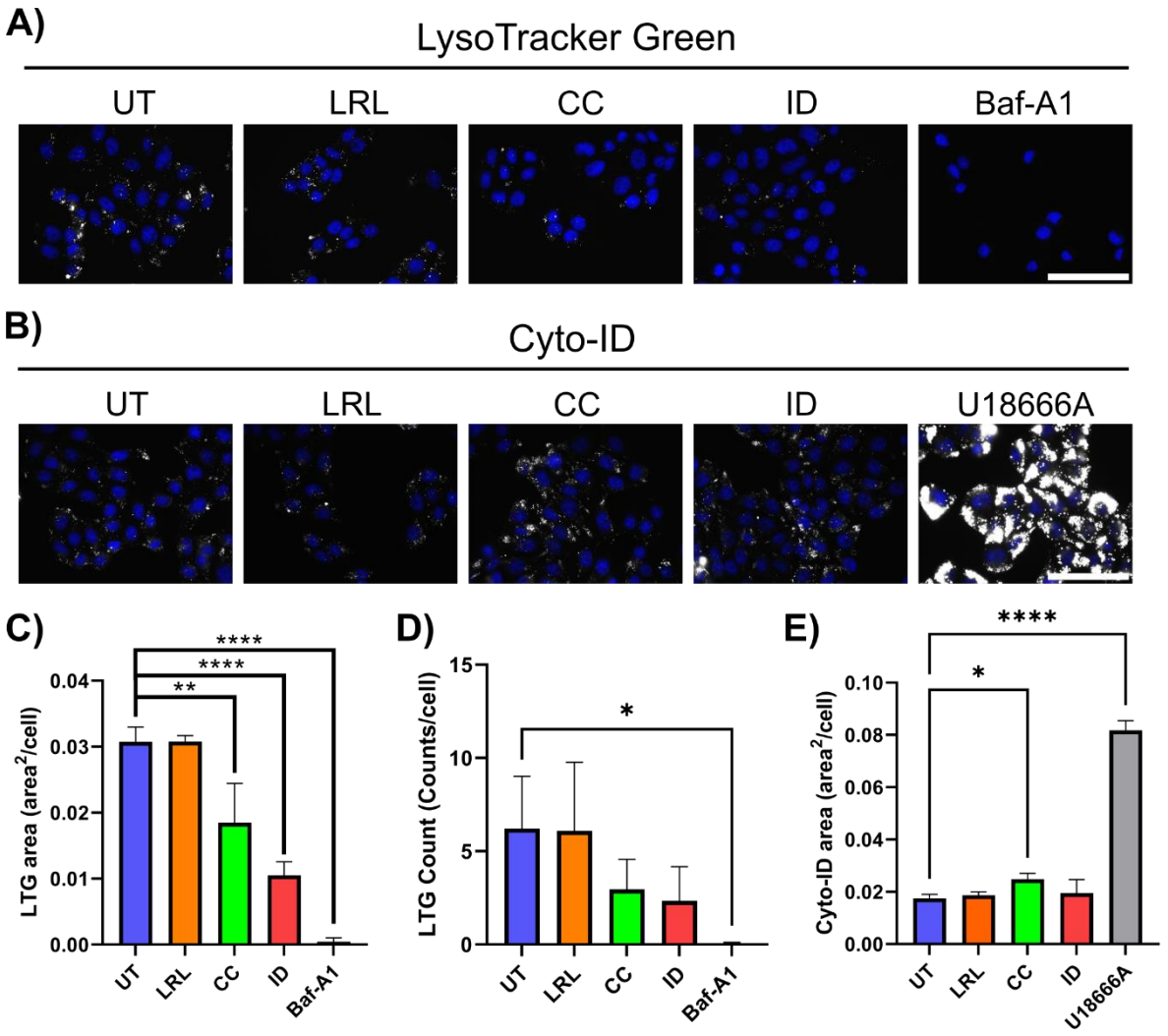

Figure 4-7: Impact of IONP treatments on cellular degradation pathways. A) Representative images, **C)** quantitative area analysis and **D)** quantitative particle count for LysoTracker green (grey scale) staining acidic vesicles in CHO H1 cells treated with IONP (24h pulse:24h chase), counterstained with Hoechst nuclear stain (blue). n=3. **B)** Representative images and **E)** quantitative area analysis for Cyto-ID (grey scale) staining autophagic vesicles in CHO H1 cells treated with IONP (24hP:24hCH), counterstained with Hoechst nuclear stain (blue). n=3. UT = untreated control cells. Scale bars = 40 µm. All image analysis from 9 representative images/treatment/repeat. Data presented as average bars ± SD and analysed using a one-way Anova test with Dunnett's post-hoc test. *p<0.05, **p<0.01, ***p<0.001, ****p<0.0001.

4.3.4 Lysosomal-related IONP phenotypes

Severe lysosomal dysfunction, which strongly reduces lysosomal degradative capacity can lead to accumulation of autofluorescent material in cells, and consequent increased cellular autofluorescence. Therefore, autofluorescence was investigated as an indicator for the

severity of lysosomal dysfunction, which had been indicated by reduced LysoTracker staining and changes to autophagy with some of the IONP treatments.

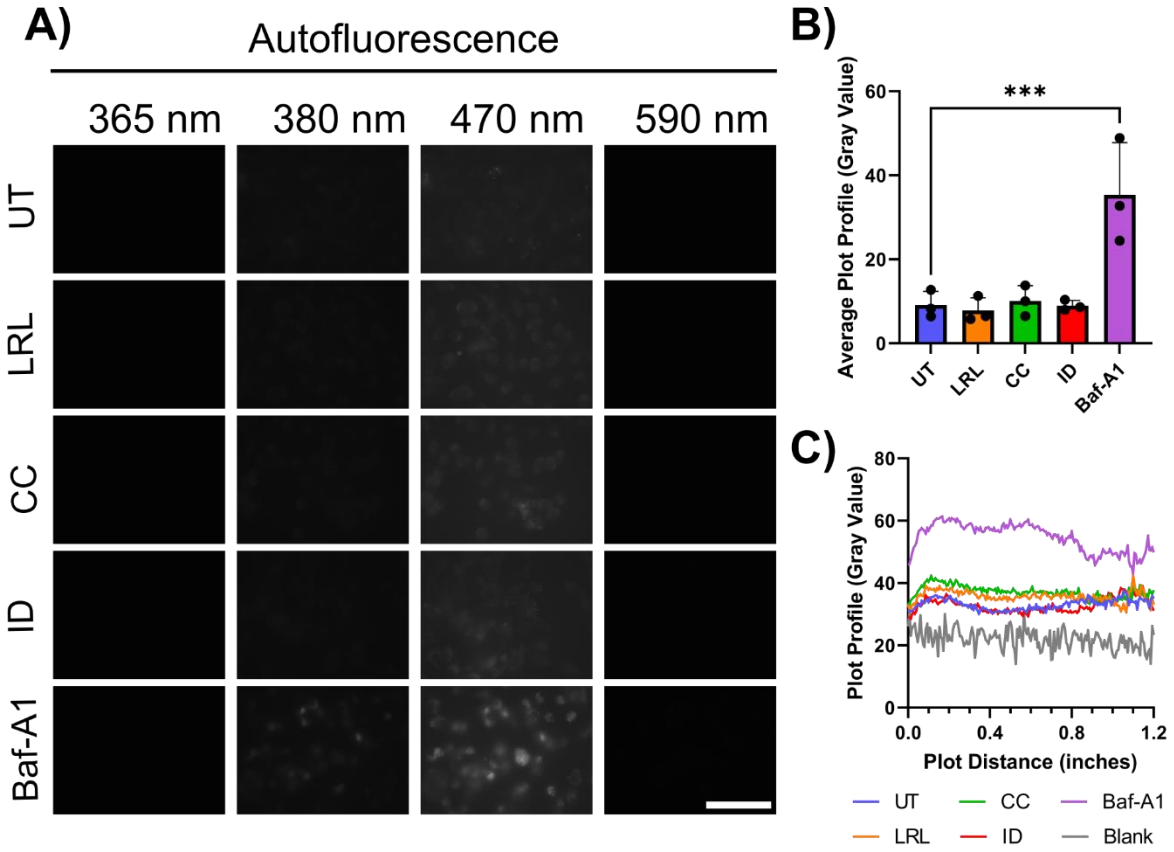

Figure 4-8: IONP treatments did not lead to increased autofluorescence. A) Representative images at 365 nm, 380 nm, 470 nm and 590 nm excitation wavelengths of unstained IONP treated CHO H1 cells (24hP:24hCH), detecting autofluorescence (grey scale) and **B)** quantification through plot profile intensity, analysing 5 representative images/treatment/repeat at 470 nm excitation wavelength. Baf-A1 (25 nM overnight incubation) included as a positive control. Scale bars = 40 µm. n=3. Data presented as average bars ± SD and analysed using a one-way Anova test with Dunnett's post-hoc test. ***p<0.001. **C)** Averaged 'plot profile' intensity across the lines drawn through cells shown graphically from which data is averaged to generate values for analysis in **B)**. UT = untreated control cells.

Images for autofluorescence were taken at four wavelengths (**Figure 4-8A**), although it is most clearly visible at 470 nm, so these images were used for data analysis (**Figure 4-8B**). All CHO H1 cells emitted low basal levels of autofluorescence compared to background including untreated control cells, as is shown by the image plot profiles (**Figure 4-8C**). None of the IONP treatments caused any increase in autofluorescence and only the positive control Baf-A1 treatment caused a significant increase in autofluorescence levels compared to untreated control cells (**Figure 4-8B**).

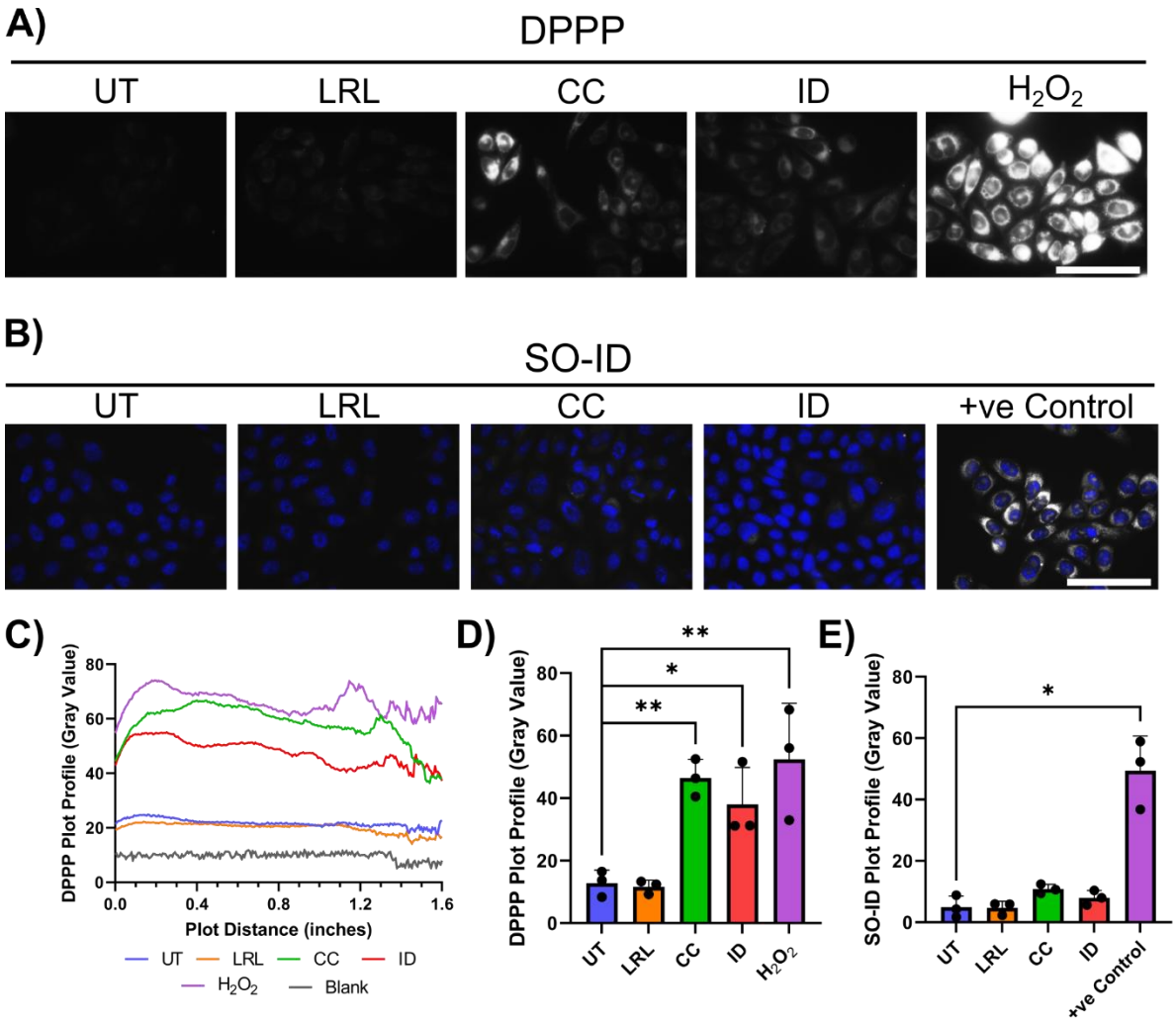

Figure 4-9: Impact of IONP treatments on cellular oxidative damage. A) Representative images, **C)** averaged 'plot profile' intensity and **D)** quantitative area analysis (9 images/treatment-/repeat) for DPPP (grey scale) staining lipid peroxidation in CHO H1 cells treated with IONP (24hP:24hCH). n=3. **B)** Representative images and **E)** quantitative area analysis (8 images/treatment/repeat) for SO-ID (grey scale) staining super oxide (not including hydroxyl radicals) in CHO H1 cells treated with IONP (24hP:24hCH), counterstained with Hoechst nuclear stain (blue). n=3. UT = untreated control cells. Scale bars = 40 µm. Data presented as average bars ± SD and analysed using a one-way Anova test with Dunnett's post-hoc test. *p<0.05, **p<0.01.

Release of free iron from nanoparticle degradation in the lysosome can lead to the production of ROS via Fenton reactions. Fenton reactions often form hydroxyl radicals which are highly reactive so are often only detectable for a short period of time but can cause peroxidative damage to lipids and proteins. As this peroxidative damage is detectable for longer, it can be a primary starting point for indicating nanoparticle induced ROS production, organelle dysfunction and in the case of lipid peroxidation, as was next investigated, indicate a factor affecting lysosomal membrane stability. The DPPP probe was

used to stain for lipid peroxidation with hydrogen peroxide (H_2O_2) treatment included as a positive control. Both CC and ID treatment caused a significant increase in DPPP staining (**Figure 4-9A, C and D**), with 262% and 196% increases, respectively, compared to untreated control cells. While LRL treated cells showed no statistically significant difference in levels of DPPP staining compared to untreated control cells.

The increased lipid peroxidation seen with some of the IONP treatments, suggests an increase in cellular ROS. The type of ROS present can indicate it's origin. Superoxide radicals are a commonly produced ROS in mitochondria from errors in the electron transport chain. As these radicals exist for longer in the cell and so are easier to detect, superoxide levels were investigated, which would indicate mitochondrial dysfunction rather than direct nanoparticle-associated ROS. Yet, no significant difference was seen in superoxide (SO-ID) staining for any of the IONP treatments (**Figure 4-9B and E**).

4.3.5 Fura-2,AM as a Ca2+ probe and free iron indicator

The lysosome is an important organelle for Ca^{2+} signalling yet having determined that some IONP treatments can affect the lysosomal membrane and alter regulation of autophagy, a process in which lysosomal Ca^{2+} signalling may play a role, it was next investigated whether IONP treatments can affect lysosomal Ca^{2+} content.

GPN was used to release and quantify lysosomal Ca^{2+} stores following the pre-addition of ionomycin to permeabilise all other stores so that they do not interfere. GPN is a substrate of cathepsin C whose hydrolysis causes osmotic lysis of the lysosomal membrane and release of Ca^{2+} into the cytoplasm for quantification by the radiometric Ca^{2+} probe, Fura-2,AM.

Lysosomal Ca^{2+} storage was altered by CC treatment, but not LRL or ID treatment (**Figure 4-10A**). CC treatment caused a large 114% increase in GPN induced Ca^{2+} release compared to control cells, indicating a more than doubling of the level of Ca^{2+} storage. Ten representative traces are shown for each treatment, the first larger peak after addition of Ionomycin, representing non-lysosomal Ca^{2+} store permeabilisation and the second much smaller peak (enlarged at the top right of each graph) after GPN treatment representing lysosomal Ca^{2+} (**Figure 4-10C-F**). A ten times higher concentration of ID (10 mg/mL) (**Figure 4-10H**) was also

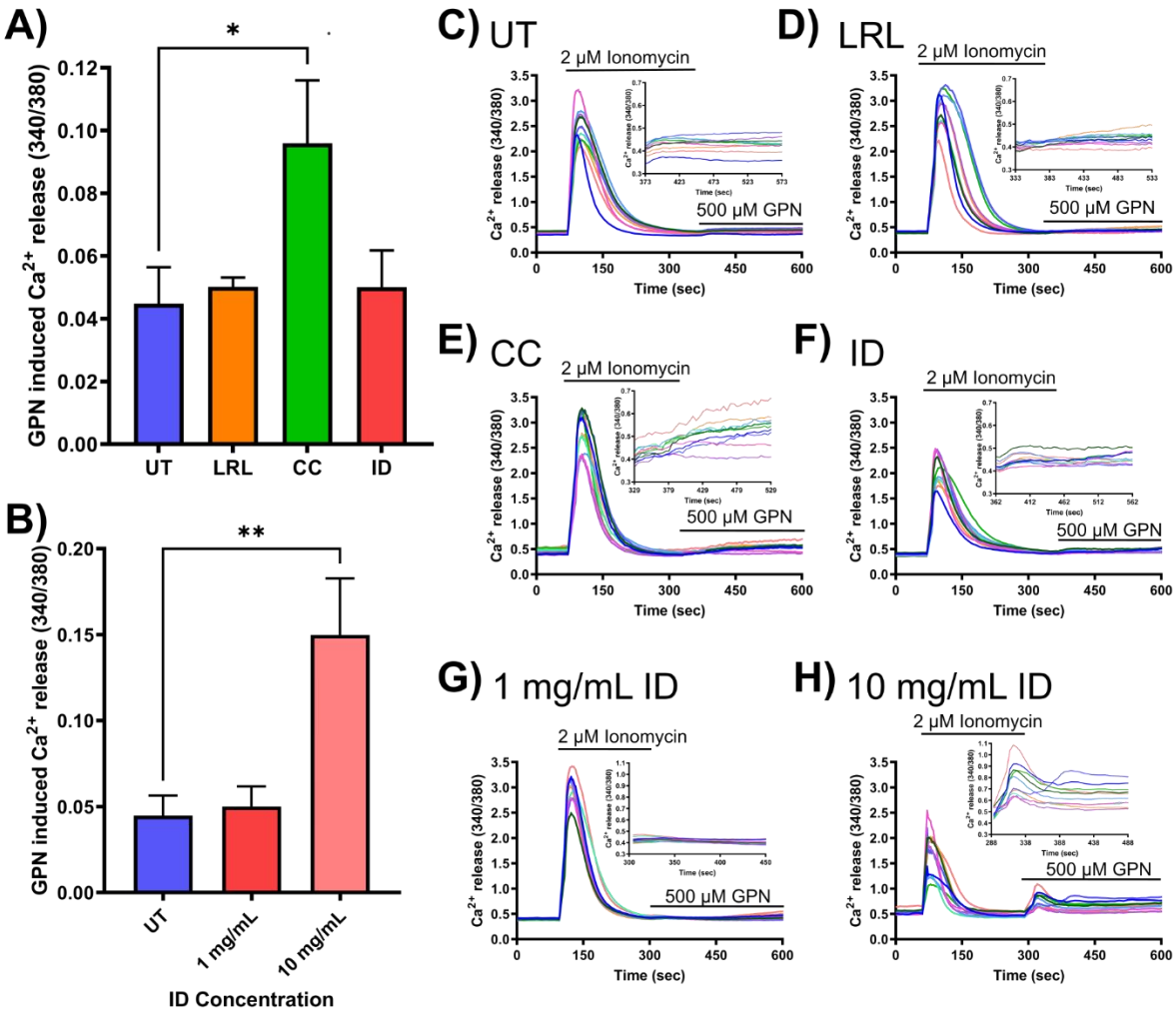

Figure 4-10: Certain IONP treatments can alter lysosomal Ca^{2+}. CHO H1 cells were treated with **A)** 1 mg/mL IONPs or **B)** 1 mg/mL and 10 mg/mL ID (24hP:36hCH) before ratiometric quantification of lysosomal Ca^{2+} release. **C-H)** Cells were loaded with Fura-2,AM and treated with 2 μM ionomycin to quench non-lysosomal Ca^{2+} stores, followed by GPN (500 μM) to measure lysosomal Ca^{2+} release. Representative traces from one experiment are shown with 10 cells per treatment and an enlargement of the region after addition of GPN. n=3. UT = untreated control cells. Data presented as average bars ± SD and analysed using a one-way Anova test with Dunnett's post-hoc test. *p<0.05, **p<0.01.

tested against the normal 1 mg/mL ID (**Figure 4-10G**), with the higher concentration causing a large significant increase in GPN-mediated lysosomal Ca^{2+} release compared to the untreated controls, despite no significant difference with the lower concentration (**Figure 4-10B**). The 10 mg/mL concentration of ID caused a large 235% increase in lysosomal Ca^{2+} release, larger than the difference induced by CC treatment.

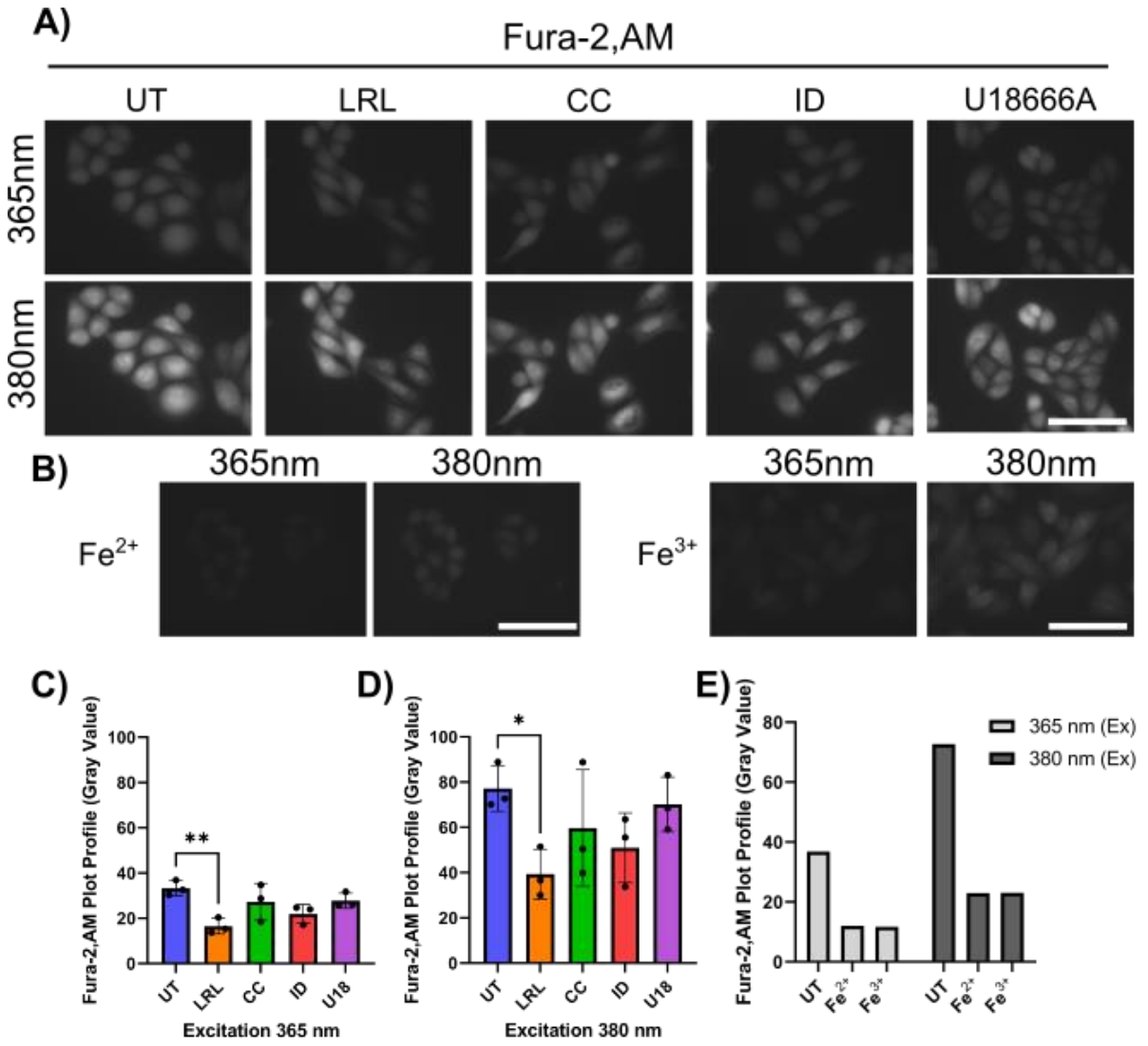

Figure 4-11: Investigating Fura-2,AM fluorescence in IONP treated cells. Representative images of Fura-2,AM staining at 365 nm and 380 nm excitation wavelengths in CHO H1 cells treated with **A)** IONP (24hP:24hCH; n=3) and **B)** 10 mM Fe^{2+} or Fe^{3+} containing solutions (30-minute incubation; n=1). Images were analysed (5 images/treatment/repeat) by ImageJ for averaged 'plot profile' intensity for IONP treatments at **C)** 365 nm and **D)** 380 nm excitation wavelengths, and for **E)** Fe^{2+} and Fe^{3+} containing solutions. UT = untreated control cells. U18 = U18666A treatment. Scale bars = 40 µm. Data presented as average bars ± SD and analysed using a one-way Anova test with Dunnett's post-hoc test. *p<0.05, **p<0.01.

Imaging Fura-2,AM staining of cells at rest can indicate resting Ca^{2+} levels in the cells, but the stain can also be quenched by free iron. Images taken at two excitation wavelengths, 365 nm and 380 nm, showed a similar pattern of intensity across both wavelengths (**Figure 4-11A**). At 365 nm and 380 nm excitation, LRL was the only significantly reduced treatment compared to control cells, with around 50% reduction compared to control cells (**Figure 4-**

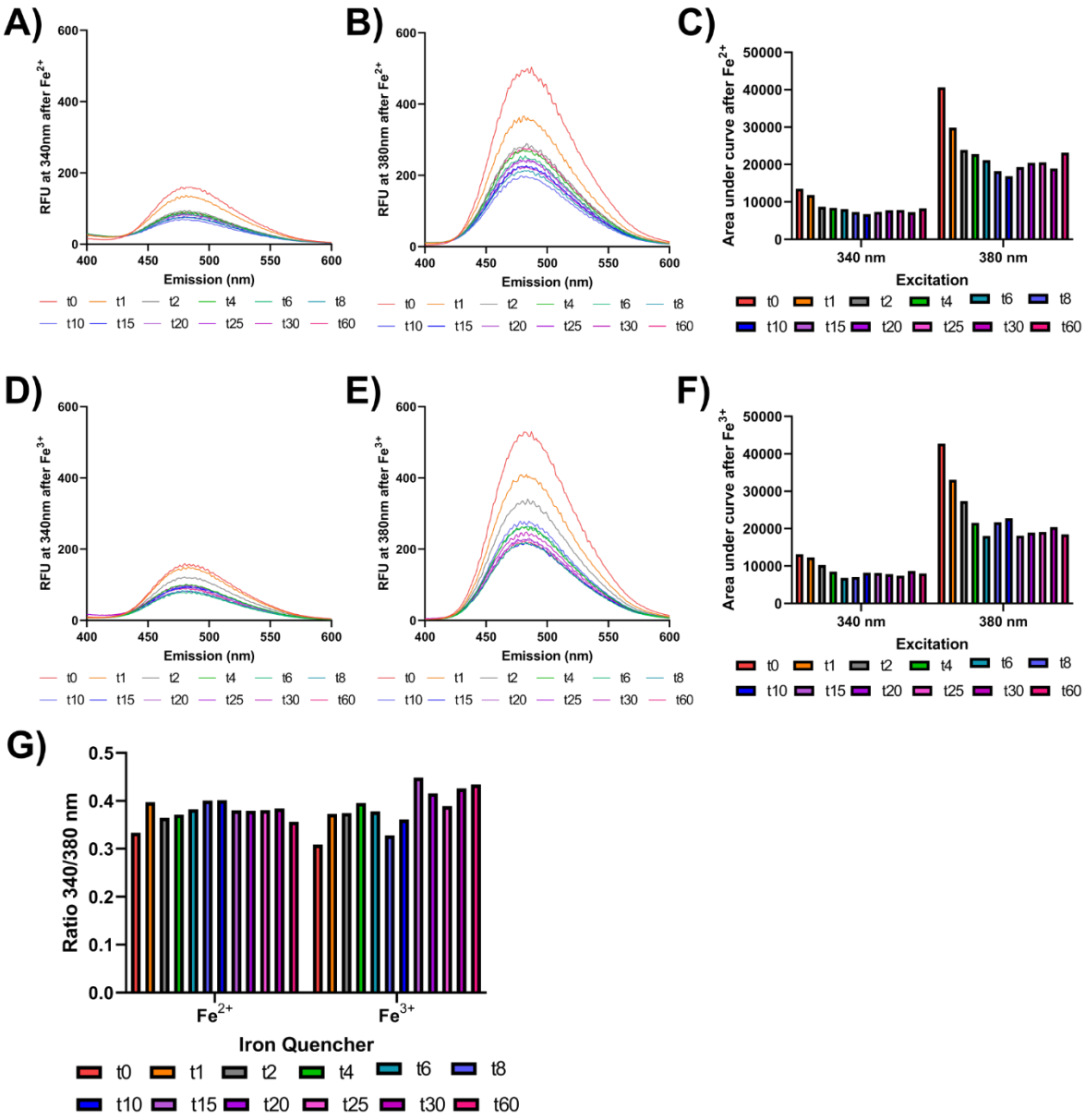

Figure 4-12: Time-course for quenching of Fura-2,AM by Fe^{2+} and Fe^{3+}. Spectrophotometry data for Fura-2,AM quenching by 10 mM Fe^{2+} and Fe^{3+} solutions over 60 minutes. Emission spectra curves after addition of Fe^{2+} at **A)** 340 nm excitation and **B)** 380 nm excitation with averaged total area (sum) of curves plotted in **C)**. Emission spectra curves after addition of Fe^{3+} at **D)** 340 nm excitation and **E)** 380 nm excitation with averaged total area (sum) of curves plotted in **F)**. **G)** Ratio of 340 nm data from **C)** divided by 380 nm data from **F)**. n=1

11C and D). The Fura-2,AM staining is brighter at 380 nm compared to 365 nm, but the pattern between different IONP treatments is strongly similar between the two wavelengths, showing the stain is not ratiometric. It was unclear if the changes in staining intensity were due to differences in dye loading or due to quenching by free iron. Fura-2,AM staining after incubation of control cells with a 10 mM Fe^{2+} or Fe^{3+} containing solution for 30

minutes was checked to confirm if the probe was in fact sensitive to both or just one of the iron species (**Figure 4-11B).** This suggested that both Fe^{2+} and Fe^{3+} appeared to dramatically quench the Fura-2,AM, to a very similar degree (**Figure 4-11E**), with both ions at both wavelengths reducing staining intensity by ~67-68% (not statistically analysed due to one technical replicate). On the images of CC treated cells, dark vacuoles could be seen in the cells, resembling the acidic lysosomal compartments seen in acridine orange staining of the CC treated cells (**Figure 4-11A**).

To check on the effects of iron quenching of Fura-2,AM without the complication of differential Ca^{2+} binding, cell-free spectrophotometry of the probe treated with free iron solutions was performed. Fura-2,AM solution showed a small amount of quenching in the emission spectrum with 340 nm excitation after 10 mM Fe^{2+} (**Figure 4-12A and C**) or 10 mM Fe^{3+} (**Figure 4-12D and F**) containing solutions were added, with the same pattern of quenching in the emission spectrum from 380 nm excitation after addition of 10 mM Fe^{2+} (**Figure 4-12B and C**) or 10 mM Fe^{3+} (**Figure 4-12E and F**). The quenching for both iron species, at both emission wavelengths, occurred within one minute after addition of the free iron solutions, reaching the lowest recorded level after 10 minutes and remaining at this level for the duration of the experiment (60 minutes). A ratio of 340/380 data, for both free iron solutions, was calculated (**Figure 4-12G**) which suggested the probe was not ratiometrically sensitive to iron quenching, as it is to Ca^{2+} quenching.

4.3.6 Mitochondrial-related phenotypes

The effect of the IONP treatments on mitochondrial function was next investigated, as iron is an important component for the functioning of mitochondria and because mitochondria are particularly sensitive to ROS-induced damage. Initial peroxidative damage of mitochondria can lead to further production of ROS in a positive feedback loop, while increased levels of dysfunctional mitochondria can affect cell metabolism and trigger autophagy. MitoTracker Green was used for initial detection, as this determines all mitochondrial area, not differentiating functional and dysfunctional mitochondria.

MitoTracker Green staining area was increased in CC and ID treated cells, but not LRL treated cells, compared to untreated controls (**Figure 4-13A**). CC treatment led to the

largest increase in MitoTracker area with a significant 24% increase, while ID led to a significant 20% increase (**Figure 4-13B**).

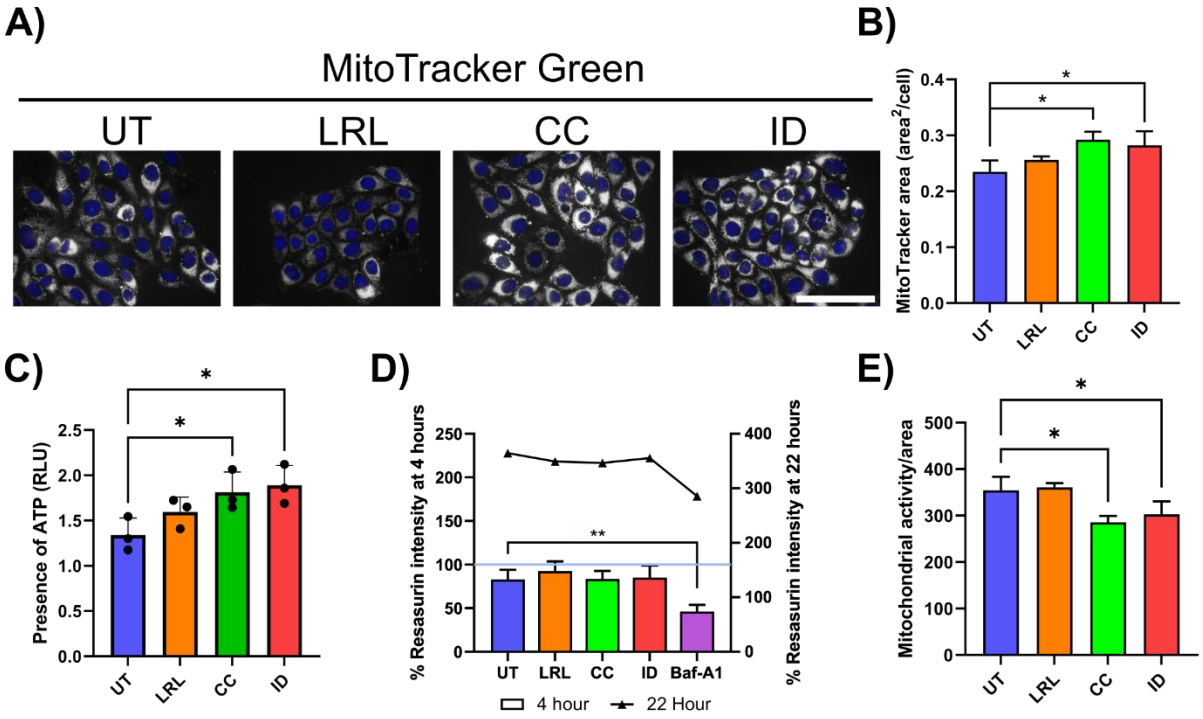

Figure 4-13: Effects of IONP treatments on mitochondria and mitochondrial activity. Measurements of mitochondrial phenotypes in IONP treated (24hP:24hCH) CHO H1 cells. **A)** Representative images and **B)** quantitative area analysis (9 images/treatment/repeat) for MitoTracker green (grey scale) staining mitochondria, counterstained with Hoechst nuclear stain (blue). n=3. **C)** Quantitative data for the CellTiter-Glo Luminescent Viability assay to quantify ATP and normalised to Bafilomycin A1 treated control cells. n=3. **D)** Quantitative data for the Resazurin assay to quantify metabolic activity after a 4-hour and 22-hour (plotted on right y-axis for qualitative interest only) incubation with the assay substrate. Only 4-hour data was statistically analysed. n=3. **E)** Ratio of mitochondrial activity (Resazurin) divided by mitochondrial area (MitoTracker green) to indicate general activity per mitochondria. UT = untreated control cells. Scale bars = 40 µm. All data presented as average bars ± SD and analysed using a one-way Anova test with Dunnett's post-hoc test. *p<0.05, **p<0.01.

To investigate mitochondrial function in a quantitative plate assay, a CellTiter-Glo luminescent viability assay was run on the nanoparticle treated cells to detect ATP. The pattern of ATP quantification was similar to the MitoTracker green area quantification, with CC and ID treatments significantly increased compared to untreated control cells, but no significant difference for LRL treated cells (**Figure 4-13C**). ID treatment caused the greatest increase in ATP quantification with a significant 41% increase, while CC treatment had a similar effect with a significant 35% increase.

A resazurin assay was then used to measure mitochondrial activity to determine if the increased levels of mitochondrial area and ATP in the CC and ID treated cells led to increased metabolic activity or was due to increased levels of dysfunctional mitochondria. None of the nanoparticle treatments showed a significant difference to untreated control cells in metabolic rate after a 4-hour incubation with the resazurin substrate (**Figure 4-13D**) . After 22 hours, both the untreated cells and IONP treated cells, had metabolised all the substrate and the assay had plateaued, showing no lasting defect in metabolic rate.

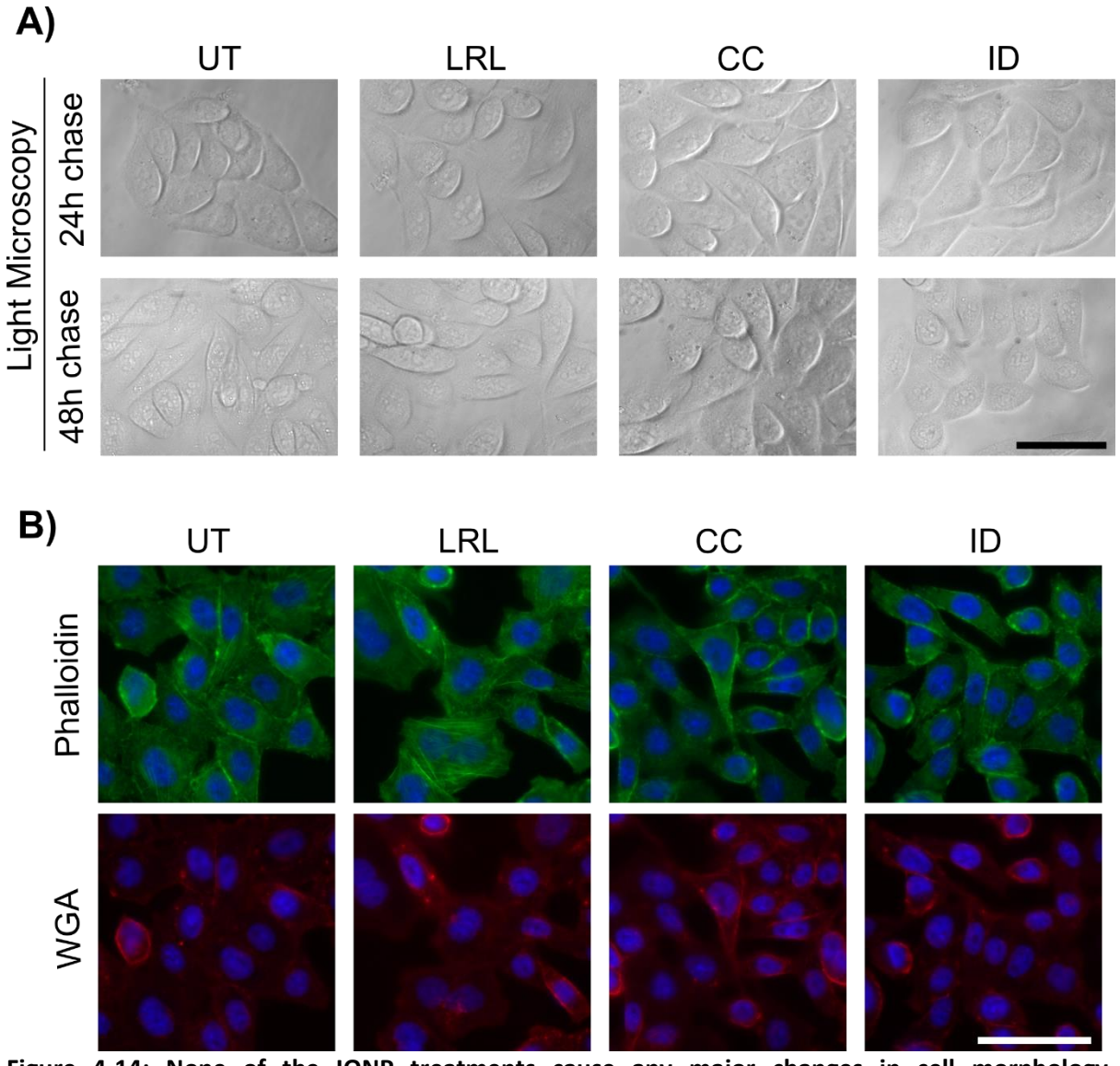

Figure 4-14: None of the IONP treatments cause any major changes in cell morphology. A) Representative images of cell morphology by light microscopy for IONP treated CHO-H1 cells (24hP:24h/48hCH). n=3. **B)** Representative images of IONP treated (24hP:24hCH) CHO-H1 cells, (top row) cytoskeletal stain, phalloidin (green), and (bottom row) cell membrane stain, wheat germ agglutinin (WGA - red), both counterstained with Hoechst nuclear stain (blue). n=3. UT=untreated control cells. Scale bars = 40 µm.

For the IONP treatments where mitochondrial area was raised, a reduced ratio of mitochondrial activity (resazurin data) to mitochondrial area (MitoTracker area data) would indicate an increase in dysfunctional mitochondria, while an increased or equal ratio would indicate in increase in active mitochondria. Determination of the mitochondrial activity/area

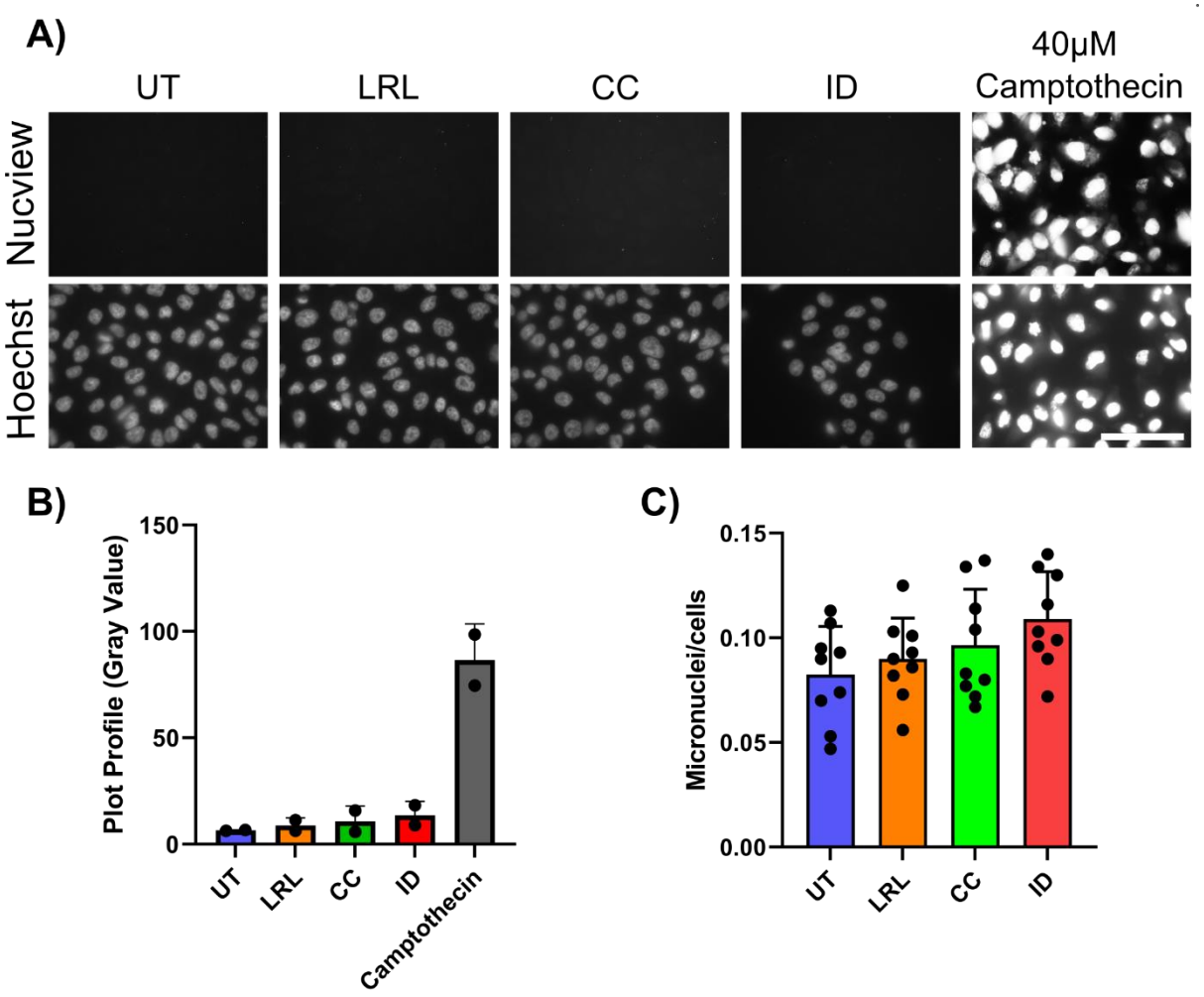

Figure 4-15: No evidence of Caspase3-mediated apoptosis or micronuclei-related genotoxicity was found for any of the IONP treatments. A) Representative images for (top row) Nucview (caspase3-mediated apoptosis) stained CHO H1 cells treated with IONP (24hP:24hCH) and (bottom row) the same cells counterstained with Hoechst nuclear stain. **B)** Nucview stained images fluorescence intensity quantified by plot profile (8 images/treatment/repeat). Camptothecin is a positive control for caspase3-mediated apoptosis. Scale bar = 40 μm. Data presented as average bars ± SD. n=2. **C)** Number of micronuclei/cells counted manually using Hoechst staining (9 images/treatment/repeat) of IONP treated cells (24hP:24hCH). Data represents mean ± SD and analysis by One-way ANOVA with Dunnett's post hoc test; no significance detected. n=9. UT=untreated control cells.

ratio for the IONP treated cell showed both CC and ID treatments led to a ratio reduction (**Figure 4-13E**). CC and ID treated cells showed significant 19% and 15% reductions, respectively, while LRL treatment was not significantly different to the untreated control cells.

4.3.7 Cellular toxicity of IONP treatments

Light microscopy images of dextran coated IONP treated CHO H1 cells showed no visible morphological defects (e.g. no blebbing or reduced adhesion of the cells), in comparison to the untreated cells, after a 24-hour pulse and either a 24-hour or 48-hour chase with nanoparticles (**Figure 4-14A**). This result was supported by cytoskeleton and membrane staining in the CHO H1 cells after IONP treatment (24h pulse :24h chase), images of which showed general cell shape and size was consistent between treated and control cells (**Figure 4-14B**). Cells from all IONP treatment groups were, in a similar manner to the untreated control cells, abundant and mostly well-adhered to the plate surface and not rounding up (a sign of apoptosis).

Staining with the Nucview probe suggested there was no induction of caspase3-mediated apoptosis in IONP-treated cells (24hP:24hCH), but due to only two repeats the data could not be statistically analysed (**Figure 4-15A and B**).

In cells, increased micronuclei production can be an indicator of genotoxicity, with cells trying to eject damaged DNA in extra-nuclear bodies called micronuclei (**Figure 4-15D**). Yet none of the coated IONP treatments (24hP:24hCH) significantly increased micronuclei production (micronuclei count/cell count) compared to in the untreated control cells (**Figure 4-15C**).

4.4 Discussion

4.4.1 Electron microscopy (EM) for IONP characterisation

The IONPs in this chapter were each chosen for being a mix of iron oxide and dextran in different conformations, for comparison of the different compositions. The LRL and CC nanoparticles both have iron oxide cores coated with dextran, but different core iron compositions, with the LRL nanoparticle more magnetite (Fe_3O_4) than maghemite (γ-Fe_2O_3) and the CC nanoparticle an equal balance of magnetite and maghemite. The average CC nanoparticle cores are also larger than the average LRL cores, with a wider range of core sizes and a less circular and more hexagonal crystalline confirmation. For both LRL and CC nanoparticles these core sizes indicated by TEM, conform to the core sizes indicated for these nanoparticles by the company from which they were obtained. The ID nanoparticles majorly differ from the other two in both having a dextran core and iron oxide coating. This inverse conformation compared to the other two nanoparticles makes the iron oxide more bioavailable. Secondly the iron oxide in ID nanoparticles is FeO compared to a magnetite/maghemite mix, so ID nanoparticles are not SPIONs and will not demonstrate superparamagnetic properties. Therefore, although these nanoparticles are all iron oxide, dextran mixes, they differ considerably in conformation, composition, size and magnetism, all of which may impact toxicity.

4.4.2 Degradation of IONP to release free iron.

Phen green quenching suggested increased free iron (most strongly binds Fe^{2+} but also Fe^{3+}) in CC and ID treated cells, indicating these nanoparticles degrade more quickly *in cellulo* than LRL nanoparticles. Despite the broad range of ions that Phen green can detect, it is most strongly quenched by iron and copper ions (Petrat et al. 1999; Shingles et al. 2004). The identified changes are likely to be due to Fe^{2+} and Fe^{3+} as the treated cells are being exposed to a high concentrations of iron oxide in the form of nanoparticles. Yet it is possible that if the free iron is mostly contained in the lysosomes it could impact on the flux of other metal ions into the cytoplasm, which could also impact the Phen green quenching. *In vivo* mouse and rat data suggests iron overload depletes serum and liver copper levels (Wang et al. 2018) and may alter zinc levels (Vayenas et al. 1998). However, the Calcein-AM also supports the Phen green data, with CC and ID showing significant quenching *in cellulo*. Both

these stains are likely showing the presence of free iron in the cytoplasm, with calcein shown to only weakly fluoresce at the low pH of lysosomes (Tenopoulou et al. 2007), while Phen green may fluoresce in endo-lysosomes (Petrat et al. 1999; Nash et al. 2019). For also detecting late-endosomal/lysosomal free iron with Calcein-AM, taking this experiment a step further by bursting the lysosomes to release the free iron and detecting how this affects calcein quenching in IONP treated cells compared to control cells, could independently indicate lysosomal free iron levels.

The ferrozine assays demonstrated that degradation of the nanoparticles to release Fe^{2+} was strongly pH dependent, with a lower pH linked to faster nanoparticle degradation. The stability of the IONP enhanced by the dextran coat did not prevent Fe^{2+} or Fe^{3+} release by 24-hour (37°C) incubation at pH3 compared to pH7, and to a lesser degree at pH5 compared to pH7 with this as the more representative pH for cellular experiments being closer to physiological lysosomal pH. This supports previous data suggesting nanoparticles breakdown more rapidly in low pH environments, such as the lysosome, with much lower degradation in more neutral pH environments, such as the cytosol (Lévy et al. 2010; Briceño et al. 2017). The correlation of iron nanoparticle degradation with pH, seen in this study also closely matches previous *in vitro* experiments detecting iron release by solution colour change, which found that under physiological conditions (pH4.5/37°C) magnetite nanoparticle solutions changed colour from dark orange to yellow within 24 h, indicating major degradation (Gutiérrez et al. 2015). Incubation of the nanoparticles in this chapter at 37°C was to represent human body temperature, to determine if IONP start to undergo breakdown to release Fe^{2+} and Fe^{3+} within 24-hours of reaching an acidic environment in cells (~pH5), such as the lysosome. Previous work in the lab has shown that LRL nanoparticles can be endocytosed and reach late endosomes/lysosomes with an acidic environment within 24 hours (Walker 2015; Walker and Lloyd-Evans 2015). It is known to take around 2-4 hours (cell type dependent) for endocytosed material to move through the endolysosomal system into the lysosome, although this may be longer in cells with trafficking defects, for example in lysosomal storage disease cells, such as NPC1 mutant cells (Lloyd-Evans et al. 2008).

In support of the Phen green data, the ferrozine assays, showed that the LRL nanoparticles degraded to release significant Fe^{2+} increases by 2-hours in pH3 buffer, yet at neither 2-hour

nor 24-hour incubation time points was pH5 significantly different to pH7 degradation. This suggests that at pH5 (near physiological lysosomal pH) LRL does not degrade significantly more than at neutral pH7, but is very strongly affected by very low pH, such as pH3, which is below the physiological lysosomal pH exhibited by cells. The ferrozine assays also suggested there was differences in how quickly the nanoparticles would start to cause increased Fe^{2+} in low pH citrate-phosphate buffer. The CC nanoparticles exhibited very quick Fe^{2+} release in pH3 buffer compared to pH7 buffer, within the plating and incubation times (~30-40 minutes). This release in pH3 buffer was then fairly consistent across all three time points, suggesting CC nanoparticles are strongly sensitive to very low pH buffer. Yet it was not until 24-hours that a change was identified between free iron release in pH5 buffer compared to pH7 buffer, with this being the only nanoparticle to release a significant increase in Fe^{2+} at pH5. ID nanoparticles caused increased free iron concentrations only after 24 hours of incubation, suggesting in a buffer-only environment these nanoparticles breakdown much slower. After 24-hours incubation at physiological lysosomal pH5, ID nanoparticles only released a significant difference in Fe^{3+}, also being the only nanoparticle of the three to release a significant amount of Fe^{3+} at any time point. When observing the changes in pH5 data, this matches the Phen green staining to show no significant release of either Fe^{2+} or Fe^{3+} for LRL nanoparticles, significant Fe^{2+} release at 24-hours for CC nanoparticles and significant Fe^{3+} release at 24-hours for ID nanoparticles. The difference in the major iron species released by CC and ID will likely affect their toxicity to the lysosome and the cell. As Fe^{3+} cannot cross cell membranes unless bound to transferrin or other transport molecules, it may have a greater effect within the lysosome, compared to Fe^{2+}. Several channels can transport Fe^{2+} out of the lysosome, including, DMT1, ZIP14 and TRPML1 (Gunshin et al. 1997; Dong et al. 2008), while Fe^{3+} needs to be converted to Fe^{2+} by ascorbate or an endosomal reductase in the acidic environment of a late endosome or lysosome. Based on the ferrozine assay data it would be of interest to further investigate which iron species are being released but to observe this in the cellular environment to see if the degradative effects are the same *in cellulo*. The use of an Fe^{2+} specific iron probe, such as FeRhoNox, may be a useful next step in this direction (Hirayama et al. 2013).

The ferrozine assay used a citrate-phosphate buffer to mimic the lysosomal environment, along with utilising the buffers wide pH range. Yet use of this buffer does not encompass all

the characteristics of the lysosome. Perhaps importantly the effect of proteins interacting with nanoparticles is ignored. Certain proteins, such as serum albumin, can provide a protective effect against nanoparticle degradation at low pH by attaching to the dextran coat and/or to the uncoated surface of the nanoparticles, known as a protein corona (Sakulkhu et al. 2014). A protein corona has been shown to reduce cytotoxicity of both uncoated and PEG-coated IONP (Escamilla-Rivera et al. 2016). The presence of a protein corona can reduce the uptake of uncoated IONP, while promoting a decrease in ROS and preventing secretion of inflammatory cytokines IL-1β and TNF-α in PEG coated IONP, but not affecting their uptake (Escamilla-Rivera et al. 2016). A protective effect was evidenced with LRL nanoparticles by preincubating them with bovine serum albumin (BSA) prior to the ferrozine assay. Decreased nanoparticle breakdown was shown, in samples of both uncoated magnetite nanoparticles (3 nm) and LRL nanoparticles preincubated with BSA protein, suggesting this protective effect can act on the uncoated core of a nanoparticle and does not require the presence of a dextran coat. In particular, dextran, as a nanoparticle coating, has been shown to breakdown faster under lower (lysosomal range) pH values in the presence citrate or similar metallic chelates that could be found in the lysosome (Arbab et al. 2005). It is unknown how quickly the dextran degrades on the LRL, CC and ID lysosomes used in these experiments, which could be an area for further study.

4.4.3 Impacts of IONPs on lysosomal function and autophagy

The results of the acridine orange lysosomal stability assay support the Phen green staining in that IONP degradation is occurring and that Fe^{2+} and Fe^{3+} are being released in the lysosomes of cells treated with CC nanoparticles, but not with LRL. Release of Fe^{2+} or Fe^{3+} from nanoparticle degradation in acidic organelles, such as the lysosome, can lead to Fenton and Haber-Weiss reactions that produce ROS, namely hydroxyl radicals, which can alter or damage the lysosomal membrane. The presence of punctate dimerised (red) staining in the acridine orange-stained cells at the beginning of the experiment, suggests lysosomal membranes are intact and at least partially acidified, yet the acridine orange membrane stability assay indicates, in the case of CC nanoparticles, that the lysosomal membrane is more susceptible to damage from events like the UV induced destabilisation used in the assay.

While CC treatment caused significantly increased monomer (green) acridine orange fluorescence compared to control cells by 2 minutes, LRL and ID treatments did not affect fluorescence increase to the same extent and were not significantly different to control cells. This may be suggestive that lysosomal membranes have not been destabilised as greatly, if at all, in the LRL and ID treated cells. So, while CC and ID treatments both caused similar Phen green quenching, suggesting a similar iron ion release from these nanoparticles in cells, only CC treatment led to significantly increased lysosomal membrane instability. This may suggest that the concentration of free iron itself is not key to toxicity and that phenotypic toxicity varies according to the specific degradation pathway of the nanoparticle. However, it may also be the case that if the greater free iron release, suggested by Phen green staining in ID treated cells, has already greatly damaged lysosomal membranes prior to the acridine orange experiment, there may be fewer acidic vesicles accumulating dimerised acridine orange to have their membranes destabilised. If this were the case it would ameliorate the ability of the acridine orange experiment to evaluate lysosomal membrane stability comparatively in these cells. This possibility should be further evaluated by imaging acridine orange staining in the cells without UV (365 nm) light to compare and quantify dimerised acridine orange fluorescence (acidic vesicles) between treatment and control cells. Hydrogen peroxide, a type of ROS, has been shown to produce a drop in dimerised acridine orange fluorescence, indicating reduced acidic compartments mainly late endosomes and lysosomes, in acridine orange-stained cells (Boya and Kroemer 2008). Dimerised acridine orange fluorescence has also been shown to be attenuated by 10-50 µg Fe/mL carboxydextran-coated magnetite/maghemite nanoparticles in microglial cells (Wu et al. 2013a).

Despite CC and LRL nanoparticles both having an iron oxide core and dextran coat, both Phen green and acridine orange staining suggest that the LRL nanoparticles have greater stability than CC nanoparticles, with potentially less *in situ* degradation and lysosomal membrane toxicity. This then suggests that a dextran coat may not protect all nanoparticles to the same extent and does not provide a blanket stability against degradation to all nanoparticles equally.

A change in LysoTracker staining after CC and ID treatments, but not LRL, is an important finding as the lysosome is likely to be the cellular organelle first, and possibly most, affected

by iron ion release from nanoparticle degradation. Release of free iron, particularly Fe^{2+} can lead to the production of ROS which can damage the lysosomal membrane and cause lysosomal deacidification, which abolishes LysoTracker green staining if the pH rises above pH 5.4. Previous studies have shown that IONP can localise to lysosomes by LysoTracker staining in microglial cells (Wu et al. 2013a) and MCF-7 cells (Zhang et al. 2016a), electron microscopy in THP-1 macrophages (Escamilla-Rivera et al. 2016), light microscopy and electron microscopy in RAW macrophages (Park et al. 2014a) and LAMP-1 staining in adipose tissue-derived stem cells (Kasten et al. 2014). Uptake of the LRL nanoparticles in CHO H1 cells and strong co-localisation with the lysosomes after a 24-hour pulse and 24-hour chase has also been demonstrated (Walker 2015). The ability of certain IONP to reduce LysoTracker staining also corroborates findings of a previous study which found that exposure to iron oxide nanocubes and nanoclusters (100 µg/mL) significantly reduced LysoTracker fluorescence detected in Alexander, HepG2 and Huh7 cells (Levada et al. 2020). Although this is a quick and reliable cell stain that many studies have used to assess lysosomal localisation, fairly few studies have gone on to quantify the LysoTracker fluorescence and compare nanoparticle treated cells to control cells. The significant reduction in LysoTracker staining found in this study, suggests it should be a staple initial phenotype for investigation of cellular nanoparticle toxicity.

An acidic environment is necessary for LysoTracker fluorescence and deacidification of the lysosome above pH 5.4 abolishes LysoTracker fluorescence. This is the mechanism of action for the negative control Bafilomycin A1, where deacidification of the entire endocytic system causes a major increase in pH. Reduced LysoTracker area after IONP treatments may suggest a reduced number of lysosomes through reduced production or increased depletion, or may suggest deacidification of lysosomes due to membrane damage. Deacidification of lysosomes after nanoparticle degradation in cells, has previously been suggested to be due to the production of ROS from the free iron causing lysosomal membrane permeabilisation (Levada et al. 2020) as a result of lipid peroxidation (Johansson et al. 2010). Chronic iron overload (100 µM $FeSO_4$) has been shown to reduce lysosomal pH, while increasing LysoTracker staining in human macrophage cells (Kao et al. 2016). A carboxydextran-coated magnetite/maghemite nanoparticle treatment in murine microglial cells attenuated acridine orange red fluorescence, suggesting increased membrane

permeability while also demonstrating a markedly reduced fluorescence of Lysosensor staining indicating an increase in lysosomal pH (Wu et al. 2013a). Yet, at least in CC cells, the acridine orange lysosomal membrane stability assay indicates the lysosomal membrane is likely intact and not permeabilised.

A mild increase in autophagic vesicles was seen in CC treated cells, while no defect was seen in ID treated cells suggesting iron ion release between these two IONPs affects the cell differently. Previous studies have also found IONP treatments can induce autophagy (Khan et al. 2012; Park et al. 2014a; Wu et al. 2017b). Accumulation of autophagosomes, the primary macro-autophagy vesicle, can result from promotion of autophagy induction or blockage of autophagosome turnover by lysosomes (Mizushima et al. 2010). The Cyto-ID increase seen in CC treated cells could be due to both; lysosomal-autophagosome fusion could be blocked by damage to the lysosomes from ROS and lipid peroxidation. It is equally possible that autophagy is induced by nanoparticle treatment and indeed previous work on dextran coated IONPs has shown that the autophagosome accumulation is induced by induction of autophagy rather than a blockade of autophagy flux (Wu et al. 2017b). Silver nanoparticles have been shown to cause nuclear translocation of TFEB, which acts as the master regulator of autophagy and lysosomal biogenesis, in an mTORC1 independent pathway (Lin et al. 2018). While a study with carboxymethyldextran coated magnetite nanoparticle from Chemicell (same company as CC nanoparticles in this study) showed evidence that lysosomal dysfunction caused by the nanoparticle treatment led to changes in subcellular localisation of phosphorylated mTOR and p53, with subsequent initiation of autophagic flux (Uzhytchak et al. 2020). In a murine alveolar macrophage cell line, magnetite treated cells showed an increase in the number of autophagosome vacuoles while maghemite treated cells formed large vacuoles in the cytosol (Park et al. 2014b). However, a different study using uncoated magnetite nanoparticles found they induced autophagosome accumulation (increased autophagy) through multiple mechanisms, namely lysosome impairment, mitochondrial damage, and ER stress (Zhang et al. 2016a). It is not clear across the field that there is any one key mechanism for autophagy induction, except that is seems highly variable, probably inducible by several mechanisms simultaneously. It is likely that nanoparticle composition and coating have a strong impact on probability and mechanism of autophagy induction as well as being affected by cell type.

ID treatment, which affected lysotracker staining, did not alter autophagy, unlike CC treatment. This then suggests it is not just the lysosomal dysfunction that is leading to autophagy induction but may be more about the mechanism of free iron release or which organelles are most affected, with damage to lysosomes, mitochondria or the ER able to trigger induction of autophagy (Stern et al. 2012). Some studies suggest a pro-survival effect of autophagy induced by nanoparticle treatment, with autophagy acting to reduce oxidative stress by aiming to sequester nanoparticles in autophagosomes and lysosomes and remove organelles and cellular components which have been damaged by nanoparticle-related activities (Duan et al. 2019; Jin et al. 2019). To indicate if this is the case and to what degree autophagic flux is affected by CC treatment, further investigation of this phenotype would be a useful next step for this project.

4.4.4 Lysosomal-related IONP phenotypes

Increased cellular autofluorescence can be a sign of lysosomal enzyme dysfunction leading to increased production and accumulation of autofluorescent substrates, such as lipofuscin (Kennedy et al. 1995; Guha et al. 2014). This process is often seen in aging of non-proliferative cells and in some lysosomal storage disorders where certain lysosomal enzyme function is altered due to genetic mutation (Moreno-García et al. 2018). No increase in autofluorescence was seen with any of the coated IONP treatments, suggesting that during the treatment period, the IONP-related lysosomal dysfunction was not to a level of severity that led to the accumulation autofluorescent material. In this study, a fairly short incubation time was used to identify early toxicity after a relatively high dose of IONP, but if a longer incubation period is investigated in the future, then autofluorescence may be worth reinvestigating.

The significantly increased lipid peroxidation seen in CC and ID treated cells suggests that there is increased ROS production in these cells which is causing damage to the lipids. Lipid peroxidation is a very common cytotoxic effect of heavy metal nanoparticle treatments, particularly strongly associated to free iron (Minotti 1993). There is evidence for increased lipid peroxidation in cells/tissues after iron oxides treatments with both magnetite nanoparticles (Wang et al. 2014; Gao et al. 2021) or maghemite nanoparticles (Alarifi et al. 2014; Gaharwar et al. 2020). Therefore, the identification of lipid peroxidation after IONP

treatments in this study supports similar findings in the field. The increased lipid peroxidation in the CC and ID but not the LRL treated cells, fits with the pattern of increased free iron and lysosomal dysfunction seen with CC and ID treatments. One study has shown that increased lipid peroxidation after IONP treatment is dependent on acidic (lysosomal) pH, with no changes seen at cytosolic pH (Wang et al. 2014). Therefore, the increased lipid peroxidation of CC and ID may also act as further evidence of free iron release in the acidic lysosomal (or late endosomal) compartments. This data also demonstrates that the attributes of the LRL nanoparticles that reduce/slow its degradation and lysosomal toxicity are also having a protective effect against lipid peroxidation. In use of this nanoparticle toxicity model, a Malondialdehyde (MDA) assay (Gao et al. 2021) could also be run on the nanoparticle treated cells, to confirm the lipid peroxidation phenotype when detected by DPPP staining. This assay works by measuring MDA levels in the cells, as MDA is a by-product of lipid peroxidation during oxidative stress.

To investigate further what type of reactive oxygen species may be causing the lipid peroxidation identified, super oxide-ID (SO-ID) staining was performed on the cells. SO-ID does not detect hydroxyl radicals, which are the dominant form of reactive oxygen species induced by Fenton reactions (Neyens and Baeyens 2003). Hydroxyl radicals have specifically been shown to be produced by Fenton reactions on the surface of iron oxide nanoparticles (Voinov et al. 2011). The hydroxyl radical has a very short half-life as it is highly reactive and so can be more difficult to detect than other reactive oxygen species, such as super oxide (Goldstein et al. 1993). Therefore, the lack of superoxide staining in any of the nanoparticle treated cells may be suggestive that if the lipid peroxidation and reduced lysosomal staining are triggered by ROS, that it is likely to be primarily hydroxyl radicals rather than superoxide, which is often produced by faults in the electron transport chain of mitochondria. A future aim of the project should be to confirm whether increased reactive oxygen species other than superoxide are present using a detection method that has the capability to detect hydroxyl radicals, such as the total ROS detection assay kit (ENZO). Even if their short life makes the hydroxyl radicals undetectable by alternative assays, by ruling out the longer-lived ROS, this may be a further indication of the role of hydroxyl radicals in the identified lipid peroxidation.

4.4.5 Fura-2,AM as a Ca2+ probe and free iron indicator

The lysosome is an important hub for regulating intracellular Ca^{2+} signalling as well as acting as a Ca^{2+} store (Lloyd-Evans and Platt 2011). Therefore, when investigating defects in the lysosome, Ca^{2+} signalling should also be investigated, as this is a major way that lysosomal defects can affect cellular signalling and other cellular organelles. An increase in lysosomal Ca^{2+} content was only seen in CC treated cells, not in LRL or ID treated cells. Oxidative stress, as often seen in nanoparticle treatments, has been shown to alter intracellular Ca^{2+} (Ermak and Davies 2002). Yet, in this project, as none of the IONP treatments showed reduced lysosomal Ca^{2+} content, this suggests the lysosomal membranes remained intact. Although the acridine orange lysosomal membrane stability assay suggests the lysosomes of CC treated cells may have reduced membrane stability, the raised lysosomal Ca^{2+} content indicates they are stressed and not completely destabilised. Yet decreased lysosomal pH and lysosomal defects, as often seen in lysosomal storage disorders, normally reduce lysosomal Ca^{2+} (Alshehri 2019; Lloyd-Evans and Waller-Evans 2020).

The CC nanoparticle treatment was the only one to have caused significantly increased autophagy, and to have significantly dysregulated lysosomal Ca^{2+} release. It has been shown that increased TFEB expression can increase lysosomal Ca^{2+} (Sbano et al. 2017) and that induction of autophagy induced TFEB expression can upregulate TFEB expression in a positive feedback loop (Zhang et al. 2020b). In this way, induction of autophagy in CC treated cells by ROS or lipid peroxidation caused by nanoparticle degradation and free iron, could in turn upregulate TFEB and then increase lysosomal Ca^{2+} levels. Therefore, determination of TFEB localisations in the IONP treated cells would be an important next step for the project.

As early as the 1980s, quenching of Ca^{2+} sensitive probes by heavy metals, including Fe^{2+} was identified, first in quin-2 (Arslan et al. 1985) then in Fura-2 (Snitsarev et al. 1996). A subsequent study by Kress et al. (2002) found that in primary cultured cells, Fura-2 can be used as an indicator of free ferrous iron (Fe^{2+}) levels by measuring quenching of the probe. The results of this study similarly suggest Fe^{2+} can quench Fura-2 staining both in cellular and non-cellular environments, but also found Fe^{3+} could quench Fura-2 to an equal degree, although repeats are needed so this data can be statistically analysed. LRL was shown as the only nanoparticle in this study to significantly affect Fura-2,AM staining, differing compared

to the Phen green and calcien data which suggested highest levels of free iron after CC and ID treatments. Iron quenching of the Fura-2,AM probe does not appear to be ratiometric between 340/365nm and 380nm excitation, as it is for detecting Ca^{2+}, so it is difficult to tell if this change in fluorescence is due to a difference in loading of the probe, or due to free iron-related quenching. It is also possible that the probe is affected by differences in intracellular Ca^{2+} levels between the different treatments. For use as a quantifiable measure of free iron, a further experiment to check equal loading of the probe and to check the quenching is truly due to free iron would be needed. This could be best achieved through demonstrating unquenching of Fura-2,AM upon treatment with either a membrane permeant iron chelator or ionophore.

4.4.6 Mitochondrial-related phenotypes

MitoTracker green staining suggested an increased number of mitochondria or larger mitochondria in the CC and ID treated cells. This was supported by quantification of ATP levels, which were also elevated for CC and ID. Neither mitochondrial marker was significantly raised after LRL treatment, similar to the previous phenotypes, suggesting LRL has little effect on mitochondrial function compared to CC and ID treatments. Mitochondrial activity, measured by a resazurin assay showed that the overall metabolism in the treated cells was not changing. The ratio of mitochondrial activity to mitochondrial area is the key finding, demonstrating that in CC and ID treated cells, while there is an increase in mitochondria, the activity per mitochondria is significantly reduced. This finding suggests the cells are increasing mitochondrial biogenesis, reducing mitochondrial degradation or that there is an increased level of mitochondrial autophagy, to maintain a normal level of cellular metabolism despite falling mitochondrial activity. In CC treated cells, autophagy is increased, which likely accounts for these changes, however in ID an increase in autophagy is not detected and so in these cells the changes seen in mitochondria may have been driven by a different process.

In support of this finding, Zhang et al. (2020a) have recently shown that dendritic cells treated with PEG-COOH-coated Fe_3O_4 nanoparticles also exhibited increased mitochondrial biogenesis. Their nanoparticle treatment led to mitochondrial fragmentation and ultrastructural changes inducing mitochondrial dysfunction that would affect metabolism, a

change also found in this study. However, Zhang et al. (2020a) also found that the PEG-COOH-coated Fe_3O_4 nanoparticles reduced autophagy in opposition to the findings in this study. This difference could be due to the differences between PEG-COOH and dextran coating of the nanoparticles. Several studies have suggested that the induction of autophagy in IONP treated cells can be triggered by mitochondrial damage caused by the nanoparticles (Park et al. 2014a; Zhang et al. 2016a). When mitochondria become damaged by ROS, autophagy can be induced to mitigate the damage by degrading damaged mitochondria. MCF-7 cells treated with Fe_3O_4 nanoparticles for 24 hours exhibited a decrease in mitochondrial membrane potential and an increase in ROS production alongside autophagy induction (Zhang et al. 2016a). Mitochondrial damage can lead to a decrease in ATP which is detected by AMPK in the cytoplasm triggering its phosphorylation so it can inhibit mTOR to induce autophagy (Kim et al. 2011). The increased ATP seen in this study is likely a secondary effect from the increased mitochondrial biosynthesis, also triggered by mitochondrial damage. Yet whereas mitochondrial damage could be an inducer of autophagy in the CC treated cells, no increase of autophagy was seen in the ID treated cells. This suggests that either the mitochondrial damage in ID treated cells is different to that in the CC, one inducing autophagy and the other not, or that the induction of autophagy in the CC treated cells is not primarily driven by the mitochondrial damage. As previously discussed, (Section 4.4.3) there are also several mechanisms by which lysosomal dysfunction can induce autophagy. For a large or quick induction of autophagy both lysosomal and mitochondrial defects may be necessary, while this process and the specifications are likely cell type dependent.

It has been shown that coating magnetite nanoparticles with a polymer, poly(lactic-co-glycolic acid), can reduce their toxicity abolishing the mitochondrial membrane potential defect and ROS accumulation seen with the same nanoparticles uncoated (Zhang et al. 2016a). In this thesis chapter the LRL nanoparticles' dextran coating appears to be highly protective, as no mitochondrial defects or lipid peroxidation was induced in the cells. However, the CC nanoparticle is also dextran coated, but in this case the dextran coat does not appear to provide equally protective effects.

In one study using isolated mitochondria (*in vitro*) extracted from several different mouse organs and incubated with Fe_3O_4 nanoparticles across a large concentration range (100 -500

µg/mL), no mitochondrial impairment in mitochondrial respiratory chain complexes activities or coupling occurred (Baratli et al. 2013). The lack of mitochondrial defects despite the high concentrations is presumably because of the neutral pH the nanoparticles were exposed to in the isolated mitochondria. This is most likely suggestive of the initial need for exposure of the nanoparticles to an acidic compartment, such as the lysosome, which can promote degradation, releasing iron ions, which through Fenton reactions can produce ROS that in turn can damage mitochondria. Without the degradation step, which is only likely to occur at the necessary speed for toxicity in acidified lysosomes, IONP may be significantly less toxic.

4.4.7 Cellular toxicity of IONP treatments

Despite a fairly high concentration of iron (1 mg/mL) being added to the cells, no changes in cell morphology were seen after a 24-hour pulse and 24- or 48-hour chase with any of the dextran-coated IONPs. Neither were changes seen in the cell cytoskeleton or membrane morphology after a 24-hour pulse and 24-hour chase with the IONPs. Caspase3-mediated apoptosis has previously been identified as a potential cell death pathway for nanoparticle induced toxicity in silver nanoparticles (Siddiqi et al. 2012), so was also briefly investigated in this study. A concentration-dependent increase in micronuclei production has also been identified in HEP-G2 cells treated with a dextran coated SPION (Seo et al. 2017). Yet no increase in Caspase3-mediated apoptosis or micronuclei-related genotoxicity was seen in this study for CHO H1 cells treated with the dextran coated IONP for a 24-hour pulse: 24-hour chase, supporting the morphology findings that cytotoxicity for all three IONPs appears low.

Together, these results suggest none of the dextran: IONP treatments in this study strongly impact cell survival after 2-3 day (pulse: chase) incubations, despite high nanoparticle uptake by the cells (unpublished data from lab). This corroborates the findings of many previous studies for the protective effect of dextran on IONP toxicity in a range of cell types (Kunzmann et al. 2011; Saraswathy et al. 2014; Remya et al. 2016; Shaterabadi et al. 2017; Unterweger et al. 2018).

Table 4-1: Comparison of phenotypes between LRL, CC and ID nanoparticles. In the table (-) stands for no significant change from control cells, (L) signifies the phenotype was significantly reduced (low) and (H) signifies the phenotype was significantly increased (high) compared to control cells. Colours signify the groupings of phenotypes: free iron release (blue), lysosomal-related (orange), mitochondria-related (green), cell morphology (purple) and cell death/toxicity (red).

Stain or Assay	LRL	CC	ID
Phen Green (free iron quenching)	-	L	L
Calcein (free iron quenching)	-	L	L
Acridine Orange (lysosomal membrane stability)	-	L	-
LysoTracker (lysosomal area)	-	L	L
Cyto-ID (autophagy)	-	H	-
Autofluorescence (lipofuscin production)	-	-	-
DPPP (lipid peroxidation)	-	H	H
SO-ID (super oxide)	-	-	-
Fura-2,AM + Ionomycin/GPN (Lysosomal Ca^{2+})	-	H	-
MitoTracker (mitochondrial area)	-	H	H
CellTiter-Glo (ATP quantification)	-	H	H
Resazurin (cell metabolism)	-	-	-
Light microscopy (cell morphology)	-	-	-
Phalloidin/WGA (cell cytoskeleton)	-	-	-
Nucview (caspase-3 mediated apoptosis)	-	-	-
Micronuclei (genotoxicity)	-	-	-
Ferrozine (main iron species released)	-	Fe^{2+}	Fe^{3+}

4.4.8 Overall Conclusions

The data in this chapter provides compelling evidence for the differential effects on cellular toxicity between similar nanoparticles with minor differences in iron composition and coating. The CC and ID nanoparticles caused a range of toxicity phenotypes, but each with independent profiles. Experiments suggested that CC and ID nanoparticle treatments released the greatest levels of free iron in the cells, both causing reduction in acidified (pH<5.4) lysosomal area, increased lipid peroxidation and inducing mitochondrial defects (**Table 4-1**). Yet *in vitro* these two nanoparticle treatments differed in the iron species being

produced, with CC mainly producing Fe^{2+} and ID mainly producing Fe^{3+} after a 24-hour incubation at the lysosomal relevant pH5. Only the CC treatment also led to additional defects, including decreased lysosomal membrane stability, increased autophagy and increased lysosomal Ca^{2+}. It is likely these phenotypes could be related, as changes in lysosomal Ca^{2+} as well as increased production of ROS (which can damage or partially destabilise the lysosomal membrane) can lead to increased cellular autophagy.

LRL nanoparticles proved to have very low toxicity across all the experiments, demonstrating low release of Fe^{2+} and Fe^{3+} at lysosomal pH (~5) both in *in vitro* and *in cellulo* experiments. The LRL nanoparticles did not affect lysosomal area, lysosomal membrane stability, autophagy, lipid peroxidation, lysosomal Ca^{2+} or mitochondrial phenotypes (**Table 4-1**). The small size of the LRL nanoparticles, leading to a higher dextran to iron ratio, may be a factor in their lower cytotoxicity, while the dextran coating also likely contributes to the nanoparticle's high stability. The consistency of the LRL nanoparticles in both size and shape, as shown by TEM, suggests an effective and reproducible manufacturing process, which may also indicate a strongly bonded dextran coating process, in comparison to CC nanoparticles. The ratio of LRL being more prominently magnetite, rather than CC with a more equal mix, may also improve the general stability of this nanoparticle.

For use in lysosomal extraction, the chosen nanoparticle needs to have low toxicity to lysosomes and low general cytotoxicity to ensure high lysosomal yields and ensure that lysosomal phenotypes are unaffected by the nanoparticles. As these experiments were using a nanoparticle concentration and pulse:chase timeframe that would be necessary for lysosomal extraction, this data indicates that LRL nanoparticles have low toxicity on the cell, validating its ongoing use for magnetic lysosomal extraction.

5 Chapter Five: Investigating toxicity of LRL and ID nanoparticles in an *in vivo* developmental zebrafish model

5.1 Introduction

5.1.1 Introduction to zebrafish

The Zebrafish (*Danio rerio*) is a tropical freshwater fish from the minnow family, with populations in India, Nepal, and Bangladesh (Parichy 2015). Zebrafish are aptly named for the distinctive horizontal stripes along the sides of their body. Typically, zebrafish have four to five horizontal blue/black stripes on each side formed by pigment cells called melanophores (Kossack and Draper 2019). While this is the classic form, there are many diverse zebrafish strains which differ morphologically, genetically, physiologically and to some degree behaviourally (Seguret et al. 2016; van den Bos et al. 2017).

In captivity, the zebrafish can live for over 5 years, however, normally they live for only 2-3 years, but reach sexual maturity at ~3 months when grown optimally at 37° (Kishi et al. 2009; Parichy et al. 2009). Their typical habitat in the wild consists of shallow, slow-moving streams and still pools, with wild zebrafish as omnivores feeding on small organisms (insects, crustaceans, and zooplankton) or plant material and detritus that lives in or enters their stream environment (Parichy 2015).

5.1.2 Zebrafish breeding

An advantage of zebrafish is that the lab strains can breed all year round with a female able to produce enough eggs to breed every 5 days, although for optimum clutch numbers and greater embryonic survival 10 days between breeding is best (Hisaoka and Firlit 1962; Niimi and LaHam 1974). Zebrafish have a range of courtship and mating behaviours, and while the females can lay clutches of several hundred eggs at once, they may also lay fewer dependent on the male involved (Spence and Smith 2006). Single pair-mating of one female with one male should be set up in the afternoon prior to the day of breeding to give the zebrafish time to get acquainted with the space and each other, as breeding nearly always occurs just after daybreak (Hisaoka and Firlit 1962). In a laboratory environment 'daybreak'

can be controlled by altering the light-dark cycle in the room where the zebrafish are kept, making embryo collection at an early developmental stage soon after fertilisation easier as breeding times are predictable.

5.1.3 Embryonic development in zebrafish

Zebrafish embryos develop into larvae very quickly, with a newly fertilised egg in the zygote period for around 40 minutes after fertilisation until the first cleavage occurs, splitting the single cell into two, able to develop from an embryo into a larvae that hatches from its chorion (an acellular envelope surrounding mature eggs) by 48-72 hours after fertilisation (Kimmel et al. 1995). A full description of the zebrafish developmental stages (with pictorial representations of each stage included) can be found in the review article by Kimmel et al. (1995).

At ~10-24 hours post fertilisation (hpf), the embryo enters the segmentation stage, where the brain regions start to form and first co-ordinated movements occur (Kimmel et al. 1995). At ~17 hours post fertilisation the embryo starts to exhibit spontaneous coiling (visible tail coiling movements), which are the result of a primitive spinal circuit rather than direct brain input and can be an easy to detect indicator of the embryos developmental progress (Saint-Amant and Drapeau 1998). Spontaneous coiling appears to peak at ~19 hours post fertilisation and then slowly declines until hatching from the chorion, a process probably aided by the coiling movements (Saint-Amant and Drapeau 1998). When development is delayed, for example by incubating embryos at a lower temperature, the peak and decline in coiling can be delayed (Saint-Amant and Drapeau 1998).

The pharyngula stage (24-48 hpf) sees rapid lengthening of the embryo and the beginning of pigmentation, with the heart becoming visible and starting to beat, pumping blood (Kimmel et al. 1995). Finally, the hatching period (48-72 hpf) occurs, when the embryo will typically break out of its protective chorion (Kimmel et al. 1995). In this stage, there is rapid development of the jaw, gills and pigmentation (Kimmel et al. 1995). After the end of the third day, the zebrafish stop being referred to as embryos and start being referred to as larvae, having mostly completed morphogenesis (Kimmel et al. 1995). Once hatched, larvae start to actively swim around, active respiration occurs and the gut becomes complete enabling larvae to eat, although they are still mostly reliant on nutrients from the yolk sac,

not showing 'independent feeding' until ~5 days post fertilisation (dpf) (Kimmel et al. 1995; Strähle et al. 2012). At this stage, the escape response (also known as startle response) develops, where larvae will rapidly move away when exposed to abrupt stimuli, such as touch, sound, or light (Burgess and Granato 2007; Emran et al. 2008). This has evolved in the larvae as an early survival response to swim away from threatening stimuli (Budick and O'Malley 2000), but can be a useful tool in the lab to check development of neuromuscular circuits. In comparison to spontaneous coiling, which is linked to a spinal circuit, the later development of this response means it can be linked to a neuronal circuit activating selective command neurones in the hindbrain (Kohashi and Oda 2008).

5.1.4 The zebrafish chorion

As mentioned above, the chorion is a protective acellular envelope composed mainly of proteins and glycoproteins, with low levels of lipids, surrounding the zebrafish embryo until hatching occurs around 3 dpf (Bonsignorio et al. 1996; Hachicho et al. 2015). The chorion can pose as an obstacle in some embryonic experiments as it acts as a barrier to certain molecules, dependent on size and charge, can obstruct vision of the embryo, and block physical manipulation. The chorion can be removed either manually with forceps or by treatment with digestive enzyme solutions, such as pronase (Henn and Braunbeck 2011). However, premature removal of the chorion can both reduce embryo survival rates and effect behavioural responses (Henn and Braunbeck 2011). The chorion membrane complex consists of three separate layers together building a barrier around 1.5-2.5 µm in thickness; shown by electron microscopy to have electron-dense outer and inner-most layers separated by an electron-lucent middle layer (Rawson 2000). The middle and inner layers are pierced by cone shaped pore canals with an outer opening 0.5-0.7 µm distanced around 1.5-2 µm apart to allow selective molecules through the chorion (Rawson 2000).

5.1.5 Zebrafish as model organisms

The Zebrafish is swiftly growing in popularity as a model organism across many fields including genetic manipulation, disease models, drug testing, toxicology, and environmental change. There are many advantages to using zebrafish over traditional models, such as rats and mice, the primary of these being the far cheaper housing and maintenance costs alongside easy and quick breeding practises and accelerated development (embryonic

stages complete in 3 days) (Lieschke and Currie 2007). Furthermore, *ex vivo* fertilisation and embryogenesis in zebrafish, combined with the optical transparency of the embryos and larvae are useful attributes in developmental studies and for embryonic genetic manipulation (Lieschke and Currie 2007). Zebrafish are also particularly amenable to genetic manipulation, e.g. by morpholino, CRISPR-Cas9 and TALENs (Adamson et al. 2018). For these reasons they are often being used for genetic studies by gene knockdown or overexpression to investigate vertebrate gene function as well as the study of human disease (Lieschke and Currie 2007; Cook et al. 2020b). This has led to a push forward in mapping out the zebrafish genome, which has been completed for several of the main *Danio rerio* strains (Bradford et al. 2011).

One reason many scientists choose to work with mice and rats is the importance of genetic similarity in a model system and, not being mammals, fish are further from humans in terms of evolutionary distance (Howe et al. 2013). However, zebrafish share a high degree of genetic similarity to humans, with zebrafish homologues for 71% of human genes (Howe et al. 2013). This is especially evident regarding disease modelling, as 82% of human disease-associated genes have zebrafish homologues (Howe et al. 2013).

A further growing advantage of zebrafish is their utility in high-throughput drug screening and toxicology assays, allowing the significant acceleration of, and reduced costs for, drug discovery (Wiley et al. 2017). The high reproductive capacity of zebrafish, their small size and amenability of embryos/larvae to plate assay style analysis are key to their utility in these kinds of experiments (Quevedo et al. 2019). Importantly, the results of zebrafish screening seem to show a good correlation to commonly used mammalian models of toxicology (Horzmann and Freeman 2018). The development of new technologies is key to reaching the full potential for using zebrafish in high-throughput testing. One such new technology, the DanioVision, provides an environmentally controlled, plate-based imaging chamber with high sensitivity detection software that can automatically monitor and track movement of individual larvae simultaneously (Capriello et al. 2019).

Zebrafish are commonly used in heart research, as alongside their other advantages they have a rare ability to be able to repair heart muscle as well as having regenerative capabilities for their fins, spinal cord, retina, and kidney (Beffagna 2019). They are also increasingly used in neuroscience research, with the CLN3 fish model able to faithfully

recapitulate the pathological signs of CLN3 disease to a greater degree than most mouse models and having provided a model for high-throughput screening to progress the search for new small molecule therapies in this rare lysosomal storage disease (Wager et al. 2016).

A further point to address, is the ethical consideration of using zebrafish. While ethically animal use should be kept as low as possible, in cases where it is compulsory, such as in drug testing and *in vivo* system studies, zebrafish are considered as a fairly ethical alternative to mammalian studies (Simonetti 2016). The three "Rs" (refinement, replacement and reduction) is now a central doctrine in ethical research, and in accordance with this, use of zebrafish can be minimise animal pain, suffering and distress, particularly when choosing embryos and young larvae (up to 5 dpf) where their nervous system is yet to be fully developed and they are not yet independently feeding (Strähle et al. 2012). Use of zebrafish models at earlier stages of research may reduce the need for as many mammalian animals to be used in later stage testing and be a method to rule out unnecessary, ineffective, or less ethical treatments from further animal testing (Bailone et al. 2020).

5.1.6 Heavy metal water pollution

Pollution is a growing concern world-wide as the human lifestyle becomes increasingly unsustainable. There is a large range of polluting chemicals in aquatic environments including heavy metals, detergents, microfibers (both plastic and non-plastic), agrochemicals (fertilizers and pesticides), antibiotics, and transport-related pollutants (Bashir et al. 2020). For many of these pollutants, aquatic environments can be a major route for distribution and can act as the ultimate sink (Bashir et al. 2020).

Iron is a more complicated metal to consider as a pollutant, because it is naturally highly abundant in the Earth's crust, is naturally found in all freshwater ecosystems (Vuori 1995), and is essential to life - as discussed in Section 1.2.1. Excess iron is commonly introduced into freshwater ecosystems by iron and coal ore mining, industrial and urban run-off and from precipitated iron in transport-related air pollution (Vuori 1995). Yet the additional impact of iron release from nanoparticle sources, such as magnetite and maghemite nanoparticles, is not well understood. A 2014 report for freshwater guidelines in England and Wales suggests freshwater iron levels should be kept below 1 µg/L (WFD 2014). The US has a criterion of 1 mg/L water iron levels for protection of aquatic life, based on limited

data collected in the 1970s, but a recent study suggests this should be re-evaluated to under 0.5 mg/L and that sensitive species may need it even lower (Cadmus et al. 2018). In many other countries freshwater iron levels are not well regulated and, in some areas, can get as high as 80-100 mg/L (Ruas et al. 2008; Su et al. 2017).

IONPs in aquatic environments may affect aquatic life in their nanoparticle form or may be degraded in the water to release free iron species. In an aqueous environment the molecular species of the iron can vary based on environmental conditions. In highly oxygenated water at a near neutral pH, Fe^{2+} is readily oxidised to form Fe^{3+} based hydrous iron oxides, minerals with a mixture of iron, hydroxide and weakly bound water (Lienemann et al. 1999), that often complex with organic matter (Tipping 1981). In this way environmental conditions can have a strong impact on the iron states present in an aquatic system, such as the conditions shown in **Figure 5-1**.

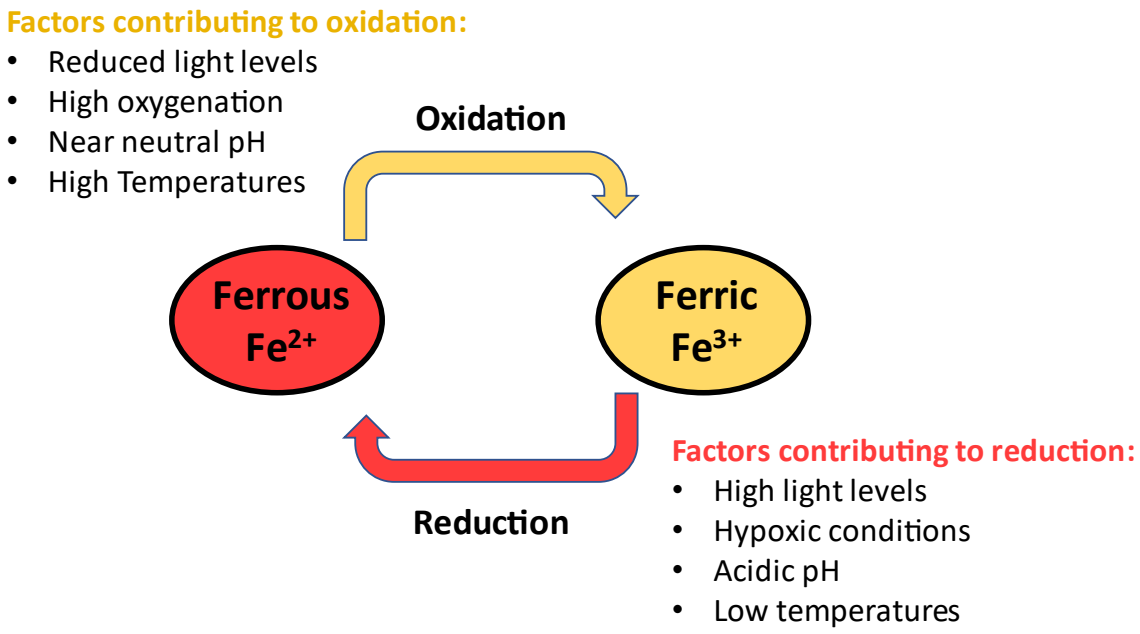

Figure 5-1: Environmental conditions can affect the balance of iron between the more toxic ferrous (Fe^{2+}) and less toxic ferric (Fe^{3+}) states. High light levels can cause photoreduction of complexed ferric iron. As oxygen is needed for oxidation, high oxygen levels can increase oxidation of ferrous iron. Ferrous iron is more stable and has higher solubility at low pH, reducing oxidation to the ferric state. High temperatures increase oxidation of ferrous iron to its ferric state.

There have been few studies on the impact on iron oxide nanoparticles (IONPs) as a water pollutant, despite their ability to release high levels of free iron, with more emphasis on their use as a potential water remediation agent, despite acknowledgement of the necessity of their subsequent removal from water supplies for environmental and public health (Aragaw et al. 2021). There is evidence of negative effects of uncoated maghemite (γ-Fe_2O_3) nanoparticles on survival and growth of green algae (Zhang et al. 2016b) and effects of haematite (α-Fe_2O_3) nanoparticles on the development of zebrafish larvae causing mortality, hatching delay, and malformation. In one review, magnetite nanoparticles (100-1000 nm) were found in water samples from several low-polluted aquatic environments, whether of natural or human-linked production being unknown (von der Heyden et al. 2019). Yet further investigation of the prevalence of engineered or human activity-derived iron oxide nanoparticles is necessary to indicate the extent of their influence on water pollution.

Accumulation of iron, particularly in the liver and gills of fish exposed to high water iron concentrations has been shown (Avenant-Oldewage and Marx 2000; Abalaka 2015). Along with liver histopathology, other changes linked to iron overexposure in fish include, skeletal malformations, embryonic defects, and macrophage aggregates, as well as destabilised lysosomal membrane integrity, and lipopigment accumulation (Au 2004). When iron levels cross a set threshold and the iron cannot be quickly chelated, then it can lead to the production of damaging oxygen radicals (Singh et al. 2019). Sublethal iron overload in the fish species *Labeo rohita* caused significant lipid peroxidation and significant reduction in free radical scavenger's (super oxide dismutase and catalase) (Singh et al. 2019). Yet the effects of different compositions of IONPs on aquatic life is an area that requires further study.

5.1.7 Zebrafish as a toxicity and pollution model

The ZET (zebrafish embryotoxicity test) is a commonly established set of testing criteria that has been used to study nanomaterial toxicity (Pereira et al. 2019). Under the ZET four specific groups of morphological alteration induced by nanomaterials have been characterised: circulatory changes, pigmentation, musculoskeletal disorders, and yolk sac alterations (Lammer et al. 2009; Pereira et al. 2019). Most of the publications of inorganic nanomaterials for zebrafish toxicity testing investigate silver, silicon, titanium and zinc, with

one publication recoded for an iron oxide, haematite (α-Fe_2O_3) (Zhu et al. 2012; Pereira et al. 2019). Therefore, it is clear there is a clear need for more research into the toxicity of iron oxide nanoparticle in the zebrafish model, a niche this study hopes to address.

While the use of zebrafish as a toxicology model has become popular as an alternative to mammalian models, it has also been growing in popularity as a model for environmental pollution. Searching the terms ((Zebrafish) AND (pollution)) AND (environmental) on PubMed and Google Scholar shows a clear and dramatic increase in the number of publications involving zebrafish and environmental pollution over the last 30 years (**Figure 5-2**). From just 9 PubMed and 479 Google Scholar articles being identified in the search

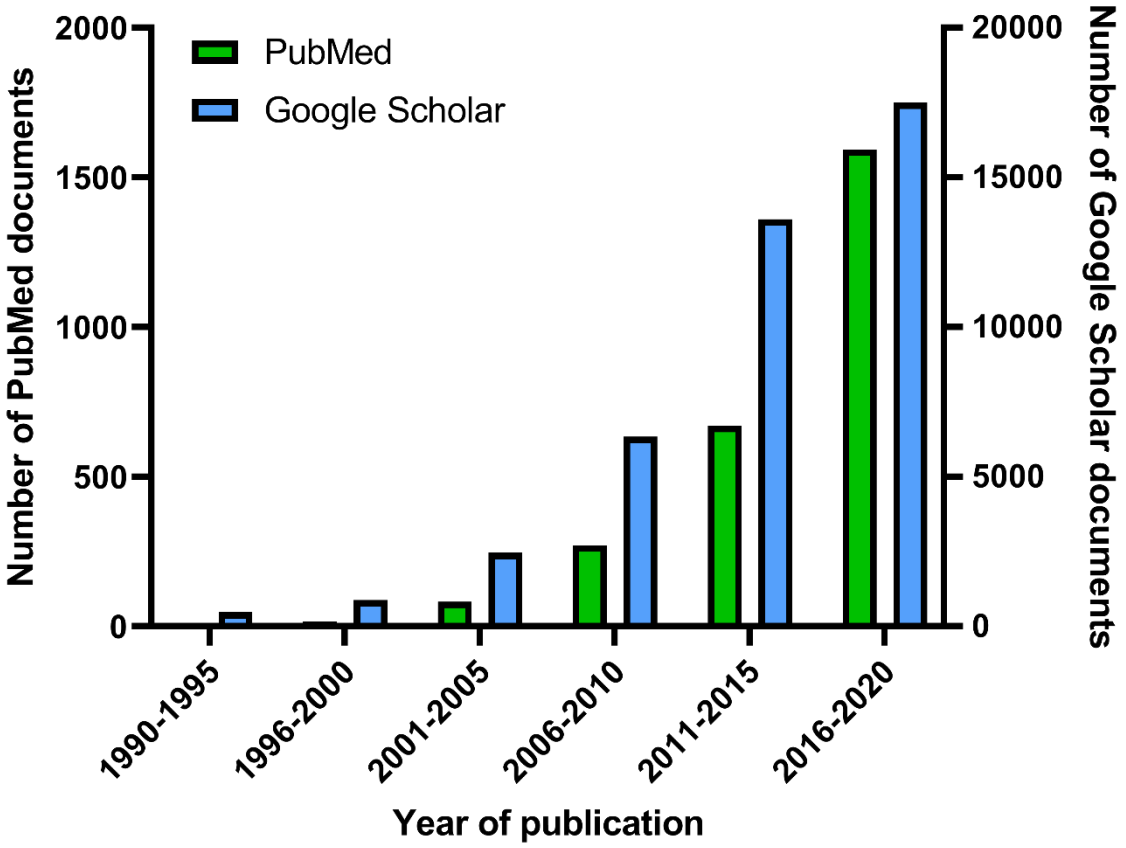

Figure 5-2: Use of zebrafish in researching environmental pollution has increased rapidly over the last 30 years. Numbers of papers published during the years 1990 to 2020 corresponding to the search terms ((Zebrafish) AND (pollution)) AND (environmental). Searches were done on two popular academic search engines, PubMed shown in green (left Y-axis) and Google Scholar shown in blue (right Y-axis). Terms search conducted in May 2021.

period of 1990-1995, rising to 1593 PubMed and 17,500 google scholar articles identified in the search period 2016-2020.

5.1.8 Aims of Chapter Five

This chapter moves from analysing the *in vitro* and *in cellulo* effects of IONPs to examining them in an *in vivo* model. It is important to see if the adverse effects generated by the nanoparticles in cells are not only occurring under *in vitro* conditions and if they contribute to defects in whole organisms, in this case using zebrafish embryos/larvae. The lysosomal purification method described for use in cells in the previous chapter, may also be a feasible method for extracting lysosomes from zebrafish as long as the treatment does not affect survival or induce toxicity. With the development of lysosomal storage disease models in zebrafish, such as the previously described CLN3 model fish, the extraction of fish lysosomes could also be a useful technique. Zebrafish embryos/larvae make an excellent *in vivo* model due to their many desirable characteristics, including production of large batches of eggs, external fertilisation/development, and relatively fast progression through the embryonic stages.

The nanoparticles used is this chapter are LRL and ID (refer to **Figure 4-2**), linking this chapter to Chapter 4 as the *in vivo* application of the same nanoparticles. The dextran coated nanoparticles sediment less, are more biocompatible and do not aggregate as much as uncoated iron oxides, so were ideal for optimising use of developing zebrafish as a model for testing nanoparticle toxicity. The preliminary aim was to identify any phenotypes and defects caused in embryo and larvae development which can be used as tests to compare toxicity between the two types of IONPs. The nanoparticle treated zebrafish embryos and larvae were investigated for general toxicity testing, looking at the effects on embryo survival and development, followed by motor development and movement testing.

5.2 Materials and Methods

*Maintenance and breeding of Zebrafish is detailed in methods Sections 2.6.1-2.6.3. Embryos/larvae were grown and tested in E3 fish medium (Section 2.6.3**).***

5.2.1 Nanoparticle treatment of developing zebrafish

At 8 hours hpf embryos were put 10/per well into a 24-well plate and treated with 1 mg/mL or 0.5 mg/mL concentrations of either LRL or ID nanoparticles (nanoparticle solutions diluted into E3 fish medium) and 100 mg/ml or 50 mg/ml for ID nanoparticles in survival studies only. Every morning after treatment, the embryos/larvae were washed in E3 fish medium and then used for experiments as necessary, before retreatment with fresh nanoparticle solution diluted in E3 fish medium after experimental recordings were completed. When not in use for experiments all embryos/larvae were kept in a 28 °C incubator. Measurements of treatment time follows days post fertilisation (dpf) or hours post fertilisation (hpf).

5.2.2 Imaging zebrafish experiments

Images, videos and observations were recorded using an Amscope trinocular stereo zoom microscope (Amscope) equipped with a Watec WAT902H CCD W85BC monochrome camera module (Watec) and Corel Video Studio 11 image capture software (Corel).

5.2.3 Survival and morphology

To evaluate survival rate, zebrafish embryos/larvae were observed during morning water change every 24 hours at 1, 2, 3 and 4 dpf and the number of surviving embryos counted and tallied as a percentage. Images were taken of the embryos at 24 and 48 hpf to show morphology and hence developmental progress.

5.2.4 Spontaneous coiling

Spontaneous coiling is the earliest motor behaviour in zebrafish embryos starting at ~17 hpf and is clearly visible as a one-sided tail coiling. To assess the effects of the nanoparticles on motor development, videos of spontaneous coiling events over 3 minutes were recorded at 24, 36 and 48 hpf and by re-watching videos the coiling events were counted manually for each embryo.

5.2.5 Heart rate

At 3 dpf, the heart rate of the zebrafish larvae over 1 minute was recorded by imaging the fish at an angle where the heart could be seen, due to the transparency of zebrafish at this age. Heart rates were counted manually as number of beats in 1 minute (beats per minute) by watching the videos in slow motion using a counting device.

5.2.6 Escape Response

At 3 dpf, the zebrafish larvae were tested for the speed of their escape response. To measure escape response an embryo was set in the centre of the camera frame, with its tail pointing into the corner of the frame and while recording it was gently touched with the end of a small pipette tip to elicit an escape response. Time taken for fish to swim out of the frame was calculated by analysing image frames at 40 ms intervals and recording the time taken for the fish to leave the field of view after touch was evoked. To watch the videos by frame and calculate frame times MPC-HC x64 video software was used.

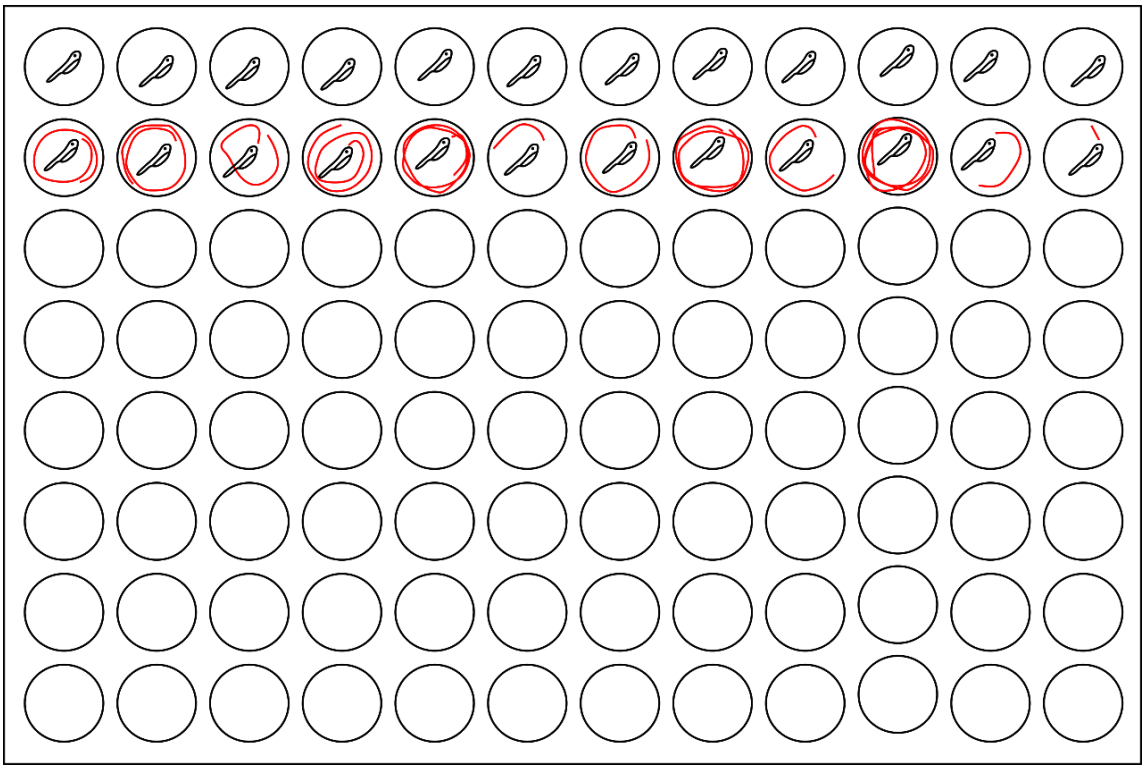

Figure 5-3: Daniovision imaging system set-up. A single zebrafish larvae can be added to each well of the plate (as shown in the top row of plate), with the Daniovision system set up to track each individual. The Daniovision system tracks and records the path of movement of each larvae (shown in red in row two) giving readouts of both visual path tracking (red) and quantitative movement distance and velocity. All wells in the plate can be filled with zebrafish larvae and tracked simultaneously.

5.2.7 DanioVision embryo movement tracking system

At 3dpf, zebrafish larvae were plated out into 96-well plates, with one embryo/well. One plate at a time can then be placed into the DanioVision chamber, which is able to regulate the environmental temperature at 28°C, keeping the larvae in optimal conditions. The settings on the DanioVision need to be adjusted to track the individual zebrafish and identify the space in each individual well (**Figure 5-3**). Once set-up, the Daniovision was run to record movement and velocity of the zebrafish for 30 minutes.

5.3 Results

5.3.1 High ID concentrations are embryonically lethal

The first aim for creating an *in vivo* zebrafish model for nanoparticle treatment toxicity in development, was to ascertain sensible dosing that would be sub-lethal, yet high enough for any defects to be detectable. Initial concentrations for nanoparticle testing were based on the 1 mg/mL concentrations of these nanoparticles found to be sub-lethal in cells in the previous chapter 4, and a half concentration (0.5 mg/mL) to test for does dependency of any potential defects.

At concentrations of 1 mg/mL and 0.5 mg/mL neither LRL nor ID nanoparticles led to reduced survival up to 4 dpf (days post fertilisation) (**Figure 5-4A**). Both the higher doses of ID (5 mg/mL and 10 mg/mL) caused death of all embryos in the treatment group within 3 dpf, with 70-80% dead in the first 24 hours. The toxicity was dose dependent with the highest dose, 10 mg/mL, causing 100% embryo death by 2 dpf and 5 mg/mL causing the same outcome by 3 dpf.

The morphology of all embryos at 24 hpf was similar and showed good development, except for the 5 and 10 mg/mL ID treated embryos (**Figure 5-4B**). These were either dead or showed significantly delayed development, still in the early segmentation stage (normally 10-16 hpf) before the tail starts to elongate. By 48 hpf, nearly all 5 and 10 mg/mL ID treated embryos were dead, and in the few embryos where some morphology could still be seen it appeared as if development had arrested at the 24-hour developmental stage. With the rest of the treatments, the developmental stage appeared similar to the UT controls at 48 hpf. However, at 1 mg/mL and 0.5 mg/mL ID treated embryos may have a reduction in pigmentation at 48 hpf compared to LRL treated and untreated embryos. As the two very high concentrations of ID caused such high levels of embryonic death by 24hpf, only the 1mg/mL and 0.5 mg/mL concentrations were used for further experiments.

5.3.2 ID nanoparticles can cause defects in early motor and cardiac development

Defects in spontaneous coiling (a repeating tail coiling event) are often an early sign of defects in motor development in zebrafish embryos, so rate of coiling was investigated in the nanoparticle treated embryos. Rate of spontaneous coiling was affected in the embryos

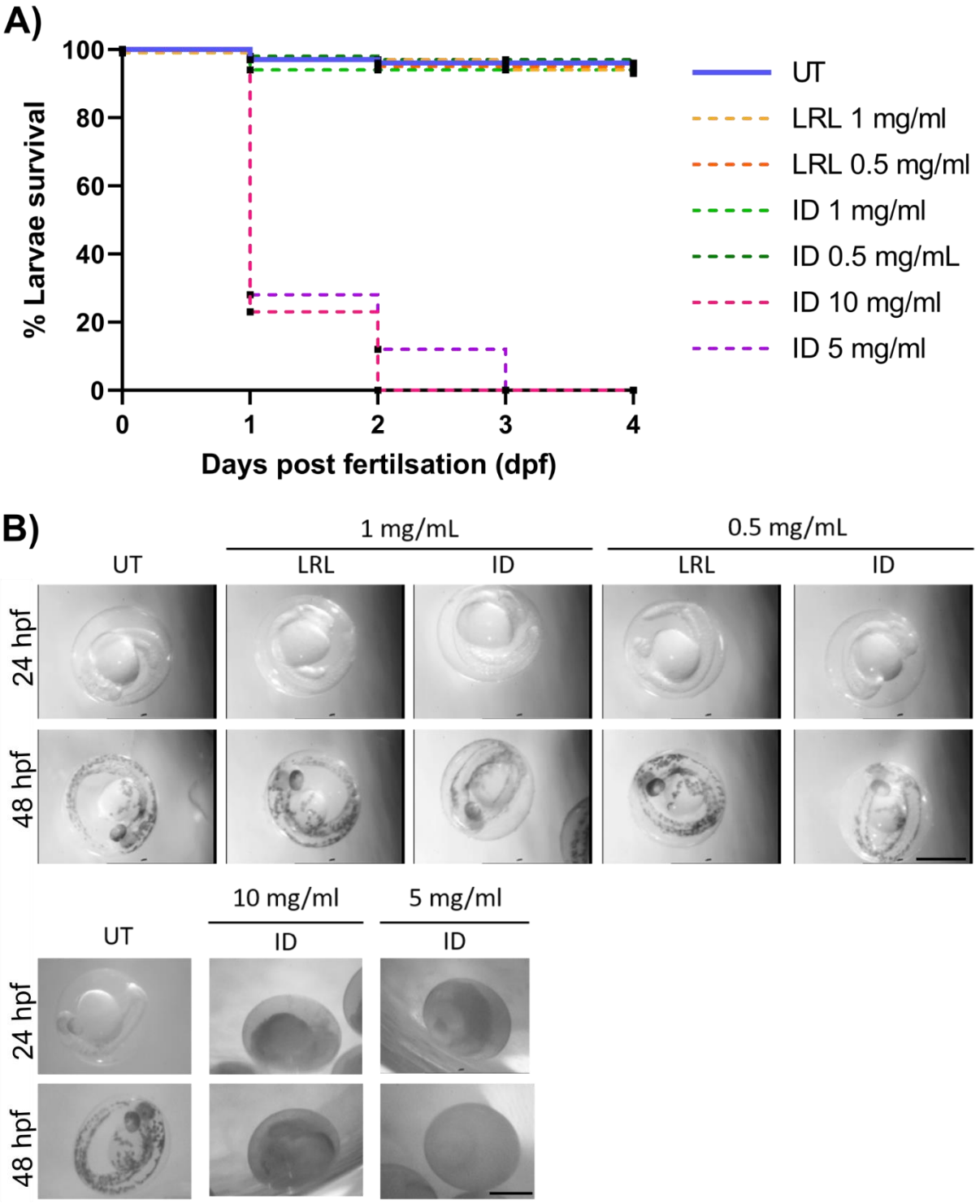

Figure 5-4: High concentrations of iron dextran (ID) nanoparticles are toxic to developing Aβ-LT zebrafish embryos. Zebrafish embryos were treated with LRL or ID nanoparticles at 0.5 or 1 mg/mL and ID only at 10 and 5 mg/mL alongside respective untreated controls (UT). **A)** Zebrafish survival as a percentage, counting every 24 hours to 4 days post fertilisation (dpf), when treated with metallic nanoparticles LRL or ID at a range of concentrations. Number of embryos per treatment = 90-120. **B)** Representative morphology images of a single embryo from each treatment group at 24- and 48-hours post fertilisation (hpf). Number of embryos per treatment = 8. Scale bars = 0.6 mm.

by the higher concentration of ID treatment (**Figure 5-5A and B**). Treatment with 1 mg/mL ID caused a significant 45% decrease in spontaneous coiling at 24 hpf compared to untreated control fish (**Figure 5-5A**). While the lower, 0.5 mg/mL, ID concentration did not cause a significant change in spontaneous coiling at 24hpf compared to untreated control fish, suggesting the effect is concentration dependent with a correlation between increasing iron dextran concentrations and reduced spontaneous coiling at 24 hpf.

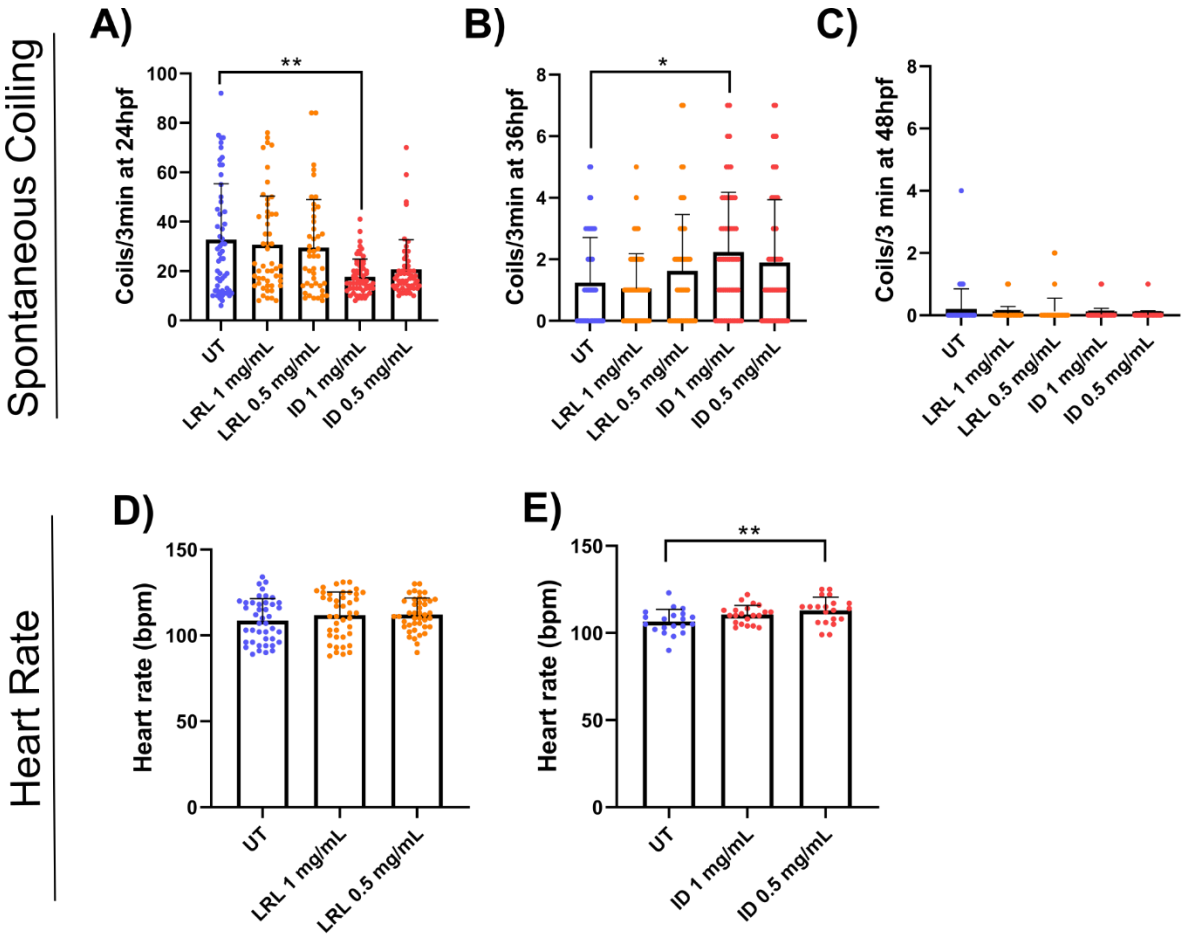

Figure 5-5: Iron dextran treatments can cause spontaneous coiling and heart rate defects in developing Aβ-LT zebrafish. Zebrafish embryos were treated with LRL or ID nanoparticles at 0.5 mg/mL or 1 mg/mL concentrations alongside untreated controls (UT). Number of spontaneous coiling events over 3 minutes were recorded for each embryo at **A)** 24 hours post fertilisation (hpf) **B)** 36 hpf and **C)** 48 hpf. Number of embryos per treatment: A=45-59, B=48-58 and C=49-58 (2 technical repeats). Heart rate of 3 dpf larvae by was counted after treatment with either **D)** LRL or **E)** ID nanoparticles. Number of embryos per treatment: D=42 (4 technical replicates), E=20-21 (2 technical replicates). All analysis by Kruskal-Wallis test, with post hoc Dunn's multiple comparison test comparing treatments to their respective untreated controls. * $p<0.05$, ** $p<0.01$.

At 36 hpf the effect on spontaneous coiling caused by ID treatment was reversed, with the higher 1 mg/mL ID treatment causing a significant 80% increase compared to untreated controls (**Figure 5-5B**). Again, the lower dose of 0.5 mg/mL ID nanoparticles was not significant, suggesting a dose-dependent effect. By 48 hpf, spontaneous coiling was very low in all treatment groups, as would be expected in normal zebrafish development (**Figure 5-5C**). In contrast to ID, neither concentration of the LRL nanoparticle had any effect on rate of

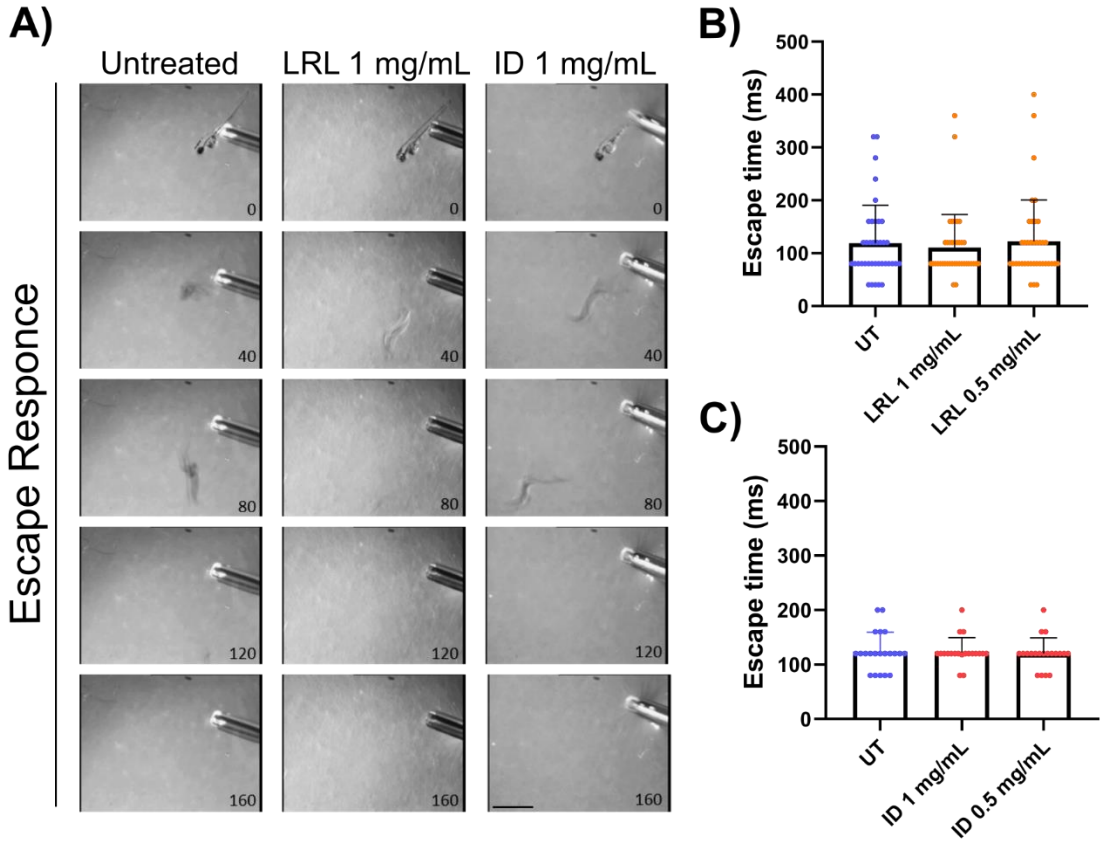

Figure 5-6: Development of an effective escape response in 3 days post fertilisation Aβ-LT zebrafish larvae was not affected by treatment with either LRL or ID nanoparticles. Zebrafish embryos were treated with LRL or ID nanoparticles at 0.5 mg/mL or 1 mg/mL concentrations alongside untreated controls (UT). **A)** Representative image frame sequences are shown for the higher concentration used of both LRL and ID nanoparticles. The time in milliseconds of each frame from initiation of response is labelled in the bottom right corner of each frame. Scale bar = 1.75 mm. Data is shown separately in graphs for **B)** LRL and **C)** ID nanoparticle treatments, counting milliseconds (ms) taken for embryos to leave the frame once the escape response is initiated. Number of embryos per treatment: B= 38-39 (4 technical replicates) and C= 20-21 (2 technical replicates). Analysis by Kruskal-Wallis test, with post hoc Dunn's multiple comparison test comparing treatments to their respective untreated controls (all treatments non-significant).

spontaneous coiling at either, 24, 36 or 48 hpf (**Figure 5-5A-C**). Similarly, neither concentration of the LRL nanoparticles had any effect on larvae heart rate at 3 dpf (**Figure 5-5D**). Only the 0.5 mg/mL ID nanoparticle treatment affected 3 dpf larvae heart rate, with a small but significant 6% increase compared to untreated control fish, meanwhile the 1 mg/mL ID treatment did not cause a significant change (**Figure 5-5E**).

5.3.3 Neither LRL nor ID treatments affected escape response development

Escape response is a rapid movement away from a stimulus (such as touch) evolved early in fish development to protect against predators (as described in Section 5.1.4). This response presents after spontaneous coiling stops and the embryo breaks out of its chorion, and so was investigated next for potential developmental defects in the nanoparticle treated zebrafish. As can be seen in **Figure 5-6A** once touched by a pipette tip the fish would rapidly swim away out of the frame of imaging. By counting the time of frames from initiation of

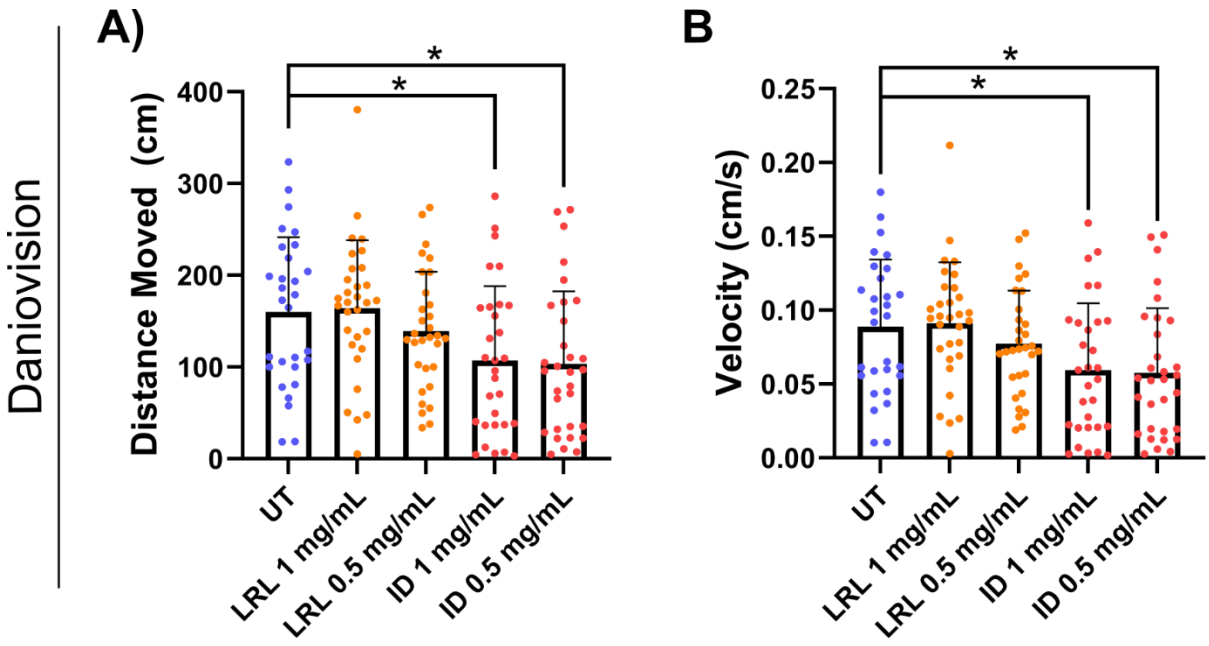

Figure 5-7: ID nanoparticles caused a reduction in distance moved and velocity of movement in 3 days post fertilisation Aβ-LT zebrafish larvae. Zebrafish embryos were treated with LRL or ID nanoparticles at 0.5 mg/mL or 1 mg/mL concentrations alongside untreated controls (UT). Zebrafish were individually tracked by the Daniovision imaging system for 30 minutes to analyse **A)** movement distance of the larvae, and **B)** mean velocity. Number of embryos per treatment: A and B = 29-31 (three technical replicates). Analysis by Kruskal-Wallis test, with post hoc Dunn's multiple comparison test comparing treatments to their respective untreated controls. * $p<0.05$.

response to the fish leaving the frame of view, the length of escape response in milliseconds could be measured quantitatively. For both LRL treatments (**Figure 5-6B**) and ID treatments (**Figure 5-5C**) there was no significant change in escape response duration.

5.3.4 ID nanoparticles affect movement behaviour of 3dpf zebrafish larvae

The DanioVision imaging system allows tracking of movement behaviour for individual zebrafish larvae, the set-up for which is shown in **Figure 5-7A**. In this study the DanioVision system was used to track movement of individual zebrafish over 30 minutes, providing distance moved and average velocity of movement data, defects in which can be a sign of developmental abnormalities in zebrafish larvae. Despite the large intragroup variation, a clearly significant reduction in both movement distance (**Figure 5-7B**) and velocity (**Figure 5-7C**) became apparent after treatment with both concentrations (1 and 0.5 mg/mL) of ID nanoparticles. This equates to a 33% and 35% decrease for 1 mg/mL and 0.5 mg/mL ID treatment, respectively, compared to untreated control fish, the same for both movement distance and velocity. However, there was no significant difference in either movement distance (**Figure 5-7B**) or velocity (**Figure 5-7C**) after treatment with either concentration of LRL nanoparticles.

5.4 Discussion

This study has successfully created an effective zebrafish model for assessing embryonic/larvae toxicity of different iron oxide nanoparticles, using high concentrations of nanoparticle to compare effects over a short 4-day exposure time during initial development. Defects in several easily examined behavioural responses were found after ID treatment relating to survival, motor development and cardiac development. While LRL treatment was found to be non-toxic for all the behavioural responses that were tested, suggesting this nanoparticle may also be a promising candidate for developing a zebrafish magnetic lysosomal extraction method.

5.4.1 Setting up a nanoparticle toxicity *in vivo* zebrafish model

Zebrafish are growing increasingly popular as model organisms for all the reasons previously highlighted in Section 5.1.5. The importance of using zebrafish embryos/larvae in this study, was the ease of measuring developmental effects in externally developing, transparent embryos and the supportive ethical implications, considering this was early-stage modelling.

LRL and ID nanoparticles were both evaluated in cells in Chapter 4. As LRL is used for lysosomal purification in cells, determination of its *in vivo* toxicity played the dual role of investigating organism level toxicity and to determine if it could also be used for developing a magnetic lysosomal purification method to be used in zebrafish, as these are regularly used as models of lysosomal storage diseases (Keatinge et al. 2015; Wager et al. 2016; Cook et al. 2020b; Zhang and Peterson 2020). In cells, LRL appeared to be highly stable and rarely led to defects in cellular function in any of the processes that were tested. For comparison, ID nanoparticles, which were far more toxic in cells causing changes in lysosomal area, lipid peroxidation and mitochondrial area/ATP quantification, were also investigated in the zebrafish (described in chapter 4). ID nanoparticles were chosen for comparison over CC nanoparticles due to their historic use as an anaemia treatment, still utilised in some, often less developed, countries (Johnson 1979; Ayub et al. 2008; Auerbach et al. 2015). Use of this nanoparticle in the zebrafish would aid determination of whether a nanoparticle able to induce defects in cells, would at the same concentration cause defects in zebrafish development at the whole organism level.

5.4.2 High ID concentrations are embryonically lethal

Concentrations of LRL and ID nanoparticles to use in the zebrafish were derived from those used in the cellular tests (Chapter 4). In cell work a concentration of 1 mg/mL was used, at which the differential responses of LRL and ID were identified. Therefore, a concentration of 1 mg/mL was also a starting point for the fish work and to detect if effects are concentration dependent, a 50% lower concentration of 0.5 mg/mL was also included to test for dose dependency of potential phenotypes. Neither of these concentrations influenced zebrafish survival to 4 dpf, suggesting they could be effective sublethal doses for investigating defects. The chorion can reduce access of the nanoparticles to the developing embryo before hatching, meaning nanoparticle induced toxicity may be lower in the *in vivo* zebrafish model than in cells. Therefore, 10x higher concentrations of ID (as the more toxic nanoparticle in the cell experiments) were included (5 and 10 mg/mL), to see if the point of lethality could be assessed. This proved accurate, as both higher concentrations proved lethal by 3 dpf in a dose dependent manner. Showing that 1 mg/mL was below, but not too far below lethal concentration and would probably be high enough to induce defects in behaviours that would be susceptible.

The ~70% lethality induced by 5 mg/mL concentration In the first day after treatment, suggests that this value must be slightly higher than the 24-hour LC50 (concentration causing lethality in 50% of test animals) value for iron dextran (ID nanoparticles) in embryonic zebrafish. A study of uncoated α-Fe_2O_3 (haematite) nanoparticles in zebrafish embryos found the 168-hour LC50 value to be 53.35 µg/mL (Zhu et al. 2012). They found mortality in treated zebrafish was low until about 96 hpf, the point at which the experiment with ID ended. After this point in the Zhu et al. (2012) study, survival dropped rapidly from the higher nanoparticle concentrations (100 and 50 mg/L), likely due to higher uptake around this period when gills and feeding behaviours develop. Supportive of this, are the results of a study by Skjolding et al. (2017) who found, using lightsheet microscopy, the highest area of uptake for aqueous fluorescent nanoparticles in juvenile 4-6 week old zebrafish were indeed in the gills and gastrointestinal system.

As higher concentrations of LRL were not tested, it's concentration causing lethality cannot be inferred. Yet, the low toxicity at the 1 and 0.5 mg/mL concentrations across the 4-day period, indicates high biocompatibility and *in vivo* tolerance in the developing zebrafish.

While this period is short it is able to represent the incubation time likely needed for lysosomal purification-related treatment of a model disease organism (e.g. lysosomal storage disease, CLN3 morphant).

This chapter suggested that high ID concentrations may halt development around the early segmentation stage before triggering mortality. Both this and the reduction in pigmentation at 48 hpf seen in ID treated embryos, are potential defects that should be further investigated. Changes in pigmentation have been noted after treatment with other transition metals including zinc and magnesium (Pereira et al. 2019), however, there is a notable dearth of research into this area.

5.4.3 ID nanoparticles can cause defects in early motor and cardiac development

Iron dextran treatment at 1 mg/mL led to reduced spontaneous coiling at 24 hpf and increased spontaneous coiling at 36 hpf, suggesting a developmental delay in motor development of this reflex. The normalisation back to low levels of coiling by 48 hpf, suggests the defect is not highly severe and that development is only slightly delayed and is preceding normally again by the 48 hpf stage. This is supported by the morphology imaging, which clearly shows morphological development is not severely delayed with either the 1 mg/ml or 0.5 mg/mL treatments. A previous study of spontaneous coiling (26-28 hpf) in developing zebrafish found that 24-hour treatment with 5 mg/L of iron ions reduced spontaneous coiling compared to control fish, while concentrations up to 10 mg/L of citrate-functionalized maghemite nanoparticles, under the same conditions, did not affect spontaneous coiling (Pereira et al. 2020). However, this study used much lower concentrations of IONPs, than for LRL and ID in this thesis, with the spontaneous coiling reduction seen for the free iron treatment then similar to the effect seen with ID treatment at 24hpf. No studies on the effect of magnetite nanoparticles on spontaneous coiling were found in the literature.

Cardiovascular effects are well documented in zebrafish after treatment with transition metals (Pereira et al. 2019). So, it was not unexpected to see a defect in heart rate from nanoparticle treatment. The defect was only identified in the lower ID dose of 0.5 mg/mL, and not in the 1 mg/mL which could be due to a reduction in heart rate if the zebrafish are less healthy, with this cancelling out some of the effects increasing heart rate for the lower

dose. It could suggest that the effect is dose sensitive in a bell-shaped curve, with no effect at higher and lower doses. What can make the study of heart defects difficult in zebrafish larvae is their rare ability to be able to repair damaged heart muscle (Lien et al. 2012). The point at which this system kicks in (it may only start after a certain level of damage is reached) makes it difficult to with certainty say that heart damage has not occurred, but instead the heart could be under constant repair. It is, however, known that tissue regeneration can occur to repair damage at just 3-4 dpf (Zhang et al. 2013), and this could mitigate identification of heart rate defects in this model. A previous study of developing zebrafish treated with 0.3 mg/L citrate-functionalized maghemite nanoparticles for a 48-hour exposure (50-52 hpf) instead found reduced heart rate in the IONP treated fish compared to untreated controls.

5.4.4 Neither LRL nor ID nanoparticles affect development of escape response

It was not surprising that no defect in escape response was seen, as this requires considerable damage to motor neurons and or neuromasts (water movement sensory cells) (Sonnack et al. 2015). One study has demonstrated the requirement for around a quarter of motor neurones to be ablated to significantly reduce the frequency of touch responses (Reimer et al. 2013).

5.4.5 ID nanoparticles affect movement behaviour of 3 dpf zebrafish larvae

Despite the lack of very serious motor neurone damage that can trigger a defect in escape response, a defect in general movement of the ID treated zebrafish was found with both nanoparticle concentrations when using DanioVision tracking software at 3dpf. This supports the idea of ongoing neuromuscular developmental defects from affected spontaneous coiling at 24-36 hpf to reduced movement at 3dpf. No previous studies using a Daniovision imaging system to record larvae movement after IONP treatment were found in the literature, with no specific tests of larvae movement distances noted either. Due to the difficulty in manually tracking movement of fish individually over longer periods of time, it is clear that the DanioVision imaging system could be a very helpful and sensitive tool for detecting heavy metal-related movement defects in zebrafish larvae.

5.4.6 Developmental toxicity of LRL and ID nanoparticles on zebrafish

The LRL nanoparticles did not lead to a defect in any of the treatment groups, despite a very similar iron load. Although there are several differences between the two particles, it is likely the structure of the dextran may have a big effect, with the dextran coating on the LRL nanoparticle being far more protective than having a dextran core like the ID nanoparticle. The relatively high stability and biocompatibility of the LRL nanoparticle may also be contributed to by its small size, magnetite: maghemite composition, structure, and preparation method. As LRL nanoparticles did not cause a defect in any of the developmental tests, especially in comparison to ID nanoparticles, which were shown to have greater toxicity, this suggests they also have a high biocompatibility in developing zebrafish, similar to results in CHO cells (chapter 4). As disease phenotypes can be recorded in disease model zebrafish from developmental tests (Cook et al. 2020b), including those in this chapter, within the time frame of nanoparticle treatments and testing (4dpf), it can be assumed that adding LRL nanoparticles across this time frame would be biocompatible and likely have little impact on zebrafish development and developmental phenotypes. This supports the use of LRL nanoparticles for use in developing a magnetic lysosomal extraction method in zebrafish. The next stage to test would be to check if LRL nanoparticles led to increased toxicity in a diseased model compared to non-diseased fish, as inducing a disease state may sensitise the fish to effects of the nanoparticles.

Across this study, ID treatments caused circulatory and motor development defects. While iron dextran use has previously been shown to be safe for anaemia treatment in pregnant women (Ayub et al. 2008), rare effects on foetal heart rate have been observed with some types of low-molecular-weight intravenous iron treatments (Woodward et al. 2015). The findings on ID in this study do suggest that high doses of iron dextran are potentially developmentally toxic, especially in comparison to other IONPs, such as the LRL nanoparticles.

5.4.7 Future developmental experiments

Another test that would be of future interest is 3 dpf hatching rate as this is shown to be a common defect from metal ion treatments (Pereira et al. 2019). Hatching rate has been linked to spontaneous coiling, proposedly because muscle twitching can aid in the escape of the embryo from the chorion at 3dpf and defects in spontaneous coiling seem to be linked

with defects in hatching rate (Ogungbemi et al. 2019; Aldavood et al. 2020), making this a useful test to investigate alongside spontaneous coiling experiments.

Previous work has indicated that α-Fe_2O_3 (maghemite) nanoparticles (with an average size of 30 nm that form aggregates of ~1 µm) can adhere/adsorb to the chorion surface, where nanoparticle aggregation may change surface mechanical properties or interfere with the function of chorion digestive enzymes to delay hatching (Zhu et al. 2011). Pores are naturally present in the chorion as a means for specific uptake of nutrients from the water before the embryo hatches, with crossing dependent on size and charge of the molecules (Chen et al. 2020). Crossing the chorion through the pores is the most likely uptake method for nanoparticle present in the water to contact the developing embryo. There has been inconsistency between studies measuring the size of the chorion pores by electron microscopy, with one study suggesting the pores are ~170nm^2 (Cheng et al. 2009), while another suggests they are larger, ~770 nm (Chen et al. 2020). Presumably only particles smaller that the size of the pores would get through to the developing embryos. As LRL and ID nanoparticles are predicted to have a considerably smaller diameter than either of the suspected pore sizes above, they would likely be small enough to cross the chorion, however, this would also be dependent on other factors such as charge. Even when attached to the outside of the chorion and unable to cross, nanoparticles can still impact the developing embryo as surface adherence/adsorption can block the pores, resulting in decreased nutrient and oxygen exchange between the embryo and environment, and resulting in embryo hypoxia (Cheng et al. 2009). This would be interesting to investigate further with fluorescently tagged iron dextran or LRL nanoparticles.

Considering differential toxicity of magnetite and maghemite nanoparticles in cells, it would be logical to test the *in vivo* effects of each of these IONPs individually (LRL being a mix) and in uncoated forms, to compare toxicity, which has been suggested to be higher than for coated nanoparticle by de Oliveira et al. (2017). Preliminary tests have shown that the uncoated nanoparticles display greater adherence/adsorption onto the chorion compared to dextran coated, along with a larger degree of sedimentation of the nanoparticles at the bottom of the wells, where the embryos are also mainly found (data not shown). This is similar to what Zhu et al. (2012) found when treating zebrafish embryos with uncoated α-Fe_2O_3 (maghemite) nanoparticles. A next step may be to look at the effects of these

nanoparticles on both chorionated and dechorionated embryos as both will give data with different implications. Regarding the toxicity of iron oxide water pollution to aquatic life and the implications of iron build-up blocking chorion pores and potentially nutrient and oxygen exchange, it would be more appropriate to study chorionated embryos. While the direct effects of the iron oxide nanoparticles on early embryonic development would be better highlighted by using dechorionated embryos. To what degree release of metal ions directly into the water (without first entering cells and being degraded by the low lysosomal pH), is of consideration. This could lead to free iron ions and reactive oxygen species (ROS) being produced in the water and these may then affect the developing fish directly, especially if aggregation and sedimentation of the uncoated nanoparticles leads to localised high concentrations. Dechorionation of embryos may also be necessary for high nanoparticle uptake needed for magnetic lysosomal purification from zebrafish embryos, so testing the impact of chorionation state nanoparticle induced phenotypes may also be helpful for development of this new method.

Chen et al. (2020) found increased ROS and lysosomal activity in zebrafish embryos exposed to silver nanoparticles, indicating a lysosomal related role to the nanoparticle effects in the zebrafish. As this study found strong links between the lysosome and toxic effects of ID nanoparticles in cells (chapter 2) and defects caused by ID treatment in fish, it is likely lysosomal phenotypes may be detectable in the zebrafish model generated in this study. Therefore, it would be worth investigating lysosomes, ROS, and potentially autophagy (as this is closely linked to lysosomal function) in this model after treatment with the ID nanoparticles. Light sheet microscopy would be ideal for imaging these properties in whole live or fixed zebrafish larvae, as it can provide three-dimensional imaging at high resolution with a wide field of view, utilising the transparent nature of zebrafish in early development (Cook et al. 2020b).

5.4.8 Conclusions

In conclusion, this study has produced a viable zebrafish development toxicity model for the LRL and ID nanoparticles; a system that could easily be adapted for any other nanoparticles of interest. While ID (iron dextran nanoparticles) cause concentration dependent defects in spontaneous coiling at 24 and 36 hpf, and defects in heart rate and general movement at 3

dpf, LRL nanoparticles are comparatively non-toxic. The high biocompatibility of LRL nanoparticles in developing zebrafish clearly shows that these nanoparticles can be used for short term incubations (up to 4 dpf) with zebrafish embryo and larvae models of disease to allow for magnetic lysosomal purification in a non-toxic manner. Development of this new tool would be of great use for further investigation of many rare lysosomal storage diseases in zebrafish models.

6 Chapter Six: Comparison of the toxicity of magnetite and maghemite nanoparticles in a human microglial cell line

6.1 Introduction

6.1.1 The main cells of the brain

There are two main groups of cells in the brain: the neurones and the glial cells, likely with a 1:1 ratio in the brain (Azevedo et al. 2009; von Bartheld et al. 2016). There is evidence of alternating ratios across different regions of the brain, for example the forebrain is suggested to have a higher (~4:1) ratio of glial to neuronal cells (Azevedo et al. 2009).

In the adult central nervous system (CNS), neurones exist as postmitotic cells due to the constant action of neurones to hold the cell cycle arrested (Herrup and Yang 2007). Although morphology can differ between types of brain neurones, all have the same basic structure, with a cell body, dendrites, the axon and axon terminals, giving the neurones a large surface area. Most neurones have multiple dendrites which extend from the cell body to receive chemical signals from the axon termini of other neurones (Grafstein and Forman 1980). The neuron can convert the chemical signal it receives at the dendrites into an electrical action potential which it can quickly conduct along its axon and transmit to other connected neurones at its axon termini. Neurones are very sensitive cells, due to their high metabolic requirements and low regenerative capabilities.

The group of glial cells is composed two groups; macroglia (neuroglial cells of neural origin) including astrocytes and oligodendrocytes, and microglia which are thought to originate from macrophages that invade the brain during early development (Kim and de Vellis 2005).

The astrocytes are the most abundant neuroglial cell type with a star-shaped morphology and essential functions in blood-brain barrier (BBB) maintenance, neuronal survival, and synapse formation and turnover (Barres 2008). Protoplasmic astrocytes are found in grey matter and often have many processes (frequently in the thousands) that can enclose synapses to aid chemical transmission or wrap around blood vessels as part of the BBB. Oligodendrocytes are the myelinating glia of the CNS (Nave and Werner 2014). The myelin

sheath is a modified and extended part of the oligodendrocyte plasma membrane that enwraps around axons to improve the conduction rate of action potentials and maintain axon integrity.

6.1.2 Microglia

Microglia are the primary innate immune cells in the CNS and are estimated to constitute ~10-20% of CNS glia (Vaughan and Peters 1974). In humans, microglia colonise the brain in early development with primitive microglia seen near the mesenchymal tissue capillaries before appearing in neural tissue around 4.5 weeks of gestation and are then present in the neural tissue by 5.5 weeks of gestation (Andjelkovic et al. 1998; Monier et al. 2006).

Microglia have an essential role in clearing dying cells, protecting the brain from pathogens, and engulfing certain molecules recognised by their receptors. They mainly carry out these roles, either through release of diffusible factors or phagocytosis. The release of diffusible factors from microglia can support myelination/oligodendrogenesis, neurogenesis and axon-axon interactions, while it can also induce cell death or survival or stimulate synaptic formation and maturation (Ueno et al. 2013; Pont-Lezica et al. 2014; Bennett et al. 2016; Miyamoto et al. 2016). Microglial phagocytosis is important for degrading and regulating synapses, synaptic elements, living cells, dying or dead cells and neuronal axons (Fu et al. 2014; Miyamoto et al. 2016). Microglia have also been shown to be capable of high levels of constitutive macropinocytosis and as the predominant cell type for pinocytosis within the brain parenchyma (Booth and Thomas 1991; Ranson and Thomas 1991). In microglia, micropinocytosis is the main pathway for uptake of soluble amyloid-β (Mandrekar et al. 2009) and oligodendrocyte exosomes (Fitzner et al. 2011). While primary rat microglial cells can endocytose fluorescent IONPs within three hours and traffic them to the lysosomes (Luther et al. 2013). It is also possible when acting in the brain that microglia may uptake nanoparticles from endocytosis of other cells that have themselves endocytosed nanoparticles or from endocytosis of extracellular brain material; for example IONPs have been shown to interact with amyloid-β to either inhibit or enhance fibrillation, the process forming an amyloid plaque (Mahmoudi et al. 2013).

Microglia in the brain appear to form a heterogeneous cellular population in terms of morphology and activity, depending on developmental stage, location and activation state

(Rezaie and Male 1999). Microglia in the pre-natal and early post-natal brain have very different morphologies and expression patterns than in the adult brain. Data from rats suggests microglia largely possess an amoeboid morphology in these early stages of development, which has a wider and more rounded structure, with a rounded nucleus, copious cytoplasm and shorter, thicker often unramified processes (Schwarz et al. 2012). By the second post-natal week mouse microglia have been shown to develop a ramified morphology, producing an elongated cell with a small, flattened or angular nucleus, pale and scanty cytoplasm accumulating at the poles of the cell and many, thin processes, this being the more common morphology of microglia in a healthy adult brain. (Bennett et al. 2016).

In a healthy brain, microglia are termed in a resting state, or a surveying state as they act as sensitive sensors in the brain. These microglia in a ramified form are far from dormant. Time-lapse imaging suggests the microglia are constantly building processes to gently scan an area without disturbing the finely-wired neuronal structures, followed by withdrawal and rebuilding of these processes, so that the complete brain parenchyma could be monitored every few hours (Nimmerjahn et al. 2005; Bernier et al. 2019). This state is characterised by low expression of major histocompatibility complex (MHC) proteins and other antigen-presenting surface receptors (Aloisi 2001).

Once injury is detected, random scanning is then replaced by directed movement of microglia towards the site of injury (Haynes et al. 2006). Upon detection of brain insult, the microglia can enter an activated state and undergo dramatic structural alterations to an amoeboid morphology, believed to favour phagocytosis and motility (Lull and Block 2010). However, this activated amoeboid state is not the same as the amoeboid state of the microglia in early development, having different gene expression profiles and reactivities (Bennett et al. 2016; Krasemann et al. 2017). Recognition of specific ligands, such as for the detection of viral, bacterial or fungal structures, can induce activation, while it can also be induced by any detected abnormality, such as impairment of neuronal integrity without ligand binding (Hanisch and Kettenmann 2007). In this way the microglia can respond to both known and unknown signs of injury or disturbance.

6.1.3 Comparing human and rodent microglia

A majority of microglial research has been performed in rodent models and while there is a basic shared similarity between these cells across the two species, integral differences have also been identified (Smith and Dragunow 2014). The responses of human microglia to macrophage colony-stimulating factor (Smith et al. 2013) and lipopolysaccharide (Melief et al. 2012) have been shown to be mostly comparable between human and mouse microglia. As lipopolysaccharide is commonly used in activating microglia for cell-based experiments this is an important similarity to confirm. Human microglia appear to assume similar activation states (M1 and M2 phenotypes) compared to rodent microglia, which is an important change noted in many disease states linked to microglia (Durafourt et al. 2012). However, adult human microglia have been found to have reduced MHC-II expression and increased interleukin-10 production compared to rodent microglia (Smith and Dragunow 2014). There are also several genes involved in the regulation of phagocytosis that are expressed in human microglia, but are not present in mice, including C4 isoforms (components of the complement pathway) and Siglec-11 (Lenz and Nelson 2018). A study of astrocytes compared to other glial cells (including microglia) suggested only 30% of human astrocyte-enriched genes were also identified as enriched in mouse astrocytes (Zhang et al. 2016c), indicating mice and human glia may have very different expression profiles. One of the major problems has also been the differences in reactions to pharmacology between rodent and human microglia. Valproic acid has been shown to induce apoptosis and increase phagocytosis in mouse microglia, yet similar concentrations do not induce apoptosis in human microglia and instead reduce phagocytosis (Smith and Dragunow 2014).

Even in growth and proliferation human and mouse microglia can differ. *In vitro* rodent microglia are found to sit atop of other cells in culture, whilst human microglia have been shown to be very adherent to culture surfaces (Smith and Dragunow 2014). A key difference was found in microglial proliferation between rodent and human models of Alzheimer's disease. Several studies have shown microglia proliferation changes as a marker in rodent models of Alzheimer's disease (Kamphuis et al. 2012; Gómez-Nicola et al. 2013). While a study in human microglia suggested an increase in glia cell activation markers MHC-II and glial fibrillary acidic protein (GFAP), but no increase in total glial numbers (Serrano-Pozo et al. 2013). Notably, in the case of Alzheimer's disease mouse microglia have been found to assume an activated neurotoxic phenotype, data which has subsequently been the basis for

numerous drug development studies (Smith and Dragunow 2014). However, observations of human microglia in Alzheimer's disease brains showed changes in morphology and cytorrhexis (a fragmentation of cytoplasm), not seen in the rodent microglia that may instead be suggestive of a neuroprotective role (Streit et al. 2009; Streit and Xue 2010). These differences highlight the importance of species in cellular models, especially when there is a significant dearth of research pertaining to the behaviour of human cell types for comparison.

6.1.4 HMC3 Cell Line

The human microglia clone 3 (HMC3) cell line was established in 1995, through SV40-dependent immortalisation of human embryonic microglial cells and has been authenticated by the American Type Culture Collection (ATCC®) named HMC3 (ATCC®CRL-3304) (Dello Russo et al. 2018). Immortalisation of the cells from a primary culture, led to a more rapid growth capacity but they retained most phenotypic and morphological properties of the primary microglial source, with slightly lower phagocytic activity (Janabi et al. 1995; Dello Russo et al. 2018). Antigenic expression was found to be stable for at least 35 passages of tissue culture in these cells. Initially these cells were found to have a morphology either globular or elongated with thick processes, similar when grown in EMEM or DMEM (Janabi et al. 1995; Hjorth et al. 2010; Liu et al. 2013), with a wider range of morphological phenotypes identified, including globular, bipolar, and very elongated cells, after the cells were gown in DMEM F-12 with high FCS (Etemad et al. 2012). This cell line has been shown to react to the bacterial endotoxin, LSP, and the amyloid β1–40 peptide involved in the Alzheimer's disease pathogenesis, with changes in Interleukin production suggesting a switch in activation state (Lindberg et al. 2005; Baldassarre et al. 2017).

6.1.5 The impacts of air pollution related SPION exposure on the brain

Super paramagnetic iron oxide nanoparticles (SPIONs) in environmental air pollution, especially from vehicular-related pollution (such as brake disc wear), have a high chance of being inhaled by humans in the close vicinity. This is likely common for pedestrians walking in close proximity to busy traffic who may experience high concentrations very near the source of release and for people living near busy roads or in highly polluted urban areas who may experience long-term exposure (Zhou and Levy 2007). Air pollution has been linked to

many human diseases, as was outlined in Section 1.1.6, but of particular concern was the connection to neurodegeneration and related disorders, such as Alzheimer's disease (Maher et al. 2016; Wang et al. 2021a).

Maher et al. (2016) showed the abundant presence of magnetite (Fe_3O_4) nanoparticles in the post-mortem brains of subjects from Mexico City and Manchester. Two different particle morphologies were identified, angular or faceted particles attributed to endogenous formation in the size range of tens and hundreds of nanometres, and rounded particles with diameters from 8 nm-60 nm that appeared to have been formed at higher temperatures than experienced by the human body, but which could occur from vehicle-derived nanoparticles, suggesting these had an environmental source. Their findings suggested a greater nanoparticle concentration in the brains of those from Mexico City at a younger age, likely due to a higher level of air pollution in Mexico City. This study was one of the first to highlight the possible ability of environmentally derived nanoparticles to accumulate in the human brain and led to the question of how the nanoparticles were able to penetrate into the brain despite its selective and tightly regulated uptake pathways. Nanoparticle inhalation has been linked to changes in the brain in animal models. For example, chronic inhalation of reaerosolised nanoparticle sized particulate matter from air pollution in mice decreased levels of the neuronal glutamate receptor subunit (GluA1) in the hippocampus and led to activation of glia along with induction of the inflammatory cytokines interleukin-1α and tumour necrosis factor-α in the cerebral cortex (Morgan et al. 2011b).

Two main possibilities for brain entry have been explored, firstly via alveolo-capillary translocation of nanoparticles, from the lungs to the blood, after which some nanoparticle may be able to cross the blood brain barrier (BBB) and enter the brain (De Jong and Borm 2008). Secondly via translocation of the nanoparticles along the olfactory nerves entered in the nasal passage and leading to deposition in the olfactory bulb of the brain.

6.1.6 Nanoparticle transport across the BBB

The blood vessels that vascularise the CNS possess a unique surrounding structure termed the blood brain barrier (BBB) (Xie et al. 2019). The BBB is a physical and metabolic barrier that limits transportation of ions, molecules and cells between the blood circulating the

brain and the neural tissues. This barrier is critical to tightly regulate CNS homeostasis and protects the CNS from toxins, pathogens, inflammation, injury and disease.

Several studies provide evidence of the possible transport of nanoparticles between the alveoli and the blood circulation. Rat inhalation studies have shown that elemental ^{13}C particles accumulated to a large degree in the liver of rats after 24-hour exposure, indicating efficient translocation into the blood circulation from the lungs (Oberdörster et al. 2002). In humans, inhalation of labelled ultrafine carbon particles resulted in their rapid appearance in the blood circulation and liver shortly after exposure, also indicating the likelihood of translocation of small inhaled particles into the blood (Nemmar et al. 2002a). Taking this process, a step further, Oberdorster et al. (2004) showed rats with inhalable exposure to ultrafine elemental ^{13}C particles for 6 hours showed significant and continuous increases of ^{13}C in the olfactory bulb throughout the 7-day postexposure period, while the cerebrum and cerebellum also showed significant increases on two of the postexposure days. Combined with the ability of inhaled ^{13}C to enter the blood stream this study shows that inhaled ^{13}C can also then enter the brain but does not indicate by which route.

There is evidence nanoparticles can cross layers of brain capillary endothelial cells, the first level of defence in the BBB. In an *in vitro* model of the BBB, coated magnetite SPIONs have been shown to pass into and through a layer of brain capillary endothelial cells and enter astrocytes cultured beneath (Thomsen et al. 2013). This movement was shown to be significantly enhanced (32-120 times greater translocation) when an external magnetic force was applied (ferrite block magnet), with no evidence of damage to the integrity of the endothelial cells or dragging of the SPIONs through the cells by the magnetic force. Synthetic bare magnetite SPIONs have been shown to be internalised into, and translocate across, a monolayer of rat brain microvascular endothelial cells, appearing in medium of the opposite chamber of a trans-well tank after 24-hour incubation (Gárate-Vélez et al. 2020). Similar results were shown with bare and surface-functionalised magnetite nanoparticles through a human cerebral microvascular endothelial cell monolayer, where 30% internalisation and 13% transcytosis had occurred after 24-hour exposure to bare magnetite with increased values for the coated nanoparticles (Ivask et al. 2018).

Exposure of mice to vehicle-emissions via inhalation has been shown to increase permeability of the BBB (Oppenheim et al. 2013) which can increase nanoparticle uptake

from the blood circulation (Conti et al. 2019). Permeabilization of the BBB has also been linked to several neurodegenerative diseases, including Alzheimer's disease (Sweeney et al. 2018), suggesting individuals with these conditions may also experience increased nanoparticle uptake from the blood into the brain across the BBB and that air pollution-derived nanoparticles may have different toxicities in these individuals.

6.1.7 Nanoparticle transport via the olfactory nerves

There is more evidence for the passage of nanoparticles along the olfactory nerves, exposed in the nose and crossing into the olfactory bulb of the brain, than there is for direct crossing of the BBB, although it is likely that in humans both may have a role. Post-mortem studies of brains from individuals living in Mexico City compared to individuals from less polluted areas, suggested the Mexico City inhabitants had higher levels of inflammation-associated markers linked to heavy metal particulate matter than controls and that the olfactory bulb and frontal cortex are major targets for inflammation in exposed individuals (Calderón-Garcidueñas et al. 2010; Calderón-Garcidueñas et al. 2013). While nasal pathology in children chronically exposed to air pollutants exhibit a wide range of histopathologic alterations compared to children raised in less polluted areas (Calderón-Garcidueñas et al. 2001)

A study in dogs from the highly polluted Mexico City compared to controls from less polluted areas suggested exposure to high levels of air pollution caused alterations of the blood-brain barrier (BBB) and damage to brain cells, particularly in the region of the olfactory bulb and frontal cortex (Calderon-Garciduenas et al. 2002). Older dogs also exhibited nasal respiratory and olfactory pathology similar to that seen in human after high air pollution exposure. A suggested route of metal nanoparticle particulate matter into the brain is indicated by the presence of a gradient of particulate matter metals, nickel and vanadium, with olfactory mucosa > olfactory bulb > frontal cortex, suggesting this may be an exploited route for nanoparticles to enter the frontal cortex of the brain (Calderon-Garciduenas et al. 2003).

A study of magnetite nanoparticles in rats that were intranasally instilled for seven days, showed particles deposited at particularly high concentrations in the rat striata, hippocampi and olfactory bulb (Wu et al. 2013b). Mice exposed to reaerolised nanosized urban traffic

particulate matter (<200 nm) for 5, 20, and 45 cumulative hours over 3 weeks showed a rapid increase in oxidative stress in the olfactory epithelium (Cheng et al. 2016). A study of mice exposed via inhalation to iron-soot combustion particles (6 hours/day, 5 days/week for 5 consecutive weeks), showed that there was uptake of iron in the nerve fascicles of the olfactory epithelium, suggesting this could be a method of their translocation to the brain (Hopkins et al. 2018). Although notably despite iron staining found deeper in the olfactory bulb, there was less abundant staining in the glomerular layer, where you might expect iron entering from the olfactory nerves to deposit. This also could be evidence of iron entering the olfactory bulb from the systemic circulation.

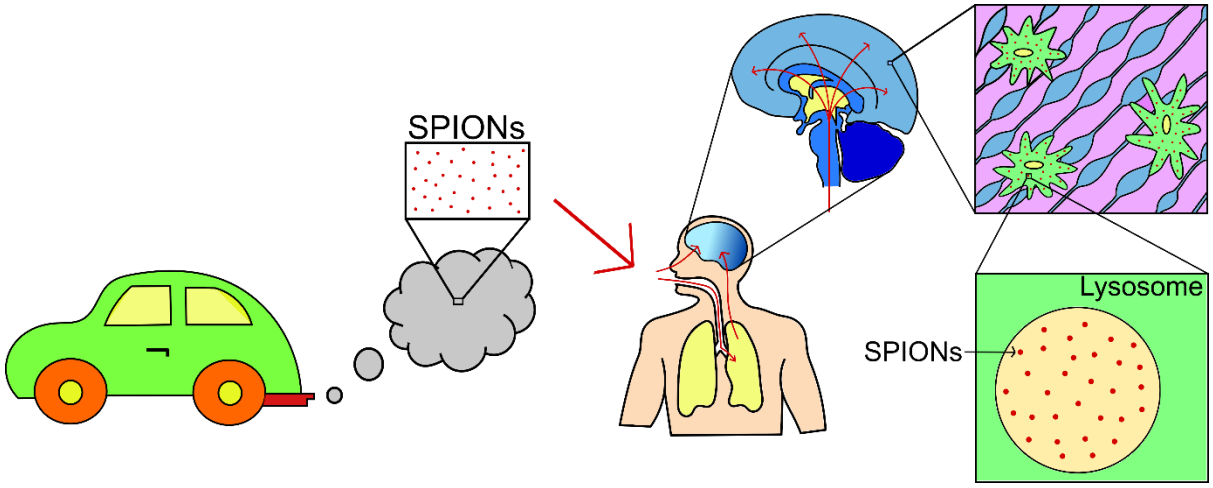

Figure 6-1: Superparamagnetic nanoparticles (SPIONs) from air pollution can reach the human brain. Traffic-related SPIONs in air pollution can be inhaled and transported to the brain either in by, crossing both the alveolar-capillary barrier into the blood and blood-brain barriers, or via the olfactory nerve into the brain. Once in the brain many SPIONs will be endocytosed and phagocytosed by microglial cells, the brains resident immune cells. Within the microglial cells the SPIONs will be transported through the endo-lysosomal system to the lysosome.

6.1.8 Air pollution and nanoparticle toxicity in microglia

As the brains resident immune cells, microglia are likely to be the first line of defence to control/remove foreign material, such as particulate matter in air pollution, by endocytosis of the material into the microglial cells (**Figure 6-1**). This is likely to comprise a mix of phagocytosis, macropinocytosis, and for smaller particles also possibly receptor-mediated endocytosis (Rejman et al. 2004; Rennick et al. 2021).

In the context of air pollution, it has been shown that exposure of microglial cells to particulate matter extracted from combusted diesel fuel can promote inflammation by

increased ROS and cytokine production (Sama et al. 2007; Duffy et al. 2018). Mixed neuron-glia cultures treated with similar diesel particulate matter indicated selective dopaminergic neurotoxicity mediated by microglia (Block et al. 2004). While exposure of mice to nanoscale (<200 nm) particulat matter from traffic-derived emissions led to increased inflammatory microglia, white matter injury, and axonal degradation in the corpus callosum of the mice (Connor et al. 2021). These effects indicate particulate matter air pollution is likely linked to microglial activation, brain inflammation and damage, particularly of neurones. Furthermore, a mix of cellular and rat experiments have suggested traffic-derived particulate matter can induce cytotoxicity, lipid peroxidation, microglial activation, inflammation, increased autophagy, and increased caspase-3 activity (related to apoptosis) in microglia (Bai et al. 2019). Inhalation of iron-soot combustion nanoparticles in mice also led to increased microglial cell activation and to neural inflammation in the olfactory bulb of the mouse brains (Hopkins et al. 2018).

An increase in free iron has been shown to affect microglial cells, as can occur after iron overload, or from mis-regulation of iron in disease. A study by Yauger et al. (2019) demonstrated that addition of free iron releasing compounds to microglial cells (mouse or rat) increases their ROS production, and without an increase in pro-inflammatory markers, this alone can contribute to microglia-induced neurotoxicity. Addition of free iron releasing compounds was also shown to significantly accentuate ROS production in lipopolysaccharide-activated microglia in a concentration-dependent manner.

Microglial cells have a large capacity to uptake magnetite (Fe_3O_4), the presence of which in primary cell culture has been shown to cause microglial cell proliferation (Pinkernelle *et al.* 2012). Microglial cells accumulate low concentrations of magnetite more efficiently than astrocytes and neurones (Petters *et al.* 2016). Short doses of high magnetite concentrations cause ROS production and reduced cell viability in microglia but not in astrocytes and neurones. This demonstrates the importance of microglia in reacting to the presence of free magnetite in the brain. There is also evidence that maghemite (γ-Fe_2O_3) nanoparticle treatment increases microglial proliferation and phagocytosis, while also suggesting increased generation of ROS and NO, however, microglia were less responsive to haematite (α-Fe_2O_3) nanoparticles (Wang et al. 2011b). A second study also found haematite (α-Fe_2O_3) not to be cytotoxic to microglia (Lewis et al. 2016).

6.1.9 Alzheimer's disease overview

Alzheimer's disease is the most common cause of dementia, affecting around 850,000 people in the UK (Alzheimer's Society 2014). There are two major forms of Alzheimer's disease. The first, familial (early-onset) Alzheimer's disease, has symptom-onset before the age of 65 and is normally linked to specific genes, so is hereditary. However, the majority of suffers (~95%) develop the disease over the age of 65, known as sporadic or late-onset Alzheimer's which has many risk factors, both genetic and environmental.

Symptoms can vary considerably, changes often seen in memory, reasoning, language and mood; making misdiagnosis easy in the early stages (McKhann et al. 2011). Alzheimer's disease is associated with a shortened life expectancy, on average between 3 and 10 years (Zanetti et al. 2009). Neurodegeneration is the main neurological change seen in Alzheimer's disease and is responsible for most of the physical symptoms in patients (Moya-Alvarado et al. 2016; Bature et al. 2017). Presently, the only way to make a conclusive diagnosis of Alzheimer's disease is by histological observation of the brain post-mortem (Jack et al. 2011). The fundamental characteristics being the presence of at least a moderate number of amyloid-β containing neuritic plaques in the neocortex and neurofibrillary tangle pathology. Although research has discovered much about the pathological changes involved in the development of Alzheimer's disease, the complete mechanisms behind the disease are still not fully understood. Presently, there are no treatments that can slow or stop disease progression; only those that try to treat symptoms (Yiannopoulou and Papageorgiou 2013).

Most cases of familial Alzheimer's disease have been linked to mutations in one of three known genes; amyloid precursor protein (*APP*), presenilin-1 (*PSEN1*), and presenilin-2 (*PSEN2*) (Sorbi et al. 2001; Williamson et al. 2009). The proteins encoded by these three genes all have a direct role in β-amyloid processing. APP is the protein that when processed by the β-secretase and γ-secretase complex produces the amyloid β (Aβ) peptide (Tanzi et al. 1992). The presenilin's form the catalytic subunit of γ-secretase (Rogaev et al. 2019).

Figure 6-2: Non-genetic risk factors for the development of Alzheimer's disease. Blue arrows linked to purple boxes represent risk factors, orange arrows linked to red outlined boxes represent details about how those factors are associated to disease risk, green arrows link two risk factors together and pink boxes indicate an association with microglial cells.

Sporadic Alzheimer's disease is multi-factorial, with a large range of genetic and environmental risk factors. Even when considering the effect of multiple genes, these are only partial predictors for a person's risk of developing Alzheimer's disease and age of onset. Many environmental factors have now been found to impact disease risk, several of which are identified in **Figure 6-2**. The biggest risk factor by far is age, with a 14x increased risk of developing Alzheimer's disease over the age of 85 than between 65-69 (Hebert et al. 1995).

6.1.10 Air Pollution as a risk factor for Alzheimer's disease

Living in close proximity <200 m from a major traffic road has been linked to increased risk of developing Alzheimer's disease, but not Parkinson's or multiple sclerosis (Chen et al. 2017). Higher risk was associated with closest proximity, in this case <50 m. A similar study showed that living in closer proximity to a main road may increase structural brain aging, reducing cerebral brain volume (Wilker et al. 2015).

Studies in urban dogs have supported these trends (Calderon-Garciduenas et al. 2002; Calderon-Garciduenas et al. 2003). Dogs in more polluted cities demonstrated a range of phenotypes linked to Alzheimer's disease in humans, included alterations of the blood-brain barrier (BBB), DNA damage in Alzheimer-related brain regions, degenerating cortical neurons, deposition of apolipoprotein E (apoE)-positive lipid droplets in smooth muscle cells and pericytes, diffuse plaques and neurofibrillary tangles. Both children and dogs from the highly polluted Mexico City had a high level of white matter prefrontal lesions in the brain, found in 56.5% of Mexico City children compared to only 7.6% of children in a less polluted control city (Calderón-Garcidueñas et al. 2008). The children in Mexico City also exhibited deficits in fluid cognition, memory, and executive function compared to children living in a less polluted urban environments. Residents of highly polluted cities in Mexico have been shown to have significantly higher amyloid-β accumulation in the brain when compared to age-matched controls in less polluted cities (Calderón-Garcidueñas et al. 2004).

Traffic-related air pollution has been associated with poorer cognitive performance in older populations of both men and women (Ranft et al. 2009; Power et al. 2011). While environmentally relevant levels of PM2.5 exposure for 3 months in a mouse model of AD, was shown to exacerbate AD pathology, with an increase in amyloid-β levels, plaque load, reactive gliosis and pro-inflammatory cytokines (Sahu et al. 2021).

6.1.11 Iron and Alzheimer's disease

There have now been many studies demonstrating that metal ions, such as copper, zinc and iron, are involved in the occurrence and development of Alzheimer's disease. Iron levels are elevated in Alzheimer brains (Pankhurst et al. 2008) and the iron is shown to bind to amyloid-β inducing aggregation (Liu et al. 2011) and to tau inducing hyper-phosphorylation (Yamamoto et al. 2002). Iron binding to both amyloid-β and tau increases their toxicity to neurones.

Iron in the form of magnetite (Fe_3O_4) is commonly found endogenously in human brains (Kirschvink et al. 1992). The original papers that discovered magnetite in human brains, identified a nanoscale form with a euhedral crystal shape, thought to form by normal biological processes (Kirschvink et al. 1992; Schultheiss-Grassi et al. 1999). Subsequent studies found magnetite at elevated levels in the brains of Alzheimer's sufferers (Hautot et

al. 2003; Collingwood et al. 2005; Pankhurst et al. 2008) and then a further study found a possible link for the increased brain magnetite to an environment air pollution derived source (Maher et al. 2016). Maher et al. (2016) studied post-mortem human brains and found two forms of magnetite were common, a euhedral form associated with endogenous formations and a rounded form consistent with high-temperature formation, suggesting an environmental source as this form is abundant in airborne particulate matter pollution and the temperatures normally needed to form it would not be found in the human body.

6.1.12 Microglia in Alzheimer's disease

Microglia have been strongly implicated in the development of Alzheimer's disease as their proliferation and activation occurs prominently around amyloid plaques in the brain (Perlmutter et al. 1990; Akiyama et al. 1999; Bornemann et al. 2001). Initial microglial activation may have a protective role (anti-inflammatory) with microglia attempting to break up the plaques and catabolise the amyloid (Hamelin et al. 2016). However, it has been shown that when microglial activities and responses are altered, as occurs in Alzheimer's disease, there is activation of the pro-inflammatory phenotypes in the microglia (Fan et al. 2017). This can lead to the release of pro-inflammatory cytokines and other products harmful to neurones, which can mediate synapse loss, exacerbate tau pathology, reduce β-amyloid digestion and cause inappropriate astrocyte activation (Takuma et al. 2009; Jaworski et al. 2011). Neurone damage can lead to further microglial activation, triggering a cycle called microgliosis. However, it should also be noted that the majority of the work on the pro-inflammatory action of microglia has been done in rodent models and it has been observed that activation of human microglia in Alzheimer's disease may be different to that in mice (Streit et al. 2009; Streit and Xue 2010). Many of the Alzheimer's disease risk genes are expressed in microglial cells, suggesting microglia could be a common denominator to many of their effects (Efthymiou and Goate 2017). Especially as many of the genes could link to microglial activation early in Alzheimer's disease pathogenesis and independent of amyloid pathology (Paolicelli et al. 2017; Shi et al. 2017).

6.1.13 Lysosomal dysfunction and Alzheimer's disease

Genetic evidence points towards a role for lysosomal dysfunction in contributing to development of Alzheimer's disease pathology via risk genes that regulate lysosomal

function. Considerable evidence links the v-ATPase lysosomal proton pump, and lysosomal deacidification that is associated with its dysfunction, to Alzheimer's disease pathogenesis (Colacurcio and Nixon 2016). Mutations of presenilin-1, a ligand of the v-ATPase V0a1 subunit required for its lysosomal targeting, are commonly linked to early onset Alzheimer's disease. Cells from AD patients with presenilin-1 mutations exhibit increased lysosomal pH due to reduced v-ATPase proton-pumping capacity (Coen et al. 2012; Wolfe et al. 2013). Increased efflux of Ca^{2+} from lysosomes in presenilin-1/presenilin 2 double knock out cells has been identified with reduced levels of the lysosome-associated NAADP-dependent calcium channel, two pore channel 2 (TPC2) (Neely Kayala et al. 2012).

There is also strong links between the lysosomal proteases Cathepsins B and L, lysosomal function and Alzheimer's disease, with these proteins being strongly involved in the degradation of key Alzheimer's disease related proteins, amyloid-β peptides and C-terminal fragments of the amyloid precursor protein (Cermak et al. 2016). Several other lysosomal enzymes are also implicated in Alzheimer's disease pathogenesis including: α-mannosidase, β-Hexosaminidase, and β-Galactosidase, tripeptidyl peptidase 1 (Morena et al. 2017; Solé-Domènech et al. 2018).

Phagocytosis of iron oxide nanoparticles by microglial cells would lead to them being trafficked to the cell's lysosomes, where they would likely degrade in the acidic, degradative environment, releasing free iron, that through Fenton reactions, could produce ROS which in turn could damage the lysosome; providing a potential connection between iron oxide nanoparticles, lysosomal dysfunction and Alzheimer's disease.

6.1.14 Aims of this chapter

There are multiple links between microglia and Alzheimer's disease, iron dysregulation and Alzheimer's disease, and lysosomal function in all these cases. The dysregulation of iron can affect microglia which can have a pathological role in the development of Alzheimer's disease. This chapter aims to investigate the role that magnetite nanoparticle treatment and excess free iron can play in altering microglial phenotypes, especially focused on lysosomal phenotypes. Primary aims of the chapter include identifying optimal nanoparticle treatment conditions and concentrations and determining if the HMC3 cells have the ability to phagocytose particles under cell

culture conditions in this laboratory. Then once a model has been established the effects of nanoparticle treatment on phenotypes including lysosomal area, cathepsin B activity and autophagy will be explored. The effect of iron nanoparticles in microglia, not only has significance for the impact of air pollution nanoparticles in the brain, but also may have an impact on development of brain diseases, and in particular can be related to the role air pollution related iron, any associated lysosomal dysfunction and microglia might play in Alzheimer's disease pathogenesis. A key improvement of this model is also the use of a human microglial cell line, in comparison to rodent microglia that have predominated Alzheimer's disease research and the few published studies that explore nanoparticle toxicity in microglia.

6.2 Materials and Methods

6.2.1 Superparamagnetic iron oxide nanoparticles (SPIONs)

Several different uncoated SPIONs were used for these experiments all brought from the company US research nanomaterials (Houston, USA) as nanoparticle dispersions in H_2O: (**Figure 6-3**)

- Magnetite (Fe_3O_4)
    - 3 nm magnetite
    - 8 nm magnetite
    - 15-20 nm magnetite (furthermore denoted as 20 nm magnetite)
- Maghemite (γ-Fe_2O_3)
    - 5 nm maghemite

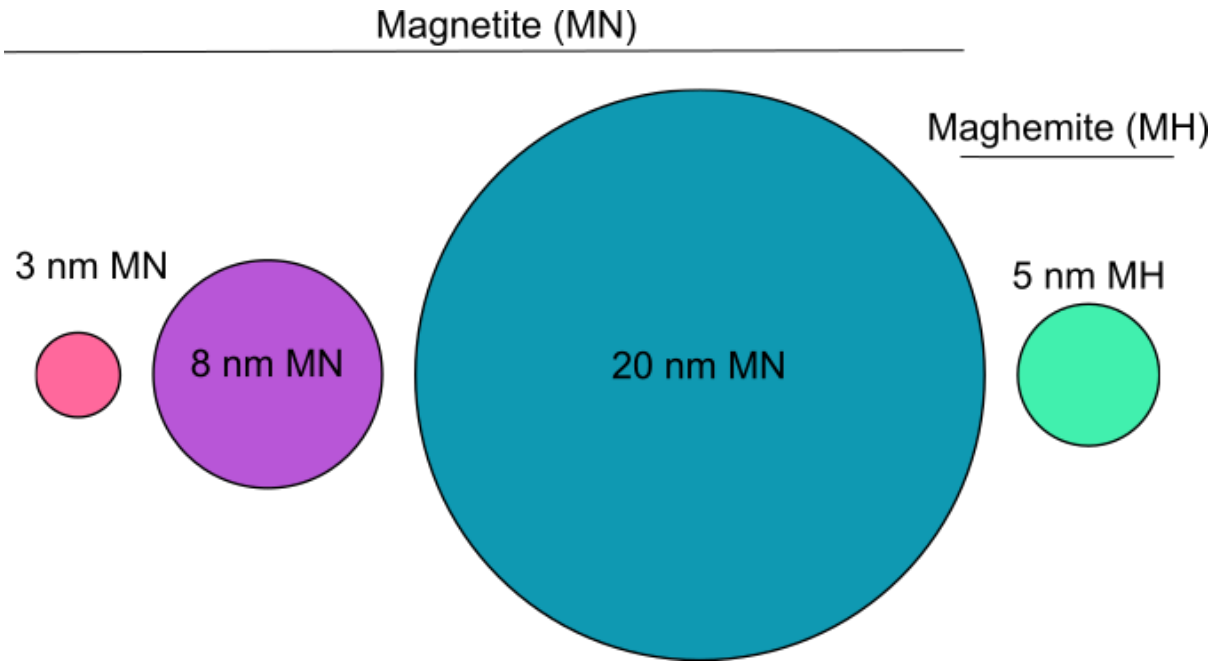

Figure 6-3: Size and composition comparisons of SPIONs from the company US Research Nanomaterials. Three magnetite (MN) nanoparticles of sizes 3 nm 8 nm and 20 nm to the left and one maghemite (MH) nanoparticle of the size 5 nm to the right.

A range of small sizes of nanoparticles were chosen between 3-20 nm of magnetite, as smaller inhaled particles likely have a greater chance to cross the BBB or be transported across olfactory nerves to enter the brain, where the particles would likely encounter

microglial cells. These sizes were the listed sizes of each of the nanoparticle solutions according to the manufacturers website and so the nanoparticles are simply referred to for the rest of the chapter under their listed size. It should be noted that the 5 nm maghemite was chosen as a SPION control as it was the smallest maghemite nanoparticle that was commercially available from the same company.

All the nanoparticle solutions were noted on the manufacturer's website as 99.9% pure nanopowder water dispersions, laser synthesized, that settle upon storage and must be mixed (shaken up) before use. In this thesis electron microscopy (refer to methods Section 2.2.2) was used to visually characterise the nanoparticles.

6.2.2 SPION treatments of HMC3 cells

SPION stock solutions were sonicated in a UXB5 Digital Ultrasonic Bath (Grant, Shepreth, UK) for 10 minutes at 100% power, before use in experiments. Concentrated nanoparticle solution was mixed with 1 µl/mL poly(ethylene glycol) (PEG) BioUltra 400 solution via vortexing the solutions for at least 30 seconds or as long as required for mixing. Addition of PEG to the nanoparticle solutions was included when first optimising their use to reduce sedimentation and aggregation of the nanoparticles in the well, however, as it is not bound to the nanoparticles it should disperse as pH is reduced (during trafficking to the lysosome). The SPION solutions were diluted to the correct concentration in complete medium with 10 µM potassium phosphate buffer (PPB) at pH7.4. Then solutions were again vortexed for at least 1 minute or until nanoparticle solutions were well suspended.

HMC3 cells (general culture methods detailed in methods Section 2.1.1 were used as the exclusive cell type in this chapter and were incubated overnight to adhere to the culture surface before nanoparticle treatments. HMC3 cells were treated with SPIONs at variable concentrations, normally 4 µg/mL (low), 40 µg/mL (medium) or 400 µg/mL (high) for a 5-hour, 1-day or 4-day incubation.

After treatment, the cells were then washed thrice with PBS to remove nanoparticle solutions. Due to the sedimentation of the nanoparticles, pulse chase experiments were less efficient because it became difficult to remove all nanoparticle solution from the bottom of the wells and so a single incubation period with no chase was chosen as the best treatment

method. For cell imaging experiments cells were detached from the plate with trypsin, spun down, and replated after cell counting into an IbiTreat 8-well µ slide (Thistle Scientific).

6.2.3 Treatment Controls

For each experiment, control cells were treated with an equal concentration of PEG and PPB (cell medium buffer) compared to treated cells, while untreated (UT) controls were also included with cells grown in complete medium only (no PEG and buffer). Other than the changes in PEG, PPB and SPION treatment, control cells were grown, treated, and washed under the same conditions as the SPION treated cells and in the same plates.

Other controls were included as necessary, commonly 25 nM Bafilomycin-A1 (Baf-A1; Tocris) and 2 µg/mL U18666A (Calbiotech) drug treatments with an overnight incubation on untreated cells. Baf-A1 is an inhibitor of vacuolar type H^+-ATPase (V-ATPase) so causes lysosomal deacidification and inhibits autophagy. U18666A is an inhibitor of the lysosomal membrane transporter, NPC1, and induces phenotypes similar to Niemann–Pick type C disease.

6.2.4 Optimising SPION concentration for HMC3 cell treatments

For cell counting experiments the HMC3 cells were treated at 4-400 µg/mL concentrations of SPIONs either overnight (~24 hours) or for 4 days (~96 hours) and then cell counted according to the protocol in methods Section 2.1.2. From the counts, cell number per well for each treatment was estimated to investigate cell growth/survival rate. CellTiter-Glo Luminescent Viability assay (refer to methods Section 2.5.1) was used to quantify ATP and hence, cell survival rate.

6.2.5 Primary confirmation of SPION uptake by HMC3 cells

The ability of the HMC3 cells to phagocytose large external particles was indicated by the phagocytosis assay (refer to method Section 2.4.14). Light microscopy (refer to method Section 2.4.7) was used to indicate if nanoparticles localised in the region of cells could be identified in unstained nanoparticle treated cells and to investigate cell morphology.

6.2.6 pH dependent release of iron ions from SPIONs

Ferrozine assays (refer to method Section 2.5.2) were used to investigate if nanoparticle degradation was pH dependent.

6.2.7 Impacts of SPION treatment conditions on lysosomal phenotypes

LysoTracker Green fluorescent staining (refer to method Section 2.4.9) was used to indicate lysosomal area/cell. Count analysis of staining intensity was used to preliminarily indicate the variation in LysoTracker staining between individual cells and was measured by manually counting the number of cells that were either strongly above or below the 'normal' threshold (mid-level of staining in control cells) and calculating the percentage of each from the total cells in the image. Magic red fluorescent staining (refer to method Section 2.4.10) was used to indicate cathepsin B activity in the cells.

6.2.8 Impact of SPION treatments on autophagy and production of ROS

Cyto-ID fluorescence staining (refer to method Section 2.4.4) was used to measure autophagic vesicles and monitor autophagic flux. SO-ID fluorescence staining (refer to method Section 2.4.17) was used to indicate superoxide levels.

6.3 Results

6.3.1 Electron Microscopy (EM) for SPION characterisation

The focus of this chapter is on magnetite (Fe_3O_4) nanoparticles which are labelled by their average particle sizes according to the manufacturer, as 3 nm, 8 nm and 20 nm, with a 5 nm maghemite (γ-Fe_2O_3) nanoparticle, for comparison, all obtained from the company US research nanomaterials.

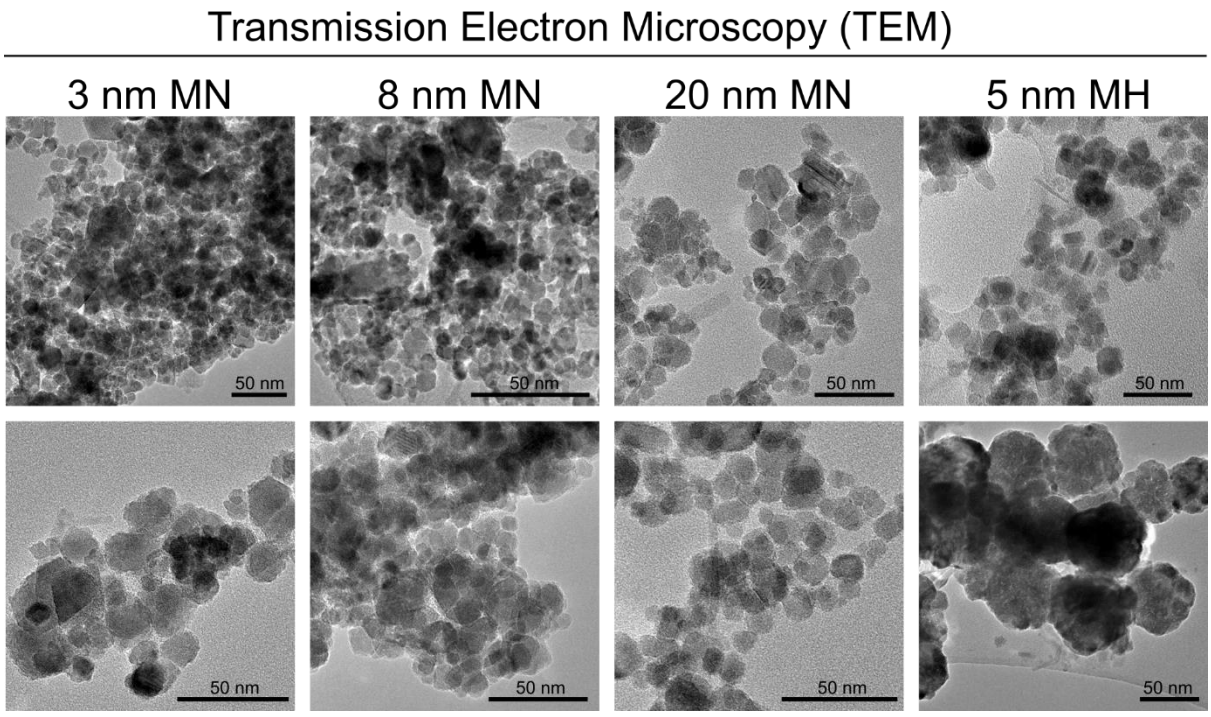

Figure 6-4: Characterisation of SPION structures under electron microscopy. Images were taken by TEM with representative images of magnetite (MN, Fe_3O_4) and maghemite (MH, Fe_2O_3) nanoparticles of the indicated average particle sizes according to manufacturer. Scale bars = 50 nm.

The magnetite and maghemite nanoparticles were analysed by transmission electron microscopy (TEM). The TEM images (**Figure 6-4**) show the magnetite and maghemite SPIONs have a crystalline morphology, hexagonal to octagonal shape with a strong tendency to aggregate (not monodisperse) and have a wide range of particle sizes. Prior to TEM these nanoparticles were not sonicated or vortexed with PEG as is done before they are used in experiments, both of which will improve their dispersion. Most of the structures distinguishable in the TEM images are aggregates of smaller nanoparticles, most clearly observable in the image of the 5 nm maghemite (bottom right image of **Figure 6-4**). With

the high degree of particle aggregation, it is difficult to determine if there is any difference in average particle size between the three magnetite SPIONs. The sedimentation rate of the nanoparticles was not directly monitored, but after 24 hours in cell culture medium or water, a layer of uncoated nanoparticles was observed at the bottom of the well. While addition of PEG to the nanoparticle solutions caused sedimentation to occur more slowly. Concentrated magnetite and maghemite solutions could be visually differentiated by colour, with the magnetite solutions a dark brown and the maghemite solution instead orange (**Figure 6-5C**).

6.3.2 Optimising SPION concentration for HMC3 cell treatments

Determining the optimal concentration with which to treat the cells was a primary aim. Cytotoxicity can also vary between cell lines, especially with a phagocytic cell line, such as HMC3, which is likely to be capable of greater internalisation of nanoparticles than a non-phagocytic cell line, such as the CHO H1 cell line in Chapter 4. A range of concentrations was tested from 4 μg/mL to 400 μg/mL for the magnetite SPIONs (3, 8 and 20 nm).

A basic cell count of cells after either 1 day or 4 days of growth with the SPION treatments demonstrated significant differences in the counts between the higher nanoparticle treatments and control cells (**Figure 6-5A**). Significantly reduced counts were recorded after a 1-day incubation for 20-400 μg/mL of 3 nm magnetite, 20-400 μg/mL of 8 nm magnetite and 40-400 μg/mL 20 nm magnetite. The highest concentration of 400 μg/mL led to similar levels of reduction with all three magnetite SPIONs after 1-day incubation, with a 62% reduction for 3 nm magnetite, 64% reduction for 8 nm magnetite and 69% reduction for 20 nm magnetite. In comparison none of the 4 μg/mL nanoparticle treatments were significantly different to control cells. The 4-day incubation data showed a similar trend with the highest SPION concentrations being significantly different to the control cells. For 400 μg/mL SPION treatments compared to controls cells, there was a 76% reduction for 3 nm magnetite, an 86% reduction for 8 nm magnetite and an 86% reduction for 20 nm magnetite, all larger than the reduction at the same concentration after 1-day incubation. While this was the only concentration that was significantly different to controls for 3 nm magnetite, the 100 μg/mL values were also significant for 8 nm magnetite and 20 nm

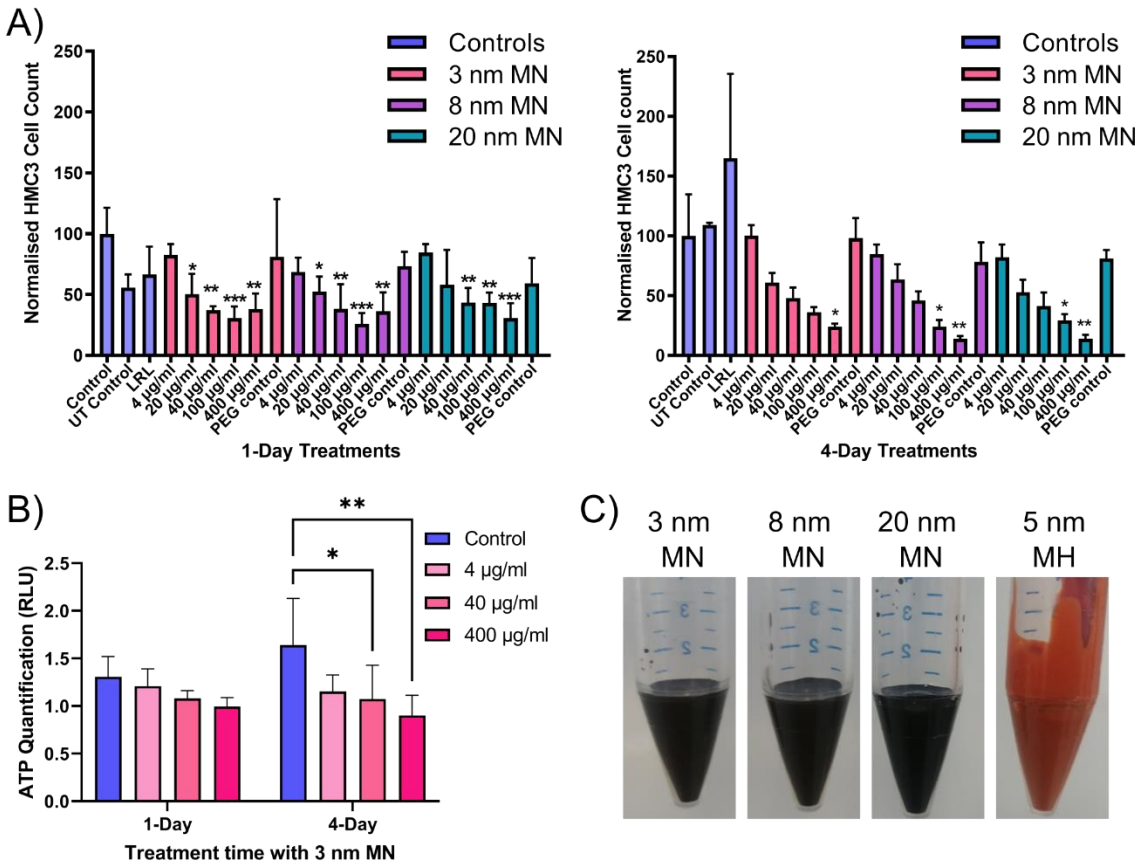

Figure 6-5: Toxicity of SPION treatments to cells is concentration dependent. A) Values of HMC3 cell counting normalised to the control cells after 24-hour treatment (left graph) or 4-day treatment (right graph) with 4-400 µg/mL of 3 nm, 8 nm or 20 nm magnetite (MN) compared to control cells, with UT control (no PEG or buffer) and 1 mg/mL LRL (dextran coated magnetite/maghemite mix nanoparticle). Data normalised to control cells and presented as average bars ± SEM and analysed using a one-way Anova test with Dunnett's post-hoc test, with significance denoted above relevant bars comparing that data to the control cells at the far left of the graph. *p<0.05, **p<0.01, ***p<0.001. n=3/4. **B)** ATP quantification from a CellTiter Glo assay in the HMC3 cells treated with 4-400 µg/mL 3 nm magnetite (MN) , for 1-day or 4-day treatment, compared to control cells. Data normalised to Bafilomycin A1 treated control cells and presented as average bars ± SD and analysed using a two-way Anova test with Dunnett's post-hoc test *p<0.05, **p<0.01. n=3. **C)** Visual appearance of SPION nanoparticles in concentrated stock solutions. Magnetite = MN and Maghemite = MH.

magnetite. The 4-day data was far more variable than the 1-day due to the difficulty of plating and growing cells consistently over longer time periods (**Figure 6-5A**).

The 4 µg/mL data for all SPION treatments at both incubation times matched closely to the values for each of the nanoparticles at 4 µg/mL minus PEG, taken as an indication PEG was not affecting the cell count when considered with the SPION treatment or without (UT control data) (**Figure 6-5A**). A dextran coated SPION, LRL, was included at a higher 1 mg/mL

concentration to compare toxicity to a highly biocompatible dextran coated nanoparticle. The LRL treatment did not significantly affect cell growth or proliferation at either time point in the cell counting experiments.

The CellTiter Glo reagent was used to quantify total ATP levels for groups of cells grown with three concentrations of 3 nm magnetite between 4-400 μg/mL, as a secondary estimation of cell survival/proliferation (**Figure 6-5B**). Due to the high cost of this reagent and time constraints this assay was only run with one representative nanoparticle treatment, choosing 3 nm magnetite as the most consistent treatment in the 1-day cell counts. After 1-day treatment none of the concentrations of 3 nm magnetite were significantly different to the relevant control cells. While after 4-day treatment both 400 μg/mL and 40 μg/mL of 3 nm magnetite had significantly reduced ATP levels compared to the control cells, with a 45% reduction and a 35% reduction, respectively.

6.3.3 Primary confirmation of particle uptake by HMC3 cells

Large 3 μm (3000 nm) fluorescent microspheres were used to investigate whether the HMC3 cell line is phagocytotic. As these particles are very large, they are unlikely to be engulfed by non-phagocytic forms of endocytosis. Fluorescent microsphere density per cell increased with the incubation time, reaching a peak by 30-60 minutes (**Figure 6-6**). The Baf-A1 treatment reduced the particle uptake to lower levels than the untreated cells.

Light microscopy can visualise larger aggregated magnetite and maghemite nanoparticles as dark particles against the lighter cells (**Figure 6-7**). The dark nanoparticles appear in association with the cells in all magnetite (3, 8 and 20 nm) and the maghemite (5 nm) treated cells. The magnetite SPIONs seem to aggregate into larger particles than the maghemite SPIONs. Most, but not all, of the SPION treated cells appear to be in association with SPIONs visible by light microscopy.

6.3.4 pH dependent release of iron ions from SPIONs

To compare the degradation of uncoated magnetite and maghemite, *in vitro*, cell free ferrozine assay were run with the different nanoparticles to compare their degradation between pH 3, 5 and 7 buffers (**Figure 6-8A-H**). Samples were incubated at 37°C

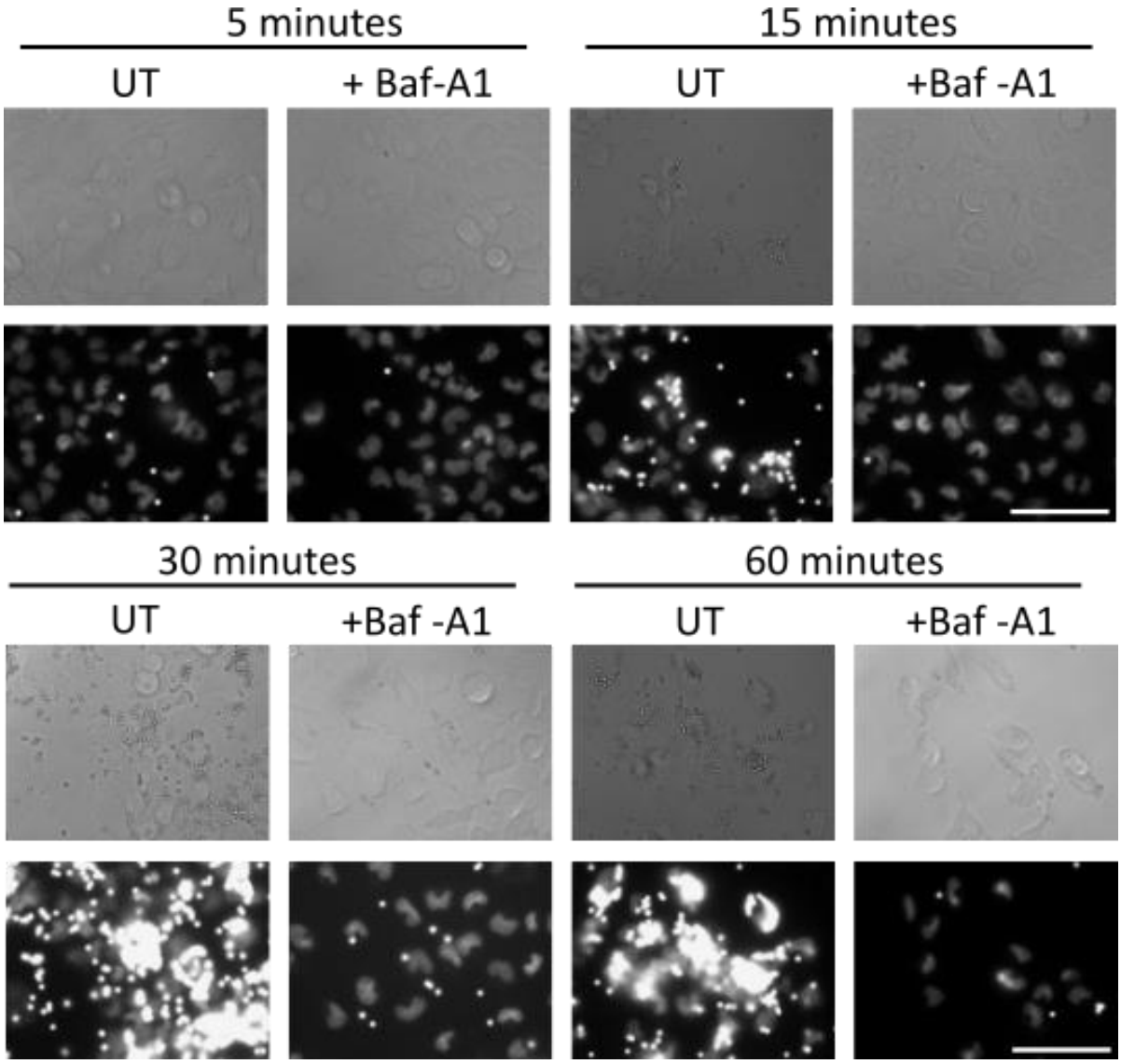

Figure 6-6: Association of HMC3 cells with fluorescent microspheres suggests the cells capable of phagocytosis within a 60 minute incubation. HMC3 cells were incubated with fluorescent ~3 µm microspheres for either 5, 15, 30 or 60 minutes (as labelled in figure), run consecutively to imaged together. For each incubation time, HMC3 cells either untreated (UT) or treated with 25 nM bafilomycin A-1 overnight (+Baf-A1) were exposed to fluorescent ~3 µm microspheres. For each treatment category the top row of images is by light microscopy with the same image below showing Hoechst nuclear stain (light grey) and the fluorescent microspheres (bright white). Scale bars = 40 µm.

(representing human body temperature) for 0, 2 and 24 hours to detect Fe^{2+}, and via addition of vitamin C, to also detect Fe^{3+}. The pattern of the free iron release was very similar between the three sizes of magnetite (**Figure 6-8A-F**). In the ferrozine assay between pH7 and pH3 buffers a significant Fe^{2+} release was detected after a 24-hour incubation for 3 nm magnetite SPIONs with a 19-fold increase (**Figure 6-8A**), for 8 nm magnetite SPIONs (**Figure 6-8C**) with a 33-fold increase and for 20 nm magnetite SPIONs with a 55-fold

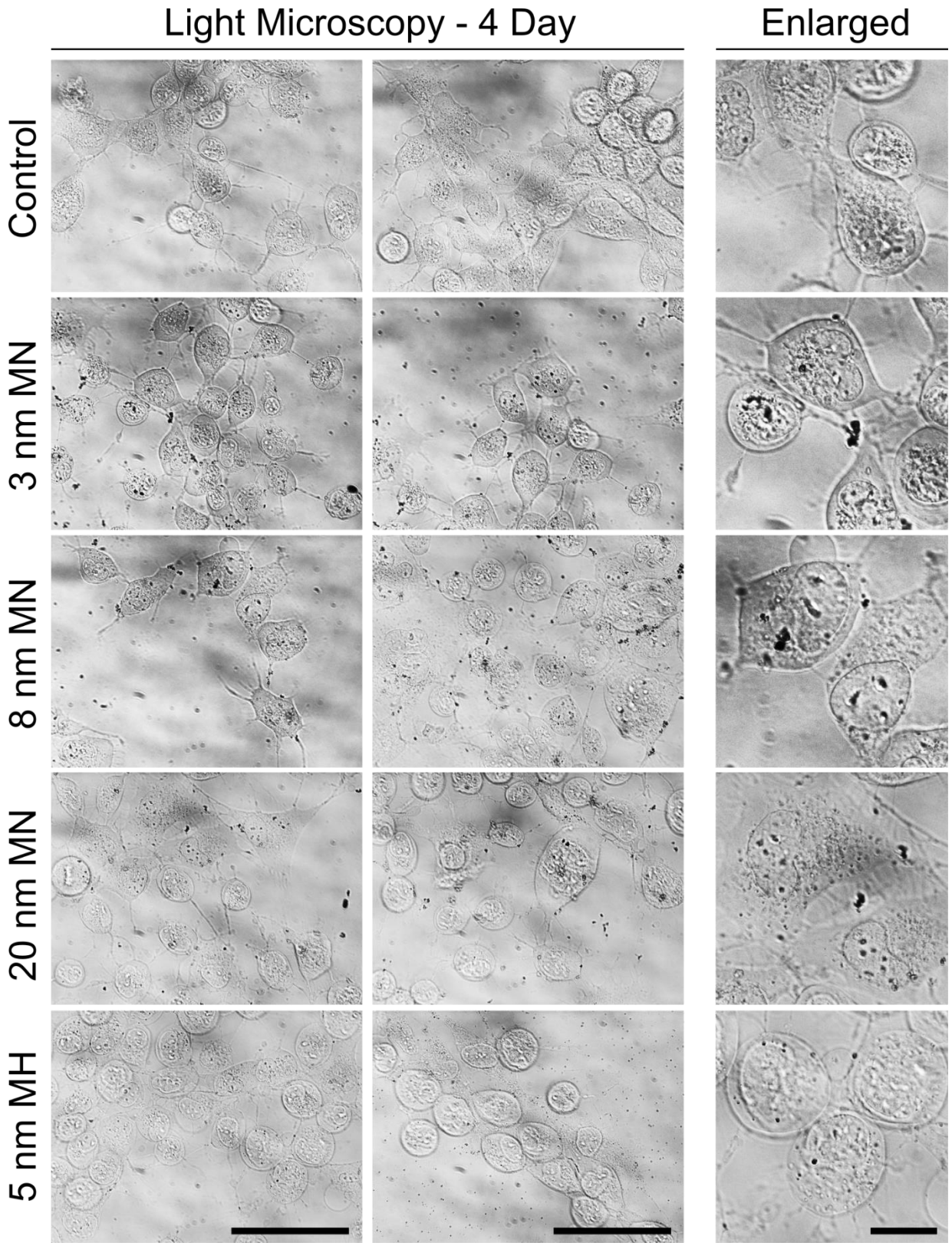

Figure 6-7: Agglomerated SPIONs are visible by light microscopy in the region of cells. Representative images (9 images/treatment) of HMC3 cell morphology (grey against background) by light microscopy with agglomerated SPIONs (black particles) visible in the regions of the cells after a 4-day treatment of 4 µg/mL SPIONs. Magnetite = MN and Maghemite = MH. Scale bars of full images = 40 µm and for enlarged sections scale bar = 10 µm. n=1.

increase (**Figure 6-8E**). All three magnetite treatments showed significant Fe^{2+} release only after 24-hour incubation, with the size of the fold increase between Fe^{2+} release at pH 7 and pH 3 having a positive correlation to increased average nanoparticle size. While 5 nm maghemite SPIONs showed no significant differences in Fe^{2+} release between any of the pH buffers at any of the measured incubation times (**Figure 6-8G**).

The 3 nm magnetite SPIONs also showed significantly increased Fe^{3+} production between pH buffers after a 24-hour incubation, with a 2.5-fold increase and a 2.95-fold increase between pH7 and pH3 or between pH5 and pH3 buffers, respectively (**Figure 6-8B**). The 8 nm magnetite SPIONs showed a similar pattern in Fe^{3+} after a 24-hour incubation with a significant 2.92-fold increase and 3.04-fold increase between pH7 and pH3 or between pH5 and pH3 buffers, respectively (**Figure 6-8D**). The 20 nm magnetite SPIONs revealed a significant 1.37-fold and a significant 0.97-fold increase , in Fe^{3+} between pH7 and pH3 or between pH5 and pH3 buffers, respectively, after a 24-hour incubation time (**Figure 6-8F**). While 5 nm maghemite also showed a difference in Fe^{3+} production between pH7 and pH3 buffer after a 24-hour incubation with a significant 1.13-fold increase. None of the treatments led to a significant difference in Fe^{2+} or Fe^{3+} between pH buffers at the initial 0-hour baseline reading or after the 2-hour incubation time. Only Fe^{3+} release was recorded for all of the magnetite nanoparticles at the physiological lysosomal pH5 compared to pH7, while no differences between pH5 and pH7 were recorded for the 5 nm maghemite.

Under *in vivo* conditions, the nanoparticles in cells would be surrounded by many proteins, which can form a coat, called the protein corona, around the nanoparticles that protects them from degradation. To determine to what degree this might be affecting the degradation of these nanoparticles, the 3 nm magnetite was pre-incubated with proteins. Pre-incubation of the 3 nm magnetite SPION solutions with bovine serum albumin (BSA) protein (at a concentration in final solution of 2 mg/mL) led to a reduction in colour change of the solution (indicative of decreased SPION degradation) at pH5, between BSA and non-BSA treated IONP samples (**Supplementary Figure 4-1**).

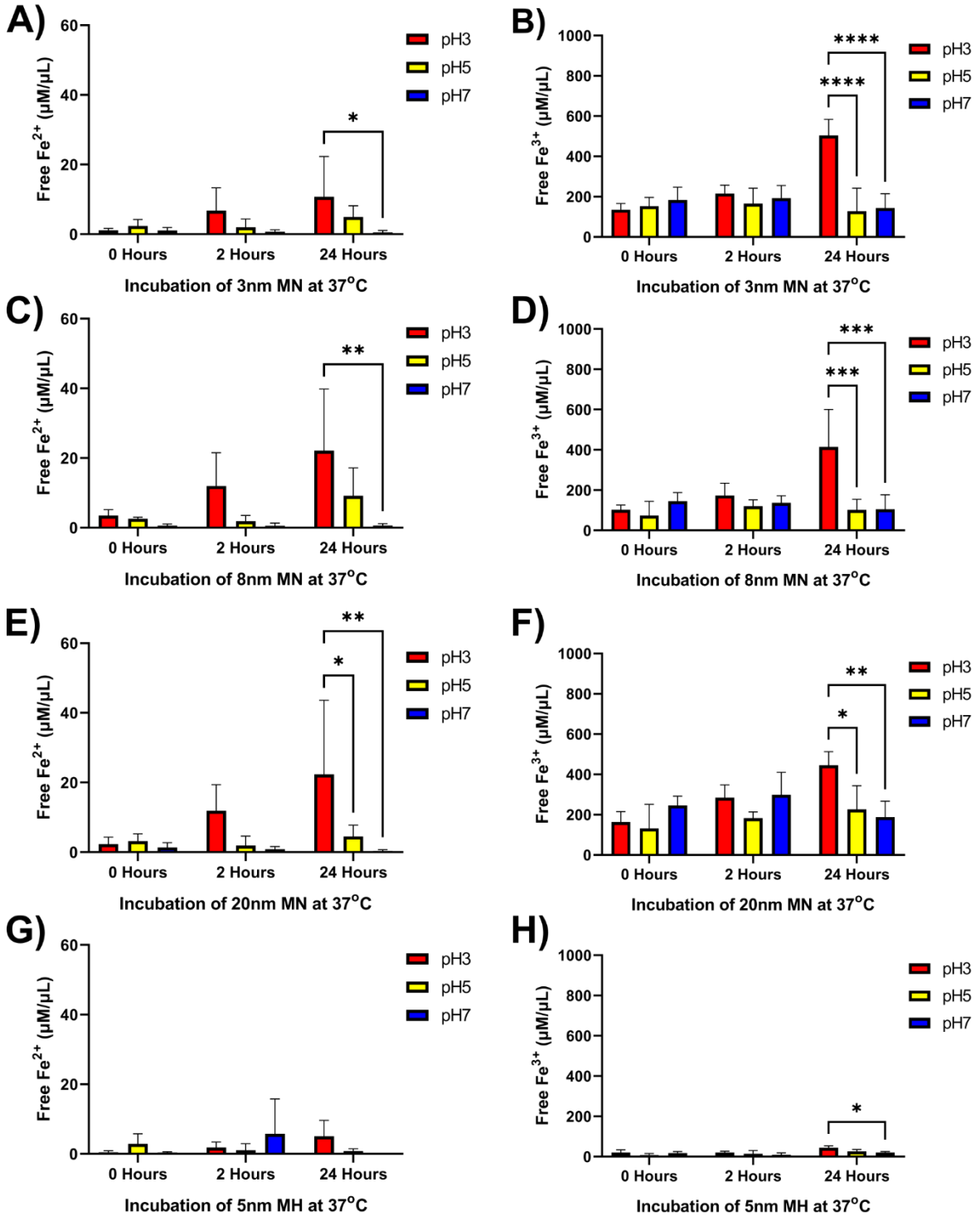

Figure 6-8: SPIONs can degrade at acidic pH to release Fe^{2+} or Fe^{3+}. A-H) Ferrozine assays on SPION solutions of magnetite (MN) or maghemite (MH) in pH3 (red), pH5 (yellow) pH7 (blue) citrate-phosphate buffer incubated at 37°C for 2 or 24 hours, or added at the start of the experiment (0 hours). Ferrozine assays were normalised to an iron standard for quantification of Fe^{2+} only or, by addition of vitamin C, total iron (Fe^{2+} and Fe^{3+}) through which Fe^{3+} was calculated. For **A)** 3 nm magnetite Fe^{2+} or **B)** 3 nm magnetite Fe^{3+}, **C)** 8 nm magnetite Fe^{2+} or **D)** 8 nm magnetite Fe^{3+}, **E)** 20 nm magnetite Fe^{2+} or **F)** 20 nm magnetite Fe^{3+} and **G)** 5 nm maghemite Fe^{2+} or **H)** 5 nm maghemite Fe^{3+}. Data presented as average bars ± SD and analysed using a two-way Anova test with Tukey's post-hoc test comparing within each incubation time grouping. *p<0.05, **p<0.01, ***p<0.001, ****p<0.0001. n=3.

6.3.5 Impacts of SPION treatment conditions on lysosomal phenotypes

When SPIONs are endocytosed, including phagocytosis, by the HMC3 cells they are mainly transported through the endolysosomal system to accumulate in the lysosome, where the acidic pH and degradative conditions may lead to breakdown of the nanoparticles, releasing free iron. If large quantities of free iron are released from nanoparticles, it can lead to the production of ROS through Fenton reactions, which can then damage the lysosome. Therefore, as lysosomes are likely to be the cellular region first affected by iron overload and subsequent ROS production, they are the first cellular organelle investigated here for potential defects.

To assess the if lysosomal toxicity from SPION treatment occurred in a time-dependent manner, LysoTracker staining was preformed across three incubation times, 5-hour, 1-day and 4-day treatments. The representative images of the LysoTracker data with 4 µg/mL SPIONs show that by 4-day incubation, a subset of the magnetite treated cells were very brightly stained by LysoTracker, indicative of lysosomal expansion (**Figure 6-9A**). However, there were also a subset of cells with very little staining, or none. Analysis of the SPION data (compared within each incubation period) showed only 5 nm maghemite after 1-day incubation was significantly different to control cells, with a 51% decrease (**Figure 6-9C**). The data can also be analysed by comparing the treatments across the different incubation times, which showed that both 3 nm magnetite and 8 nm magnetite treatments have significantly increased LysoTracker staining after 4-day incubation compared to after 5-hour incubation (**Figure 6-9D**). The LysoTracker green staining in the UT control cells (without PEG or PPB buffer) was not significantly different to the control cells (with PEG and PPB buffer) suggesting neither PEG nor PPB buffer affected this phenotype (**Figure 6-9B**). A positive (U18666A) and negative (Baf-A1) control were also included for reference and to confirm lysosomal staining.

To further assess the impact of the nanoparticles, despite the complexity of potential increases and decreases in LysoTracker staining between individual cells, the experiment was repeated with a 10 x higher (medium) SPION concentration of 40 µg/mL (**Figure 6-10A-D**). Visible in the representative images, the 4-day treatment showed an increased number of brightly stained cells with magnetite SPION treatments compared to control cells (**Figure 6-10A**). Again, the controls were all as expected with similar control and UT control cells and

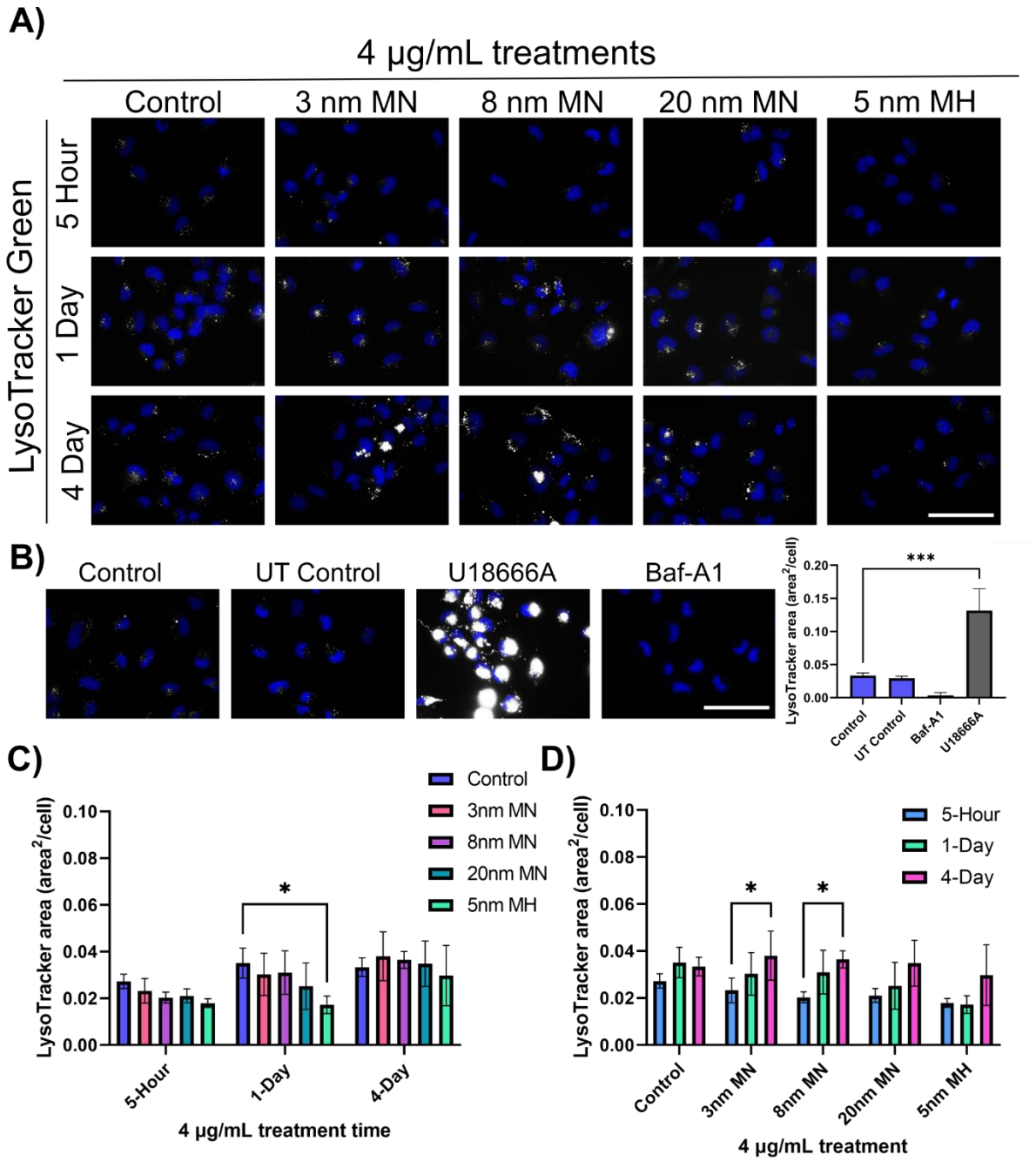

Figure 6-9: Effect of low concentration SPIONs on lysosomal area. Representative images of **A)** SPION treated HMC3 cells and **B)** control treatments (with area analysis) with **C-D)** quantitative area analysis (9 images/treatment/repeat) for LysoTracker Green (grey scale) in HMC3 cells after a 4-day treatment with 4 µg/mL SPIONs, counterstained for nuclei with Hoechst (blue). Magnetite = MN and Maghemite = MH. Control includes all treatment conditions except nanoparticles, while UT control is just cell culture medium. Scale bars = 40 µm. Data presented as average bars ± SD and analysed using a one-way Anova test with Dunnett's post-hoc test. *p<0.05, ***p<0.001. n=3.

working positive (U18666A) and negative (Baf-A1) controls (**Figure 6-10B**). With the higher SPION concentration there was still a significant decrease with 5 nm maghemite, with a 62%

decrease compared to control cells (**Figure 6-10C**). With the higher concentration of SPIONs, 3 nm magnetite and 8 nm magnetite treatment led to a significant increase in LysoTracker

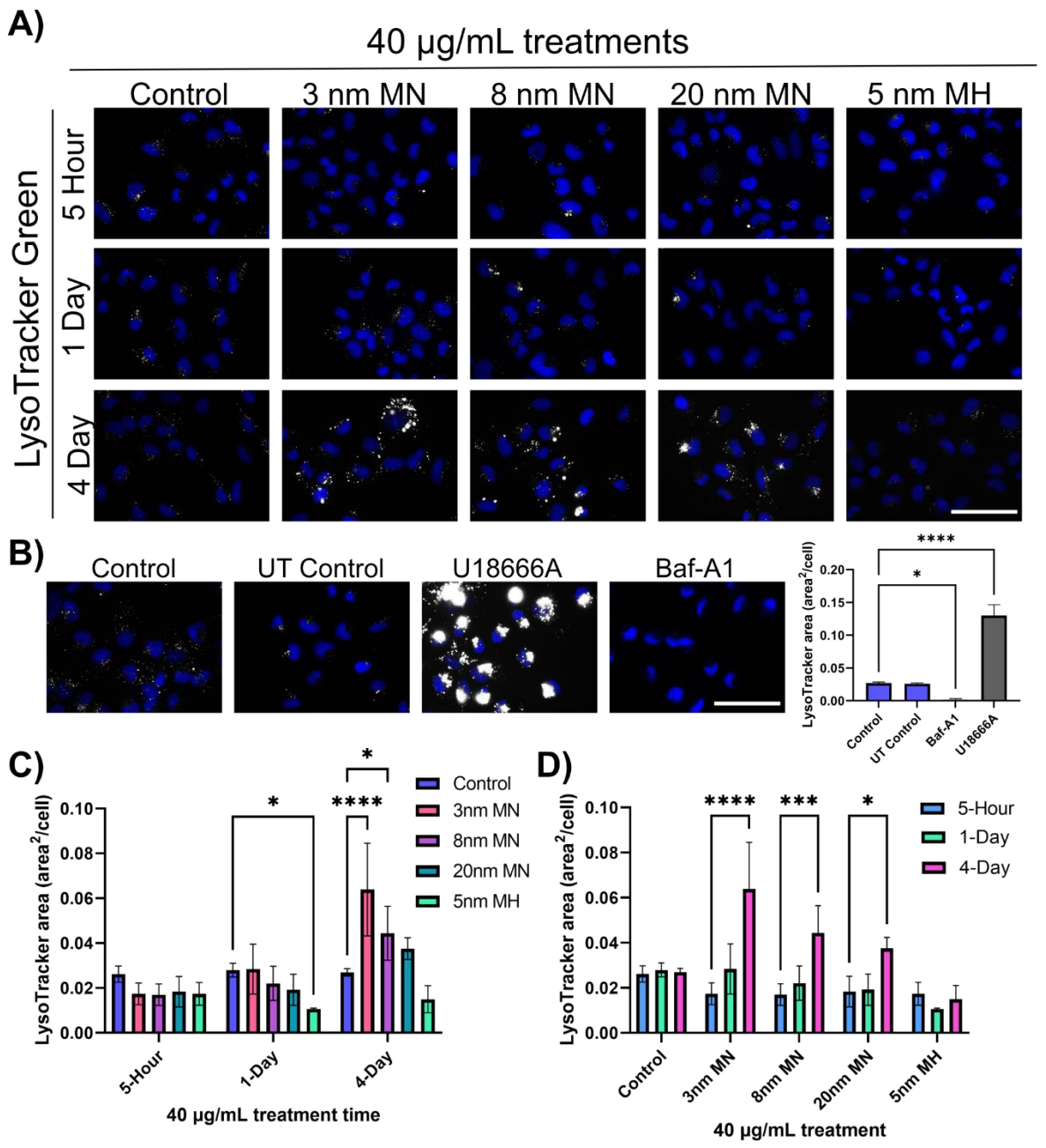

Figure 6-10: Effect of medium concentration SPIONs on lysosomal area. Representative images of **A)** SPION treated HMC3 cells and **B)** control treatments (with area analysis) with **C-D)** quantitative area analysis (9 images/treatment/repeat) for LysoTracker Green (grey scale) a probe for acidic vesicles (lysosomes and late endosomes) in HMC3 cells after a 4-day treatment with 40 µg/mL SPIONs, counterstained for nuclei with Hoechst (blue). Magnetite = MN and Maghemite = MH. Scale bars = 40 µm. Data presented as average bars ± SD and analysed using a one-way Anova test with Dunnett's post-hoc test. *p<0.05, ***p<0.001, ****p<0.0001. n=3.

staining area compared to control cells after the 4-day incubation, with 137% and 65% increases, respectively. By instead comparing the LysoTracker staining of the SPION treated cells at the different incubation times, all three magnetite SPION treatments (3 nm, 8 nm and 20 nm) led to a significant increase in staining area between 5-hour and 4-day incubation times (**Figure 6-10D**).

LysoTracker staining of HMC3 cell treated with a high SPION concentration of 400 μg/mL, was completed only once, and suggested a concentration dependent increase compared to the lower concentrations, with an even greater increase of 215% with 3 nm magnetite and 280% with 8 nm magnetite seen in 4-day treated cells compared to control cells (**Supplementary Figure 6-1 A-D**). The 20 nm magnetite treated cells appeared less healthy at 1-day treatment and did not survive to 4-days of treatment, hence no data on 20 nm magnetite was attained. With this experiment only preformed once, no statistical analysis could be performed.

LysoTracker loading appeared variable between cells, as the fluorescence is dependent on both lysosomal pH and lysosomal size. To indicate whether there might be increased variation in LysoTracker staining between cells within each treatment group, the content of brightly stained and dimly stained cells within each image was measured using average control cells as the baseline standard for normal fluorescence (**Supplementary Figure 6-2A-F**). The aim of this count was not as conclusive evidence of a change, but before further experiments could be run it could indicate to what degree these changes might be affecting the SPION treated cells compared to the controls. For both 4 μg/mL and 40 μg/mL treated HMC3, the count analysis supported an increase of mainly dim cells after 5-hour SPION treatments (**Supplementary Figure 6-2A and B**). After 1-day treatment, 5 nm maghemite treated cells still had significantly increased proportions of dim cells, while at the higher concentration of SPIONs, 20 nm magnetite also had a significantly increased dim cells, yet at the lower concentration for the magnetite treated cells there appeared to be a higher ratio of bright to dim cells, with 8 nm magnetite having a significantly increased proportion of bright cells compared to the control (**Supplementary Figure 6-2C and D**). By the 4-day treatments there was no significant difference in bright or dim cells compared to control cells for the lower SPION concentration of 4 μg/mL (**Supplementary Figure 6-2E and F**). Yet in the higher concentration of SPION treated cells (40 μg/mL) all three magnetite treatments

had a significantly greater proportion of bright cells, while the 5 nm maghemite still consistently had a significantly increased proportion of dim cells compared to the control, with 3 nm magnetite and 20 nm magnetite also having increased proportions of dim cells.

The Magic Red-cathepsin B probe was used to measure the activity of cathepsin B, a lysosomal cysteine protease, in live cells. Compared to control HMC3 cells, magic red staining was significantly increased only in 3 nm magnetite SPION-treated cells, with a 114% increase, much lower than the positive control U18666A, which led to a 511% increase (**Figure 6-11**).

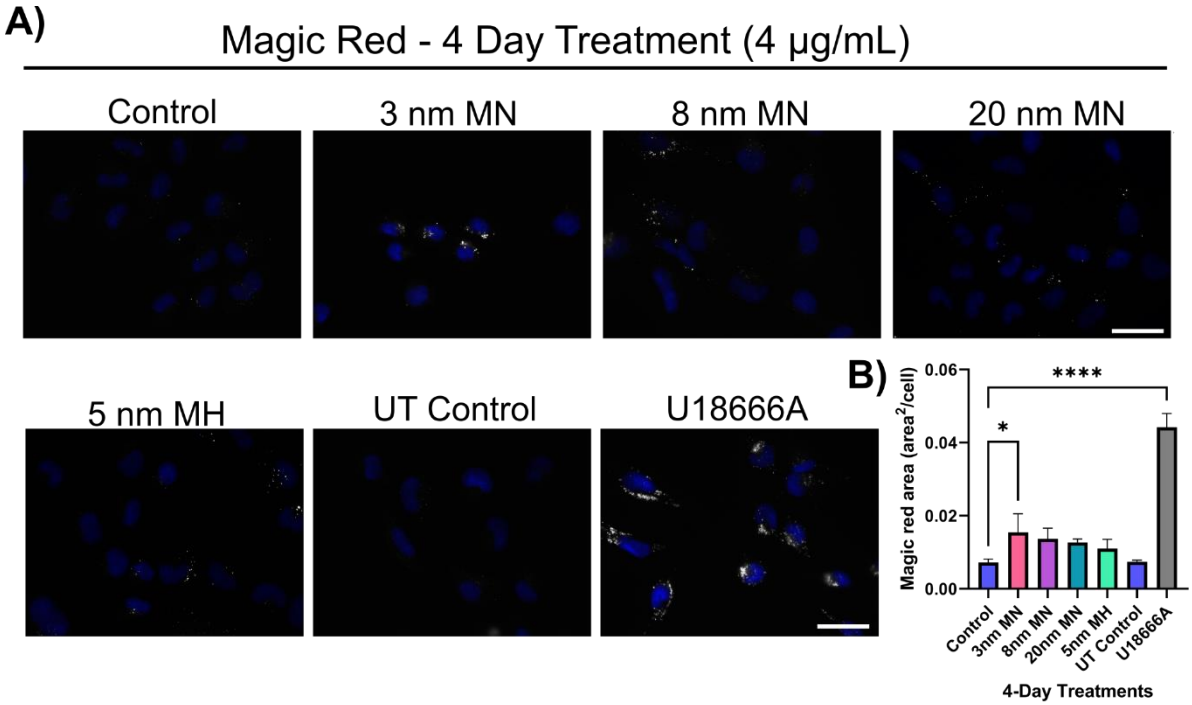

Figure 6-11: Impact of SPION treatment on Cathepsin B activity. A) Representative images and **B)** quantitative area analysis (9 images/treatment/repeat) of Magic red-cathepsin B (grey scale), staining for cathepsin B activity in HMC3 cells after a 4-day treatment with 4 µg/mL SPIONs, counterstained for nuclei with Hoechst (blue). Magnetite = MN and Maghemite = MH. Scale bars = 20 µm. Data presented as average bars ± SD and analysed using a one-way Anova test with Dunnett's post-hoc test. *p<0.05, ****p<0.0001. n=3.

2.2.1 Impact of SPION treatments on autophagy and production of ROS

As we had observed alterations in lysosomal area and lysosomal enzyme activity, we next tested the effect of SPIONS on autophagy, which is reliant on normal lysosomal function.

Autophagy can be measured by Cyto-ID staining for autophagic vacuoles. After a 4-day incubation with 4 µg/mL nanoparticles, only the 8 nm magnetite treatment showed significantly increased autophagy compared to control cells, with a 115% increase (**Figure 6-12A and B**). As an effect was only found with a single magnetite treatment, this phenotype was further investigated to identify if the effect was present and expanded by a 10x increased SPION concentration with a single experiment (**Supplementary Figure 6-3A and B**). The 40 µg/mL concentration suggested a large increase in cyto-ID staining for all the magnetite SPIONs at this higher concentration (n=1, not statistically analysed).

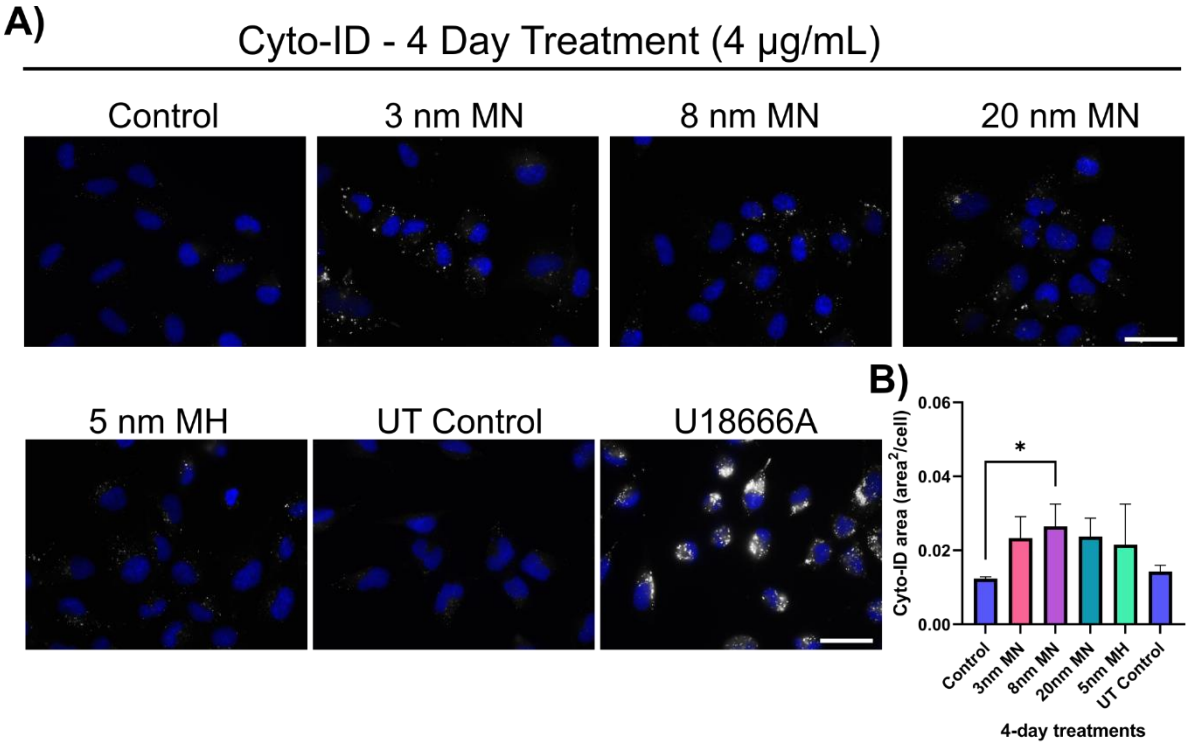

Figure 6-12: Impact of SPION treatment on autophagy. A) Representative images and **B)** quantitative area analysis (9 images/treatment/repeat) for Cyto-ID (grey scale) staining autophagic vesicles in HMC3 cells after a 4-day treatment with 4 µg/mL SPIONs, counterstained for nuclei with Hoechst (blue). Magnetite = MN and Maghemite = MH. Scale bars = 20 µm. Data presented as average bars ± SD and analysed using a one-way Anova test with Dunnett's post-hoc test. *p<0.05. n=3/4.

SO-ID stains for super oxide, a type of reactive oxygen species, but not for hydroxyl radicals (main species produced by Fenton reactions) as these are very short lived and highly reactive so more difficult to measure. No significant difference was seen in non-hydroxyl

superoxide (SO-ID) staining for any of the SPION treatments compared to control cells (**Figure 6-13A and B**).

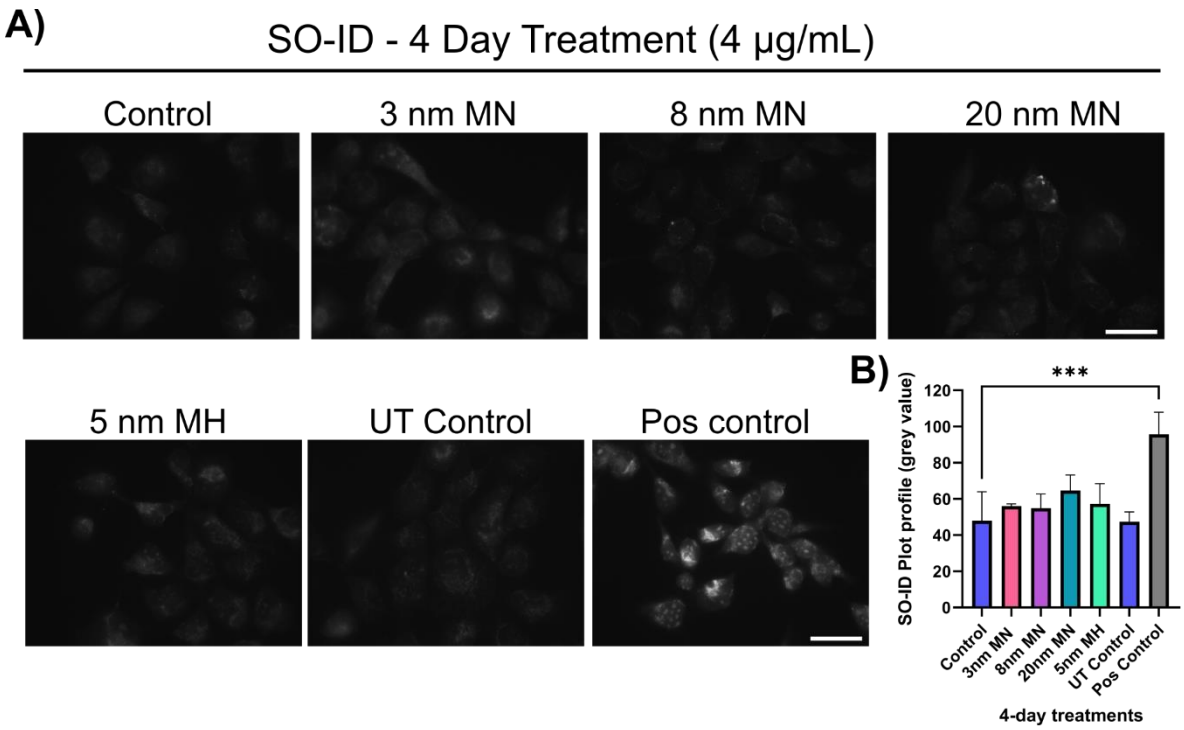

Figure 6-13: SPION treatment has no effect on super oxide production. SO-ID is a superoxide detection probe, that is unable to detect other reactive oxygen species such as hydroxyl radicals. **A)** Representative images and **B)** quantitative area analysis (6 images/treatment/repeat) for SO-ID (grey scale) staining superoxide in HMC3 cells after a 4-day treatment with SPIONs, along with a positive (Pos) control. Magnetite = MN and Maghemite = MH. Scale bars = 20 µm. Data presented as average bars ± SD and analysed using a one-way Anova test with Dunnett's post-hoc test. ***p<0.001. n=3.

6.4 Discussion

This chapter was able to successfully optimise treatment conditions for a human microglial based model of the superparamagnetic nanoparticles (SPIONs), magnetite and maghemite, and to identify changes in lysosomal-related phenotypes induced by the nanoparticle treatments.

6.4.1 Coated SPION characterisation

The SPIONs in this chapter were uncoated magnetite (Fe_3O_4) in three specified sizes according to the manufacturer, 3 nm, 8 nm and 20 nm average diameter and an uncoated maghemite (γ-Fe_2O_3) nanoparticle described as 5 nm average size. The TEM showed the nanoparticles displayed a strong tendency to aggregate forming larger particles, as had been visualised with their use in cell treatments (data not shown). The TEM was run on nanoparticles not dispersed by sonication and PEG as was included for cell treatments, suggesting particles may be more dispersed in the experiments than for the TEM images. However, even if initially dispersed, uncoated magnetite is known to have a strong tendency to reaggregate and sediment (Vikesland et al. 2016). The magnetite nanoparticles looked very similar in crystal structure to many used in existing literature (Kouassi et al. 2005; Wang et al. 2011a; Shundo et al. 2012), the same being true for the maghemite nanoparticles (Múzquiz-Ramos et al. 2015; Martín et al. 2016; Kuchma et al. 2017). All three sizes of magnetite nanoparticles appeared structurally similar to each other and to the maghemite nanoparticles, all with a crystalline morphology and hexagonal to octagonal shape. The average size of the nanoparticles by TEM were difficult to ascertain due to their aggregation, with no clearly visible difference in size between the 3, 8 and 20 nm magnetite nanoparticles. However, when sonicated and mixed with PEG, as was performed before cell treatments, this may breakdown some of the aggregates.

6.4.2 Optimising SPION concentration for HMC3 cell treatments

As the uncoated SPIONs from US research nanomaterials had not previously been used in the lab, first cell treatment concentrations were optimised. A concentration that could significantly reduce cell survival was considered suboptimal, as surviving cells are needed to assess phenotypes. Yet a concentration that is below the threshold to induce phenotypes

would also be less ideal for determining potential impacts of SPION treatments. An environmentally relevant dose may be too low for optimal cell exposure in these experiments, as it would likely take many years for disease-relevant exposure, for example sporadic Alzheimer's disease (for which SPION exposure may be a risk factor) normally develops after age 65. Instead, higher SPION concentrations were used to indicate affected phenotypes in a shorter treatment time, more efficient for this kind of early-stage project. Cell counting and ATP quantification experiments suggested that 4 μg/mL concentrations produced survival/proliferation rates that were not significantly different to control cells, while 40 μg/mL concentrations did significantly affect survival or proliferation of the treated HMC3 cells but not to an extent that affected data collection. These two concentrations were chosen for initial assessment of phenotypes.

Previous studies have found magnetite nanoparticles to have different cytotoxicity between cell types (Coccini et al. 2017) and for toxicity to be greater in microglia than in astrocytes or neurones (Petters et al. 2016). A study comparing astrocytoma (D384) and human neuroblastoma (SH-SY5Y) cells, found magnetite nanoparticles to be significantly affecting cell viability in the astrocytoma cells at 10 μg/mL after a 24-hour incubation and at 1 μg/mL after a 48-hour incubation and neuroblastoma cells at 10 μg/mL after a 48-hour incubation (Coccini et al. 2017). The magnetite nanoparticle cytotoxicity in this study that appeared between 40-400 μg/mL after 1-day incubation in HMC3 cells, suggests the HMC3 cells may be more robust against the nanoparticle treatments than these cancer cell lines. Other studies in microglial cells showed 6-hour exposure to a high 3 mM concentration of magnetite nanoparticles led to increased cell death and cytotoxicity (Petters et al. 2016),while 150 μM an 450 μM concentrations of IONPs have been shown to induce significant cytotoxicity in 4 and 6 hours, respectively (Luther et al. 2013). Although this indicates toxicity to high SPION concentrations occurs quickly in microglial cells, these two studies both used rodent microglia, which may have a different sensitivity to nanoparticles compared to human microglia.

The importance of using a human microglial line (HMC3) in this chapter, instead of more established microglial lines, such as those of rodent microglia is due to the wide number of differences now being identified between these cells in the two species, as was evaluated in Section 6.1.3. A cell line was chosen, instead of primary human microglial cells, as these are

difficult to obtain and grow consistently, necessitating extraction from a human brain either from aborted foetal tissue, biopsies from epileptic patients, normal tissue from brain tumour excisions, or post-mortem brain tissue. While IPSC cells would also have been a viable option, these take many months to differentiate into the desired role and to subsequently characterise and compare across differentiation groups. This would have considerably slowed the optimisation process.

6.4.3 Primary confirmation of particle uptake by HMC3 cells

In this study, the phagocytosis assay in the HMC3 cells suggested they may be capable of endocytosing large ~3 µm fluorescent particles in ~1 hour. Phagocytosis is the main pathway for uptake of large particles >0.5 µm, which may be slowly aided by large macropinocytic vesicles, while the 3 µm fluorescence spheres are too large for clathrin mediated endocytosis or caveolae-mediated endocytosis (Aderem and Underhill 1999).

The HMC3 cell line was initially described to have lower levels of phagocytosis after immortalisation compared to the primary culture (Janabi et al. 1995). The ability of these cells to phagocytose particles was then confirmed by demonstrating uptake of fluorescent amyloid-β (Hjorth et al. 2010; Hjorth et al. 2013). Phagocytic ability of the HMC3 has also been confirmed by measuring uptake of latex beads (Liu et al. 2013). Furthermore, HMC3 cells have been shown to display effective phagocytosis capacity for uptake of fluorescently labelled *Staphylococcus aures* bacteria, however, in that study the phagocytic activity of the cells was considered low when compared to peripheral dendritic cells (Etemad et al. 2012). The ability of the HMC3 cells in this study, to phagocytose particles is, therefore, in line with previous studies, especially considering that in this study the cells were not activated to a phagocytosis enhancing state before assaying. Pre-incubation with IFNγ alone or in combination with IL-1β has been shown to increase the phagocytic ability of the HMC3 cells and is likely in line with their activation state, with an M-2 state suggested to be optimal for their phagocytic activity (Ransohoff et al. 2015; Zhu et al. 2016). The ability of these cells to phagocytose is important for their accurate representation of both nanoparticle uptake and for modelling changes in Alzheimer's disease.

A previous study of iron oxide nanoparticle treatment across three different types of brain cells, suggested uptake and lysosomal localisation of the nanoparticles occurred more

quickly (within 6 hours) in microglial cells, than in astrocytes or neurones (Petters et al. 2016). While a 24-hour incubation led to lysosomal localisation in the microglia and astrocytes, but still not in the neurones. The timing of lysosomal localisation with the nanoparticles coincided with increased ROS staining in these cell lines, suggesting more rapid uptake/transport to the lysosomes may be a major factor in why the nanoparticles had greater toxicity in the microglia compared to astrocytes and neurones in this study. Phagocytic ability in microglial cells would lead to faster nanoparticle uptake than in cell lines relying on low levels of macropinocytosis or random uptake in other endocytic vesicles. Therefore, the ability of the HMC3 cells to phagocytose is important for modelling microglial responses to nanoparticle treatments compared to other brain cells.

Light microscopy indicated it is possible to identify large, aggregated magnetite and maghemite particles in the region of cells by contrast of the brown particles against the grey background of the cell. Light microscopy may also be useful in future experiments for determining co-localisation of large aggregates with probes or phenotypes when staining the cells. The ability to identify SPION aggregates by light microscopy led to the planning of using an IncuCyte imaging system to complete live cell imaging of a section of cells, which may have been able to capture uptake and internalisation of larger particles by the cells. While this was unable to be completed in the project, using this imaging system in the future would provide an alternative way to ascertain the mechanisms of particle uptake, along with trafficking and localisation of particles within the live cells. This may also provide valuable information on whether nanoparticle exposure or uptake leads to changes in cellular morphology and if this is related to cellular localisation. While localisation and SPION uptake data could be also achieved by fluorescence microscopy, addition of a fluorophore may change SPION behaviour, charge and size and can be difficult to attach to uncoated particles.

The ideal experiment planned to detect nanoparticle uptake into the HMC3 cells and determine a lysosomal localisation was by electron microscopy. The cell samples were prepped for electron microscopy, but it could not be completed in the time frame for this thesis. This will also determine particle size during uptake to determine if the nanoparticles are more dispersed and less aggregated when endocytosed into cells.

6.4.4 pH dependent release of iron ions from SPIONs

The ferrozine assays suggested that release of free iron from the SPIONs is pH dependent, with the greatest release at lower pH. For both Fe^{2+} and Fe^{3+}, significantly different ion release between different pH only occurred after 24-hour incubation, suggesting that SPION breakdown was not instantaneous or very fast (2-hour incubation). For Fe^{2+} detection in the magnetite SPIONs in general there was greater release at pH3, reduced release at pH5 and substantially lower, near baseline, release at pH7. There was significant release of Fe^{3+} between pH3 and pH7 for all the magnetite nanoparticles. Only significant Fe^{3+} release was detected in the 5 nm maghemite SPION between pH3 and pH7 after 24-hours, although levels were much lower than compared to the magnetite SPIONs. A previous study has also shown pH dependent Fe^{3+} release from maghemite nanoparticles at pH4.5 compared to pH7 at 24-hours, although these were dextran coated and showed significantly faster Fe^{3+} release after 48 hours of incubation, likely due to the majority of the dextran coat having been degraded by this time point (Singh et al. 2012).

The release of purely Fe^{3+} by maghemite is due to the positioning of Fe^{3+} in both its tetrahedral and octahedral sites, making it essentially Fe^{2+} deficient (Greaves 1983). While magnetite having Fe^{3+} in its octahedral sites, has a mixture of Fe^{2+} and Fe^{3+} in its tetrahedral sites, correlating with the ferrozine data in this chapter seeing both significant Fe^{2+} and Fe^{3+} release at 24-hours incubation with all three magnetite nanoparticles. The reduced degradation of the maghemite compared to the magnetite also follows previous literature, with one study showing oxidisation of magnetite to maghemite corresponded to increased stability against low pH related degradation (Barrow et al. 2018). Relating to the lysosomal environment in cells with a pH~5, no significant differences were noted compared to at pH7, suggesting that at lysosomal pH there would be relatively low release of either free iron component. A longer incubation period for the SPIONs in the pH buffers before running the ferrozine assays, may indicate if degradation at pH5 starts occurring over longer incubations time. Although how this relates to the degradation in cells needs to be further examined with iron-dependent staining, such as Phen green and FehRoNox.

Pertinent to treatment of microglia with SPIONs is the added complication that certain activation states of microglia have been linked to a drop in lysosomal pH (Majumdar et al. 2007; Majumdar et al. 2011). While that may mean resting (surveying) microglia have a

higher lysosomal pH and are more resilient to acidic SPION breakdown, activated microglia which are linked to increased phagocytosis may have a decreased lysosomal acidity, where nanoparticles now breakdown more readily. As microglia are known to be activated in Alzheimer's disease (Hamelin et al. 2016) and reduced microglial lysosomal pH linked to increased degradation of amyloid-β (Majumdar et al. 2007), a concomitant insult of increased magnetite degradation, due to environmentally-derived magnetite particles in the brain, could lead to lysosomal damage in these activated microglia which would in turn impact amyloid-β degradation.

6.4.5 Impacts of SPION treatment conditions on lysosomal phenotypes

The microglia showed a complex relationship in terms of the acidified (<pH5.5) lysosomal area after exposure to the magnetite SPIONs, with suggestions that some cells have increased LysoTracker staining while in others it appears decreased. At the lower 4 μg/mL concentration there was no overall change detected in LysoTracker area between the magnetite SPION treatments and controls, according to the area analysis. The only significant difference between controls and SPION treatments at each time point, was for maghemite after 1-day incubation. Although some of the particles did show significant changes between their 5-hour and 4-day LysoTracker area values. The experiment was repeated with a 10x increased SPION concentration (40 μg/mL), which exacerbated the effects and made them more pronounced. This did lead to significant increases in LysoTracker staining for 3 nm magnetite and 8 nm magnetite after 4-day incubation, suggesting a dose-dependent phenotype exists after 4-day incubation. In support of this, one repeat of the experiment with a nanoparticle dose again ten times greater (400 μg/mL) also suggested this may lead to a further increase in the LysoTracker staining. The idea of competing oppositional changes in LysoTracker staining occurring between the microglial cells treated with SPIONs in this chapter was supported by evidence from counting staining intensity of cells. As discussed in the previous chapter, the ability of iron oxide nanoparticles to damage lysosomes has been previously documented (Ferrati et al. 2014; Levada et al. 2020). A dose-dependent increase in macrophage/microglia specific lysosomal membrane protein ectodermal dysplasia (ED)-1, has been previously identified in lipopolysaccharide - stimulated microglia treated with iron oxide nanoparticles, suggesting an increased lysosomal area in the nanoparticle treated cells (Wu et al. 2013a). This experiment does

differ to the present study in that the microglia had been purposely activated prior to nanoparticle treatment, which may change the cells behaviour, and ED-1 is not sensitive to deacidification as is LysoTracker. However, the increased lysosomal area seen in both studies is comparable. There is also evidence of changes in LysoTracker staining after treatment of non-activated microglial cells with BP-IONP, although this was not quantified in the experiments as it was mainly being used to demonstrate co-localisation of the nanoparticles with the lysosomes (Luther et al. 2013). Although these two studies used primary microglia from mice and rats, respectively, it does indicate that increased LysoTracker staining after IONP or SPION treatment may be specific to certain cell types, to immune cells, or to microglia. Another method to detect whether lysosomal expansion is being triggered in a subset of cells, would be to measure transcription factor EB (TFEB) nuclear translocation. TFEB is the master regulator of the lysosome-autophagy system and nuclear translocation of TFEB encourages expression of lysosomal and autophagic related genes acting as a trigger of lysosomal biogenesis and autophagy (Settembre et al. 2011).

In both experiments there was no change in lysosomal area after 5-hour SPION incubation, likely as this is too quick for nanoparticles to have been endocytosed, reach lysosomes, degrade and induce ROS production that can damage lysosomes. After 1-day incubation, only the maghemite SPIONs caused a significant change compared to the control, with decreased lysosomal area. The existence of this phenotype at both 4 μg/mL and 40 μg/mL concentrations acting as a confirmation of this effect, however, in both experiments this phenotype has disappeared by 4-day incubation, possibly suggesting the cells' ability to counteract this change over longer periods of time.

In this chapter, cathepsin B activity (magic red staining) was found to be significantly increased after one of the three magnetite treatments (3 nm magnetite) at the 4-day treatment incubation time with a low (4 μg/mL) SPION concentration. This could be due to lysosomal expansion suggested in a sub-set of the cells, despite the lack of a significant increase in lysosomal area for this concentration and incubation time. A decrease in LysoTracker staining in a sub-set of the cells, does not necessarily indicate that lysosomes have been destroyed, or less produced, it also could be a sign of lysosomal deacidification, as LysoTracker Green only fluoresces in an acidic (<pH5.4) environment. Potentially in partially deacidified lysosomes Cathepsin B could still be active while LysoTracker is not

retained and fluorescent. A further experiment suggested that in the HMC3 cell line cathepsin B has an activity range between pH 4-7, with an optimal pH5.5-6.5 (**Figure 6-14**). This does contrast to published data on cathepsin B pH optima, which has suggested a maximal activity at pH 5.0 and a steep decrease in activity down to pH 7, though it does need to be considered that this was calculated for a purified cathepsin B from human liver, and it is likely the enzyme may differ between cell types (Almeida et al. 2001). It certainly appears that in the HMC3 cells, cathepsin B has a wide pH range and activity does not drop as significantly at higher pH, which may explain why cathepsin B activity could be high while LysoTracker area does not appear increased. An increase in cathepsin B activity in the SPION treated microglia is also in contrast to data from IONP-treated microglial cells stimulated with lipopolysaccharide, in which cathepsin B activity was seen to significantly decrease with increased nanoparticle concentration, however, the contrast of induced activation state change by lipopolysaccharide in these cells, may change their response compared to non-activated microglial cells (Wu et al. 2013a).

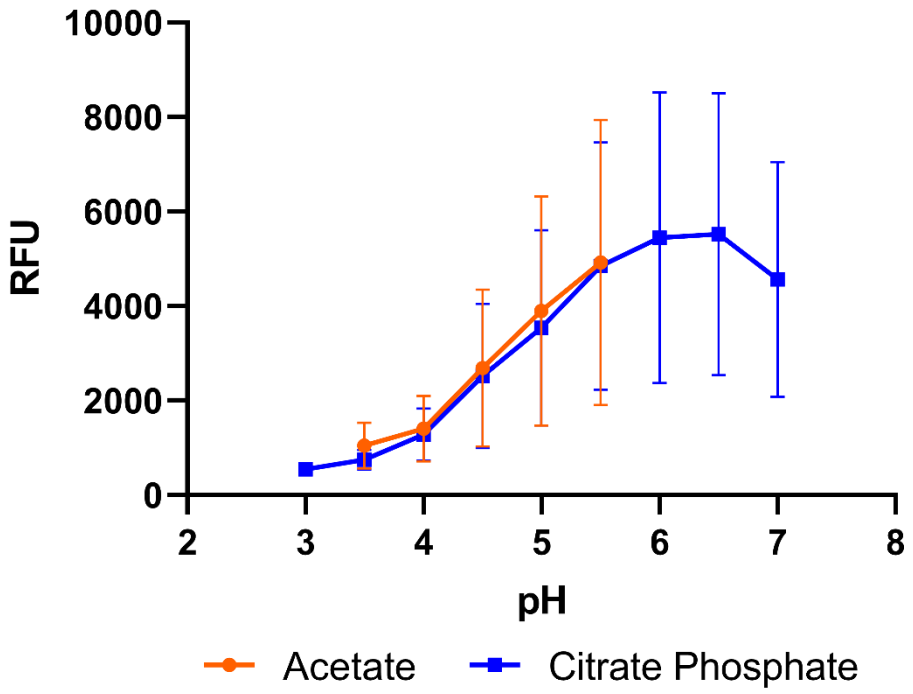

Figure 6-14: Cathepsin B activity in HMC3 cells across a range of pH. Cathepsin B activity in relative fluorescent units (RFU) from plate assays of HMC3 cell homogenate, measured every 0.5 pH units from pH 3 to pH 7 in citrate-phosphate buffer (blue) and from pH 3.5 to pH 5.5 in acetate buffer (orange).

Several papers have suggested that exposure to IONPs treatments does not activate microglial cells (Pickard and Chari 2010; Luther et al. 2013). However, for the investigation of the link between increased brain magnetite, likely from environmental sources, and Alzheimer's disease, it may be of use to also preform experiments on phenotyping human microglial cells response to nanoparticle treatment after activating the cells with exposure to amyloid-β or in a genetic or drug cellular model of the disease. To have an account of phenotypic cellular changes after nanoparticle treatment in a human microglial cell line and comparison of these same phenotypes after addition of further Alzheimer's related insults, could be important for informing if the toxicity of the nanoparticles changes under disease conditions. Once a model of the SPION induced phenotypic changes has been completed in these cells these may then be the next logical steps, concentrating on phenotypes in the cellular pathways found to be most affected.

6.4.6 Impact of SPION treatments on autophagy and production of ROS

Autophagy was not significantly raised at the lower 4 μg/mL SPION concentration after 4-day incubation. As values for the magnetite SPIONs were all consistently higher than controls in all repeats, this prompted one repeat with the 10 times concentration (40 μg/mL), which suggested autophagy may be greater in magnetite treated cells than in controls and suggests this is a phenotype worth further exploration and completion with the higher concentration to 3 repeats. Increased autophagy has previously been identified as a phenotype of iron oxide nanoparticle treatment (Khan et al. 2012; Park et al. 2014a; Zhang et al. 2016a; Wu et al. 2017b). SPIONs have been shown to induce autophagy in a mouse monocyte macrophage cell line through an inflammatory response (Jin et al. 2019). Yet, there is very little data on autophagy in IONP treated microglial cells.

Two previous studies have strongly suggested an increase in ROS production in iron oxide nanoparticle treated microglial cells (Wang et al. 2011b; Petters et al. 2016). Maghemite and hematite have been shown to induce ROS production in a mouse microglial cell line (Wang et al. 2011b). While in primary rat brain cells, cellular ROS production was increased after 6-hour iron oxide nanoparticle treatment in microglia, but not in astrocytes or neurones, a phenotype which was ameliorated by treatment with Bafilomcyin-A1 which causes a strong deacidification phenotype in lysosomes (Petters et al. 2016). In this chapter

no increase in superoxide staining was detected in the microglia; however, this stain was unable to detect hydroxyl radicals, which are the main product of Fenton reactions, most likely to be the source of iron-induced ROS. A total ROS stain, able to detect hydroxyl radicals, should be of primary examination in continuation of this work, as ROS production has been indicated as a primary mechanism of cytotoxicity in SPION treated cells (Wang et al. 2011b; Khan et al. 2012; Petters et al. 2016). Another method for determining the extent of dysregulated ROS production in the microglial cells after SPION treatment will be to measure lipid peroxidation, which can be achieved with DPPP staining, and membrane lysosomal membrane integrity with acridine orange staining, as were both preformed on cells in Chapter 4 of this thesis.

The key role of oxidative stress in the development of Alzheimer's disease, particularly in terms of microglial cells, has also been investigated in numerous studies and summarised in review papers on the topic (Chauhan and Chauhan 2006; Huang et al. 2016). Therefore, once a nanoparticle treatment model has been established in microglial cells, the next step will be to combine this model with Alzheimer's models, to see if this extra stressor has increased impact in an Alzheimer's model, increases Alzheimer's related phenotypes or has different phenotypes to the non-diseased model. This research has the potential to lead to range of projects, from experiments initially in human microglial cell lines such as HMC3, to human iPSC cells which may represent primary cells more closely, to a mixed cellular model with neurones and other glial cells and post-mortem brain tissue and also to various in *vivo* models.

7 General Discussion

7.1 Overview of the project

This project has succeeded in achieving its main aim; to develop cellular and *in vivo* zebrafish models of iron oxide nanoparticle (IONP) treatment and identify affected pathways, phenotypes and behavioural responses, identifying which nanoparticles are associated with greater toxicity and which are more biocompatible.

IONPs are being developed as tools for bioscience-based research, such as the magnetic lysosomal extraction method, and for these kinds of applications it is important to use IONPs with low cytotoxicity and high biocompatibility. Exposure of people to magnetite nanoparticles is also likely environmentally, as they can form a major component of traffic-related air pollution (Mitchell and Maher 2009). Exposure to IONPs may also occur in a health care setting, as a few types of IONPs have been used as MRI contrast agents (Nikzamir et al. 2021), and are being developed for new treatments and therapies, mainly as drug carriers or hypothermic agents in cancer therapy (Hernández-Hernández et al. 2020). Yet research has not yet been able to fully elucidate the range of impacts IONPs may cause to human health, mostly due to the wide variation between the nanoparticles and conditions used in the different studies and the subsequent variation in toxicity and response. This study has succeeded in comparing various IONPs and investigating the effects coating, size, composition, and structure can have on nanoparticle toxicity and behaviour.

7.1.1 Summary of Chapter 3: Investigating the impact of HEPES buffer on lysosomal phenotypes.

Growing CHO H1 cells in HEPES buffer, was found to affect lysosomal phenotypes in a concentration-dependent manner. Adding HEPES buffer at 50-100 mM was found to significantly increase lysosomal area in CHO H1 cells, with lower concentrations affecting lysosomal area in stressed (overconfluent) cells. By testing a range of buffers, it was found that PIPES caused an even greater increase in lysosomal area. These experiments demonstrated the importance of choosing a suitable cell buffer for an experiment, considering phenotypes to be analysed, buffer concentration and the effect when combined with additional stressors. The results of this chapter were published (Cook et al. 2020a) and

then used to determine optimal buffers use during nanoparticle treatments in the subsequent chapters.

7.1.2 Summary of Chapter 4: Comparing cellular toxicity of dextran coated iron oxide nanoparticles.

The second data chapter focussed on identifying groups of phenotypes or cellular pathways affected by 1 mg/mL IONP treatments (24-hour pulse:24-hour chase), using three dextran coated nanoparticles of differing sizes, compositions and structures. Dextran coated LRL nanoparticles were found to have low cytotoxicity, causing no nanoparticle-induced defects detected in this study. The CC and ID nanoparticles both suggested IONP treatment can reduce lysosomal area, cause lipid peroxidation and produce mitochondrial defects in CHO H1 cells. This data suggests that when these nanoparticles are internalised by the cell, they can break down to release ROS, affecting not only the endolysosomal system, but also the mitochondria. While the CC nanoparticle alone led to an increased autophagy phenotype, likely associated with an alteration in lysosomal Ca^{2+} levels, rather than mitochondrial-related defects. These experiments showed LRL to be a highly biocompatible nanoparticle, encouraging its previous selection for use in a magnetic lysosomal extraction protocol.

7.1.3 Summary of Chapter 5: Investigating toxicity of LRL and ID nanoparticles in an *in vivo* developmental zebrafish model.

The third data chapter utilised two of the same dextran coated IONPs as in the previous chapter (LRL and ID) to set-up a nanoparticle treated zebrafish development model. Identifying the impact of nanoparticles *in vivo* is an important next step to investigating their effects in a cellular model. ID nanoparticle treatment of the embryos/larvae led to developmental delay in spontaneous coiling, a potential heart rate defect and movement defects. While no defects were detected in embryo/larvae treated with the LRL nanoparticles, again validating LRL as a strongly biocompatible nanoparticle and supporting development of a magnetic lysosomal extraction method from zebrafish larvae utilising LRL nanoparticles.

7.1.4 Summary of Chapter 6: Comparison of the toxicity of magnetite and maghemite nanoparticles in a human microglial cell line.

In the final and fourth data chapter, the impact of non-dextran coated nanoparticles of either magnetite or maghemite on a human microglial cell line was investigated. As magnetite nanoparticles linked to traffic-related air pollution have been associated as a potential environmental risk factor for Alzheimer's disease, the effect these nanoparticles on microglia, the brains immune cells, was investigated. This chapter identified differences between magnetite and maghemite nanoparticles in free iron release and dose dependent changes in lysosomal area, with potential changes in cathepsin B activity and autophagy after magnetite nanoparticle treatments.

7.2 Importance of buffers

In this study it was clear that HEPES had an impact on cell health when an additional 10 mM concentration was added to the cell culture medium for the experiment as well as growing the cells in HEPES containing cell culture medium, as this led to increased cell death in ID treated cells (Chapter 3). Yet, this cell reduced survival phenotype in HEPES treated cells only occurred in the presence of the nanoparticle treatment as an additional stressor. In light of the research by Tol et al. (2018), showing how high HEPES concentrations can cause lysosomal expansion in cultured RAW macrophages, this thesis went on to show how HEPES can also affect lysosomal area in a non-phagocytic cell line, CHO H1 cells. As well as affecting lysosomal area, addition of HEPES buffer to cells has been shown to cause concentration dependent effects on magnesium biodegradation, increased phototoxicity, ability to block Cl^- channels in some cell lines and increased ATP production (Zigler et al. 1985; Yamamoto and Suzuki 1987; Kirsch et al. 1998; Luo et al. 2010; Kannan et al. 2017). The effects seen with HEPES are also possible with other zwitterionic buffers, as many share similar structural components. Indeed, this thesis shows PIPES buffer is likely to have a similar and likely more severe impact on lysosomal area than HEPES buffer.

In this study, based on the results in chapter 3 of HEPES buffer effects, a low 10 mM concentration continued to be added during nanoparticle treatments in chapter 4, while using HEPES free culture medium. The nanoparticle treatment can affect medium pH, which can in turn be detrimental to the cells, making buffer use in this period desirable, but with

this lower concentration being below phenotypic levels. In light of the impact of HEPES, especially since it appears to be more detrimental in a phagocytic cell line (Tol et al. 2018) than in the non-phagocytic CHO H1 (chapter 2), an alternative buffer was chosen for use in the phagocytic human microglial cell line used in chapter 6 of this study. Based on the results of the buffer comparisons in Chapter 3, potassium phosphate buffer (PPB) was chosen for use in these cells during nanoparticle treatment instead. Again, a low 10 mM concentration was selected, and controls added to experiments for buffer related effects as longer (up to 4-day) incubation times were used with no chase period, making the risk of buffer related impacts greater. However, in none of the experiments were the phenotypes from the non-buffer treated cells found to be significantly different to the buffer treated control cells. This further suggests that a low concentration of potassium phosphate buffer may be a favourable cell culture buffer when considering endolysosomal-related phenotypes in live cell culture experiments.

7.3 Relevance of nanoparticle structure

The range of nanoparticles used in this thesis varied in structure and these seemed linked to their cellular and lysosomal toxicity (**Figure 7-1**). The similarity of structure between the LRL and CC nanoparticles in Chapter 4, both of which have a magnetite: maghemite mixed core and 40 kDa dextran coat, did not correlate to their behaviour in the cell. The dextran coat can protect the nanoparticles from degradation acting as a barrier between the iron core and external environment and so reduce production of free iron and reactive oxygen species. With the LRL nanoparticles this appeared to be the case, yet with the CC nanoparticles fairly high levels of iron release and phenotypic cellular damage was detected.

The ID nanoparticles with a dextran core were different, having a high level of detected iron release in live cells and being the treatment with the strongest effect on lysosomal area. As a dextran core cannot act as a physical barrier it is likely to have less impact on iron degradation in the lysosome leading to increased iron release. Yet the CC and ID nanoparticles had more similar phenotypic effects to each other and greater cytotoxicity than the LRL nanoparticles, suggesting the position of dextran in the nanoparticle structure may not be the most important factor in dextran coated nanoparticle toxicity. A previous study on anaemia treatments, comparing an iron dextran nanoparticle (similar to ID) to a

magnetite SPION coated with a semi-synthetic dextran derivative, polyglucose sorbitol carboxy-methylether (similar structure to LRL and CC), suggested these two nanoparticles also showed similar toxicity phenotypes despite their oppositional core or coating carbohydrate structures (Toblli et al. 2011). The differences in cellular toxicity between LRL and CC nanoparticles

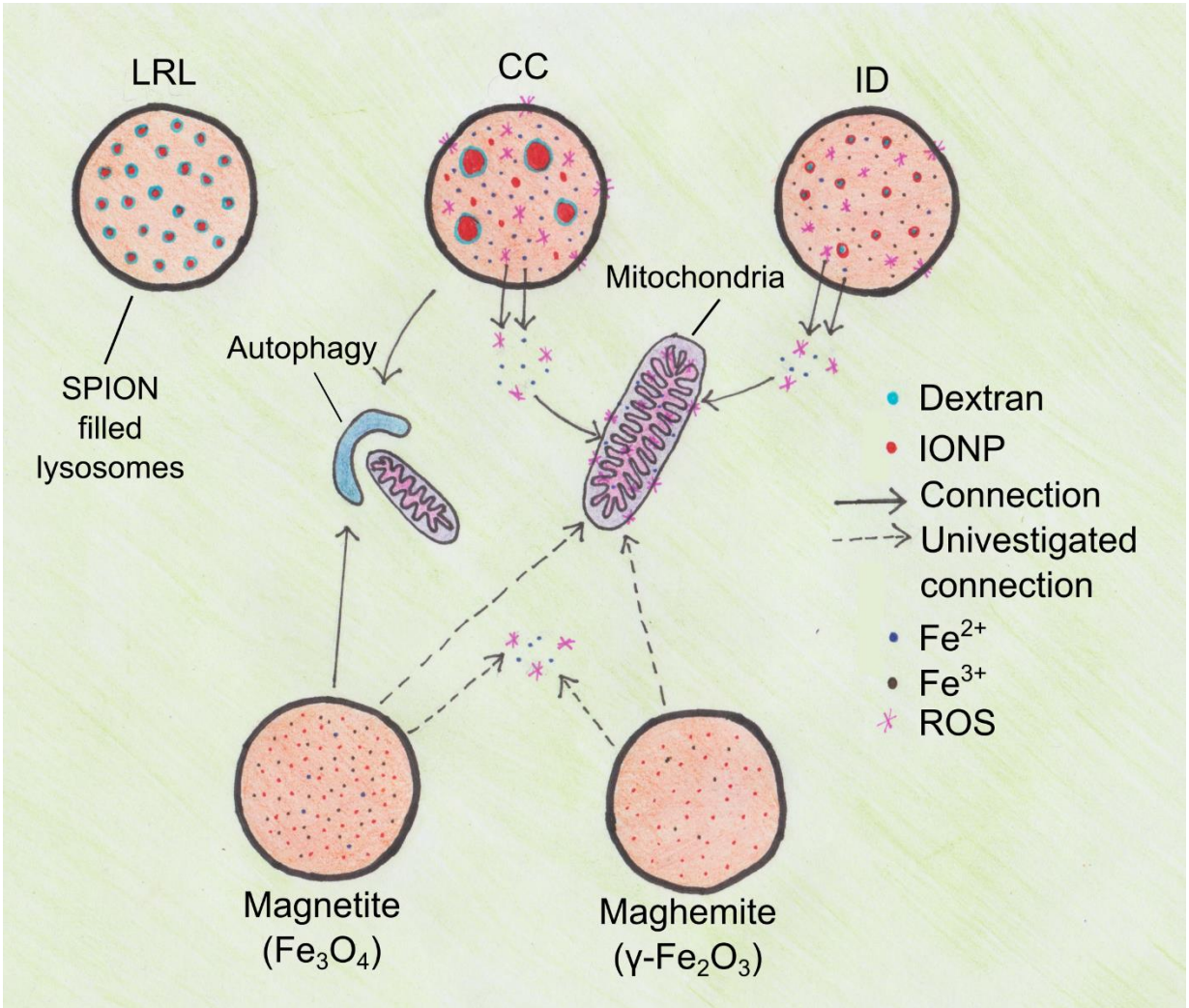

Figure 7-1: The relationships between iron oxide nanoparticle (IONP) structure and their lysosomal and cellular toxicity. Lysosomes shown each loaded with different nanoparticles from this project, LRL, CC and ID from chapter 4 (top row) and magnetite and maghemite nanoparticles from chapter 6 (bottom row). LRL and CC are dextran coated, while ID has a dextran core; magnetite and maghemite are uncoated. LRL treatment was associated with no toxicity phenotypes. Both CC and ID treatments were shown to degrade and produce reactive oxygen species (ROS), with damage to both the lysosome and to mitochondria. Both CC and some magnetite treatments led to induction of autophagy. Magnetite more than maghemite can degrade to release free iron and may damage the lysosome. Dotted lines indicate uninvestigated phenotypes.

May be due to the noted differences in the size of the nanoparticles (with LRL being smaller and more uniform), the difference in magnetite:maghemite ratio (as while the LRL nanoparticles are more magnetite, the CC nanoparticle is equally mixed, which could affect core stability), or a difference in the process of dextran coating (the strength and stability of which depends on the surface of the nanoparticle and process of attachment). The variation in uniformity of the CC nanoparticle cores may also suggest that the process for the nanoparticle production is less tightly controlled, which may also be the case with the application of the coat to the core, making them less stable against degradation. Several papers have attempted to compare multiple previous nanoparticle toxicity studies to find similarities in toxicity potential (Patil et al. 2018; Malhotra et al. 2020; Vakili-Ghartavol et al. 2020), yet as so few of the studies have similar nanoparticles or conditions it becomes difficult to corroborate findings and draw strong conclusions.

In Chapter 6, toxicity of magnetite and maghemite nanoparticles was compared. Maghemite appeared more stable against degradation, breaking down to release mostly Fe^{3+} while the magnetite released Fe^{2+} and Fe^{3+}, as has been previously determined to be their main degradation products according to their structures (Ganapathe et al. 2020). Fe^{2+} is the iron species needed for ROS producing Fenton reactions, although depending on the conditions, Fe^{3+} can be converted to Fe^{2+} and then contribute to producing ROS (Voinov et al. 2011; Schwaminger et al. 2017; Meyerstein 2021). Fenton reactions mainly produce highly damaging hydroxyl radicals that cause lipid peroxidation, damage proteins including enzymes and damage RNA/DNA (Huang et al. 2013; Ying et al. 2021). Fe^{3+} is insoluble and unable to cross lipid membranes unless bound to a chaperone, such as transferrin, meaning free Fe^{3+} is essentially contained in the lysosome (Morgan et al. 1986; Srai et al. 2002). While Fe^{2+} is soluble in biological environments and can cross the lysosomal membrane via certain transporters, such as DMT1, (Garrick et al. 2006), TRPML1 (Dong et al. 2008) and in some cell types NRAMP1 (Blackwell et al. 2000). This may suggest that production of ROS occurs more slowly when maghemite is degraded, as the cell may better be able to process and chelate the free iron when released as Fe^{3+}, as this needs conversion to Fe^{2+} before undergoing Fenton reactions.

In this study magnetite was found to have a variable response on the lysosomal area in a human microglial cell line with evidence of reducing or increasing lysosomal area across different cells in the same treatment group. This affect appeared to be concentration and time-dependent, with evidence of increasing lysosomal area at higher nanoparticle concentrations and after longer incubation time. Yet, this was in contrast to maghemite, which significantly reduced lysosomal area after 1-day incubation, but at no point led to significantly increased Lysotracker area. Some magnetite treatments, but not maghemite treatment, also indicated a link to increased cathepsin B activity and increased autophagy. This may suggest, degradation of the magnetite component in the CC nanoparticles in Chapter 4, rather than the maghemite component as they are a 50:50 mixture of each, may be responsible for the autophagy phenotype. As the LRL nanoparticles in Chapter 3 are an even higher percentage of magnetite (70%), the lack of autophagy induction with this treatment could suggest there was comparatively low degradation of these nanoparticles during the experiment.

7.4 Relevance of nanoparticle coating and size

Chapter 6 attempted to investigate the effects of nanoparticle size on toxicity by working with three different sized magnetite nanoparticles, sold by the company US research nanomaterials as 3 nm, 8 nm and 15-20 nm (denoted 20 nm) nanoparticle solutions. However, when investigated by TEM the differences in size were not apparent due to the aggregation of the particles. However, it was likely that the particles may be less aggregated after sonicating and mixing with PEG for cell treatments and when ingested by cells. This was to be investigated by TEM of the HMC3 cells after treatment with the nanoparticles, but was not achieved in the time frame, making it difficult to compare size of the nanoparticles and their toxicity. Yet by having the three magnetite nanoparticles did provide the opportunity to see if phenotypes were strong across all three nanoparticle treatments. Previously, a study using BSA coated magnetite nanoparticles of two different sizes, 40 nm and 80 nm also found it difficult to detect consistent differences in toxicity (Abakumov et al. 2018). While PEG coated IONPs with an unspecified core composition from Ocean nanotech were found to have a slightly higher cytotoxicity at the smaller size of 10 nm compared to 30 nm particles (Feng et al. 2018). The higher toxicity of smaller nanoparticles is also seen with

other metals, such as silver nanoparticles (Nguyen et al. 2013). In Chapter 6, the 3 nm and 8 nm labelled nanoparticles had the greatest effect on lysosomal area, while only the 3 nm nanoparticle treatment caused a significant increase in Cathepsin B activity and only the 8 nm nanoparticle led to a significant increase in autophagic vesicle area. This could suggest if the nanoparticles were differential sizes in correlation with their named sizes, that the smaller nanoparticles were more toxic, as has been previously shown.

Chapter 6 used uncoated SPIONs that were vortexed with PEG, to reduce settling and aggregation, yet as the PEG is only weakly combined with the nanoparticle it is likely to dissociate upon exposure to an acidic environment and is not a bound coating. The dextran coated nanoparticles in Chapter 4 had no significant impact on the growth/survival of the CHO H1 cells after a 24-hour pulse and 24-hour chase at 1 mg/mL, while the uncoated magnetite nanoparticles showed impacts on cell proliferation and survival after 1-day and 4-day incubations at lower 100-400 µg/mL concentrations. A 1 mg/mL LRL treatment was also added as a control to the cell count experiment in HMC3 cells in Chapter 6, where the greater toxicity of the uncoated magnetite nanoparticles again became apparent. The difference of toxicity by coating is well known, with studies showing polyethylenimine (PEI) coated nanoparticles to have greater toxicity than PEG coated (Feng et al. 2018) and that uncoated magnetite nanoparticles have a greater detrimental effect on cell viability/cytotoxicity than dextran coated nanoparticles (Shaterabadi et al. 2017).

This pattern is also found with coated IONP during *in vivo* experiments. An experiment in zebrafish suggested uncoated nanoparticles impacted larvae mortality, while dextran coated nanoparticles did not (de Oliveira et al. 2017). While an experiment in mice injected with differently coated iron nanoparticles and measuring iron levels across several organs after 24 hours, suggested coating may have an impact on nanoparticle organ localisation (Sharma et al. 2018). This study found that carboxymethyl-dextran coated nanoparticles were highest in the liver and spleen, PEG-PEI coated nanoparticles were highest in lungs, while uncoated and dextran coated nanoparticles mainly accumulated in the liver. Testing the nanoparticles from Chapter 6 in zebrafish embryos with differential concentrations would show if this greater toxicity compared to the dextran-coated nanoparticle also remains true *in vivo*.

Further work on the final data Chapter (6) should better distinguish which pathways are most affected by nanoparticle composition (comparing magnetite and maghemite), how nanoparticle size affects toxicity and show whether toxicity is increased with uncoated nanoparticles. Further experiments could also compare the toxicity of these nanoparticles to mixed composition nanoparticles (preferably produced by the same company and process) to determine whether magnetite, maghemite, or certain combinations of both, causes differential cytotoxicity.

Coating and size may also be two important characteristics of IONPs that determine via which pathway they are endocytosed into cells. Different studies have found multiple different uptake pathways are initiated by different IONPs and indeed different nanoparticles in general, as discussed in Section 1.3.6. Macropinocytosis and phagocytosis (which is specific to certain cell types) are the only likely uptake routes for very large particles or aggregated nanoparticles >150 nm, as other uptake pathways involve smaller vesicles. There is still fairly little known on how nanoparticles can trigger endocytic uptake by cells, so understanding this process remains an important future aim for this research theme. Greater understanding of this process would enable increased accuracy of targeted nanoparticle uptake and could improve production of biocompatible nanoparticles or ways to reduce nanoparticle uptake, which could impact diseases, such as Alzheimer's disease, where cellular nanoparticle accumulation may be involved in disease progression.

7.5 Relevance of nanoparticle biocompatibility

Different nanoparticles can have very different biocompatibilities even when similar in structure or composition. Only the LRL nanoparticles, in Chapter 4, were found to be non-cytotoxic in the CHO H1 cells, not affecting any major cell health-related phenotypes compared to control cells. This study, therefore, validates the use of LRL nanoparticles in the lysosomal extraction method where low toxicity is required. The experiments in Chapter 4 were set up to reflect the nanoparticle concentration and incubation time required for magnetic lysosomal extraction, suggesting lysosomes extracted with LRL nanoparticles should maintain their lysosomal environments. The development of this magnetic extraction method by the Lloyd-Evans lab has been an important development for research on lysosomes from lysosomal storage disease cells, where differing buoyant densities of these

lysosomes prevents efficient extraction by conventional methods. This method has led to generation of data on neuronal ceroid lipofuscinosis type 3 (CLN3) disease (Walker 2015; Schmidtke et al. 2019), on neuronal ceroid lipofuscinosis type 6 (CLN6) disease and on presillin-1 mutations linked to Alzheimer's disease (Lee et al. 2015a).

The high biocompatibility of the LRL nanoparticles, as further validated in this project, may make it an attractive nanoparticle for other low toxicity nanoparticle methods, while study of its protective properties may help determine how to produce even more biocompatible nanoparticles in the future. This study has also emphasized the importance of a complete toxicity testing profile for new IONP formulations, as despite the LRL and CC nanoparticles sharing similar compositions, with a mixed magnetite: maghemite core and 40kDa dextran coat, they do not resemble each other phenotypically in terms of toxicity.

7.6 Discussions of experimental design and data collection

There are a range of nanoparticle experiments now being published, yet what makes them hard to compare is the large variation between experiments. For nanoparticles alone there is large amount of experimental variation in nanoparticle structure, composition, size, coating, formation process, concentration, and incubation times, as well as use in a wide range of different cell types, from different species (Vakili-Ghartavol et al. 2020). Cell medium buffer and other treatment additions, as well as application processes and differences in experimental design and analysis methods, adds to the disparity between experiments. There are a multitude of differing phenotypes identified across different studies of nanoparticle treated cells, with some phenotypes, such as elevated ROS production, commonly found and others, such as induction of autophagy only observed, or even investigated, in a small proportion of studies (Mulens-Arias et al. 2020).

While in the beginnings of this research field it was enough to just determine the possibility of toxicity with any particular nanoparticle treatment in cells, future research will need to focus on the production of more specific, repeatable and comparable models and systems. Two different cells lines were used for investigating IONP and SPION toxicity in this thesis, with CHO H1 cells in Chapter 4 and HMC3 cells in Chapter 6. Identification of phenotypes and pathways affected by IONP treatment in the CHO H1 cells, allowed more direct and

informed investigation of phenotypes in the later HMC3 cells, with LysoTracker area being prioritised as a phenotype for determining what treatment conditions would be optimal for evaluating nanoparticle toxicity in these cells. This project developed a model of nanoparticle toxicity with the specific nanoparticles and conditions that were used, yet based on the utility of these phenotypes this can produce a system for investigating and comparing toxicity across different compositions, structures and coatings of nanoparticles in the future. In the same way the defects seen in the developing zebrafish larvae can be combined to produce a zebrafish larvae system for comparing nanoparticle toxicity on early zebrafish development. Production of highly effective systems that could be shared and utilised between laboratories, would help to reduce the large disparity in conditions between nanoparticle experiments at present and aid data comparison across the field.

In certain experiments in this thesis, changes were found between a 'treated' data set and control -where error bars and data points did not overlap- yet were found by statical testing to not be significantly different and could potentially be described as 'trends'. In most cases, these were not commented upon in text but is worth here stating that these differences could represent changes to cellular phenotypes where further investigation might reveal significantly altered phenotypes using parallel experiments, or in considered cases, further experimental repeats. These potential changes were considered in experiments across the thesis and in many cases dictates the description of parallel experiments described in the discussions of several chapters as further or future research.

The impact of nanoparticles themselves on fluorescent probes is also an important consideration when observing their effects in cells. For example, in this thesis the potential fluorescence-quenching phenotypes of IONPs or related free iron released in cells, was measured using the probes Fura-2,AM, Phen green and Calcein-AM to indicate levels of different species of iron in the cells. While these probes may have been used for their specific iron-related fluorescence quenching phenotypes in this study, IONPs or related free iron released in cells, may also be having quenching effects or possibly increasing fluorescence of other probes when in cells. When the probe Fura-2,AM is used to measure Ca^{2+} it acts ratiometrically and can measure changes with strong accuracy, reduce impact from differential cellular uptake of the probe, and mitigate background interference. Yet the probe was found not to act ratiometrically with free iron, making it difficult to measure iron

quenching with this probe as cellular uptake can vary substantially between cells. It is possible that iron quenching could be occurring with the Fura-2,AM probe when it was used in this thesis to indicate lysosomal Ca^{2+} levels in the IONP treated cells compared to control cells not exposed to IONPs. This could reduce or mask increases in lysosomal Ca^{2+}, with the radiometric nature of the probe unable to correct for this issue. This could lead to the observation of incorrect phenotypes or mask existing phenotypes affecting the validity of research. Therefore, the impact of IONPs or free iron species on fluorescence or even luminescent probes should ideally be tested or checked alongside experiments. This also highlights the importance of using probes where uptake differences and changes in background fluorescence can be assessed, such as ratiometric probes, where these exist, to limit factors affecting accurate data collection.

7.7 Comparing IONP toxicity with other metal nanoparticles

A whole range of metal nanoparticles have been linked to the production of ROS in cells, other than just iron oxide nanoparticles, including nanoparticles of silver, zinc oxide, gold, magnesium oxide, titanium dioxide, copper oxide and many more (Yu et al. 2020). There have also been strong links to lipid peroxidation with many of these nanoparticle treatments, likely as an effect of increased ROS production. DPPP staining has been used previously to show lipid peroxidation after silver nanoparticle treatment in human Chang liver cells (Piao et al. 2011). While lipid peroxidation has also been shown after other heavy metal nanoparticle treatments including gold nanoparticles (Siddiqi et al. 2012), zinc oxide nanoparticles (Lee et al. 2012) and titanium dioxide nanoparticles (Niska et al. 2015).

Dysfunction of lysosomes is a common phenotype associated with metal nanoparticle treatments. Citrate-coated silver nanoparticle in A549 cells colocalised with lysosomes, and reduced LysoTracker fluorescence (Miyayama and Matsuoka 2016). While lysosomal activity has been shown to be reduced by gold nanoparticle treatments in human bronchial epithelial cells and mouse mesenchymal stem cells (Manshian et al. 2018). The localisation of TFEB, as the master regulator of autophagy and lysosomal biogenesis, has been shown to be affected by some metal nanoparticle treatments. Silver nanoparticle treatment of microglial cells has been linked to nuclear translocation of TFEB, independent of mTORC1 and subsequent upregulation of autophagy- and lysosomal-related genes (Lin et al. 2018).

Similar TFEB nuclear translocation has been observed in other cell types in response to polystyrene nanoparticles (Song et al. 2015) and ceria nanoparticles (Song et al. 2014).

Silver nanoparticles have been shown to induce autophagy in a mouse microglial cell line (Shang et al. 2021) as well as inducing mitochondrial morphological and structural alterations in HepG2 cells (Li et al. 2020). Zinc oxide nanoparticle treatments can also increase mitochondrial dysfunction in neuroblastoma cells (Jeng and Swanson 2006), while titanium dioxide nanoparticle exposure has been shown to lead to morphological changes in hepatocyte mitochondria (Natarajan et al. 2015).

Defects have also been seen in zebrafish after other, non-iron, metal nanoparticle treatments. Chen et al. (2020) found increased ROS and lysosomal activity in zebrafish embryos exposed to silver nanoparticles. While analysis of spontaneous movements after treatment with nickel (0.1-5 µg/mL), showed 24 hpf spontaneous coiling was reduced (Aldavood et al. 2020). In contrast 2 µg/mL cadmium did not affect 24 hpf coiling frequency, but did significantly reduce coiling frequency later, at 38-47 hpf (Zindler et al. 2019). Furthermore, Capriello et al. (2019) have also used a DanioVision system (as was used in this thesis) and found concentrations of between 9-72 µM (~1.6-13.2 µg/mL) cadmium and 50-200 µM (~6.7-26.7 µg/mL) aluminium both caused reductions in 3dpf larvae movement.

From this selection of phenotypic metal nanoparticle treatments, both in cellular and *in vivo* (zebrafish) models suggest many of the defects seen to be induced by the iron oxide nanoparticles used in the PhD project, may also be affected by a range of other metal nanoparticles. The optimised phenotypic nanoparticle toxicity systems in both cells and embryonic zebrafish developed in this project could be easily adapted to compare a range of metal nanoparticles for future experimentation.

7.8 Significance for public health, the environment, and the lysosome

As the human population grows and knowledge of medicine increases, the importance of disease prevention rather than just treatment has grown as a public health priority. This leads to investigation of the safety of the public environment, including the air people breathe. Increased air pollution, and in particular PM2.5 air pollution, has been linked to an increase in a large number of diseases, including cardiovascular disease, cerebrovascular

disease, lung cancer, asthma and neurodegenerative diseases, as discussed in Section 1.1.6. When IONPs in air pollution are inhaled they may damage lungs and via the blood can be transported to other organs, and via the olfactory nerves can enter the brain (Calderon-Garciduenas et al. 2002; Oberdörster et al. 2002; Oberdorster et al. 2004).

Also relevant to the impact of IONPs exposure in terms of human disease is the strong link between lysosomal damage (such as that caused by IONPs exposure) and chronic inflammatory disease, mainly due to production of pro-inflammatory cytokines (Yang et al. 2019). A large range of pro-inflammatory cytokines have been shown to be upregulated in IONP treated cells, such as with carboxydextran coated IONPs in macrophage cells (Jin et al. 2019), uncoated magnetite nanoparticles in macrophage cells (Liu et al. 2018), and dextran coated SPIONs in human monocyte cells (Wu et al. 2017b). Two well-known mechanisms for nanoparticle induced inflammation include ROS production and lysosomal damage (Liu et al. 2018). Lysosomal membrane damage leading to rupture can release lysosomal enzymes into the cytosol, with the lysosomal enzyme Cathepsin B of particular interest as this enzyme has been shown to activate NOD-leucine rich repeat and pyrin containing protein 3 (NLRP3) mediated inflammation when released from the lysosome (Liu et al. 2018; Chevriaux et al. 2020). Cathepsin B has a greater pH range than many lysosomal enzymes and has relatively high activity even at increased pH, such as in the cytosol, as was indicated in Chapter 6. Certain types of IONPs shown to induce inflammatory responses have indicated that this effect is partially due to NLRP3 mediated inflammation, but that other pathways are also involved (Liu et al. 2018). The importance of this link between IONP uptake, lysosomal dysfunction and inflammation is demonstrated by the central role of inflammation in many of the diseases that have been related to increased levels of air pollution, particulate matter, and IONP exposure, as was discussed in Section 1.1.6, such as cardiovascular disease and Alzheimer's disease. Activation of NLRP3 has been shown to contribute to the pathogenesis of Alzheimer's disease by producing chronic neuroinflammation, with evidence linking Cathepsin B release from the lysosome to this process in microglia (Dempsey et al. 2017; Bai and Zhang 2021). This link makes cellular inflammation induced by IONPs of particular interest for the work in Chapter 6, and hence an important area of further study for this project.

Due to the multifactorial nature of Alzheimer's disease, with strongly contributing factors of environmental origin as well as genetic, the underlying cause/s of sporadic disease development are so far unelucidated (Carreiras et al. 2013). With no present cure, it is important to investigate environmental risk factors in the hope of finding ways to prevent or delay disease onset. The basis of the research in Chapter 6 was formed from interest of the relationship found between environmental exposure to IONPs and development of neurodegeneration, specifically Alzheimer's disease (Maher et al. 2016). If IONP-related air pollution was related to earlier onset of Alzheimer's disease, then reducing IONP-related air pollution in general or identifying genetically 'at risk' individuals and reducing their exposure to air pollution, could in turn reduce cases and give a higher quality of life for longer to individuals who are likely to develop the disease, reducing both social and economic burdens of care. Environmental risk factors possibly associated with dementia diseases (including Alzheimer's disease) include, air pollution-related factors, such as nitrogen oxide, carbon monoxide, particulate matter and ozone levels, heavy metals exposure (including arsenic, lead, aluminium and iron) and occupational exposures such as electromagnetic fields, pesticides/fertilizers/herbicides/insecticides, solvents and degreasers (Killin et al. 2016). They also include lifestyle factors, such as physical activity, sleep disturbance, diet and smoking/alcohol habits, along with health conditions such as diabetes, traumatic brain injury and epilepsy. Very few of these environmental factors can be investigated in a cellular model for examining links with Alzheimer's disease pathogenesis. Yet if the SPION treatment model produced in this project could be transferred to aged or Alzheimer's disease cell models, this link could then be more easily investigated, to indicate if Alzheimer's disease related phenotypes, such as fibular amyloid-β production and tau pathology as well as lysosomal dysfunction, progressed more rapidly in presence of the additional nanoparticle risk factor.

As a further step in this project, the nanoparticle treatment model could be used for finding potential Alzheimer's disease related drug targets. The ultimate aim in any human disease research is to find or improve treatments, often drugs that can slow, halt or reverse disease progression. By running GWAS (genome-wide association studies) on the nanoparticle treated cellular model for Alzheimer's disease, this could identify druggable genetic targets important to disease progression that interact with this environmental risk factor. Major

genetic targets found to be linked to Alzheimer's disease development, such as Apolipoprotein E (APOE) ε4 and other loci account for less than 50% of heritable Alzheimer's disease risk (Farrer 2015). GWAS have also proved helpful in suggesting genetic links for several lifestyle risk factors in conjunction with dementia risk, including smoking status, physical activity level, diet, and alcohol consumption (Lourida et al. 2019; Patten and Lein 2019).

The importance of the lysosome to the toxicity of nanoparticles has been previously established (Sabella et al. 2014). This thesis also corroborates the importance of the lysosomes' acidic environment on regulating IONP degradation and subsequent release of free iron. Breakdown of IONPs in the degradative environment of the lysosome relies on low pH but also involves the presence of certain compounds such as citrate, and degradative enzymes that can also degrade coatings that otherwise limit exposure to the metal core of coated nanoparticles. The free iron released may cause negative impacts both in the lysosome and when escaping the lysosome, such as in the cytoplasm or effecting other organelles, such as mitochondria. This also links to how the cell's normal iron homeostasis may be affected or altered by addition of IONPs, which could impact cellular distribution of free iron, iron uptake, oxidation states and protein functions. While production of ROS can negatively affect protein and lipid function through peroxidation, free iron can also likely affect enzyme activity, for example through the inhibition of CysHis cathepsins by Fe^{3+}, as well as Zn^{2+} and Cu^{2+}, which can act as a regulatory mechanism for lysosomal functions (Lockwood 2004; Sabella et al. 2014).

This project has fulfilled its ultimate aim to produce cellular and zebrafish development models of iron oxide nanoparticle toxicity that could be simply expanded to investigate further nanoparticles and to provide information on the pathways and phenotypes in the cell that are likely affected by iron oxide nanoparticle treatments. Via this project many additional avenues of research have been identified to expand each Section/Chapter, meaning this project has the potential to be continued in many future projects of this lab and has also resulted in one published paper (Chapter 3) and one paper in preparation (Chapter 4/5).

8 Supplementary Section

8.1 Supplementary Figures from Chapter 4

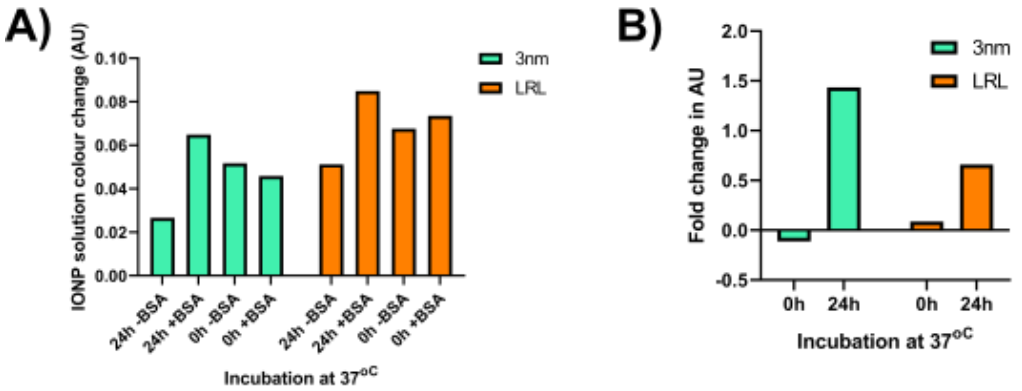

Supplementary Figure 4-1: Addition of bovine serum albumin (BSA) protein protects nanoparticles from degradation. A) Indication of nanoparticle breakdown calculated from absorbance colour change of the nanoparticles solutions measured in absorbance units (AU). Nanoparticle solutions (3nm Fe_3O_4 or LRL nanoparticles) were either pre-incubated with 2 mg/mL BSA (+BSA) or mQ H_2O (-BSA) before addition to pH 5 citrate-phosphate buffer as a 0.1 mg/mL nanoparticle solution that was either incubated at 37°C for 24 hours (24h) or not incubated (0 hours - 0h). Samples were scanned for absorbance readings, to measure colour change. n=1. **B)** The fold change in AU calculated between -BSA and +BSA readings for each incubation time of each nanoparticle.

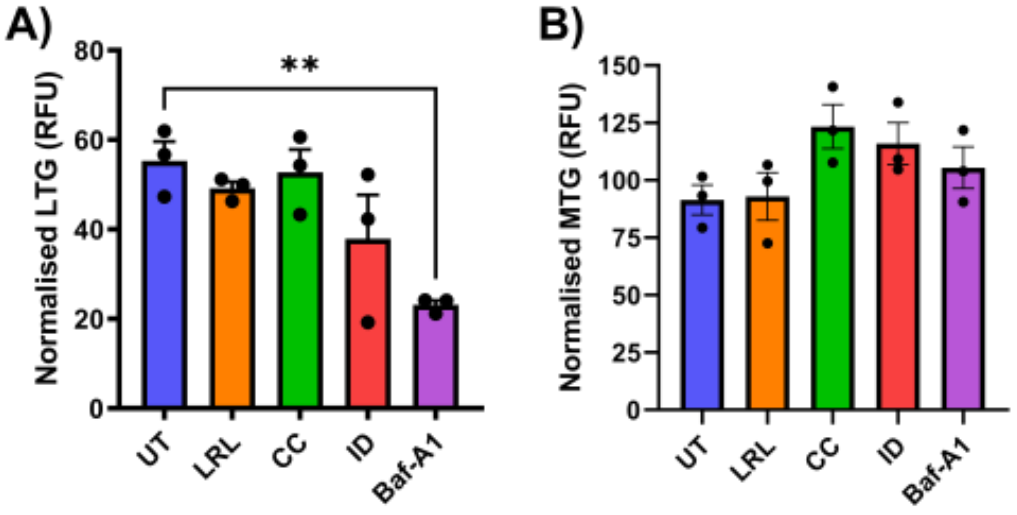

Supplementary Figure 4-2: Live cell plate assays for differentiating changes in fluorescence due to IONP treatments. A) Live cell plate assays in IONP treated CHO H1 cells (24hP:24hCH) for quantitative detection of A) LysoTracker green (LTG) fluorescence and B) MitoTracker green (MTG) fluorescence measured in relative fluorescent units (RFU) normalised to fluorescence of U18666A treated cells. Both n=3. UT = untreated control cells. All data was statistically analysed by one-way ANOVA with Dunnett's post-hoc test, **p<0.01.

8.2 Supplementary Figures from Chapter 6

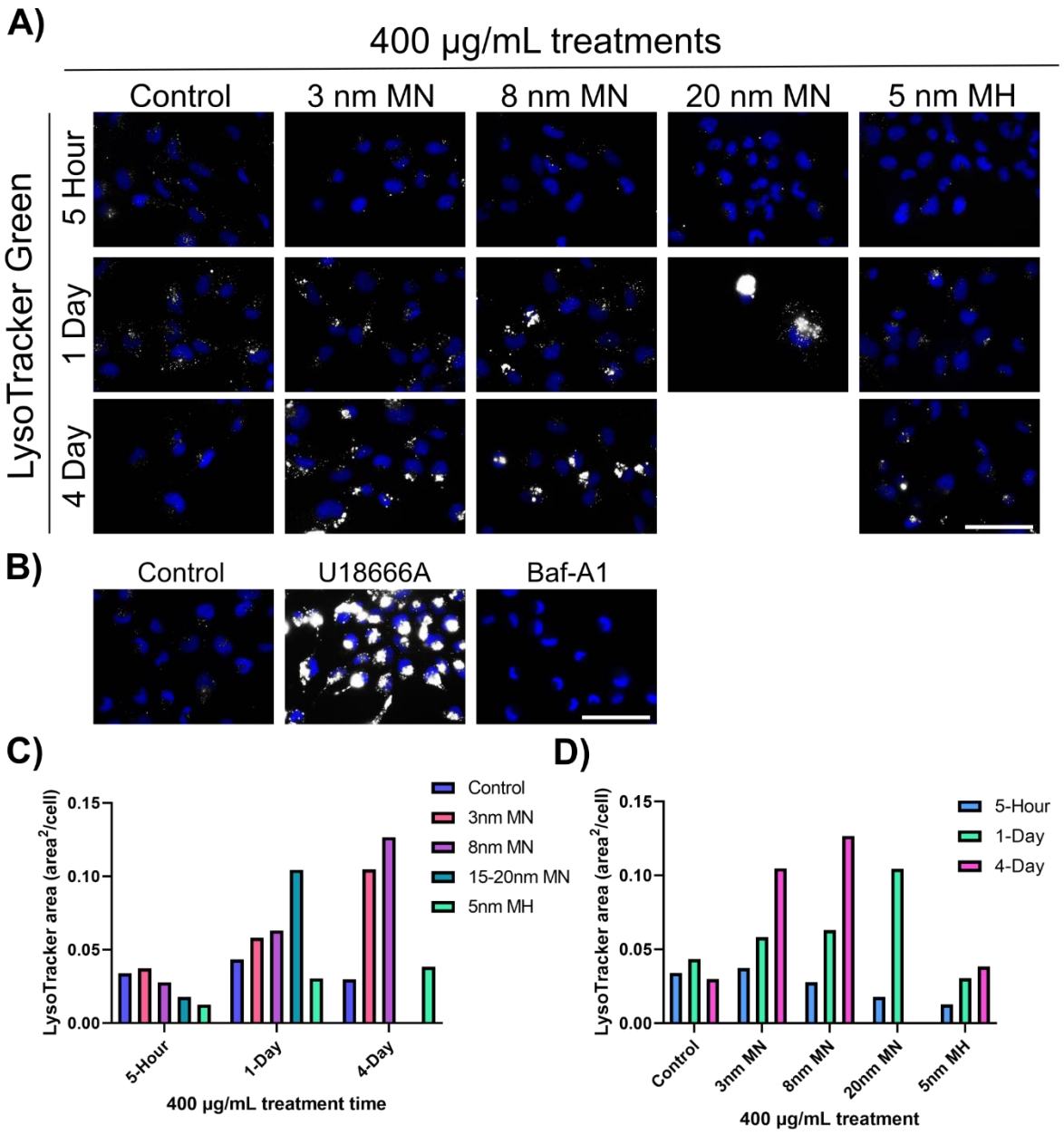

Supplemental Figure 6-1: Effect of high concentration SPIONs on lysosomal area. Representative images of **A)** SPION HMC3 treated cells and **B)** control treatments with **C-D)** quantitative area analysis for LysoTracker Green (grey scale) a probe for acidic vesicles (lysosomes and late endosomes) in HMC3 cells after a 4-day treatment with 400 µg/mL SPIONs, counterstained for nuclei with Hoechst (blue). Scale bars = 40 µm. Data presented as average bars ± SD. n=1.

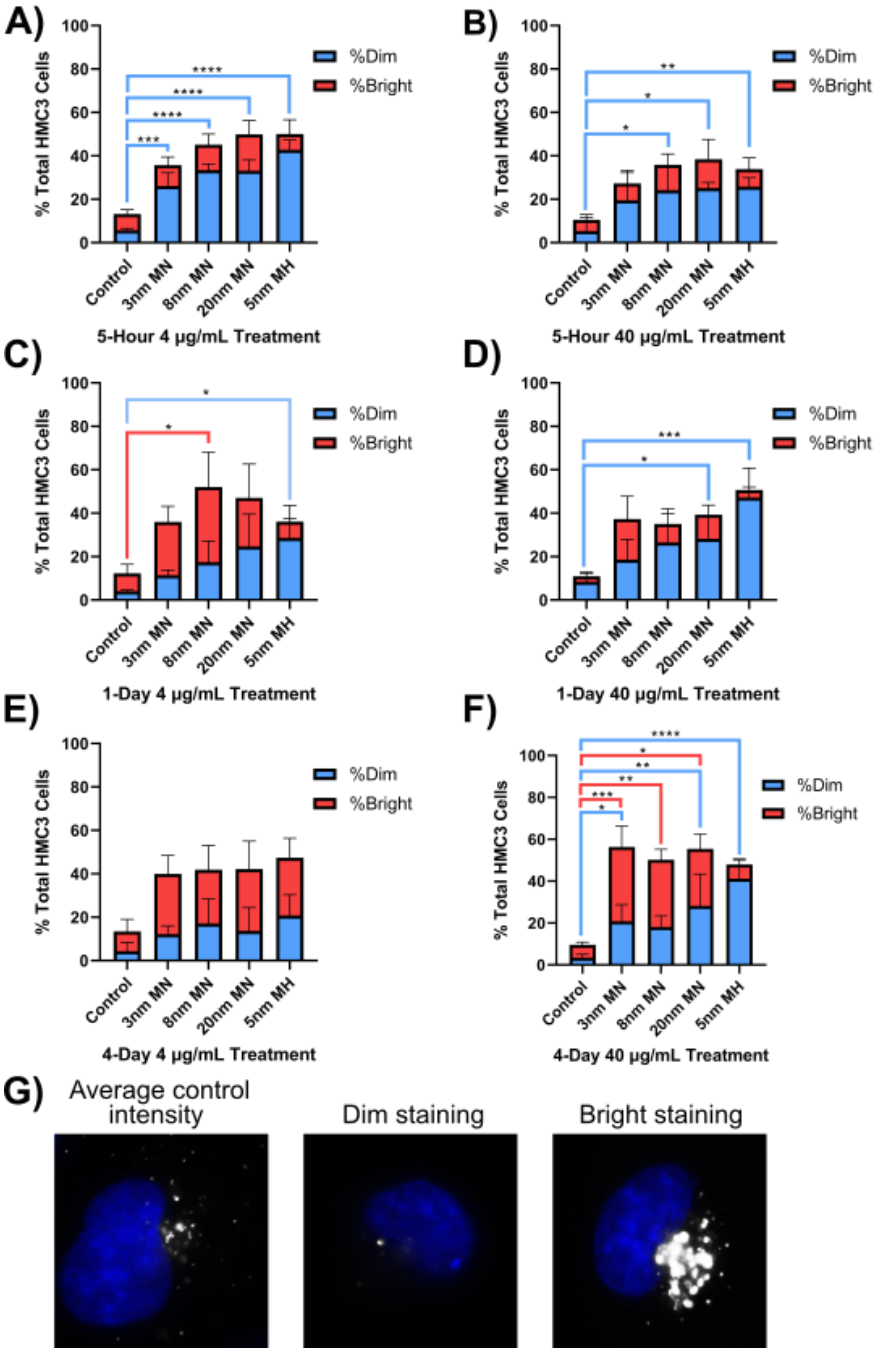

Supplementary Figure 6-2: Counts of fluorescence intensity for LysoTracker green stained SPION treated HMC3 cells. The percentage of bright or dim cells was calculated from total cells in LysoTracker Green microscopy images (9 images/treatment/repeat) and plotted in the graphs as stacked bars with %Dim stacked on the bottom (blue) and %Bright stacked on top (red). Cells were either treated with low (4 µg/mL) or medium (40 µg/mL) SPION concentrations for 5-hour, 1-day or 4-day incubations. Data plotted from SPION treated cells with a 5-hour incubation time **A)** after low **B)** medium SPION treatment, from 1-day incubation after **C)** low or **D)** medium SPION treatment and after a 4-day incubation with a **E)** low or **F)** medium) SPION treatment. G) Representative images of LysoTracker green staining (grey scale) showing average control staining intensity (majority of control cells), dim staining and bright staining, all with Hoechst nuclear stain (blue). Magnetite = MN; Maghemite = MH. Data was statistically analysed by two-way ANOVA with Dunnett's post-hoc test. *p<0.05, **p<0.01, ***p<0.001, ****p<0.0001. n=3.

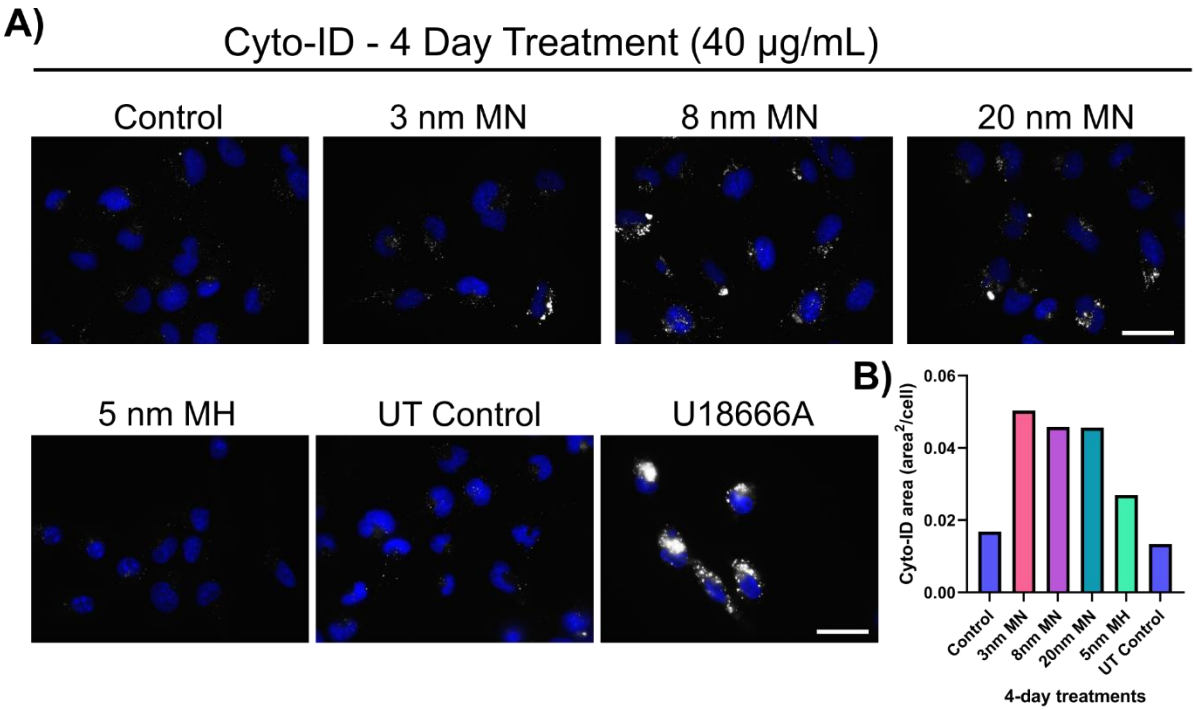

Supplementary Figure 6-3: Impact of medium SPION treatment on autophagy. A) Representative images and **B)** quantitative area analysis for Cyto-ID (grey scale) staining autophagic vesicles in HMC3 cells after a 4-day treatment with 40 µg/mL SPIONs, counterstained for nuclei with Hoechst (blue). Scale bars = 20 µm. Data presented as average bars ± SD. n=1.

Reference List

Aalam, C. S. S., C. G.; Premanand, B. 2015. Influence of Iron (II, III) Oxide Nanoparticles Fuel Additive on Exhaust Emissions and Combustion Characteristics of CRDI System Assisted Diesel Engine *IJAERS* 2(3), pp. 23-28.

Abakumov, M. A. et al. 2018. Toxicity of iron oxide nanoparticles: Size and coating effects. *J Biochem Mol Toxicol* 32(12), p. e22225. doi: 10.1002/jbt.22225

Abalaka, S. E. 2015. Heavy metals bioaccumulation and histopathological changes in Auchenoglanis occidentalis fish from Tiga dam, Nigeria. *J Environ Health Sci Eng* 13, p. 67. doi: 10.1186/s40201-015-0222-y

Adamson, K. I., Sheridan, E. and Grierson, A. J. 2018. Use of zebrafish models to investigate rare human disease. *J Med Genet* 55, pp. 641-649. doi: 10.1136/jmedgenet-2018-105358

Aderem, A. and Underhill, D. M. 1999. Mechanisms of phagocytosis in macrophages. *Annual Review of Immunology* 17(1), pp. 593-623. doi: 10.1146/annurev.immunol.17.1.593

Aghazadeh, M., Karimzadeh, I., Ganjali, M. R. and Maragheh, M. G. 2018. Electrochemical fabrication of praseodymium cations doped iron oxide nanoparticles with enhanced charge storage and magnetic capabilities. *Journal of Materials Science: Materials in Electronics* 29(6), pp. 5163-5172. doi: 10.1007/s10854-017-8481-2

Akimoto, H. 2003. Global Air Quality and Pollution. *Science* 302(5651), pp. 1716-1719. doi: 10.1126/science.1092666

Akiyama, H., Mori, H., Saido, T., Kondo, H., Ikeda, K. and McGeer, P. L. 1999. Occurrence of the diffuse amyloid beta-protein (Abeta) deposits with numerous Abeta-containing glial cells in the cerebral cortex of patients with Alzheimer's disease. *Glia* 25(4), pp. 324-331.

Alarifi, S., Ali, D., Alkahtani, S. and Alhader, M. S. 2014. Iron Oxide Nanoparticles Induce Oxidative Stress, DNA Damage, and Caspase Activation in the Human Breast Cancer Cell Line. *Biological Trace Element Research* 159(1), pp. 416-424. doi: 10.1007/s12011-014-9972-0

Aldavood, S. J., Abbott, L. C., Evans, Z. R., Griffin, D. J., Lee, M. D., Quintero-Arevalo, N. M. and Villalobos, A. R. 2020. Effect of Cadmium and Nickel Exposure on Early Development in Zebrafish (Danio rerio) Embryos. *Water* 12(11), p. 3005.

Ali, Z. S., K.; Sidra, S.; Zona, Z.; Zainab, I.; Aziz, K.; Ahmad, M.; Raza, S. T.; Nasir, Z. A.; Colbeck, I. . 2015. Seasonal variation of particulate matter in the ambient conditions of Khanspur, Pakistan. *Journal of Animal and Plant Sciences* 25(3), pp. 700-705.

Almeida, P. C. et al. 2001. Cathepsin B activity regulation: heparin-like glycosaminoglycans protect human cathepsin B from alkaline pH-induced inactivation. *Journal of Biological Chemistry* 276(2), pp. 944-951. doi: 10.1074/jbc.M003820200

Aloisi, F. 2001. Immune function of microglia. *Glia* 36(2), pp. 165-179. doi: 10.1002/glia.1106

Alshehri, A. 2019. *Identifying and characterizing lysosomal storage disease phenotypes for utilization in novel screening and monitoring assays.* Cardiff University.

Alzheimer's Society. 2014. *Dementia UK report*. Available at: https://www.alzheimers.org.uk/about-us/policy-and-influencing/dementia-uk-report

Anderson, J. O., Thundiyil, J. G. and Stolbach, A. 2012. Clearing the air: a review of the effects of particulate matter air pollution on human health. *Journal of medical toxicology : official journal of the American College of Medical Toxicology* 8(2), pp. 166-175. doi: 10.1007/s13181-011-0203-1

Andjelkovic, A. V., Nikolic, B., Pachter, J. S. and Zecevic, N. 1998. Macrophages/microglial cells in human central nervous system during development: an immunohistochemical study. *Brain Research* 814(1), pp. 13-25. doi: https://doi.org/10.1016/S0006-8993(98)00830-0

Appelmans, F., Wattiaux, R. and De Duve, C. 1955. Tissue fractionation studies. 5. The association of acid phosphatase with a special class of cytoplasmic granules in rat liver. *Biochem J* 59(3), pp. 438-445.

Aragaw, T. A., Bogale, F. M. and Aragaw, B. A. 2021. Iron-based nanoparticles in wastewater treatment: A review on synthesis methods, applications, and removal mechanisms. *Journal of Saudi Chemical Society* 25(8), p. 101280. doi: https://doi.org/10.1016/j.jscs.2021.101280

Arai, K., Kanaseki, T. and Ohkuma, S. 1991. Isolation of highly purified lysosomes from rat liver: identification of electron carrier components on lysosomal membranes. *J Biochem* 110(4), pp. 541-547. doi: 10.1093/oxfordjournals.jbchem.a123616

Arbab, A. S., Wilson, L. B., Ashari, P., Jordan, E. K., Lewis, B. K. and Frank, J. A. 2005. A model of lysosomal metabolism of dextran coated superparamagnetic iron oxide (SPIO) nanoparticles: implications for cellular magnetic resonance imaging. *NMR Biomed* 18(6), pp. 383-389. doi: 10.1002/nbm.970

Arborgh, B., Ericsson, J. L. and Glaumann, H. 1973. Method for the isolation of iron-loaded lysosomes from rat liver. *FEBS Lett* 32(1), pp. 190-194. doi: 10.1016/0014-5793(73)80769-0

Arnold, S. M., Hickey, W. J. and Harris, R. F. 1995. Degradation of Atrazine by Fenton's Reagent: Condition Optimization and Product Quantification. *Environmental Science & Technology* 29(8), pp. 2083-2089. doi: 10.1021/es00008a030

Arslan, P., Di Virgilio, F., Beltrame, M., Tsien, R. Y. and Pozzan, T. 1985. Cytosolic Ca2+ homeostasis in Ehrlich and Yoshida carcinomas. A new, membrane-permeant chelator of heavy metals reveals that these ascites tumor cell lines have normal cytosolic free Ca2+. *Journal of Biological Chemistry* 260(5), pp. 2719-2727. doi: https://doi.org/10.1016/S0021-9258(18)89421-2

Au, D. W. 2004. The application of histo-cytopathological biomarkers in marine pollution monitoring: a review. *Mar Pollut Bull* 48(9-10), pp. 817-834. doi: 10.1016/j.marpolbul.2004.02.032

Audano, M., Schneider, A. and Mitro, N. 2018. Mitochondria, lysosomes, and dysfunction: their meaning in neurodegeneration. *Journal of Neurochemistry* 147(3), pp. 291-309. doi: https://doi.org/10.1111/jnc.14471

Auerbach, M., Wong, L., McClintock, J., Lenowitz, S., London, N., Auerbach, S. and Smith, S. 2015. Safety and Efficacy of Rapid (one hour) Single Intravenous Dose Low Molecular Weight Iron Dextran for Treatment of Oral Iron Intolerant Maternal Iron Deficient Anemia. *Blood* 126, p. 3356.

Avenant-Oldewage, A. M., H. M. and Marx. 2000. Bioaccumulation of chromium, copper and iron in the organs and tissues of Clarias gariepinus in the Olifants River, Kruger National Park. *Water SA* 26(4), pp. 569-582. doi: doi:10.10520/AJA03784738_1616

Ayub, R., Tariq, N., Adil, M. M., Iqbal, M., Junaid, A. and Jaferry, T. 2008. Efficacy and safety of total dose infusion of low molecular weight iron dextran in the treatment of iron deficiency anemia during pregnancy. *J Coll Physicians Surg Pak* 18(7), pp. 424-427.

Azevedo, F. A. et al. 2009. Equal numbers of neuronal and nonneuronal cells make the human brain an isometrically scaled-up primate brain. *The Journal of comparative neurology* 513(5), pp. 532-541. doi: 10.1002/cne.21974

Azria, D., Blanquer, S., Verdier, J.-M. and Belamie, E. 2017. Nanoparticles as contrast agents for brain nuclear magnetic resonance imaging in Alzheimer's disease diagnosis. *Journal of Materials Chemistry B* 5(35), pp. 7216-7237. doi: 10.1039/C7TB01599B

Bai, H. and Zhang, Q. 2021. Activation of NLRP3 Inflammasome and Onset of Alzheimer's Disease. *Frontiers in Immunology* 12, pp. 701282-701282. doi: 10.3389/fimmu.2021.701282

Bai, K.-J. et al. 2019. Microglial activation and inflammation caused by traffic-related particulate matter. *Chemico-Biological Interactions* 311, p. 108762. doi: https://doi.org/10.1016/j.cbi.2019.108762

Bailone, R. L. et al. 2020. Zebrafish as an alternative animal model in human and animal vaccination research. *Lab Anim Res* 36, p. 13. doi: 10.1186/s42826-020-00042-4

Baldassarre, M., Baronio, C. M., Morozova-Roche, L. A. and Barth, A. 2017. Amyloid β-peptides 1-40 and 1-42 form oligomers with mixed β-sheets. *Chem Sci* 8(12), pp. 8247-8254. doi: 10.1039/c7sc01743j

Balk, J. and Schaedler, T. A. 2014. Iron cofactor assembly in plants. *Annu Rev Plant Biol* 65, pp. 125-153. doi: 10.1146/annurev-arplant-050213-035759

Bandyopadhyay, U. and Cuervo, A. M. 2008. Entering the lysosome through a transient gate by chaperone-mediated autophagy. *Autophagy* 4(8), pp. 1101-1103. doi: 10.4161/auto.7150

Bansal, M., Moharir, S. C. and Swarup, G. 2018. Autophagy receptor optineurin promotes autophagosome formation by potentiating LC3-II production and phagophore maturation. *Communicative & integrative biology* 11(2), pp. 1-4. doi: 10.1080/19420889.2018.1467189

Barahuie, F. et al. 2017. Sustained release of anticancer agent phytic acid from its chitosan-coated magnetic nanoparticles for drug-delivery system. *Int J Nanomedicine* 12, pp. 2361-2372. doi: 10.2147/ijn.S126245

Baratli, Y. et al. 2013. Impact of iron oxide nanoparticles on brain, heart, lung, liver and kidneys mitochondrial respiratory chain complexes activities and coupling. *Toxicology in Vitro* 27(8), pp. 2142-2148. doi: https://doi.org/10.1016/j.tiv.2013.09.006

Baron, Y. M. 2021. Could changes in the airborne pollutant particulate matter acting as a viral vector have exerted selective pressure to cause COVID-19 evolution? *Med Hypotheses* 146, p. 110401. doi: 10.1016/j.mehy.2020.110401

Barres, B. A. 2008. The mystery and magic of glia: a perspective on their roles in health and disease. *Neuron* 60(3), pp. 430-440. doi: 10.1016/j.neuron.2008.10.013

Barrow, M. et al. 2018. SPIONs for cell labelling and tracking using MRI: magnetite or maghemite? *Biomaterials Science* 6(1), pp. 101-106. doi: 10.1039/C7BM00515F

Bashir, I., Lone, F. A., Bhat, R. A., Mir, S. A., Dar, Z. A. and Dar, S. A. 2020. Concerns and Threats of Contamination on Aquatic Ecosystems. *Bioremediation and Biotechnology: Sustainable Approaches to Pollution Degradation*, pp. 1-26. doi: 10.1007/978-3-030-35691-0_1

Bates, R. G., Acree, S. F. 1945. pH of aqueous mixtures of potassium dihydrogen phosphate and disodium hydrogen phosphate at 0° to 60°C. *J. Res. NBS* 34, pp. 373-340.

Bature, F., Guinn, B., Pang, D. and Pappas, Y. 2017. Signs and symptoms preceding the diagnosis of Alzheimer's disease: a systematic scoping review of literature from 1937 to 2016. *BMJ Open* 7, p. e015746. doi: 10.1136/bmjopen-2016-015746

Baur, P. S. and Stacey, T. R. 1977. The use of PIPES buffer in the fixation of mammalian and marine tissues for electron microscopy. *J Microsc* 109(3), pp. 315-327. doi: 10.1111/j.1365-2818.1977.tb01145.x

Beaufay, H. and De Duve, C. 1954. [The hexosephosphatase system. VI. Attempted fractionation of microsomes containing glucose-6-phosphatase]. *Bull Soc Chim Biol (Paris)* 36(11-12), pp. 1551-1568.

Beffagna, G. 2019. Zebrafish as a Smart Model to Understand Regeneration After Heart Injury: How Fish Could Help Humans. *Front Cardiovasc Med* 6, p. 107. doi: 10.3389/fcvm.2019.00107

Ben-Sahra, I. and Manning, B. D. 2017. mTORC1 signaling and the metabolic control of cell growth. *Current opinion in cell biology* 45, pp. 72-82. doi: 10.1016/j.ceb.2017.02.012

Bennett, M. L. et al. 2016. New tools for studying microglia in the mouse and human CNS. *Proc Natl Acad Sci U S A* 113(12), pp. E1738-1746. doi: 10.1073/pnas.1525528113

Berg, T. O., Fengsrud, M., Strømhaug, P. E., Berg, T. and Seglen, P. O. 1998. Isolation and Characterization of Rat Liver Amphisomes: EVIDENCE FOR FUSION OF AUTOPHAGOSOMES WITH BOTH EARLY AND LATE ENDOSOMES *. *Journal of Biological Chemistry* 273(34), pp. 21883-21892. doi: 10.1074/jbc.273.34.21883

Bernier, L.-P. et al. 2019. Nanoscale Surveillance of the Brain by Microglia via cAMP-Regulated Filopodia. *Cell Reports* 27(10), pp. 2895-2908.e2894. doi: https://doi.org/10.1016/j.celrep.2019.05.010

Bishop, G. M., Dang, T. N., Dringen, R. and Robinson, S. R. 2011. Accumulation of Non-Transferrin-Bound Iron by Neurons, Astrocytes, and Microglia. *Neurotoxicity Research* 19(3), pp. 443-451. doi: 10.1007/s12640-010-9195-x

Blackwell, J. M., Searle, S., Goswami, T. and Miller, E. N. 2000. Understanding the multiple functions of Nramp1. *Microbes and Infection* 2(3), pp. 317-321. doi: https://doi.org/10.1016/S1286-4579(00)00295-1

Bonsignorio, D., Perego, L., Del Giacco, L. and Cotelli, F. 1996. Structure and macromolecular composition of the zebrafish egg chorion. *Zygote* 4(2), pp. 101-108. doi: 10.1017/s0967199400002975

Booth, P. L. and Thomas, W. E. 1991. Evidence for motility and pinocytosis in ramified microglia in tissue culture. *Brain Res* 548(1-2), pp. 163-171. doi: 10.1016/0006-8993(91)91118-k

Bootman, M. D., Cheek, T. R., Moreton, R. B., Bennett, D. L. and Berridge, M. J. 1994. Smoothly graded Ca2+ release from inositol 1,4,5-trisphosphate-sensitive Ca2+ stores. *Journal of Biological Chemistry* 269(40), pp. 24783-24791. doi: https://doi.org/10.1016/S0021-9258(17)31460-6

Bornemann, K. D. et al. 2001. Abeta-induced inflammatory processes in microglia cells of APP23 transgenic mice. *Am J Pathol* 158(1), pp. 63-73.

Boya, P. and Kroemer, G. 2008. Lysosomal membrane permeabilization in cell death. *Oncogene* 27(50), pp. 6434-6451. doi: 10.1038/onc.2008.310

Bradbury, M. W. B. 1997. Transport of Iron in the Blood-Brain-Cerebrospinal Fluid System. *Journal of Neurochemistry* 69(2), pp. 443-454. doi: https://doi.org/10.1046/j.1471-4159.1997.69020443.x

Bradford, Y. et al. 2011. ZFIN: enhancements and updates to the Zebrafish Model Organism Database. *Nucleic Acids Res* 39(Database issue), pp. D822-829. doi: 10.1093/nar/gkq1077

Braulke, T. and Bonifacino, J. S. 2009. Sorting of lysosomal proteins. *Biochimica et Biophysica Acta (BBA) - Molecular Cell Research* 1793(4), pp. 605-614. doi: https://doi.org/10.1016/j.bbamcr.2008.10.016

Briceño, S., Hernandez, A. C., Sojo, J., Lascano, L. and Gonzalez, G. 2017. Degradation of magnetite nanoparticles in biomimetic media. *Journal of Nanoparticle Research* 19(4), p. 140. doi: 10.1007/s11051-017-3800-3

Brissot, P., Ropert, M., Le Lan, C. and Loréal, O. 2012. Non-transferrin bound iron: A key role in iron overload and iron toxicity. *Biochimica et Biophysica Acta (BBA) - General Subjects* 1820(3), pp. 403-410. doi: https://doi.org/10.1016/j.bbagen.2011.07.014

Brissot, P., Wright, T. L., Ma, W. L. and Weisiger, R. A. 1985. Efficient clearance of non-transferrin-bound iron by rat liver. Implications for hepatic iron loading in iron overload states. *The Journal of Clinical Investigation* 76(4), pp. 1463-1470. doi: 10.1172/JCI112125

Brooke, D., Movahed, N. and Bothner, B. 2015. Universal buffers for use in biochemistry and biophysical experiments. *AIMS Biophysics* 2(3), pp. 336-342. doi: doi:10.3934/biophy.2015.3.336

Brune, K. 1980. HEPES buffered media may induce prostaglandin release from macrophages in tissue culture. *Agents Actions* 10(6), pp. 491-492. doi: 10.1007/BF02024147

Budick, S. A. and O'Malley, D. M. 2000. Locomotor repertoire of the larval zebrafish: swimming, turning and prey capture. *J Exp Biol* 203(Pt 17), pp. 2565-2579.

Burd, C. and Cullen, P. J. 2014. Retromer: a master conductor of endosome sorting. *Cold Spring Harb Perspect Biol* 6(2), doi: 10.1101/cshperspect.a016774

Burdakov, D., Petersen, O. H. and Verkhratsky, A. 2005. Intraluminal calcium as a primary regulator of endoplasmic reticulum function. *Cell Calcium* 38(3-4), pp. 303-310. doi: 10.1016/j.ceca.2005.06.010

Burgess, H. A. and Granato, M. 2007. Sensorimotor gating in larval zebrafish. *J Neurosci* 27(18), pp. 4984-4994. doi: 10.1523/JNEUROSCI.0615-07.2007

Burke, J. F. and Mogg, A. E. 1985. Suppression of a nonsense mutation in mammalian cells in vivo by the aminoglycoside antibiotics G-418 and paromomycin. *Nucleic Acids Res* 13(17), pp. 6265-6272. doi: 10.1093/nar/13.17.6265

Cadmus, P., Brinkman, S. F. and May, M. K. 2018. Chronic Toxicity of Ferric Iron for North American Aquatic Organisms: Derivation of a Chronic Water Quality Criterion Using Single Species and Mesocosm Data. *Archives of Environmental Contamination and Toxicology* 74(4), pp. 605-615. doi: 10.1007/s00244-018-0505-2

Calderon-Garciduenas, L. et al. 2002. Air pollution and brain damage. *Toxicologic Pathology* 30(3), pp. 373-389. doi: 10.1080/01926230252929954

Calderón-Garcidueñas, L. et al. 2010. Urban air pollution: influences on olfactory function and pathology in exposed children and young adults. *Exp Toxicol Pathol* 62(1), pp. 91-102. doi: 10.1016/j.etp.2009.02.117

Calderon-Garciduenas, L. et al. 2003. DNA damage in nasal and brain tissues of canines exposed to air pollutants is associated with evidence of chronic brain inflammation and neurodegeneration. *Toxicologic Pathology* 31(5), pp. 524-538. doi: 10.1080/01926230390226645

Calderón-Garcidueñas, L. et al. 2008. Air pollution, cognitive deficits and brain abnormalities: A pilot study with children and dogs. *Brain and Cognition* 68(2), pp. 117-127. doi: https://doi.org/10.1016/j.bandc.2008.04.008

Calderón-Garcidueñas, L. et al. 2004. Brain inflammation and Alzheimer's-like pathology in individuals exposed to severe air pollution. *Toxicol Pathol* 32(6), pp. 650-658. doi: 10.1080/01926230490520232

Calderón-Garcidueñas, L. et al. 2013. The impact of environmental metals in young urbanites' brains. *Experimental and toxicologic pathology : official journal of the Gesellschaft fur Toxikologische Pathologie* 65(5), pp. 503-511. doi: 10.1016/j.etp.2012.02.006

Calderón-Garcidueñas, L. et al. 2001. Ultrastructural nasal pathology in children chronically and sequentially exposed to air pollutants. *Am J Respir Cell Mol Biol* 24(2), pp. 132-138. doi: 10.1165/ajrcmb.24.2.4157

Campbell, I. 2007. Cell biology and gene expression. *Anaesthesia & Intensive Care Medicine* 8(4), pp. 163-167. doi: https://doi.org/10.1016/j.mpaic.2007.01.005

Cañete, M. et al. 2010. The endocytic penetration mechanism of iron oxide magnetic nanoparticles with positively charged cover: a morphological approach. *Int J Mol Med* 26(4), pp. 533-539. doi: 10.3892/ijmm_00000496

Canton, I. and Battaglia, G. 2012. Endocytosis at the nanoscale. *Chemical Society Reviews* 41(7), pp. 2718-2739. doi: 10.1039/C2CS15309B

Capriello, T., Grimaldi, M. C., Cofone, R., D'Aniello, S. and Ferrandino, I. 2019. Effects of aluminium and cadmium on hatching and swimming ability in developing zebrafish. *Chemosphere* 222, pp. 243-249. doi: 10.1016/j.chemosphere.2019.01.140

Carafoli, E. and Krebs, J. 2016. Why Calcium? How Calcium Became the Best Communicator. *The Journal of biological chemistry* 291(40), pp. 20849-20857. doi: 10.1074/jbc.R116.735894

Carreiras, M. C., Mendes, E., Perry, M. J., Francisco, A. P. and Marco-Contelles, J. 2013. The multifactorial nature of Alzheimer's disease for developing potential therapeutics. *Curr Top Med Chem* 13(15), pp. 1745-1770. doi: 10.2174/15680266113139990135

Ceccarini, C. and Eagle, H. 1971a. Induction and reversal of contact inhibition of growth by pH modification. *Nat New Biol* 233(43), pp. 271-273. doi: 10.1038/newbio233271a0

Ceccarini, C. and Eagle, H. 1971b. pH as a determinant of cellular growth and contact inhibition. *Proc Natl Acad Sci U S A* 68(1), pp. 229-233. doi: 10.1073/pnas.68.1.229

Cen, W.-J. et al. 2018. Iron overload induces G1 phase arrest and autophagy in murine preosteoblast cells. *Journal of Cellular Physiology* 233(9), pp. 6779-6789. doi: https://doi.org/10.1002/jcp.26405

Cermak, S., Kosicek, M., Mladenovic-Djordjevic, A., Smiljanic, K., Kanazir, S. and Hecimovic, S. 2016. Loss of Cathepsin B and L Leads to Lysosomal Dysfunction, NPC-Like Cholesterol Sequestration and Accumulation of the Key Alzheimer's Proteins. *PLoS ONE* 11(11), pp. e0167428-e0167428. doi: 10.1371/journal.pone.0167428

Chan, L. L.-Y. et al. 2012. A novel image-based cytometry method for autophagy detection in living cells. *Autophagy* 8(9), pp. 1371-1382. doi: 10.4161/auto.21028

Chandra Verma, P., Menapace, L., Bonfanti, A., Ciudin, R., Gialanella, S. and Straffelini, G. 2015. Braking pad-disc system: Wear mechanisms and formation of wear fragments. *Wear* 322-323, pp. 251-258. doi: https://doi.org/10.1016/j.wear.2014.11.019

Chang, D. et al. 2017. A meta-analysis of genome-wide association studies identifies 17 new Parkinson's disease risk loci. *Nat Genet* 49(10), pp. 1511-1516. doi: 10.1038/ng.3955

Chasteen, N. D. and Harrison, P. M. 1999. Mineralization in Ferritin: An Efficient Means of Iron Storage. *Journal of Structural Biology* 126(3), pp. 182-194. doi: https://doi.org/10.1006/jsbi.1999.4118

Chate, D. M., Rao, P. S. P., Naik, M. S., Momin, G. A., Safai, P. D. and Ali, K. 2003. Scavenging of aerosols and their chemical species by rain. *Atmospheric Environment* 37(18), pp. 2477-2484. doi: https://doi.org/10.1016/S1352-2310(03)00162-6

Chauhan, V. and Chauhan, A. 2006. Oxidative stress in Alzheimer's disease. *Pathophysiology* 13(3), pp. 195-208. doi: https://doi.org/10.1016/j.pathophys.2006.05.004

Chen, Fannie W., Gordon, Ronald E. and Ioannou, Yiannis A. 2005. NPC1 late endosomes contain elevated levels of non-esterified ('free') fatty acids and an abnormally glycosylated form of the NPC2 protein. *Biochemical Journal* 390(2), pp. 549-561. doi: 10.1042/BJ20050236

Chen, G., Jing, C. H., Liu, P. P., Ruan, D. and Wang, L. 2013a. Induction of autophagic cell death in the rat brain caused by iron. *Am J Med Sci* 345(5), pp. 369-374. doi: 10.1097/MAJ.0b013e318271c031

Chen, H. et al. 2017. Living near major roads and the incidence of dementia, Parkinson's disease, and multiple sclerosis: a population-based cohort study. *Lancet* 389(10070), pp. 718-726. doi: 10.1016/s0140-6736(16)32399-6

Chen, J. W., Pan, W., D'Souza, M. P. and August, J. T. 1985. Lysosome-associated membrane proteins: characterization of LAMP-1 of macrophage P388 and mouse embryo 3T3 cultured cells. *Arch Biochem Biophys* 239(2), pp. 574-586. doi: 10.1016/0003-9861(85)90727-1

Chen, R., Peng, R. D., Meng, X., Zhou, Z., Chen, B. and Kan, H. 2013b. Seasonal variation in the acute effect of particulate air pollution on mortality in the China Air Pollution and Health Effects Study (CAPES). *The Science of the total environment* 450-451, pp. 259-265. doi: 10.1016/j.scitotenv.2013.02.040

Chen, Y., Shah, N., Huggins, F. E. and Huffman, G. P. 2006. Microanalysis of ambient particles from Lexington, KY, by electron microscopy. *Atmospheric Environment* 40(4), pp. 651-663. doi: https://doi.org/10.1016/j.atmosenv.2005.09.036

Chen, Z.-Y. et al. 2020. The Effect of the Chorion on Size-Dependent Acute Toxicity and Underlying Mechanisms of Amine-Modified Silver Nanoparticles in Zebrafish Embryos. *International journal of molecular sciences* 21(8), p. 2864. doi: 10.3390/ijms21082864

Cheng, H., Saffari, A., Sioutas, C., Forman, H. J., Morgan, T. E. and Finch, C. E. 2016. Nanoscale Particulate Matter from Urban Traffic Rapidly Induces Oxidative Stress and Inflammation in Olfactory Epithelium with Concomitant Effects on Brain. *Environmental health perspectives* 124(10), pp. 1537-1546. doi: 10.1289/EHP134

Cheng, J., Flahaut, E. and Cheng, S. H. 2009. Effect of carbon nanotubes on developing zebrafish (Danio Rerio) embryos. *Environmental Toxicology and Chemistry* 26(4), pp. 708-716. doi: https://doi.org/10.1897/06-272R.1

Chevriaux, A. et al. 2020. Cathepsin B Is Required for NLRP3 Inflammasome Activation in Macrophages, Through NLRP3 Interaction. *Frontiers in Cell and Developmental Biology* 8, doi: 10.3389/fcell.2020.00167

Chiang, H. L., Terlecky, S. R., Plant, C. P. and Dice, J. F. 1989. A role for a 70-kilodalton heat shock protein in lysosomal degradation of intracellular proteins. *Science* 246(4928), pp. 382-385. doi: 10.1126/science.2799391

Christensen, K. A., Myers, J. T. and Swanson, J. A. 2002. pH-dependent regulation of lysosomal calcium in macrophages. *Journal of Cell Science* 115(3), pp. 599-607. doi: 10.1242/jcs.115.3.599

Christoforidis, S., McBride, H. M., Burgoyne, R. D. and Zerial, M. 1999. The Rab5 effector EEA1 is a core component of endosome docking. *Nature* 397(6720), pp. 621-625. doi: 10.1038/17618

Cichowicz, R., Wielgosiński, G. and Fetter, W. 2017. Dispersion of atmospheric air pollution in summer and winter season. *Environmental monitoring and assessment* 189(12), pp. 605-605. doi: 10.1007/s10661-017-6319-2

Ciftja, O. 2009. Lamellar-like structures in ferrofluids placed in strong magnetic fields. *Solid State Communications* 149(13), pp. 532-536. doi: https://doi.org/10.1016/j.ssc.2009.01.007

Clapham, D. E. 1995. Calcium signaling. *Cell* 80(2), pp. 259-268. doi: https://doi.org/10.1016/0092-8674(95)90408-5

Coccini, T., Caloni, F., Ramírez Cando, L. J. and De Simone, U. 2017. Cytotoxicity and proliferative capacity impairment induced on human brain cell cultures after short- and long-term exposure to magnetite nanoparticles. *Journal of Applied Toxicology* 37(3), pp. 361-373. doi: https://doi.org/10.1002/jat.3367

Coen, K. et al. 2012. Lysosomal calcium homeostasis defects, not proton pump defects, cause endo-lysosomal dysfunction in PSEN-deficient cells. *J Cell Biol* 198(1), pp. 23-35. doi: 10.1083/jcb.201201076

Colacurcio, D. J. and Nixon, R. A. 2016. Disorders of lysosomal acidification-The emerging role of v-ATPase in aging and neurodegenerative disease. *Ageing research reviews* 32, pp. 75-88. doi: 10.1016/j.arr.2016.05.004

Collingwood, J. F., Mikhaylova, A., Davidson, M., Batich, C., Streit, W. J., Terry, J. and Dobson, J. 2005. In situ characterization and mapping of iron compounds in Alzheimer's disease tissue. *J Alzheimers Dis* 7(4), pp. 267-272.

Connor, J. R. et al. 2001. Is hemochromatosis a risk factor for Alzheimer's disease? *J Alzheimers Dis* 3(5), pp. 471-477. doi: 10.3233/jad-2001-3506

Connor, M. et al. 2021. Nanoparticulate matter exposure results in white matter damage and an inflammatory microglial response in an experimental murine model. *PLoS ONE* 16(7), pp. e0253766-e0253766. doi: 10.1371/journal.pone.0253766

Conti, A. et al. 2019. Empirical and Theoretical Characterization of the Diffusion Process of Different Gadolinium-Based Nanoparticles within the Brain Tissue after Ultrasound-Induced Permeabilization of the Blood-Brain Barrier. *Contrast Media Mol Imaging* 2019, p. 6341545. doi: 10.1155/2019/6341545

Cook, N. R., Row, P. E. and Davidson, H. W. 2004. Lysosome associated membrane protein 1 (Lamp1) traffics directly from the TGN to early endosomes. *Traffic* 5(9), pp. 685-699. doi: 10.1111/j.1600-0854.2004.00212.x

Cook, S. R. et al. 2020a. Detrimental effect of zwitterionic buffers on lysosomal homeostasis in cell lines and iPSC-derived neurons. *AMRC Open Res* 2, p. 21. doi: 10.12688/amrcopenres.12903.1

Cook, S. R. et al. 2020b. Visualisation of cholesterol and ganglioside GM1 in zebrafish models of Niemann-Pick type C disease and Smith-Lemli-Opitz syndrome using light sheet microscopy. *Histochem Cell Biol* 154(5), pp. 565-578. doi: 10.1007/s00418-020-01925-2

Cotter, K., Stransky, L., McGuire, C. and Forgac, M. 2015. Recent Insights into the Structure, Regulation, and Function of the V-ATPases. *Trends in Biochemical Sciences* 40(10), pp. 611-622. doi: https://doi.org/10.1016/j.tibs.2015.08.005

Cox, T. M. and Cachón-González, M. B. 2012. The Cellular Pathology of Lysosomal Diseases. *J Pathol* 226(2), pp. 241-254. doi: 10.1002/path.3021

Craver, M. P. J. and Knoll, L. J. 2007. Increased efficiency of homologous recombination in Toxoplasma gondii dense granule protein 3 demonstrates that GRA3 is not necessary in cell culture but does contribute to virulence. *Molecular and Biochemical Parasitology* 153(2), pp. 149-157. doi: https://doi.org/10.1016/j.molbiopara.2007.02.013

Creasy, B. M., Hartmann, C. B., White, F. K. and McCoy, K. L. 2007. New assay using fluorogenic substrates and immunofluorescence staining to measure cysteine cathepsin activity in live cell subpopulations. *Cytometry A* 71(2), pp. 114-123. doi: 10.1002/cyto.a.20365

Daigneault, M., Preston, J. A., Marriott, H. M., Whyte, M. K. and Dockrell, D. H. 2010. The identification of markers of macrophage differentiation in PMA-stimulated THP-1 cells and monocyte-derived macrophages. *PLoS ONE* 5(1), p. e8668. doi: 10.1371/journal.pone.0008668

Daum, G. and Vance, J. E. 1997. Import of lipids into mitochondria. *Progress in Lipid Research* 36(2), pp. 103-130. doi: https://doi.org/10.1016/S0163-7827(97)00006-4

de Duve, C. 1963. THE LYSOSOME. *Scientific American* 208(5), pp. 64-73.

De Duve, C., Pressman, B. C., Gianetto, R., Wattiaux, R. and Appelmans, F. 1955. Tissue fractionation studies. 6. Intracellular distribution patterns of enzymes in rat-liver tissue. *The Biochemical journal* 60(4), pp. 604-617. doi: 10.1042/bj0600604

De Duve, C. and Wattiaux, R. 1966. Functions of lysosomes. *Annu Rev Physiol* 28, pp. 435-492. doi: 10.1146/annurev.ph.28.030166.002251

De Jong, W. H. and Borm, P. J. A. 2008. Drug delivery and nanoparticles:applications and hazards. *International journal of nanomedicine* 3(2), pp. 133-149. doi: 10.2147/ijn.s596

de Oliveira, G. M. T., de Oliveira, E. M. N., Pereira, T. C. B., Papaléo, R. M. and Bogo, M. R. 2017. Implications of exposure to dextran-coated and uncoated iron oxide nanoparticles to developmental toxicity in zebrafish. *Journal of Nanoparticle Research* 19(12), p. 389. doi: 10.1007/s11051-017-4074-5

de Vries, I. J. et al. 2005. Magnetic resonance tracking of dendritic cells in melanoma patients for monitoring of cellular therapy. *Nat Biotechnol* 23(11), pp. 1407-1413. doi: 10.1038/nbt1154

Dėdelė, A. and Miškinytė, A. 2019. Seasonal and site-specific variation in particulate matter pollution in Lithuania. *Atmospheric Pollution Research* 10(3), pp. 768-775. doi: https://doi.org/10.1016/j.apr.2018.12.004

Dello Russo, C. et al. 2018. The human microglial HMC3 cell line: where do we stand? A systematic literature review. *Journal of neuroinflammation* 15(1), p. 259. doi: 10.1186/s12974-018-1288-0

Demirel, Y. 2002. Chapter 12 - Thermodynamics and biological systems. In: Demirel, Y. ed. *Nonequilibrium Thermodynamics*. Amsterdam: Elsevier Science, pp. 293-355.

Dempsey, C. et al. 2017. Inhibiting the NLRP3 inflammasome with MCC950 promotes non-phlogistic clearance of amyloid-β and cognitive function in APP/PS1 mice. *Brain Behav Immun* 61, pp. 306-316. doi: 10.1016/j.bbi.2016.12.014

Depping, R. and Seeger, K. 2019. (1)H-NMR spectroscopy shows cellular uptake of HEPES buffer by human cell lines-an effect to be considered in cell culture experiments. *Anal Bioanal Chem* 411(4), pp. 797-802. doi: 10.1007/s00216-018-1518-4

Deserno, M. 2004. Elastic deformation of a fluid membrane upon colloid binding. *Physical Review E* 69(3), p. 031903. doi: 10.1103/PhysRevE.69.031903

Diettrich, O., Mills, K., Johnson, A. W., Hasilik, A. and Winchester, B. G. 1998. Application of magnetic chromatography to the isolation of lysosomes from fibroblasts of patients with lysosomal storage disorders. *FEBS Letters* 441(3), pp. 369-372. doi: https://doi.org/10.1016/S0014-5793(98)01578-6

Ding, Z. et al. 2015. Hemodynamic shear stress via ROS modulates PCSK9 expression in human vascular endothelial and smooth muscle cells and along the mouse aorta. *Antioxid Redox Signal* 22(9), pp. 760-771. doi: 10.1089/ars.2014.6054

Doherty, E. and Perl, A. 2017. Measurement of Mitochondrial Mass by Flow Cytometry during Oxidative Stress. *Reactive oxygen species (Apex, N.C.)* 4(10), pp. 275-283. doi: 10.20455/ros.2017.839

Doherty, G. J. and McMahon, H. T. 2009. Mechanisms of Endocytosis. *Annual Review of Biochemistry* 78(1), pp. 857-902. doi: 10.1146/annurev.biochem.78.081307.110540

Dong, X. P., Cheng, X., Mills, E., Delling, M., Wang, F., Kurz, T. and Xu, H. 2008. The type IV mucolipidosis-associated protein TRPML1 is an endolysosomal iron release channel. *Nature* 455(7215), pp. 992-996. doi: 10.1038/nature07311

Doodnauth, S. A., Grinstein, S. and Maxson, M. E. 2019. Constitutive and stimulated macropinocytosis in macrophages: roles in immunity and in the pathogenesis of atherosclerosis. *Philosophical Transactions of the Royal Society B: Biological Sciences* 374(1765), p. 20180147. doi: doi:10.1098/rstb.2018.0147

Drysdale, J. et al. 2002. Mitochondrial ferritin: a new player in iron metabolism. *Blood Cells Mol Dis* 29(3), pp. 376-383. doi: 10.1006/bcmd.2002.0577

Duan, J. et al. 2019. Iron oxide nanoparticles promote vascular endothelial cells survival from oxidative stress by enhancement of autophagy. *Regenerative Biomaterials* 6(4), pp. 221-229. doi: 10.1093/rb/rbz024

Duchen, M. R. 2004. Mitochondria in health and disease: perspectives on a new mitochondrial biology. *Molecular Aspects of Medicine* 25(4), pp. 365-451. doi: https://doi.org/10.1016/j.mam.2004.03.001

Duesterberg, C. K., Mylon, S. E. and Waite, T. D. 2008. pH effects on iron-catalyzed oxidation using Fenton's reagent. *Environ Sci Technol* 42(22), pp. 8522-8527. doi: 10.1021/es801720d

Durafourt, B. A. et al. 2012. Comparison of polarization properties of human adult microglia and blood-derived macrophages. *Glia* 60(5), pp. 717-727. doi: https://doi.org/10.1002/glia.22298

Duvvuri, M. and Krise, J. P. 2005. A novel assay reveals that weakly basic model compounds concentrate in lysosomes to an extent greater than pH-partitioning theory would predict. *Mol Pharm* 2(6), pp. 440-448. doi: 10.1021/mp050043s

Efeyan, A., Comb, W. C. and Sabatini, D. M. 2015. Nutrient-sensing mechanisms and pathways. *Nature* 517(7534), pp. 302-310. doi: 10.1038/nature14190

Efthymiou, A. G. and Goate, A. M. 2017. Late onset Alzheimer's disease genetics implicates microglial pathways in disease risk. *Molecular Neurodegeneration* 12(1), p. 43. doi: 10.1186/s13024-017-0184-x

Elkin, S. R., Lakoduk, A. M. and Schmid, S. L. 2016. Endocytic pathways and endosomal trafficking: a primer. *Wiener Medizinische Wochenschrift* 166(7), pp. 196-204. doi: 10.1007/s10354-016-0432-7

Emran, F., Rihel, J. and Dowling, J. E. 2008. A behavioral assay to measure responsiveness of zebrafish to changes in light intensities. *J Vis Exp* (20), doi: 10.3791/923

Erecinska, M., Deas, J. and Silver, I. A. 1995. The effect of pH on glycolysis and phosphofructokinase activity in cultured cells and synaptosomes. *J Neurochem* 65(6), pp. 2765-2772. doi: 10.1046/j.1471-4159.1995.65062765.x

Ermak, G. and Davies, K. J. A. 2002. Calcium and oxidative stress: from cell signaling to cell death. *Molecular Immunology* 38(10), pp. 713-721. doi: https://doi.org/10.1016/S0161-5890(01)00108-0

Escamilla-Rivera, V., Uribe-Ramírez, M., González-Pozos, S., Lozano, O., Lucas, S. and De Vizcaya-Ruiz, A. 2016. Protein corona acts as a protective shield against Fe3O4-PEG inflammation and ROS-induced toxicity in human macrophages. *Toxicology Letters* 240(1), pp. 172-184. doi: https://doi.org/10.1016/j.toxlet.2015.10.018

Etemad, S., Zamin, R. M., Ruitenberg, M. J. and Filgueira, L. 2012. A novel in vitro human microglia model: characterization of human monocyte-derived microglia. *J Neurosci Methods* 209(1), pp. 79-89. doi: 10.1016/j.jneumeth.2012.05.025

Evans, C. A. W., Harbuz, M. S., Ostenfeld, T., Norrish, A. and Blackwell, J. M. 2001. Nramp1 is expressed in neurons and is associated with behavioural and immune responses to stress. *Neurogenetics* 3(2), pp. 69-78. doi: 10.1007/s100480100105

Falguières, T., Luyet, P.-P., Bissig, C., Scott, C. C., Velluz, M.-C. and Gruenberg, J. 2008. In vitro budding of intralumenal vesicles into late endosomes is regulated by Alix and Tsg101. *Molecular Biology of the Cell* 19(11), pp. 4942-4955. doi: 10.1091/mbc.e08-03-0239

Fan, Z., Brooks, D. J., Okello, A. and Edison, P. 2017. An early and late peak in microglial activation in Alzheimer's disease trajectory. *Brain* 140(3), pp. 792-803. doi: 10.1093/brain/aww349

Farrer, L. A. 2015. Expanding the genomic roadmap of Alzheimer's disease. *Lancet Neurol* 14(8), pp. 783-785. doi: 10.1016/s1474-4422(15)00146-5

Fenech, M. and Morley, A. A. 1985. Measurement of micronuclei in lymphocytes. *Mutat Res* 147(1-2), pp. 29-36. doi: 10.1016/0165-1161(85)90015-9

Feng, Q., Liu, Y., Huang, J., Chen, K., Huang, J. and Xiao, K. 2018. Uptake, distribution, clearance, and toxicity of iron oxide nanoparticles with different sizes and coatings. *Scientific Reports* 8(1), p. 2082. doi: 10.1038/s41598-018-19628-z

Feng, X., Xiong, J., Lu, Y., Xia, X. and Zhu, M. X. 2014. Differential mechanisms of action of the mucolipin synthetic agonist, ML-SA1, on insect TRPML and mammalian TRPML1. *Cell Calcium* 56(6), pp. 446-456. doi: https://doi.org/10.1016/j.ceca.2014.09.004

Ferguson, W. J. et al. 1980. Hydrogen ion buffers for biological research. *Anal Biochem* 104(2), pp. 300-310. doi: 10.1016/0003-2697(80)90079-2

Ferrati, S. et al. 2014. Cellular communication via nanoparticle-transporting biovesicles. *Nanomedicine (London, England)* 9(5), pp. 581-592. doi: 10.2217/nnm.13.57

Ferreira, C. M. H., Pinto, I. S. S., Soares, E. V. and Soares, H. M. V. M. 2015. (Un)suitability of the use of pH buffers in biological, biochemical and environmental studies and their interaction with metal ions – a review. *RSC Advances* 5(39), pp. 30989-31003. doi: 10.1039/c4ra15453c

Fillebeen, C. et al. 2019. Transferrin receptor 1 controls systemic iron homeostasis by fine-tuning hepcidin expression to hepatocellular iron load. *Blood* 133(4), pp. 344-355. doi: 10.1182/blood-2018-05-850404

Fineran, P. et al. 2016. Pathogenic mycobacteria achieve cellular persistence by inhibiting the Niemann-Pick Type C disease cellular pathway. *Wellcome Open Res* 1, p. 18. doi: 10.12688/wellcomeopenres.10036.2

Fitzner, D. et al. 2011. Selective transfer of exosomes from oligodendrocytes to microglia by macropinocytosis. *J Cell Sci* 124(Pt 3), pp. 447-458. doi: 10.1242/jcs.074088

Flinck, M., Kramer, S. H. and Pedersen, S. F. 2018. Roles of pH in control of cell proliferation. *Acta Physiol (Oxf)* 223(3), p. e13068. doi: 10.1111/apha.13068

Forbes, J. R. and Gros, P. 2003. Iron, manganese, and cobalt transport by Nramp1 (Slc11a1) and Nramp2 (Slc11a2) expressed at the plasma membrane. *Blood* 102(5), pp. 1884-1892. doi: 10.1182/blood-2003-02-0425

Forouzanfar, M. H. et al. 2016. Global, regional, and national comparative risk assessment of 79 behavioural, environmental and occupational, and metabolic risks or clusters of risks, 1990–2015: a systematic analysis for the Global Burden of Disease Study 2015. *The Lancet* 388(10053), pp. 1659-1724. doi: 10.1016/S0140-6736(16)31679-8

Fu, R., Shen, Q., Xu, P., Luo, J. J. and Tang, Y. 2014. Phagocytosis of Microglia in the Central Nervous System Diseases. *Molecular Neurobiology* 49(3), pp. 1422-1434. doi: 10.1007/s12035-013-8620-6

Furuta, K., Yang, X.-L., Chen, J.-S., Hamilton, S. R. and August, J. T. 1999. Differential Expression of the Lysosome-Associated Membrane Proteins in Normal Human Tissues. *Archives of Biochemistry and Biophysics* 365(1), pp. 75-82. doi: https://doi.org/10.1006/abbi.1999.1147

Gaharwar, U. S., Kumar, S. and Rajamani, P. 2020. Iron oxide nanoparticle-induced hematopoietic and immunological response in rats. *RSC Advances* 10(59), pp. 35753-35764. doi: 10.1039/D0RA05901C

Ganapathe, L. S., Mohamed, M. A., Mohamad Yunus, R. and Berhanuddin, D. D. 2020. Magnetite (Fe3O4) Nanoparticles in Biomedical Application: From Synthesis to Surface Functionalisation. *Magnetochemistry* 6(4), doi: 10.3390/magnetochemistry6040068

Gao, J. et al. 2021. Time-course effect of ultrasmall superparamagnetic iron oxide nanoparticles on intracellular iron metabolism and ferroptosis activation. *Nanotoxicology* 15(3), pp. 366-379. doi: 10.1080/17435390.2021.1872112

Gárate-Vélez, L. et al. 2020. Anthropogenic Iron Oxide Nanoparticles Induce Damage to Brain Microvascular Endothelial Cells Forming the Blood-Brain Barrier. *J Alzheimers Dis* 76(4), pp. 1527-1539. doi: 10.3233/jad-190929

Garrick, M. D. et al. 2006. DMT1: which metals does it transport? *Biol Res* 39(1), pp. 79-85. doi: 10.4067/s0716-97602006000100009

Gerasimenko, J. V., Tepikin, A. V., Petersen, O. H. and Gerasimenko, O. V. 1998. Calcium uptake via endocytosis with rapid release from acidifying endosomes. *Current Biology* 8(24), pp. 1335-1338. doi: https://doi.org/10.1016/S0960-9822(07)00565-9

Glebov, O. O., Bright, N. A. and Nichols, B. J. 2006. Flotillin-1 defines a clathrin-independent endocytic pathway in mammalian cells. *Nature Cell Biology* 8(1), pp. 46-54. doi: 10.1038/ncb1342

Glick, D., Barth, S. and Macleod, K. F. 2010. Autophagy: cellular and molecular mechanisms. *The Journal of pathology* 221(1), pp. 3-12. doi: 10.1002/path.2697

Goldstein, S., Meyerstein, D. and Czapski, G. 1993. The Fenton reagents. *Free Radical Biology and Medicine* 15(4), pp. 435-445. doi: https://doi.org/10.1016/0891-5849(93)90043-T

Gómez-Nicola, D., Fransen, N. L., Suzzi, S. and Perry, V. H. 2013. Regulation of Microglial Proliferation during Chronic Neurodegeneration. *The Journal of Neuroscience* 33(6), p. 2481. doi: 10.1523/JNEUROSCI.4440-12.2013

Good, N. E. and Izawa, S. 1972. Hydrogen ion buffers. *Methods Enzymol* 24, pp. 53-68. doi: 10.1016/0076-6879(72)24054-x

Good, N. E., Winget, G. D., Winter, W., Connolly, T. N., Izawa, S. and Singh, R. M. 1966. Hydrogen ion buffers for biological research. *Biochemistry* 5(2), pp. 467-477. doi: 10.1021/bi00866a011

Gorman, D. S. and Levine, R. P. 1965. Cytochrome f and plastocyanin: their sequence in the photosynthetic electron transport chain of Chlamydomonas reinhardi. *Proc Natl Acad Sci U S A* 54(6), pp. 1665-1669. doi: 10.1073/pnas.54.6.1665

Goshima, K. 1973. A study on the preservation of the beating rhythm of single myocardial cells in vitro. *Exp Cell Res* 80(2), pp. 432-438. doi: 10.1016/0014-4827(73)90316-9

Grady, J. K., Chasteen, N. D. and Harris, D. C. 1988. Radicals from "Good's" buffers. *Anal Biochem* 173(1), pp. 111-115. doi: 10.1016/0003-2697(88)90167-4

Grafstein, B. and Forman, D. S. 1980. Intracellular transport in neurons. *Physiological Reviews* 60(4), pp. 1167-1283. doi: 10.1152/physrev.1980.60.4.1167

Graham, J. M. 2001. Purification of a crude mitochondrial fraction by density-gradient centrifugation. *Curr Protoc Cell Biol* Chapter 3, p. Unit 3.4. doi: 10.1002/0471143030.cb0304s04

Graham, R. M., Reutens, G. M., Herbison, C. E., Delima, R. D., Chua, A. C., Olynyk, J. K. and Trinder, D. 2008. Transferrin receptor 2 mediates uptake of transferrin-bound and non-transferrin-bound iron. *J Hepatol* 48(2), pp. 327-334. doi: 10.1016/j.jhep.2007.10.009

Grandjean, P. and Landrigan, P. J. 2014. Neurobehavioural effects of developmental toxicity. *The Lancet Neurology* 13(3), pp. 330-338. doi: 10.1016/S1474-4422(13)70278-3

Greaves, C. 1983. A powder neutron diffraction investigation of vacancy ordering and covalence in γ-Fe2O3. *Journal of Solid State Chemistry* 49(3), pp. 325-333. doi: https://doi.org/10.1016/S0022-4596(83)80010-3

Grisan, F. et al. 2021. PKA compartmentalization links cAMP signaling and autophagy. *Cell Death & Differentiation*, doi: 10.1038/s41418-021-00761-8

Guha, S., Liu, J., Baltazar, G., Laties, A. M. and Mitchell, C. H. 2014. Rescue of compromised lysosomes enhances degradation of photoreceptor outer segments and reduces lipofuscin-like autofluorescence in retinal pigmented epithelial cells. *Advances in experimental medicine and biology* 801, pp. 105-111. doi: 10.1007/978-1-4614-3209-8_14

Gunshin, H., Fujiwara, Y., Custodio, A. O., Direnzo, C., Robine, S. and Andrews, N. C. 2005. Slc11a2 is required for intestinal iron absorption and erythropoiesis but dispensable in placenta and liver. *The Journal of Clinical Investigation* 115(5), pp. 1258-1266. doi: 10.1172/JCI24356

Gunshin, H. et al. 1997. Cloning and characterization of a mammalian proton-coupled metal-ion transporter. *Nature* 388(6641), pp. 482-488. doi: 10.1038/41343

Gutiérrez, C. G., Campbell, B. K. and Webb, R. 1997. Development of a Long-Term Bovine Granulosa Cell Culture System: Induction and Maintenance of Estradiol Production, Response to Follicle-

Stimulating Hormone, and Morphological Characteristics1. *Biology of Reproduction* 56(3), pp. 608-616. doi: 10.1095/biolreprod56.3.608

Gutiérrez, L. et al. 2015. Degradation of magnetic nanoparticles mimicking lysosomal conditions followed by AC susceptibility. *Biomed Tech (Berl)* 60(5), pp. 417-425. doi: 10.1515/bmt-2015-0043

Gutierrez, M. G., Munafó, D. B., Berón, W. and Colombo, M. a. I. 2004. Rab7 is required for the normal progression of the autophagic pathway in mammalian cells. *Journal of Cell Science* 117(13), pp. 2687-2697. doi: 10.1242/jcs.01114

Guzy, J. et al. 2020. Complex Relationship between Iron Oxide Nanoparticle Degradation and the Signal Intensity in Magnetic Particle Imaging. *ACS Applied Nano Materials* 3(5), pp. 3991-3999. doi: 10.1021/acsanm.0c00779

Hachicho, N., Reithel, S., Miltner, A., Heipieper, H. J., Küster, E. and Luckenbach, T. 2015. Body Mass Parameters, Lipid Profiles and Protein Contents of Zebrafish Embryos and Effects of 2,4-Dinitrophenol Exposure. *PLoS ONE* 10(8), p. e0134755. doi: 10.1371/journal.pone.0134755

Haigler, H. T., McKanna, J. A. and Cohen, S. 1979. Rapid stimulation of pinocytosis in human carcinoma cells A-431 by epidermal growth factor. *J Cell Biol* 83(1), pp. 82-90. doi: 10.1083/jcb.83.1.82

Halbrooks, P. J., He, Q.-Y., Briggs, S. K., Everse, S. J., Smith, V. C., MacGillivray, R. T. A. and Mason, A. B. 2003. Investigation of the Mechanism of Iron Release from the C-Lobe of Human Serum Transferrin: Mutational Analysis of the Role of a pH Sensitive Triad. *Biochemistry* 42(13), pp. 3701-3707. doi: 10.1021/bi027071q

Hamanaka, R. B. and Mutlu, G. M. 2018. Particulate Matter Air Pollution: Effects on the Cardiovascular System. *Frontiers in endocrinology* 9, pp. 680-680. doi: 10.3389/fendo.2018.00680

Hamelin, L. et al. 2016. Early and protective microglial activation in Alzheimer's disease: a prospective study using 18F-DPA-714 PET imaging. *Brain* 139(Pt 4), pp. 1252-1264. doi: 10.1093/brain/aww017

Hamra, G. B. et al. 2014. Outdoor particulate matter exposure and lung cancer: a systematic review and meta-analysis. *Environmental health perspectives* 122(9), pp. 906-911. doi: 10.1289/ehp/1408092

Hanisch, U.-K. and Kettenmann, H. 2007. Microglia: active sensor and versatile effector cells in the normal and pathologic brain. *Nature Neuroscience* 10(11), pp. 1387-1394. doi: 10.1038/nn1997

Hardie, D. G. 2004. The AMP-activated protein kinase pathway – new players upstream and downstream. *Journal of Cell Science* 117(23), pp. 5479-5487. doi: 10.1242/jcs.01540

Harisinghani, M. G. et al. 2003. Noninvasive detection of clinically occult lymph-node metastases in prostate cancer. *N Engl J Med* 348(25), pp. 2491-2499. doi: 10.1056/NEJMoa022749

Harrison, R. M. and Jones, M. 1995. The chemical composition of airborne particles in the UK atmosphere. *Science of The Total Environment* 168(3), pp. 195-214. doi: https://doi.org/10.1016/0048-9697(95)04536-A

Hautot, D., Pankhurst, Q. A., Khan, N. and Dobson, J. 2003. Preliminary evaluation of nanoscale biogenic magnetite in Alzheimer's disease brain tissue. *Proc Biol Sci* 270 Suppl 1(Suppl 1), pp. S62-64. doi: 10.1098/rsbl.2003.0012

Hayashi-Nishino, M., Fujita, N., Noda, T., Yamaguchi, A., Yoshimori, T. and Yamamoto, A. 2009. A subdomain of the endoplasmic reticulum forms a cradle for autophagosome formation. *Nat Cell Biol* 11(12), pp. 1433-1437. doi: 10.1038/ncb1991

Hayflick, S. J., Westaway, S. K., Levinson, B., Zhou, B., Johnson, M. A., Ching, K. H. L. and Gitschier, J. 2003. Genetic, Clinical, and Radiographic Delineation of Hallervorden–Spatz Syndrome. *New England Journal of Medicine* 348(1), pp. 33-40. doi: 10.1056/NEJMoa020817

Haynes, S. E., Hollopeter, G., Yang, G., Kurpius, D., Dailey, M. E., Gan, W.-B. and Julius, D. 2006. The P2Y12 receptor regulates microglial activation by extracellular nucleotides. *Nature Neuroscience* 9(12), pp. 1512-1519. doi: 10.1038/nn1805

He, H., Zhong, Y., Liang, X., Tan, W., Zhu, J. and Wang, C. 2015. Natural Magnetite: an efficient catalyst for the degradation of organic contaminant. *Scientific Reports* 5, p. 10139. doi: doi:10.1038/srep10139

Hebert, L. E. et al. 1995. Age-specific incidence of Alzheimer's disease in a community population. *Jama* 273(17), pp. 1354-1359.

Henn, K. and Braunbeck, T. 2011. Dechorionation as a tool to improve the fish embryo toxicity test (FET) with the zebrafish (Danio rerio). *Comp Biochem Physiol C Toxicol Pharmacol* 153(1), pp. 91-98. doi: 10.1016/j.cbpc.2010.09.003

Henning, R. and Plattner, H. 1974. Isolation of rat liver lysosomes by loading with colloidal gold. *Biochim Biophys Acta* 354(1), pp. 114-120. doi: 10.1016/0304-4165(74)90059-2

Hernández-Hernández, A. A., Aguirre-Álvarez, G., Cariño-Cortés, R., Mendoza-Huizar, L. H. and Jiménez-Alvarado, R. 2020. Iron oxide nanoparticles: synthesis, functionalization, and applications in diagnosis and treatment of cancer. *Chemical Papers* 74(11), pp. 3809-3824. doi: 10.1007/s11696-020-01229-8

Herrup, K. and Yang, Y. 2007. Cell cycle regulation in the postmitotic neuron: oxymoron or new biology? *Nature Reviews Neuroscience* 8(5), pp. 368-378. doi: 10.1038/nrn2124

Hesketh, G. G., Wartosch, L., Davis, L. J., Bright, N. A. and Luzio, J. P. 2018. The Lysosome and Intracellular Signalling. *Prog Mol Subcell Biol* 57, pp. 151-180. doi: 10.1007/978-3-319-96704-2_6

Hewlett, L. J., Prescott, A. R. and Watts, C. 1994. The coated pit and macropinocytic pathways serve distinct endosome populations. *The Journal of cell biology* 124(5), pp. 689-703. doi: 10.1083/jcb.124.5.689

Hirayama, T., Okuda, K. and Nagasawa, H. 2013. A highly selective turn-on fluorescent probe for iron(ii) to visualize labile iron in living cells. *Chemical Science* 4(3), pp. 1250-1256. doi: 10.1039/C2SC21649C

Hisaoka, K. K. and Firlit, C. F. 1962. Ovarian Cycle and Egg Production in the Zebrafish, Brachydanio rerio. *Copeia* 1962(4), pp. 788-792. doi: 10.2307/1440680

Hjorth, E., Frenkel, D., Weiner, H. and Schultzberg, M. 2010. Effects of immunomodulatory substances on phagocytosis of abeta(1-42) by human microglia. *International Journal of Alzheimers Disease* 2010, p. 798424. doi: 10.4061/2010/798424

Hjorth, E. et al. 2013. Omega-3 fatty acids enhance phagocytosis of Alzheimer's disease-related amyloid-β42 by human microglia and decrease inflammatory markers. *J Alzheimers Dis* 35(4), pp. 697-713. doi: 10.3233/jad-130131

Hochman, J. H., Yamazaki, M., Ohe, T. and Lin, J. H. 2002. Evaluation of drug interactions with P-glycoprotein in drug discovery: in vitro assessment of the potential for drug-drug interactions with P-glycoprotein. *Curr Drug Metab* 3(3), pp. 257-273. doi: 10.2174/1389200023337559

Hopkins, L. E. et al. 2018. Repeated Iron-Soot Exposure and Nose-to-brain Transport of Inhaled Ultrafine Particles. *Toxicologic Pathology* 46(1), pp. 75-84. doi: 10.1177/0192623317729222

Horzmann, K. A. and Freeman, J. L. 2018. Making Waves: New Developments in Toxicology With the Zebrafish. *Toxicol Sci* 163(1), pp. 5-12. doi: 10.1093/toxsci/kfy044

Howe, K. et al. 2013. The zebrafish reference genome sequence and its relationship to the human genome. *Nature* 496(7446), pp. 498-503. doi: 10.1038/nature12111

Høyer-Hansen, M. et al. 2007. Control of macroautophagy by calcium, calmodulin-dependent kinase kinase-beta, and Bcl-2. *Mol Cell* 25(2), pp. 193-205. doi: 10.1016/j.molcel.2006.12.009

Hoyle, B. D., Wong, C. K. and Costerton, J. W. 1992. Disparate efficacy of tobramycin on Ca(2+)-, Mg(2+)-, and HEPES-treated Pseudomonas aeruginosa biofilms. *Can J Microbiol* 38(11), pp. 1214-1218. doi: 10.1139/m92-201

Hu, M., Butt, H.-J., Landfester, K., Bannwarth, M. B., Wooh, S. and Thérien-Aubin, H. 2019. Shaping the Assembly of Superparamagnetic Nanoparticles. *ACS Nano* 13(3), pp. 3015-3022. doi: 10.1021/acsnano.8b07783

Hu, Y.-B., Dammer, E. B., Ren, R.-J. and Wang, G. 2015. The endosomal-lysosomal system: from acidification and cargo sorting to neurodegeneration. *Translational Neurodegeneration* 4(1), p. 18. doi: 10.1186/s40035-015-0041-1

Huang, G. et al. 2013. Superparamagnetic Iron Oxide Nanoparticles: Amplifying ROS Stress to Improve Anticancer Drug Efficacy. *Theranostics* 3(2), pp. 116-126. doi: 10.7150/thno.5411

Huang, H., Lee, S.-c., Cao, J.-j., Zou, C.-w., Chen, X.-g. and Fan, S.-j. 2007. Characteristics of indoor/outdoor PM2.5 and elemental components in generic urban, roadside and industrial plant areas of Guangzhou City, China. *Journal of Environmental Sciences* 19(1), pp. 35-43. doi: https://doi.org/10.1016/S1001-0742(07)60006-0

Huang, H. and Manton, K. 2004. The role of oxidative damage in mitochondria during aging: a review. *Frontiers in bioscience : a journal and virtual library* 9, pp. 1100-1117.

Huang, W.-J., Zhang, X. and Chen, W.-W. 2016. Role of oxidative stress in Alzheimer's disease. *Biomedical reports* 4(5), pp. 519-522. doi: 10.3892/br.2016.630

Huang, Y.-W., Wu, C.-h. and Aronstam, R. S. 2010. Toxicity of Transition Metal Oxide Nanoparticles: Recent Insights from in vitro Studies. *Materials* 3(10), doi: 10.3390/ma3104842

Huhn, G., Schulz, H., Stärk, H. J., Tölle, R. and Schüürmann, G. 1995. Evaluation of regional heavy metal deposition by multivariate analysis of element contents in pine tree barks. *Water, Air, and Soil Pollution* 84(3), pp. 367-383. doi: 10.1007/BF00475349

Huong Giang, N. T. and Kim Oanh, N. T. 2014. Roadside levels and traffic emission rates of PM2.5 and BTEX in Ho Chi Minh City, Vietnam. *Atmospheric Environment* 94, pp. 806-816. doi: https://doi.org/10.1016/j.atmosenv.2014.05.074

Huotari, J. and Helenius, A. 2011. Endosome maturation. *EMBO J* 30(17), pp. 3481-3500. doi: 10.1038/emboj.2011.286

Ishida, Y., Nayak, S., Mindell, J. A. and Grabe, M. 2013. A model of lysosomal pH regulation. *The Journal of general physiology* 141(6), pp. 705-720. doi: 10.1085/jgp.201210930

Itagaki, A. and Kimura, G. 1974. Tes and HEPES buffers in mammalian cell cultures and viral studies: problem of carbon dioxide requirement. *Exp Cell Res* 83(2), pp. 351-361. doi: 10.1016/0014-4827(74)90349-8

Ivankovic, D., Chau, K. Y., Schapira, A. H. and Gegg, M. E. 2016. Mitochondrial and lysosomal biogenesis are activated following PINK1/parkin-mediated mitophagy. *J Neurochem* 136(2), pp. 388-402. doi: 10.1111/jnc.13412

Ivask, A. et al. 2018. Uptake and transcytosis of functionalized superparamagnetic iron oxide nanoparticles in an in vitro blood brain barrier model. *Biomaterials Science* 6(2), pp. 314-323. doi: 10.1039/C7BM01012E

Iversen, T.-G., Skotland, T. and Sandvig, K. 2011. Endocytosis and intracellular transport of nanoparticles: Present knowledge and need for future studies. *Nano Today* 6(2), pp. 176-185. doi: https://doi.org/10.1016/j.nantod.2011.02.003

Jack, C. et al. 2011. Introduction to Revised Criteria for the Diagnosis of Alzheimer's Disease: National Institute on Aging and the Alzheimer Association Workgroups. *Alzheimers Dement* 7(3), pp. 257-262. doi: 10.1016/j.jalz.2011.03.004

Jahng, J. W. S. et al. 2019. Iron overload inhibits late stage autophagic flux leading to insulin resistance. *EMBO reports* 20(10), p. e47911. doi: https://doi.org/10.15252/embr.201947911

Janabi, N., Peudenier, S., Héron, B., Ng, K. H. and Tardieu, M. 1995. Establishment of human microglial cell lines after transfection of primary cultures of embryonic microglial cells with the SV40 large T antigen. *Neurosci Lett* 195(2), pp. 105-108. doi: 10.1016/0304-3940(94)11792-h

Jaworski, T. et al. 2011. Dendritic degeneration, neurovascular defects, and inflammation precede neuronal loss in a mouse model for tau-mediated neurodegeneration. *Am J Pathol* 179(4), pp. 2001-2015. doi: 10.1016/j.ajpath.2011.06.025

Jeng, H. A. and Swanson, J. 2006. Toxicity of metal oxide nanoparticles in mammalian cells. *J Environ Sci Health A Tox Hazard Subst Environ Eng* 41(12), pp. 2699-2711. doi: 10.1080/10934520600966177

Jenkitkasemwong, S., Wang, C.-Y., Mackenzie, B. and Knutson, M. 2012. Physiologic implications of metal-ion transport by ZIP14 and ZIP8. *BioMetals* 25(4), pp. 643-655.

Jin, R. et al. 2019. Iron oxide nanoparticles promote macrophage autophagy and inflammatory response through activation of toll-like Receptor-4 signaling. *Biomaterials* 203, pp. 23-30. doi: https://doi.org/10.1016/j.biomaterials.2019.02.026

Jo, E. J. et al. 2017. Effects of particulate matter on respiratory disease and the impact of meteorological factors in Busan, Korea. *Respir Med* 124, pp. 79-87. doi: 10.1016/j.rmed.2017.02.010

Johansson, A.-C., Appelqvist, H., Nilsson, C., Kågedal, K., Roberg, K. and Öllinger, K. 2010. Regulation of apoptosis-associated lysosomal membrane permeabilization. *Apoptosis* 15(5), pp. 527-540. doi: 10.1007/s10495-009-0452-5

Johansson, M. and Olkkonen, V. M. 2005. Assays for interaction between Rab7 and oxysterol binding protein related protein 1L (ORP1L). *Methods Enzymol* 403, pp. 743-758. doi: 10.1016/s0076-6879(05)03065-x

Johnson, C. S. 1979. Intravenous iron-dextran in the treatment of iron deficient anemia. *J Natl Med Assoc* 71(11), pp. 1101-1105.

Kacher, Y. and Futerman, A. H. 2006. Genetic diseases of sphingolipid metabolism: pathological mechanisms and therapeutic options. *FEBS Lett* 580(23), pp. 5510-5517. doi: 10.1016/j.febslet.2006.08.041

Kaksonen, M. and Roux, A. 2018. Mechanisms of clathrin-mediated endocytosis. *Nature Reviews Molecular Cell Biology* 19(5), pp. 313-326. doi: 10.1038/nrm.2017.132

Kampa, M. and Castanas, E. 2008. Human health effects of air pollution. *Environmental Pollution* 151(2), pp. 362-367. doi: https://doi.org/10.1016/j.envpol.2007.06.012

Kamphuis, W., Orre, M., Kooijman, L., Dahmen, M. and Hol, E. M. 2012. Differential cell proliferation in the cortex of the appsweps1de9 alzheimer's disease mouse model. *Glia* 60(4), pp. 615-629. doi: https://doi.org/10.1002/glia.22295

Kannan, M. B., Khakbaz, H. and Yamamoto, A. 2017. Understanding the influence of HEPES buffer concentration on the biodegradation of pure magnesium: An electrochemical study. *Materials Chemistry and Physics* 197, pp. 47-56. doi: https://doi.org/10.1016/j.matchemphys.2017.05.024

Kao, J.-K. et al. 2016. Chronic Iron Overload Results in Impaired Bacterial Killing of THP-1 Derived Macrophage through the Inhibition of Lysosomal Acidification. *PLoS ONE* 11(5), p. e0156713. doi: 10.1371/journal.pone.0156713

Kardel, F., Wuyts, K., De Wael, K. and Samson, R. 2018. Biomonitoring of atmospheric particulate pollution via chemical composition and magnetic properties of roadside tree leaves. *Environmental Science and Pollution Research* 25(26), pp. 25994-26004. doi: 10.1007/s11356-018-2592-z

Kasten, A., Grüttner, C., Kühn, J.-P., Bader, R., Pasold, J. and Frerich, B. 2014. Comparative in vitro study on magnetic iron oxide nanoparticles for MRI tracking of adipose tissue-derived progenitor cells. *PLoS ONE* 9(9), pp. e108055-e108055. doi: 10.1371/journal.pone.0108055

Keatinge, M. et al. 2015. Glucocerebrosidase 1 deficient Danio rerio mirror key pathological aspects of human Gaucher disease and provide evidence of early microglial activation preceding alpha-synuclein-independent neuronal cell death. *Hum Mol Genet* 24(23), pp. 6640-6652. doi: 10.1093/hmg/ddv369

Keet, C. A., Keller, J. P. and Peng, R. D. 2018. Long-Term Coarse Particulate Matter Exposure Is Associated with Asthma among Children in Medicaid. *Am J Respir Crit Care Med* 197(6), pp. 737-746. doi: 10.1164/rccm.201706-1267OC

Kennedy, C. J., Rakoczy, P. E. and Constable, I. J. 1995. Lipofuscin of the retinal pigment epithelium: A review. *Eye* 9(6), pp. 763-771. doi: 10.1038/eye.1995.192

Khan, M. I., Mohammad, A., Patil, G., Naqvi, S. A. H., Chauhan, L. K. S. and Ahmad, I. 2012. Induction of ROS, mitochondrial damage and autophagy in lung epithelial cancer cells by iron oxide nanoparticles. *Biomaterials* 33(5), pp. 1477-1488. doi: https://doi.org/10.1016/j.biomaterials.2011.10.080

Khatami, M., Alijani, H. Q., Fakheri, B., Mobasseri, M. M., Heydarpour, M., Farahani, Z. K. and Khan, A. U. 2019. Super-paramagnetic iron oxide nanoparticles (SPIONs): Greener synthesis using Stevia plant and evaluation of its antioxidant properties. *Journal of Cleaner Production* 208, pp. 1171-1177. doi: https://doi.org/10.1016/j.jclepro.2018.10.182

Khuzestani, R. B., Schauer, J. J., Wei, Y., Zhang, L., Cai, T., Zhang, Y. and Zhang, Y. 2017. Quantification of the sources of long-range transport of PM2.5 pollution in the Ordos region, Inner Mongolia, China. *Environmental Pollution* 229, pp. 1019-1031. doi: https://doi.org/10.1016/j.envpol.2017.07.093

Killin, L. O. J., Starr, J. M., Shiue, I. J. and Russ, T. C. 2016. Environmental risk factors for dementia: a systematic review. *BMC Geriatrics* 16(1), p. 175. doi: 10.1186/s12877-016-0342-y

Kilpatrick, B. S. 2016. Connecting Ca(2+) and lysosomes to Parkinson disease. *Messenger (Los Angeles, Calif. : Print)* 5(1-2), pp. 76-86. doi: 10.1166/msr.2016.1059

Kim, J., Kundu, M., Viollet, B. and Guan, K. L. 2011. AMPK and mTOR regulate autophagy through direct phosphorylation of Ulk1. *Nat Cell Biol* 13(2), pp. 132-141. doi: 10.1038/ncb2152

Kim, S. U. and de Vellis, J. 2005. Microglia in health and disease. *J Neurosci Res* 81(3), pp. 302-313. doi: 10.1002/jnr.20562

Kimmel, C. B., Ballard, W. W., Kimmel, S. R., Ullmann, B. and Schilling, T. F. 1995. Stages of embryonic development of the zebrafish. *Dev Dyn* 203(3), pp. 253-310. doi: 10.1002/aja.1002030302

Kioumourtzoglou, M.-A., Schwartz, J. D., Weisskopf, M. G., Melly, S. J., Wang, Y., Dominici, F. and Zanobetti, A. 2016. Long-term PM2.5 Exposure and Neurological Hospital Admissions in the Northeastern United States. *Environmental health perspectives* 124(1), pp. 23-29. doi: 10.1289/ehp.1408973

Kirsch, M., Lomonosova, E. E., Korth, H. G., Sustmann, R. and de Groot, H. 1998. Hydrogen peroxide formation by reaction of peroxynitrite with HEPES and related tertiary amines. Implications for a general mechanism. *J Biol Chem* 273(21), pp. 12716-12724. doi: 10.1074/jbc.273.21.12716

Kirschvink, J. L., Kobayashi-Kirschvink, A. and Woodford, B. J. 1992. Magnetite biomineralization in the human brain. *Proc Natl Acad Sci U S A* 89(16), pp. 7683-7687.

Kiselyov, K. et al. 2005. TRP-ML1 is a lysosomal monovalent cation channel that undergoes proteolytic cleavage. *J Biol Chem* 280(52), pp. 43218-43223. doi: 10.1074/jbc.M508210200

Kishi, S., Slack, B. E., Uchiyama, J. and Zhdanova, I. V. 2009. Zebrafish as a genetic model in biological and behavioral gerontology: where development meets aging in vertebrates--a mini-review. *Gerontology* 55(4), pp. 430-441. doi: 10.1159/000228892

Kohashi, T. and Oda, Y. 2008. Initiation of Mauthner- or non-Mauthner-mediated fast escape evoked by different modes of sensory input. *J Neurosci* 28(42), pp. 10641-10653. doi: 10.1523/JNEUROSCI.1435-08.2008

Kossack, M. E. and Draper, B. W. 2019. Genetic regulation of sex determination and maintenance in zebrafish (Danio rerio). *Curr Top Dev Biol* 134, pp. 119-149. doi: 10.1016/bs.ctdb.2019.02.004

Kouassi, G. K., Irudayaraj, J. and McCarty, G. 2005. Activity of glucose oxidase functionalized onto magnetic nanoparticles. *BioMagnetic Research and Technology* 3(1), p. 1. doi: 10.1186/1477-044X-3-1

Krasemann, S. et al. 2017. The TREM2-APOE Pathway Drives the Transcriptional Phenotype of Dysfunctional Microglia in Neurodegenerative Diseases. *Immunity* 47(3), pp. 566-581.e569. doi: 10.1016/j.immuni.2017.08.008

Kress, G. J., Dineley, K. E. and Reynolds, I. J. 2002. The relationship between intracellular free iron and cell injury in cultured neurons, astrocytes, and oligodendrocytes. *The Journal of neuroscience : the official journal of the Society for Neuroscience* 22(14), pp. 5848-5855. doi: 10.1523/JNEUROSCI.22-14-05848.2002

Krewski, D. et al. 2009. Extended follow-up and spatial analysis of the American Cancer Society study linking particulate air pollution and mortality. *Res Rep Health Eff Inst* (140), pp. 5-114; discussion 115-136.

Krpetić, Ž., Porta, F., Caneva, E., Dal Santo, V. and Scarì, G. 2010. Phagocytosis of Biocompatible Gold Nanoparticles. *Langmuir* 26(18), pp. 14799-14805. doi: 10.1021/la102758f

Kuchma, E. A. et al. 2017. Low toxic maghemite nanoparticles for theranostic applications. *International journal of nanomedicine* 12, pp. 6365-6371. doi: 10.2147/IJN.S140368

Kulshrestha, U. C., Reddy, L. A. K., Satyanarayana, J. and Kulshrestha, M. J. 2009. Real-time wet scavenging of major chemical constituents of aerosols and role of rain intensity in Indian region. *Atmospheric Environment* 43(32), pp. 5123-5127. doi: https://doi.org/10.1016/j.atmosenv.2009.07.025

Kumari, S., Mg, S. and Mayor, S. 2010. Endocytosis unplugged: multiple ways to enter the cell. *Cell Research* 20(3), pp. 256-275. doi: 10.1038/cr.2010.19

Künzli, N. et al. 2010. Ambient air pollution and the progression of atherosclerosis in adults. *PLoS ONE* 5(2), p. e9096. doi: 10.1371/journal.pone.0009096

Kunzmann, A. et al. 2011. Efficient internalization of silica-coated iron oxide nanoparticles of different sizes by primary human macrophages and dendritic cells. *Toxicol Appl Pharmacol* 253(2), pp. 81-93. doi: 10.1016/j.taap.2011.03.011

Lafourcade, C., Sobo, K., Kieffer-Jaquinod, S., Garin, J. and van der Goot, F. G. 2008. Regulation of the V-ATPase along the endocytic pathway occurs through reversible subunit association and membrane localization. *PLoS ONE* 3 (7), p. e2758. Available at: http://europepmc.org/abstract/MED/18648502

https://www.ncbi.nlm.nih.gov/pmc/articles/pmid/18648502/pdf/?tool=EBI

https://www.ncbi.nlm.nih.gov/pmc/articles/pmid/18648502/?tool=EBI

https://doi.org/10.1371/journal.pone.0002758

https://europepmc.org/articles/PMC2447177

https://europepmc.org/articles/PMC2447177?pdf=render [Accessed: 2008/07//]. doi: 10.1371/journal.pone.0002758

Lammer, E., Carr, G. J., Wendler, K., Rawlings, J. M., Belanger, S. E. and Braunbeck, T. 2009. Is the fish embryo toxicity test (FET) with the zebrafish (Danio rerio) a potential alternative for the fish acute toxicity test? *Comparative Biochemistry and Physiology Part C: Toxicology & Pharmacology* 149(2), pp. 196-209. doi: https://doi.org/10.1016/j.cbpc.2008.11.006

Landrigan, P. J. 2017. Air pollution and health. *The Lancet Public Health* 2(1), pp. e4-e5. doi: 10.1016/S2468-2667(16)30023-8

Lane, D. J. R. et al. 2015. Cellular iron uptake, trafficking and metabolism: Key molecules and mechanisms and their roles in disease. *Biochimica et Biophysica Acta (BBA) - Molecular Cell Research* 1853(5), pp. 1130-1144. doi: https://doi.org/10.1016/j.bbamcr.2015.01.021

Lasocki, S., Gaillard, T. and Rineau, E. 2014. Iron is essential for living! *Critical care (London, England)* 18(6), pp. 678-678. doi: 10.1186/s13054-014-0678-7

Latorre-Esteves, M., Cortés, A., Torres-Lugo, M. and Rinaldi, C. 2009. Synthesis and characterization of carboxymethyl dextran-coated Mn/Zn ferrite for biomedical applications. *Journal of Magnetism and Magnetic Materials* 321(19), pp. 3061-3066. doi: https://doi.org/10.1016/j.jmmm.2009.05.023

Laurent, S., Forge, D., Port, M., Roch, A., Robic, C., Vander Elst, L. and Muller, R. N. 2008. Magnetic Iron Oxide Nanoparticles: Synthesis, Stabilization, Vectorization, Physicochemical Characterizations, and Biological Applications. *Chemical Reviews* 108(6), pp. 2064-2110. doi: 10.1021/cr068445e

Lawrence, R. E. and Zoncu, R. 2019. The lysosome as a cellular centre for signalling, metabolism and quality control. *Nature Cell Biology* 21(2), pp. 133-142. doi: 10.1038/s41556-018-0244-7

Leblanc, C., Richard, O., Kloareg, B., Viehmann, S., Zetsche, K. and Boyen, C. 1997. Origin and evolution of mitochondria: what have we learnt from red algae? *Current Genetics* 31(3), pp. 193-207. doi: 10.1007/s002940050196

Lee, J.-H. et al. 2015a. Presenilin 1 Maintains Lysosomal Ca(2+) Homeostasis via TRPML1 by Regulating vATPase-Mediated Lysosome Acidification. *Cell Reports* 12(9), pp. 1430-1444. doi: 10.1016/j.celrep.2015.07.050

Lee, N., Yoo, D., Ling, D., Cho, M. H., Hyeon, T. and Cheon, J. 2015b. Iron Oxide Based Nanoparticles for Multimodal Imaging and Magnetoresponsive Therapy. *Chemical Reviews* 115(19), pp. 10637-10689. doi: 10.1021/acs.chemrev.5b00112

Lee, S. H., Lee, H. R., Kim, Y.-R. and Kim, M.-K. 2012. Toxic response of zinc oxide nanoparticles in human epidermal keratinocyte HaCaT cells. *Toxicology and Environmental Health Sciences* 4(1), pp. 14-18. doi: 10.1007/s13530-012-0112-y

Leidgens, S. et al. 2013. Each member of the poly-r(C)-binding protein 1 (PCBP) family exhibits iron chaperone activity toward ferritin. *J Biol Chem* 288(24), pp. 17791-17802. doi: 10.1074/jbc.M113.460253

Lelouvier, B. and Puertollano, R. 2011. Mucolipin-3 Regulates Luminal Calcium, Acidification, and Membrane Fusion in the Endosomal Pathway*. *Journal of Biological Chemistry* 286(11), pp. 9826-9832. doi: https://doi.org/10.1074/jbc.M110.169185

Lenz, K. M. and Nelson, L. H. 2018. Microglia and Beyond: Innate Immune Cells As Regulators of Brain Development and Behavioral Function. *Frontiers in Immunology* 9(698), doi: 10.3389/fimmu.2018.00698

Lev, S., Zeevi, D. A., Frumkin, A., Offen-Glasner, V., Bach, G. and Minke, B. 2010. Constitutive activity of the human TRPML2 channel induces cell degeneration. *The Journal of biological chemistry* 285(4), pp. 2771-2782. doi: 10.1074/jbc.M109.046508

Levada, K. et al. 2020. Progressive lysosomal membrane permeabilization induced by iron oxide nanoparticles drives hepatic cell autophagy and apoptosis. *Nano Convergence* 7(1), p. 17. doi: 10.1186/s40580-020-00228-5

Levine, B. and Kroemer, G. 2008. Autophagy in the pathogenesis of disease. *Cell* 132(1), pp. 27-42. doi: 10.1016/j.cell.2007.12.018

Lévy, M., Lagarde, F., Maraloiu, V.-A., Blanchin, M.-G., Gendron, F., Wilhelm, C. and Gazeau, F. 2010. Degradability of superparamagnetic nanoparticles in a model of intracellular environment: follow-up of magnetic, structural and chemical properties. *Nanotechnology* 21(39), p. 395103. doi: 10.1088/0957-4484/21/39/395103

Lewis, C. S. et al. 2016. Absence of Cytotoxicity towards Microglia of Iron Oxide (alpha-Fe2O3) Nanorhombohedra. *Toxicol Res (Camb)* 5(3), pp. 836-847. doi: 10.1039/c5tx00421g

Lewis, W. H. 1937. Pinocytosis by Malignant Cells. *The American Journal of Cancer* 29(4), pp. 666-679. doi: 10.1158/ajc.1937.666

Li, D. and Ren, Y. 2018. High-Gradient Magnetic Field for Magnetic Nanoparticles Drug Delivery System. *IEEE Transactions on Applied Superconductivity* 28(6), pp. 1-7. doi: 10.1109/TASC.2018.2836999

Li, J. et al. 2020. Silver nanoparticles modulate mitochondrial dynamics and biogenesis in HepG2 cells. *Environ Pollut* 256, p. 113430. doi: 10.1016/j.envpol.2019.113430

Li, L., Chen, Y. and Gibson, S. B. 2013. Starvation-induced autophagy is regulated by mitochondrial reactive oxygen species leading to AMPK activation. *Cell Signal* 25(1), pp. 50-65. doi: 10.1016/j.cellsig.2012.09.020

Lien, C.-L., Harrison, M. R., Tuan, T.-L. and Starnes, V. A. 2012. Heart repair and regeneration: recent insights from zebrafish studies. *Wound repair and regeneration : official publication of the Wound Healing Society [and] the European Tissue Repair Society* 20(5), pp. 638-646. doi: 10.1111/j.1524-475X.2012.00814.x

Lienemann, C.-P., Monnerat, M., Dominik, J. and Perret, D. 1999. Identification of stoichiometric iron-phosphorus colloids produced in a eutrophic lake. *Aquatic Sciences* 61(2), pp. 133-149. doi: 10.1007/s000270050058

Lieschke, G. J. and Currie, P. D. 2007. Animal models of human disease: zebrafish swim into view. *Nat Rev Genet* 8(5), pp. 353-367. doi: 10.1038/nrg2091

Lim, J. P. and Gleeson, P. A. 2011. Macropinocytosis: an endocytic pathway for internalising large gulps. *Immunology & Cell Biology* 89(8), pp. 836-843. doi: https://doi.org/10.1038/icb.2011.20

Lin, J. et al. 2018. Key Role of TFEB Nucleus Translocation for Silver Nanoparticle-Induced Cytoprotective Autophagy. *Small* 14(13), p. e1703711. doi: 10.1002/smll.201703711

Lindberg, C., Crisby, M., Winblad, B. and Schultzberg, M. 2005. Effects of statins on microglia. *J Neurosci Res* 82(1), pp. 10-19. doi: 10.1002/jnr.20615

Lipowsky, R. and Döbereiner, H. G. 1998. Vesicles in contact with nanoparticles and colloids. *Europhysics Letters (EPL)* 43(2), pp. 219-225. doi: 10.1209/epl/i1998-00343-4

Liu, B. et al. 2011. Iron promotes the toxicity of amyloid beta peptide by impeding its ordered aggregation. *J Biol Chem* 286(6), pp. 4248-4256. doi: 10.1074/jbc.M110.158980

Liu, J., Hjorth, E., Zhu, M., Calzarossa, C., Samuelsson, E. B., Schultzberg, M. and Åkesson, E. 2013. Interplay between human microglia and neural stem/progenitor cells in an allogeneic co-culture model. *J Cell Mol Med* 17(11), pp. 1434-1443. doi: 10.1111/jcmm.12123

Liu, L. et al. 2018. Impact of Morphology on Iron Oxide Nanoparticles-Induced Inflammasome Activation in Macrophages. *ACS Appl Mater Interfaces* 10(48), pp. 41197-41206. doi: 10.1021/acsami.8b17474

Liu, Z., Hu, B., Wang, L., Wu, F., Gao, W. and Wang, Y. 2015. Seasonal and diurnal variation in particulate matter (PM10 and PM2.5) at an urban site of Beijing: analyses from a 9-year study. *Environmental Science and Pollution Research* 22(1), pp. 627-642. doi: 10.1007/s11356-014-3347-0

Lleu, P. L. and Rebel, G. 1991. Interference of Good's buffers and other biological buffers with protein determination. *Anal Biochem* 192(1), pp. 215-218. doi: 10.1016/0003-2697(91)90210-k

Lloyd-Evans, E. and Haslett, L. J. 2016. The Lysosomal Storage Disease Continuum With Ageing-Related Neurodegenerative Disease. *Ageing Res Rev* 32, pp. 104-121. doi: 10.1016/j.arr.2016.07.005

Lloyd-Evans, E. et al. 2008. Niemann-Pick disease type C1 is a sphingosine storage disease that causes deregulation of lysosomal calcium. *Nat Med* 14(11), pp. 1247-1255. doi: doi:10.1038/nm.1876

Lloyd-Evans, E. and Platt, F. M. 2011. Lysosomal Ca2+ homeostasis: Role in pathogenesis of lysosomal storage diseases. *Cell Calcium* 50(2), pp. 200-205. doi: https://doi.org/10.1016/j.ceca.2011.03.010

Lloyd-Evans, E. and Waller-Evans, H. 2020. Lysosomal Ca(2+) Homeostasis and Signaling in Health and Disease. *Cold Spring Harb Perspect Biol* 12(6), doi: 10.1101/cshperspect.a035311

Lloyd-Evans, E., Waller-Evans, H., Peterneva, K. and Platt, F. M. 2010. Endolysosomal calcium regulation and disease. *Biochem Soc Trans* 38(6), pp. 1458-1464. doi: 10.1042/bst0381458

Lockwood, T. D. 2004. Cys-His proteases are among the wired proteins of the cell. *Archives of Biochemistry and Biophysics* 432(1), pp. 12-24. doi: https://doi.org/10.1016/j.abb.2004.09.011

Lourida, I., Hannon, E., Littlejohns, T. J., Langa, K. M., Hyppönen, E., Kuzma, E. and Llewellyn, D. J. 2019. Association of Lifestyle and Genetic Risk With Incidence of Dementia. *Jama* 322(5), pp. 430-437. doi: 10.1001/jama.2019.9879

Lovera-Leroux, M., Crobeddu, B., Kassis, N., Petit, P. X., Janel, N., Baeza-Squiban, A. and Andreau, K. 2015. The iron component of particulate matter is antiapoptotic: A clue to the development of lung cancer after exposure to atmospheric pollutants? *Biochimie* 118, pp. 195-206. doi: https://doi.org/10.1016/j.biochi.2015.09.030

Lu, M., Cohen, M. H., Rieves, D. and Pazdur, R. 2010. FDA report: Ferumoxytol for intravenous iron therapy in adult patients with chronic kidney disease. *Am J Hematol* 85(5), pp. 315-319. doi: 10.1002/ajh.21656

Lull, M. E. and Block, M. L. 2010. Microglial activation and chronic neurodegeneration. *Neurotherapeutics* 7(4), pp. 354-365. doi: 10.1016/j.nurt.2010.05.014

Lungu, I. I., Grumezescu, A. M., Volceanov, A. and Andronescu, E. 2019. Nanobiomaterials Used in Cancer Therapy: An Up-To-Date Overview. *Molecules* 24(19), p. 3547.

Lunov, O., Zablotskii, V., Syrovets, T., Röcker, C., Tron, K., Nienhaus, G. U. and Simmet, T. 2011. Modeling receptor-mediated endocytosis of polymer-functionalized iron oxide nanoparticles by human macrophages. *Biomaterials* 32(2), pp. 547-555. doi: 10.1016/j.biomaterials.2010.08.111

Luo, S., Pal, D., Shah, S. J., Kwatra, D., Paturi, K. D. and Mitra, A. K. 2010. Effect of HEPES buffer on the uptake and transport of P-glycoprotein substrates and large neutral amino acids. *Mol Pharm* 7(2), pp. 412-420. doi: 10.1021/mp900193e

Lutgens, S. P. M., Cleutjens, K. B. J. M., Daemen, M. J. A. P. and Heeneman, S. 2007. Cathepsin cysteine proteases in cardiovascular disease. *The FASEB Journal* 21(12), pp. 3029-3041. doi: https://doi.org/10.1096/fj.06-7924com

Luther, E. M., Petters, C., Bulcke, F., Kaltz, A., Thiel, K., Bickmeyer, U. and Dringen, R. 2013. Endocytotic uptake of iron oxide nanoparticles by cultured brain microglial cells. *Acta Biomater* 9(9), pp. 8454-8465. doi: 10.1016/j.actbio.2013.05.022

Luzhna, L., Kathiria, P. and Kovalchuk, O. 2013. Micronuclei in genotoxicity assessment: from genetics to epigenetics and beyond. *Front Genet* 4, p. 131. doi: 10.3389/fgene.2013.00131

Luzio, J. P., Pryor, P. R. and Bright, N. A. 2007. Lysosomes: fusion and function. *Nature Reviews Molecular Cell Biology* 8(8), pp. 622-632. doi: 10.1038/nrm2217

Machala, L., Tuček, J. and Zbořil, R. 2011. Polymorphous Transformations of Nanometric Iron(III) Oxide: A Review. *Chemistry of Materials* 23(14), pp. 3255-3272. doi: 10.1021/cm200397g

Mackenzie, B. G., M. D. 2005. Iron Imports. II. Iron uptake at the apical membrane in the intestine. *American Journal of Physiology-Gastrointestinal and Liver Physiology* 289(6), pp. G981-G986. doi: 10.1152/ajpgi.00363.2005

Maher, B. A. 2019. Airborne Magnetite- and Iron-Rich Pollution Nanoparticles: Potential Neurotoxicants and Environmental Risk Factors for Neurodegenerative Disease, Including Alzheimer's Disease. *J Alzheimers Dis* 71(2), pp. 361-375. doi: 10.3233/jad-190204

Maher, B. A. et al. 2016. Magnetite pollution nanoparticles in the human brain. *Proc Natl Acad Sci U S A* 113(39), pp. 10797-10801. doi: 10.1073/pnas.1605941113

Maher, B. A., Moore, C. and Matzka, J. 2008. Spatial variation in vehicle-derived metal pollution identified by magnetic and elemental analysis of roadside tree leaves. *Atmospheric Environment* 42(2), pp. 364-373. doi: https://doi.org/10.1016/j.atmosenv.2007.09.013

Maheswaran, R. and Elliott, P. 2003. Stroke mortality associated with living near main roads in England and wales: a geographical study. *Stroke* 34(12), pp. 2776-2780. doi: 10.1161/01.Str.0000101750.77547.11

Mahmoudi, M., Quinlan-Pluck, F., Monopoli, M. P., Sheibani, S., Vali, H., Dawson, K. A. and Lynch, I. 2013. Influence of the physiochemical properties of superparamagnetic iron oxide nanoparticles on amyloid β protein fibrillation in solution. *ACS Chemical Neuroscience* 4(3), pp. 475-485. doi: 10.1021/cn300196n

Majumdar, A., Capetillo-Zarate, E., Cruz, D., Gouras, G. K. and Maxfield, F. R. 2011. Degradation of Alzheimer's amyloid fibrils by microglia requires delivery of ClC-7 to lysosomes. *Mol Biol Cell* 22(10), pp. 1664-1676. doi: 10.1091/mbc.E10-09-0745

Majumdar, A., Cruz, D., Asamoah, N., Buxbaum, A., Sohar, I., Lobel, P. and Maxfield, F. R. 2007. Activation of microglia acidifies lysosomes and leads to degradation of Alzheimer amyloid fibrils. *Mol Biol Cell* 18(4), pp. 1490-1496. doi: 10.1091/mbc.e06-10-0975

Malhotra, N., Lee, J.-S., Liman, R. A. D., Ruallo, J. M. S., Villaflores, O. B., Ger, T.-R. and Hsiao, C.-D. 2020. Potential Toxicity of Iron Oxide Magnetic Nanoparticles: A Review. *Molecules (Basel, Switzerland)* 25(14), p. 3159. doi: 10.3390/molecules25143159

Mandrekar, S., Jiang, Q., Lee, C. Y., Koenigsknecht-Talboo, J., Holtzman, D. M. and Landreth, G. E. 2009. Microglia mediate the clearance of soluble Abeta through fluid phase macropinocytosis. *J Neurosci* 29(13), pp. 4252-4262. doi: 10.1523/jneurosci.5572-08.2009

Manjunatha, M., Srinivas Reddy, G., Damle, R., Mallikarjunaiah, K. J. and Ramesh, K. P. 2019. Estimation of structural composition of the inverse spinel ferrites using 57Fe-Zero Field Nuclear Magnetic Resonance. *Ceramics International* 45(7, Part A), pp. 9245-9253. doi: https://doi.org/10.1016/j.ceramint.2019.02.002

Manke, A., Wang, L. and Rojanasakul, Y. 2013. Mechanisms of Nanoparticle-Induced Oxidative Stress and Toxicity. *BioMed research international* 2013, p. 942916. doi: 10.1155/2013/942916

Manshian, B. B., Pokhrel, S., Mädler, L. and Soenen, S. J. 2018. The impact of nanoparticle-driven lysosomal alkalinization on cellular functionality. *Journal of Nanobiotechnology* 16(1), p. 85. doi: 10.1186/s12951-018-0413-7

Marie-Anaïs, F., Mazzolini, J., Herit, F. and Niedergang, F. 2016. Dynamin-Actin Cross Talk Contributes to Phagosome Formation and Closure. *Traffic* 17(5), pp. 487-499. doi: 10.1111/tra.12386

Marshansky, V. and Futai, M. 2008. The V-type H+-ATPase in vesicular trafficking: targeting, regulation and function. *Current opinion in cell biology* 20(4), pp. 415-426. doi: 10.1016/j.ceb.2008.03.015

Martín, M. et al. 2016. Magnetic study on biodistribution and biodegradation of oral magnetic nanostructures in the rat gastrointestinal tract. *Nanoscale* 8(32), pp. 15041-15047. doi: 10.1039/C6NR04678A

Mattson, M. P., Barger, S. W., Begley, J. G. and Mark, R. J. 1995. Chapter 10 Calcium, Free Radicals, and Excitotoxic Neuronal Death in Primary Cell Culture. In: Schwartz, L.M. and Osborne, B.A. eds. *Methods in Cell Biology*. Vol. 46. Academic Press, pp. 187-216.

May, R. C. and Machesky, L. M. 2001. Phagocytosis and the actin cytoskeleton. *J Cell Sci* 114(Pt 6), pp. 1061-1077.

Mayor, S., Parton, R. G. and Donaldson, J. G. 2014. Clathrin-independent pathways of endocytosis. *Cold Spring Harb Perspect Biol* 6(6), doi: 10.1101/cshperspect.a016758

McBrayer, M. and Nixon, Ralph A. 2013. Lysosome and calcium dysregulation in Alzheimer's disease: partners in crime. *Biochemical Society Transactions* 41(6), pp. 1495-1502. doi: 10.1042/bst20130201

McKhann, G. et al. 2011. The diagnosis of dementia due to Alzheimer's disease: Recommendations from the National Institute on Aging-Alzheimer's Association workgroups on diagnostic guidelines for Alzheimer's disease. *Alzheimers Dementia* 7(3), pp. 263-269. doi: 10.1016/j.jalz.2011.03.005

Medina, D. L. et al. 2015. Lysosomal calcium signalling regulates autophagy through calcineurin and TFEB. *Nature Cell Biology* 17(3), pp. 288-299. doi: 10.1038/ncb3114

Medzon, E. L. and Gedies, A. 1971. Substitution of 4-(2-hydroxyethyl)-1-piperazineethane sulfonic acid (HEPES) for bicarbonate in protein-free animal cell culture medium: application to vaccinia virus quantitation and fluorogenic acetylesterase assay in living LM cells. *Canadian Journal of Microbiology* 17(5), pp. 651-653. doi: 10.1139/m71-105

Mehta, R., Chakraborty, M. and Parikh, P. 2014. Nanofuels: Combustion, engine performance and emissions. *Fuel* 120(15), pp. 91-97. doi: 10.1016/j.fuel.2013.12.008

Melief, J. et al. 2012. Phenotyping primary human microglia: Tight regulation of LPS responsiveness. *Glia* 60(10), pp. 1506-1517. doi: https://doi.org/10.1002/glia.22370

Mercer, J. and Helenius, A. 2012. Gulping rather than sipping: macropinocytosis as a way of virus entry. *Curr Opin Microbiol* 15(4), pp. 490-499. doi: 10.1016/j.mib.2012.05.016

Meyerstein, D. 2021. Re-examining Fenton and Fenton-like reactions. *Nature Reviews Chemistry* 5(9), pp. 595-597. doi: 10.1038/s41570-021-00310-4

Michell, R. H., Heath, V. L., Lemmon, M. A. and Dove, S. K. 2006. Phosphatidylinositol 3,5-bisphosphate: metabolism and cellular functions. *Trends in Biochemical Sciences* 31(1), pp. 52-63. doi: https://doi.org/10.1016/j.tibs.2005.11.013

Michl, J., Park, K. C. and Swietach, P. 2019. Evidence-based guidelines for controlling pH in mammalian live-cell culture systems. *Commun Biol* 2, p. 144. doi: 10.1038/s42003-019-0393-7

Millard, E. E., Srivastava, K., Traub, L. M., Schaffer, J. E. and Ory, D. S. 2000. Niemann-Pick Type C1 (NPC1) Overexpression Alters Cellular Cholesterol Homeostasis *. *Journal of Biological Chemistry* 275(49), pp. 38445-38451. doi: 10.1074/jbc.M003180200

Miller, M. A., Arlauckas, S. and Weissleder, R. 2017. Prediction of Anti-cancer Nanotherapy Efficacy by Imaging. *Nanotheranostics* 1(3), pp. 296-312. doi: 10.7150/ntno.20564

Minotti, G. 1993. Sources and role of iron in lipid peroxidation. *Chemical Research in Toxicology* 6(2), pp. 134-146. doi: 10.1021/tx00032a001

Mishra, R., Krishnamoorthy, P., Gangamma, S., Raut, A. A. and Kumar, H. 2020. Particulate matter (PM(10)) enhances RNA virus infection through modulation of innate immune responses. *Environ Pollut* 266(Pt 1), p. 115148. doi: 10.1016/j.envpol.2020.115148

Mitchell, R. and Maher, B. 2009. Evaluation and application of biomagnetic monitoring of traffic-derived particulate pollution. *Atmospheric Environment* 43(13), pp. 2095-2103. doi: https://doi.org/10.1016/j.atmosenv.2009.01.042

Miyamoto, A. et al. 2016. Microglia contact induces synapse formation in developing somatosensory cortex. *Nat Commun* 7, p. 12540. doi: 10.1038/ncomms12540

Miyayama, T. and Matsuoka, M. 2016. Involvement of lysosomal dysfunction in silver nanoparticle-induced cellular damage in A549 human lung alveolar epithelial cells. *Journal of Occupational Medicine and Toxicology* 11(1), p. 1. doi: 10.1186/s12995-016-0090-0

Mizushima, N., Yoshimori, T. and Levine, B. 2010. Methods in mammalian autophagy research. *Cell* 140(3), pp. 313-326. doi: 10.1016/j.cell.2010.01.028

Monier, A., Evrard, P., Gressens, P. and Verney, C. 2006. Distribution and differentiation of microglia in the human encephalon during the first two trimesters of gestation. *Journal of Comparative Neurology* 499(4), pp. 565-582. doi: https://doi.org/10.1002/cne.21123

Montesano, R., Roth, J., Robert, A. and Orci, L. 1982. Non-coated membrane invaginations are involved in binding and internalization of cholera and tetanus toxins. *Nature* 296(5858), pp. 651-653. doi: 10.1038/296651a0

Moos, T. 1996. Immunohistochemical localization of intraneuronal transferrin receptor immunoreactivity in the adult mouse central nervous system. *Journal of Comparative Neurology* 375(4), pp. 675-692. doi: https://doi.org/10.1002/(SICI)1096-9861(19961125)375:4<675::AID-CNE8>3.0.CO;2-Z

Morena, F. et al. 2017. A Comparison of Lysosomal Enzymes Expression Levels in Peripheral Blood of Mild- and Severe-Alzheimer's Disease and MCI Patients: Implications for Regenerative Medicine Approaches. *International journal of molecular sciences* 18(8), p. 1806. doi: 10.3390/ijms18081806

Moreno-García, A., Kun, A., Calero, O., Medina, M. and Calero, M. 2018. An Overview of the Role of Lipofuscin in Age-Related Neurodegeneration. *Frontiers in Neuroscience* 12(464), doi: 10.3389/fnins.2018.00464

Morgan, A. J., Platt, F. M., Lloyd-Evans, E. and Galione, A. 2011a. Molecular mechanisms of endolysosomal Ca2+ signalling in health and disease. *Biochem J* 439(3), pp. 349-374. doi: 10.1042/bj20110949

Morgan, E. H., Smith, G. D. and Peters, T. J. 1986. Uptake and subcellular processing of 59Fe-125I-labelled transferrin by rat liver. *The Biochemical journal* 237(1), pp. 163-173. doi: 10.1042/bj2370163

Morgan, T. E. et al. 2011b. Glutamatergic neurons in rodent models respond to nanoscale particulate urban air pollutants in vivo and in vitro. *Environmental health perspectives* 119(7), pp. 1003-1009. doi: 10.1289/ehp.1002973

Morita, M., Gravel, S. P., Hulea, L., Larsson, O., Pollak, M., St-Pierre, J. and Topisirovic, I. 2015. mTOR coordinates protein synthesis, mitochondrial activity and proliferation. *Cell Cycle* 14(4), pp. 473-480. doi: 10.4161/15384101.2014.991572

Moya-Alvarado, G., Gershoni-Emek, N., Perlson, E. and Bronfman, F. C. 2016. Neurodegeneration and Alzheimer's disease (AD). What Can Proteomics Tell Us About the Alzheimer's Brain? *Molecular and Cellular Proteomics* 15(2), pp. 409-425. doi: 10.1074/mcp.R115.053330

Mukhopadhyay, A. and Weiner, H. 2007. Delivery of drugs and macromolecules to mitochondria. *Advanced Drug Delivery Reviews* 59(8), pp. 729-738. doi: https://doi.org/10.1016/j.addr.2007.06.004

Mulder, D. W., Phiri, M. M., Jordaan, A. and Vorster, B. C. Modified HEPES one-pot synthetic strategy for gold nanostars. *Royal Society Open Science* 6(6), p. 190160. doi: 10.1098/rsos.190160

Mulens-Arias, V., Rojas, J. M. and Barber, D. F. 2020. The Intrinsic Biological Identities of Iron Oxide Nanoparticles and Their Coatings: Unexplored Territory for Combinatorial Therapies. *Nanomaterials (Basel)* 10(5), doi: 10.3390/nano10050837

Müller, O., Sattler, T., Flötenmeyer, M., Schwarz, H., Plattner, H. and Mayer, A. 2000. Autophagic tubes: vacuolar invaginations involved in lateral membrane sorting and inverse vesicle budding. *J Cell Biol* 151(3), pp. 519-528. doi: 10.1083/jcb.151.3.519

Múzquiz-Ramos, E. M., Guerrero-Chávez, V., Macías-Martínez, B. I., López-Badillo, C. M. and García-Cerda, L. A. 2015. Synthesis and characterization of maghemite nanoparticles for hyperthermia applications. *Ceramics International* 41(1, Part A), pp. 397-402. doi: https://doi.org/10.1016/j.ceramint.2014.08.083

Nagira, K. et al. 1995. Effects of organic pH buffers on a cell growth and an antibody production of human-human hybridoma HB4C5 cells in a serum-free culture. *Cytotechnology* 17(2), pp. 117-125. doi: 10.1007/BF00749399

Naqvi, S., Samim, M., Abdin, M., Ahmed, F. J., Maitra, A., Prashant, C. and Dinda, A. K. 2010. Concentration-dependent toxicity of iron oxide nanoparticles mediated by increased oxidative stress. *Int J Nanomedicine* 5, pp. 983-989. doi: 10.2147/ijn.S13244

Nash, B. et al. 2019. Morphine-Induced Modulation of Endolysosomal Iron Mediates Upregulation of Ferritin Heavy Chain in Cortical Neurons. *eneuro* 6(4), pp. ENEURO.0237-0219.2019. doi: 10.1523/ENEURO.0237-19.2019

Natarajan, V., Wilson, C. L., Hayward, S. L. and Kidambi, S. 2015. Titanium Dioxide Nanoparticles Trigger Loss of Function and Perturbation of Mitochondrial Dynamics in Primary Hepatocytes. *PLoS ONE* 10(8), p. e0134541. doi: 10.1371/journal.pone.0134541

National Statistics UK. 2021. *Air quality statistics in the UK, 1987 to 2020 - Particulate matter (PM10/PM2.5)*. Department for Environment, Food & Rural Affairs: Available at: https://www.gov.uk/government/statistics/air-quality-statistics/concentrations-of-particulate-matter-pm10-and-pm25 [Accessed: 12/07/].

Nave, K.-A. and Werner, H. B. 2014. Myelination of the Nervous System: Mechanisms and Functions. *Annual Review of Cell and Developmental Biology* 30(1), pp. 503-533. doi: 10.1146/annurev-cellbio-100913-013101

Neely Kayala, K. M., Dickinson, G. D., Minassian, A., Walls, K. C., Green, K. N. and Laferla, F. M. 2012. Presenilin-null cells have altered two-pore calcium channel expression and lysosomal calcium: implications for lysosomal function. *Brain Res* 1489, pp. 8-16. doi: 10.1016/j.brainres.2012.10.036

Neiss, W. F. 1984. A coat of glycoconjugates on the inner surface of the lysosomal membrane in the rat kidney. *Histochemistry* 80(6), pp. 603-608.

Nemmar, A. et al. 2002a. Passage of inhaled particles into the blood circulation in humans. *Circulation* 105(4), pp. 411-414. doi: 10.1161/hc0402.104118

Nemmar, A. et al. 2002b. Passage of Inhaled Particles Into the Blood Circulation in Humans. *Circulation* 105(4), pp. 411-414. doi: 10.1161/hc0402.104118

Neyens, E. and Baeyens, J. 2003. A review of classic Fenton's peroxidation as an advanced oxidation technique. *Journal of Hazardous Materials* 98(1), pp. 33-50. doi: https://doi.org/10.1016/S0304-3894(02)00282-0

Nguyen, K. C., Seligy, V. L., Massarsky, A., Moon, T. W., Rippstein, P., Tan, J. and Tayabali, A. F. 2013. Comparison of toxicity of uncoated and coated silver nanoparticles. *Journal of Physics: Conference Series* 429, p. 012025. doi: 10.1088/1742-6596/429/1/012025

Nie, J., Mahato, S. and Zelhof, A. C. 2015. Imaging the Drosophila retina: zwitterionic buffers PIPES and HEPES induce morphological artifacts in tissue fixation. *BMC Dev Biol* 15, p. 10. doi: 10.1186/s12861-015-0056-y

Nielsen, E., Severin, F., Backer, J. M., Hyman, A. A. and Zerial, M. 1999. Rab5 regulates motility of early endosomes on microtubules. *Nature Cell Biology* 1(6), pp. 376-382. doi: 10.1038/14075

Niimi, A. J. and LaHam, Q. N. 1974. Influence of breeding time interval on egg number, mortality, and hatching of the zebra fish Brachydanio verio. *Can J Zool* 52(4), pp. 515-517. doi: 10.1139/z74-063

Nikzamir, M., Akbarzadeh, A. and Panahi, Y. 2021. An overview on nanoparticles used in biomedicine and their cytotoxicity. *Journal of Drug Delivery Science and Technology* 61, p. 102316. doi: https://doi.org/10.1016/j.jddst.2020.102316

Nimmerjahn, A., Kirchhoff, F. and Helmchen, F. 2005. Resting microglial cells are highly dynamic surveillants of brain parenchyma in vivo. *Science* 308(5726), pp. 1314-1318. doi: 10.1126/science.1110647

Niska, K., Pyszka, K., Tukaj, C., Wozniak, M., Radomski, M. W. and Inkielewicz-Stepniak, I. 2015. Titanium dioxide nanoparticles enhance production of superoxide anion and alter the antioxidant system in human osteoblast cells. *International journal of nanomedicine* 10, pp. 1095-1107. doi: 10.2147/IJN.S73557

Norbury, C. C., Hewlett, L. J., Prescott, A. R., Shastri, N. and Watts, C. 1995. Class I MHC presentation of exogenous soluble antigen via macropinocytosis in bone marrow macrophages. *Immunity* 3(6), pp. 783-791. doi: 10.1016/1074-7613(95)90067-5

Oberdorster, G., Sharp, Z., Atudorei, V., Elder, A., Gelein, R., Kreyling, W. and Cox, C. 2004. Translocation of inhaled ultrafine particles to the brain. *Inhal Toxicol* 16(6-7), pp. 437-445. doi: 10.1080/08958370490439597

Oberdörster, G. et al. 2002. Extrapulmonary translocation of ultrafine carbon particles following whole-body inhalation exposure of rats. *Journal of Toxicology and Environmental Health, Part A* 65(20), pp. 1531-1543. doi: 10.1080/00984100290071658

Ogungbemi, A., Leuthold, D., Scholz, S. and Küster, E. 2019. Hypo- or hyperactivity of zebrafish embryos provoked by neuroactive substances: a review on how experimental parameters impact the predictability of behavior changes. *Environmental Sciences Europe* 31(1), p. 88. doi: 10.1186/s12302-019-0270-5

Oppenheim, H. A., Lucero, J., Guyot, A. C., Herbert, L. M., McDonald, J. D., Mabondzo, A. and Lund, A. K. 2013. Exposure to vehicle emissions results in altered blood brain barrier permeability and expression of matrix metalloproteinases and tight junction proteins in mice. *Particle and fibre toxicology* 10, p. 62. doi: 10.1186/1743-8977-10-62

Orel, V. E. et al. 2019. The comparison between superparamagnetic and ferromagnetic iron oxide nanoparticles for cancer nanotherapy in the magnetic resonance system. *Nanotechnology* 30(41), p. 415701. doi: 10.1088/1361-6528/ab2ea7

Pagano, R. E. 2003. Endocytic trafficking of glycosphingolipids in sphingolipid storage diseases. *Philos Trans R Soc Lond B Biol Sci* 358(1433), pp. 885-891. doi: 10.1098/rstb.2003.1275

Pagano, R. E., Puri, V., Dominguez, M. and Marks, D. L. 2000. Membrane traffic in sphingolipid storage diseases. *Traffic* 1(11), pp. 807-815. doi: 10.1034/j.1600-0854.2000.011101.x

Pamarthy, S., Kulshrestha, A., Katara, G. K. and Beaman, K. D. 2018. The curious case of vacuolar ATPase: regulation of signaling pathways. *Molecular Cancer* 17(1), p. 41. doi: 10.1186/s12943-018-0811-3

Pang, Y. et al. 2021. Associations of long-term exposure to traffic-related air pollution with risk of valvular heart disease based on a cross-sectional study. *Ecotoxicology and Environmental Safety* 209, p. 111753. doi: https://doi.org/10.1016/j.ecoenv.2020.111753

Pankhurst, Q., Hautot, D., Khan, N. and Dobson, J. 2008. Increased levels of magnetic iron compounds in Alzheimer's disease. *J Alzheimers Dis* 13(1), pp. 49-52.

Paolicelli, R. C. et al. 2017. TDP-43 Depletion in Microglia Promotes Amyloid Clearance but Also Induces Synapse Loss. *Neuron* 95(2), pp. 297-308.e296. doi: 10.1016/j.neuron.2017.05.037

10.1016/j.neuron.2017.05.037. Epub 2017 Jun 29.

Parichy, D. M. 2015. Advancing biology through a deeper understanding of zebrafish ecology and evolution. *eLife* 4, doi: 10.7554/eLife.05635

Parichy, D. M., Elizondo, M. R., Mills, M. G., Gordon, T. N. and Engeszer, R. E. 2009. Normal table of postembryonic zebrafish development: Staging by externally visible anatomy of the living fish. *Developmental Dynamics* 238(12), pp. 2975-3015. doi: https://doi.org/10.1002/dvdy.22113

Park, E.-J. et al. 2014a. Magnetic iron oxide nanoparticles induce autophagy preceding apoptosis through mitochondrial damage and ER stress in RAW264.7 cells. *Toxicology in Vitro* 28(8), pp. 1402-1412. doi: https://doi.org/10.1016/j.tiv.2014.07.010

Park, E.-J. et al. 2014b. Magnetite- and maghemite-induced different toxicity in murine alveolar macrophage cells. *Archives of Toxicology* 88(8), pp. 1607-1618. doi: 10.1007/s00204-014-1210-1

Park, J. et al. 2011. Size dependent macrophage responses and toxicological effects of Ag nanoparticles. *Chemical Communications* 47(15), pp. 4382-4384. doi: 10.1039/C1CC10357A

Patil, R. M. et al. 2018. Comprehensive cytotoxicity studies of superparamagnetic iron oxide nanoparticles. *Biochemistry and Biophysics Reports* 13, pp. 63-72. doi: https://doi.org/10.1016/j.bbrep.2017.12.002

Pattammattel, A. et al. 2021. Iron speciation in particulate matter (PM2.5) from urban Los Angeles using spectro-microscopy methods. *Atmospheric Environment* 245, p. 117988. doi: https://doi.org/10.1016/j.atmosenv.2020.117988

Patten, K. T. and Lein, P. J. 2019. Gene-environment interactions determine risk for dementia: the influence of lifestyle on genetic risk for dementia. *Annals of translational medicine* 7(Suppl 8), pp. S322-S322. doi: 10.21037/atm.2019.09.155

Paul, B. T., Manz, D. H., Torti, F. M. and Torti, S. V. 2017. Mitochondria and Iron: current questions. *Expert review of hematology* 10(1), pp. 65-79. doi: 10.1080/17474086.2016.1268047

Peña-Llopis, S. et al. 2011. Regulation of TFEB and V-ATPases by mTORC1. *EMBO J* 30(16), pp. 3242-3258. doi: 10.1038/emboj.2011.257

Pereira, A. C., Gomes, T., Ferreira Machado, M. R. and Rocha, T. L. 2019. The zebrafish embryotoxicity test (ZET) for nanotoxicity assessment: from morphological to molecular approach. *Environmental Pollution* 252, pp. 1841-1853. doi: https://doi.org/10.1016/j.envpol.2019.06.100

Pereira, A. C., Gonçalves, B. B., Brito, R. d. S., Vieira, L. G., Lima, E. C. d. O. and Rocha, T. L. 2020. Comparative developmental toxicity of iron oxide nanoparticles and ferric chloride to zebrafish (Danio rerio) after static and semi-static exposure. *Chemosphere* 254, p. 126792. doi: https://doi.org/10.1016/j.chemosphere.2020.126792

Perera, R. M. and Zoncu, R. 2016. The Lysosome as a Regulatory Hub. *Annual Review of Cell and Developmental Biology* 32(1), pp. 223-253. doi: 10.1146/annurev-cellbio-111315-125125

Perlmutter, L. S., Barron, E. and Chui, H. C. 1990. Morphologic association between microglia and senile plaque amyloid in Alzheimer's disease. *Neurosci Lett* 119(1), pp. 32-36.

Petrat, F., Rauen, U. and de Groot, H. 1999. Determination of the chelatable iron pool of isolated rat hepatocytes by digital fluorescence microscopy using the fluorescent probe, phen green SK. *Hepatology* 29(4), pp. 1171-1179. doi: 10.1002/hep.510290435

Petters, C., Thiel, K. and Dringen, R. 2016. Lysosomal iron liberation is responsible for the vulnerability of brain microglial cells to iron oxide nanoparticles: comparison with neurons and astrocytes. *Nanotoxicology* 10(3), pp. 332-342. doi: 10.3109/17435390.2015.1071445

Pham, X. N., Nguyen, T. P., Pham, T. N., Tran, T. T. N. and Tran, T. V. T. 2016. Synthesis and characterization of chitosan-coated magnetite nanoparticles and their application in curcumin drug delivery. *Advances in Natural Sciences: Nanoscience and Nanotechnology* 7(4), p. 045010. doi: 10.1088/2043-6262/7/4/045010

Piao, M. J. et al. 2011. Silver nanoparticles induce oxidative cell damage in human liver cells through inhibition of reduced glutathione and induction of mitochondria-involved apoptosis. *Toxicol Lett* 201(1), pp. 92-100. doi: 10.1016/j.toxlet.2010.12.010

Pickard, M. R. and Chari, D. M. 2010. Robust Uptake of Magnetic Nanoparticles (MNPs) by Central Nervous System (CNS) Microglia: Implications for Particle Uptake in Mixed Neural Cell Populations. *International journal of molecular sciences* 11(3), doi: 10.3390/ijms11030967

Pierzyńska-Mach, A., Janowski, P. A. and Dobrucki, J. W. 2014. Evaluation of acridine orange, LysoTracker Red, and quinacrine as fluorescent probes for long-term tracking of acidic vesicles. *Cytometry Part A* 85(8), pp. 729-737. doi: https://doi.org/10.1002/cyto.a.22495

Pipal, A. S., Kulshrestha, A. and Taneja, A. 2011. Characterization and morphological analysis of airborne PM2.5 and PM10 in Agra located in north central India. *Atmospheric Environment* 45(21), pp. 3621-3630. doi: https://doi.org/10.1016/j.atmosenv.2011.03.062

Piper, R. C., Dikic, I. and Lukacs, G. L. 2014. Ubiquitin-dependent sorting in endocytosis. *Cold Spring Harbor perspectives in biology* 6(1), p. a016808. doi: 10.1101/cshperspect.a016808

Platt, F. M., Boland, B. and van der Spoel, A. C. 2012. Lysosomal storage disorders: The cellular impact of lysosomal dysfunction. *Journal of Cell Biology* 199(5), pp. 723-734. doi: 10.1083/jcb.201208152

Platt, F. M. and Lachmann, R. H. 2009. Treating lysosomal storage disorders: current practice and future prospects. *Biochim Biophys Acta* 1793(4), pp. 737-745. doi: 10.1016/j.bbamcr.2008.08.009

Pont-Lezica, L., Beumer, W., Colasse, S., Drexhage, H., Versnel, M. and Bessis, A. 2014. Microglia shape corpus callosum axon tract fasciculation: functional impact of prenatal inflammation. *Eur J Neurosci* 39(10), pp. 1551-1557. doi: 10.1111/ejn.12508

Poole, C. A., Reilly, H. C. and Flint, M. H. 1982. The adverse effects of HEPES, TES, and BES zwitterion buffers on the ultrastructure of cultured chick embryo epiphyseal chondrocytes. *In Vitro* 18(9), pp. 755-765. doi: 10.1007/BF02796499

Power, M. C., Weisskopf, M. G., Alexeeff, S. E., Coull, B. A., Spiro, A., 3rd and Schwartz, J. 2011. Traffic-related air pollution and cognitive function in a cohort of older men. *Environmental health perspectives* 119(5), pp. 682-687. doi: 10.1289/ehp.1002767

Predescu, A. M. et al. Synthesis and characterization of dextran-coated iron oxide nanoparticles. *Royal Society Open Science* 5(3), p. 171525. doi: 10.1098/rsos.171525

Preker, A. S., Adeyi, O. O., Lapetra, M. G., Simon, D.-C. and Keuffel, E. 2016. Health Care Expenditures Associated With Pollution: Exploratory Methods and Findings. *Annals of Global Health* 82(5), pp. 711-721. doi: https://doi.org/10.1016/j.aogh.2016.12.003

Provenzano, R., Schiller, B., Rao, M., Coyne, D., Brenner, L. and Pereira, B. J. 2009. Ferumoxytol as an intravenous iron replacement therapy in hemodialysis patients. *Clin J Am Soc Nephrol* 4(2), pp. 386-393. doi: 10.2215/cjn.02840608

Puertollano, R. and Kiselyov, K. 2009. TRPMLs: in sickness and in health. *American journal of physiology. Renal physiology* 296(6), pp. F1245-F1254. doi: 10.1152/ajprenal.90522.2008

Puett, R. C. et al. 2009. Chronic fine and coarse particulate exposure, mortality, and coronary heart disease in the Nurses' Health Study. *Environmental health perspectives* 117(11), pp. 1697-1701. doi: 10.1289/ehp.0900572

Quevedo, C., Behl, M., Ryan, K., Paules, R. S., Alday, A., Muriana, A. and Alzualde, A. 2019. Detection and Prioritization of Developmentally Neurotoxic and/or Neurotoxic Compounds Using Zebrafish. *Toxicol Sci* 168(1), pp. 225-240. doi: 10.1093/toxsci/kfy291

Raaschou-Nielsen, O. et al. 2013. Air pollution and lung cancer incidence in 17 European cohorts: prospective analyses from the European Study of Cohorts for Air Pollution Effects (ESCAPE). *The Lancet Oncology* 14(9), pp. 813-822. doi: https://doi.org/10.1016/S1470-2045(13)70279-1

Rabinovitch, M. 1995. Professional and non-professional phagocytes: an introduction. *Trends in Cell Biology* 5(3), pp. 85-87. doi: https://doi.org/10.1016/S0962-8924(00)88955-2

Racoosin, E. L. and Swanson, J. A. 1989. Macrophage colony-stimulating factor (rM-CSF) stimulates pinocytosis in bone marrow-derived macrophages. *J Exp Med* 170(5), pp. 1635-1648. doi: 10.1084/jem.170.5.1635

Ramanathan, V. and Feng, Y. 2009. Air pollution, greenhouse gases and climate change: Global and regional perspectives. *Atmospheric Environment* 43(1), pp. 37-50. doi: https://doi.org/10.1016/j.atmosenv.2008.09.063

Ranft, U., Schikowski, T., Sugiri, D., Krutmann, J. and Krämer, U. 2009. Long-term exposure to traffic-related particulate matter impairs cognitive function in the elderly. *Environ Res* 109(8), pp. 1004-1011. doi: 10.1016/j.envres.2009.08.003

Ransohoff, R. M., Schafer, D., Vincent, A., Blachère, N. E. and Bar-Or, A. 2015. Neuroinflammation: Ways in Which the Immune System Affects the Brain. *Neurotherapeutics* 12(4), pp. 896-909. doi: 10.1007/s13311-015-0385-3

Ranson, P. A. and Thomas, W. E. 1991. Pinocytosis as a select marker of ramified microglia in vivo and in vitro. *Journal of Histochemistry & Cytochemistry* 39(6), pp. 853-858. doi: 10.1177/39.6.2033242

Rawson, D., Zhang, T., Kalicharan, D., & Jongebloed, WL. 2000. Field emission scanning electron microscopy and transmission electron microscopy studies of the chorion, plasma membrane and syncytial layers of the gastrula-stage embryo of the zebrafish Brachydanio rerio: a consideration of the structural and functional relationships with respect to cryoprotectant penetration. *Aquaculture research* 31(3), pp. 325-336.

Razani, B., Woodman, S. E. and Lisanti, M. P. 2002. Caveolae: From Cell Biology to Animal Physiology. *Pharmacological Reviews* 54(3), pp. 431-467. doi: 10.1124/pr.54.3.431

Reggiori, F. and Ungermann, C. 2017. Autophagosome Maturation and Fusion. *Journal of Molecular Biology* 429(4), pp. 486-496. doi: https://doi.org/10.1016/j.jmb.2017.01.002

Reichle Jr, H. G. et al. 1986. Middle and upper tropospheric carbon monoxide mixing ratios as measured by a satellite-borne remote sensor during November 1981. *Journal of Geophysical Research: Atmospheres* 91(D10), pp. 10865-10887. doi: https://doi.org/10.1029/JD091iD10p10865

Reimer, M. M. et al. 2013. Dopamine from the brain promotes spinal motor neuron generation during development and adult regeneration. *Dev Cell* 25(5), pp. 478-491. doi: 10.1016/j.devcel.2013.04.012

Rejman, J., Oberle, V., Zuhorn, I. S. and Hoekstra, D. 2004. Size-dependent internalization of particles via the pathways of clathrin- and caveolae-mediated endocytosis. *Biochemical Journal* 377(1), pp. 159-169. doi: 10.1042/bj20031253

Remya, N. S., Syama, S., Sabareeswaran, A. and Mohanan, P. V. 2016. Toxicity, toxicokinetics and biodistribution of dextran stabilized Iron oxide Nanoparticles for biomedical applications. *International Journal of Pharmaceutics* 511(1), pp. 586-598. doi: https://doi.org/10.1016/j.ijpharm.2016.06.119

Rennick, J. J., Johnston, A. P. R. and Parton, R. G. 2021. Key principles and methods for studying the endocytosis of biological and nanoparticle therapeutics. *Nature Nanotechnology* 16(3), pp. 266-276. doi: 10.1038/s41565-021-00858-8

Requia, W. J. and Koutrakis, P. 2018. Mapping distance-decay of premature mortality attributable to PM2.5-related traffic congestion. *Environmental Pollution* 243, pp. 9-16. doi: https://doi.org/10.1016/j.envpol.2018.08.056

Rezaie, P. and Male, D. 1999. Colonisation of the developing human brain and spinal cord by microglia: a review. *Microscopy Research and Technique* 45(6), pp. 359-382. doi: https://doi.org/10.1002/(SICI)1097-0029(19990615)45:6<359::AID-JEMT4>3.0.CO;2-D

Ridnour, L. A., Sim, J. E., Hayward, M. A., Wink, D. A., Martin, S. M., Buettner, G. R. and Spitz, D. R. 2000. A Spectrophotometric Method for the Direct Detection and Quantitation of Nitric Oxide, Nitrite, and Nitrate in Cell Culture Media. *Analytical Biochemistry* 281(2), pp. 223-229. doi: https://doi.org/10.1006/abio.2000.4583

Rizzoli, S. O. and Betz, W. J. 2004. The Structural Organization of the Readily Releasable Pool of Synaptic Vesicles. *Science* 303(5666), p. 2037. doi: 10.1126/science.1094682

Roczniak-Ferguson, A. et al. 2012. The transcription factor TFEB links mTORC1 signaling to transcriptional control of lysosome homeostasis. *Sci Signal* 5(228), p. ra42. doi: 10.1126/scisignal.2002790

Rodriguez-Paris, J. M., Nolta, K. V. and Steck, T. L. 1993. Characterization of lysosomes isolated from Dictyostelium discoideum by magnetic fractionation. *Journal of Biological Chemistry* 268(12), pp. 9110-9116. doi: https://doi.org/10.1016/S0021-9258(18)52984-7

Rogaev, E. I. et al. 2019. Familial Alzheimer's disease in kindreds with missense mutations in a gene on chromosome 1 related to the Alzheimer's disease type 3 gene. *Nature* 376(6543), p. 775. doi: doi:10.1038/376775a0

Rosales, C. and Uribe-Querol, E. 2017. Phagocytosis: A Fundamental Process in Immunity. *BioMed research international* 2017, pp. 9042851-9042851. doi: 10.1155/2017/9042851

Rosenbloom, J. I., Wilker, E. H., Mukamal, K. J., Schwartz, J. and Mittleman, M. A. 2012. Residential proximity to major roadway and 10-year all-cause mortality after myocardial infarction. *Circulation* 125(18), pp. 2197-2203. doi: 10.1161/circulationaha.111.085811

Roy, R., Mrad, D., Lord, P., Carlsten, J., Good, W., Allsup, P., Roy, L., Kuhler, K., Koch, W., Wu, Y. 1998. Thermodynamics of the Second Dissociation Constant and Standards for pH of 3-(AMMorpholino) Propanesulfonic Acid (MOPS) Buffers from 5 to 55°C. *Journal of Solution Chemistry* 27(1), pp. 73-87.

Ruas, C. B. G., Carvalho, C. d. S., de Araújo, H. S. S., Espíndola, E. L. G. and Fernandes, M. N. 2008. Oxidative stress biomarkers of exposure in the blood of cichlid species from a metal-contaminated river. *Ecotoxicology and Environmental Safety* 71(1), pp. 86-93. doi: https://doi.org/10.1016/j.ecoenv.2007.08.018

Rusyn, E., Mousallem, T., Persaud-Sawin, D. A., Miller, S. and Boustany, R. M. 2008. CLN3p impacts galactosylceramide transport, raft morphology, and lipid content. *Pediatr Res* 63(6), pp. 625-631. doi: 10.1203/PDR.0b013e31816fdc17

Sabatini, D. D. and Adesnik, M. 2013. Christian de Duve: Explorer of the cell who discovered new organelles by using a centrifuge. *Proceedings of the National Academy of Sciences* 110(33), pp. 13234-13235. doi: 10.1073/pnas.1312084110

Sabella, S. et al. 2014. A general mechanism for intracellular toxicity of metal-containing nanoparticles. *Nanoscale* 6(12), pp. 7052-7061. doi: 10.1039/C4NR01234H

Sahu, B., Mackos, A. R., Floden, A. M., Wold, L. E. and Combs, C. K. 2021. Particulate Matter Exposure Exacerbates Amyloid-β Plaque Deposition and Gliosis in APP/PS1 Mice. *Journal of Alzheimer's disease : JAD* 80(2), pp. 761-774. doi: 10.3233/JAD-200919

Saint-Amant, L. and Drapeau, P. 1998. Time course of the development of motor behaviors in the zebrafish embryo. *J Neurobiol* 37(4), pp. 622-632. doi: 10.1002/(sici)1097-4695(199812)37:4<622::aid-neu10>3.0.co;2-s

Sakulkhu, U., Mahmoudi, M., Maurizi, L., Salaklang, J. and Hofmann, H. 2014. Protein Corona Composition of Superparamagnetic Iron Oxide Nanoparticles with Various Physico-Chemical Properties and Coatings. *Scientific Reports* 4(1), p. 5020. doi: 10.1038/srep05020

Samara, C. and Tsitouridou, R. 2000. Fine and Coarse Ionic Aerosol Components in Relation to Wet and Dry Deposition. *Water, Air, and Soil Pollution* 120(1), pp. 71-88. doi: 10.1023/A:1005267021828

Sander, M., Hofstetter, T. B. and Gorski, C. A. 2015. Electrochemical analyses of redox-active iron minerals: a review of nonmediated and mediated approaches. *Environ Sci Technol* 49(10), pp. 5862-5878. doi: 10.1021/acs.est.5b00006

Sanders, P. G., Xu, N., Dalka, T. M. and Maricq, M. M. 2003. Airborne Brake Wear Debris: Size Distributions, Composition, and a Comparison of Dynamometer and Vehicle Tests. *Environmental Science & Technology* 37(18), pp. 4060-4069. doi: 10.1021/es034145s

Saraswathy, A., Nazeer, S. S., Nimi, N., Arumugam, S., Shenoy, S. J. and Jayasree, R. S. 2014. Synthesis and characterization of dextran stabilized superparamagnetic iron oxide nanoparticles for in vivo MR imaging of liver fibrosis. *Carbohydrate Polymers* 101, pp. 760-768. doi: https://doi.org/10.1016/j.carbpol.2013.10.015

Sawcer, S. et al. 2011. Genetic risk and a primary role for cell-mediated immune mechanisms in multiple sclerosis. *Nature* 476(7359), pp. 214-219. doi: 10.1038/nature10251

Saxton, R. A. and Sabatini, D. M. 2017. mTOR Signaling in Growth, Metabolism, and Disease. *Cell* 169(2), pp. 361-371. doi: 10.1016/j.cell.2017.03.035

Sbano, L. et al. 2017. TFEB-mediated increase in peripheral lysosomes regulates store-operated calcium entry. *Scientific Reports* 7(1), p. 40797. doi: 10.1038/srep40797

Schiff, R. I. and Gennaro, J. F., Jr. 1979. The influence of the buffer on maintenance of tissue lipid in specimens for scanning electron microscopy. *Scan Electron Microsc* (3), pp. 449-458.

Schmees, C., Villaseñor, R., Zheng, W., Ma, H., Zerial, M., Heldin, C. H. and Hellberg, C. 2012. Macropinocytosis of the PDGF β-receptor promotes fibroblast transformation by H-RasG12V. *Mol Biol Cell* 23(13), pp. 2571-2582. doi: 10.1091/mbc.E11-04-0317

Schmidtke, C. et al. 2019. Lysosomal proteome analysis reveals that CLN3-defective cells have multiple enzyme deficiencies associated with changes in intracellular trafficking. *J Biol Chem* 294(24), pp. 9592-9604. doi: 10.1074/jbc.RA119.008852

Schnitzer, J. E., Oh, P., Pinney, E. and Allard, J. 1994. Filipin-sensitive caveolae-mediated transport in endothelium: reduced transcytosis, scavenger endocytosis, and capillary permeability of select macromolecules. *Journal of Cell Biology* 127(5), pp. 1217-1232. doi: 10.1083/jcb.127.5.1217

Schultheiss-Grassi, P., Wessiken, R. and Dobson, J. 1999. TEM investigations of biogenic magnetite extracted from the human hippocampus. *Biochim Biophys Acta* 1426(1), pp. 212-216.

Schulz, A. et al. 2006. The CLN9 protein, a regulator of dihydroceramide synthase. *J Biol Chem* 281(5), pp. 2784-2794. doi: 10.1074/jbc.M509483200

Schulze, H., Kolter, T. and Sandhoff, K. 2009. Principles of lysosomal membrane degradation: Cellular topology and biochemistry of lysosomal lipid degradation. *Biochimica et Biophysica Acta (BBA) - Molecular Cell Research* 1793(4), pp. 674-683. doi: https://doi.org/10.1016/j.bbamcr.2008.09.020

Schwaminger, S., Bauer, D., Fraga-García, P., Wagner, F. and Berensmeier, S. 2017. Oxidation of magnetite nanoparticles: impact on surface and crystal properties. *CrystEngComm* 19, pp. 246-255. doi: 10.1039/C6CE02421A

Schwarz, J. M., Sholar, P. W. and Bilbo, S. D. 2012. Sex differences in microglial colonization of the developing rat brain. *Journal of Neurochemistry* 120(6), pp. 948-963. doi: 10.1111/j.1471-4159.2011.07630.x

Scott, C. C., Vacca, F. and Gruenberg, J. 2014. Endosome maturation, transport and functions. *Seminars in Cell & Developmental Biology* 31, pp. 2-10. doi: https://doi.org/10.1016/j.semcdb.2014.03.034

Seabra, A. B., Pelegrino, M. T. and Haddad, P. S. 2017. Chapter 24 - Antimicrobial Applications of Superparamagnetic Iron Oxide Nanoparticles: Perspectives and Challenges. In: Ficai, A. and Grumezescu, A.M. eds. *Nanostructures for Antimicrobial Therapy*. Elsevier, pp. 531-550.

Seguret, A., Collignon, B. and Halloy, J. 2016. Strain differences in the collective behaviour of zebrafish (Danio rerio) in heterogeneous environment. *R Soc Open Sci* 3(10), p. 160451. doi: 10.1098/rsos.160451

Senkevich, K. and Gan-Or, Z. 2020. Autophagy lysosomal pathway dysfunction in Parkinson's disease; evidence from human genetics. *Parkinsonism & Related Disorders* 73, pp. 60-71. doi: https://doi.org/10.1016/j.parkreldis.2019.11.015

Seo, D. Y., Jin, M., Ryu, J.-C. and Kim, Y.-J. 2017. Investigation of the genetic toxicity by dextran-coated superparamagnetic iron oxide nanoparticles (SPION) in HepG2 cells using the comet assay and cytokinesis-block micronucleus assay. *Toxicology and Environmental Health Sciences* 9(1), pp. 23-29. doi: 10.1007/s13530-017-0299-z

Serrano-Pozo, A., Gómez-Isla, T., Growdon, J. H., Frosch, M. P. and Hyman, B. T. 2013. A Phenotypic Change But Not Proliferation Underlies Glial Responses in Alzheimer Disease. *The American Journal of Pathology* 182(6), pp. 2332-2344. doi: https://doi.org/10.1016/j.ajpath.2013.02.031

Settembre, C. et al. 2011. TFEB Links Autophagy to Lysosomal Biogenesis. *Science* 332(6036), p. 1429. doi: 10.1126/science.1204592

Settembre, C. et al. 2012. A lysosome-to-nucleus signalling mechanism senses and regulates the lysosome via mTOR and TFEB. *EMBO J* 31(5), pp. 1095-1108. doi: 10.1038/emboj.2012.32

Shah, S. D., Cocker, D. R., 3rd, Miller, J. W. and Norbeck, J. M. 2004. Emission rates of particulate matter and elemental and organic carbon from in-use diesel engines. *Environ Sci Technol* 38(9), pp. 2544-2550. doi: 10.1021/es0350583

Shang, M. et al. 2021. The key role of autophagy in silver nanoparticle-induced BV2 cells inflammation and polarization. *Food and Chemical Toxicology* 154, p. 112324. doi: https://doi.org/10.1016/j.fct.2021.112324

Sharma, A. et al. 2018. Physical characterization and in vivo organ distribution of coated iron oxide nanoparticles. *Scientific Reports* 8(1), p. 4916. doi: 10.1038/s41598-018-23317-2

Sharma, V. P., Arora, H. C. and Gupta, R. K. 1983. Atmospheric pollution studies at Kanpur—suspended particulate matter. *Atmospheric Environment (1967)* 17(7), pp. 1307-1313. doi: https://doi.org/10.1016/0004-6981(83)90405-5

Sharrock, M. P. and Bodnar, R. E. 1985. Magnetic materials for recording: An overview with special emphasis on particles (invited). *Journal of Applied Physics* 57(8), pp. 3919-3924. doi: 10.1063/1.334917

Shaterabadi, Z., Nabiyouni, G. and Soleymani, M. 2017. High impact of in situ dextran coating on biocompatibility, stability and magnetic properties of iron oxide nanoparticles. *Materials Science and Engineering: C* 75, pp. 947-956. doi: https://doi.org/10.1016/j.msec.2017.02.143

Shen, X., Yao, Z., Huo, H., He, K., Zhang, Y., Liu, H. and Ye, Y. 2014. PM2.5 emissions from light-duty gasoline vehicles in Beijing, China. *Science of The Total Environment* 487, pp. 521-527. doi: https://doi.org/10.1016/j.scitotenv.2014.04.059

Shi, H., Bencze, K. Z., Stemmler, T. L. and Philpott, C. C. 2008. A Cytosolic Iron Chaperone That Delivers Iron to Ferritin. *Science* 320(5880), pp. 1207-1210. doi: 10.1126/science.1157643

Shi, Q. et al. 2017. Complement C3 deficiency protects against neurodegeneration in aged plaque-rich APP/PS1 mice. *Science Translational Medicine* 9(392), p. eaaf6295. doi: 10.1126/scitranslmed.aaf6295

Shingles, R., Wimmers, L. E. and McCarty, R. E. 2004. Copper transport across pea thylakoid membranes. *Plant Physiol* 135(1), pp. 145-151. doi: 10.1104/pp.103.037895

Shipman, C., Jr. 1969. Evaluation of 4-(2-hydroxyethyl)-1-piperazineethanesulfonic acid (HEPES) as a tissue culture buffer. *Proc Soc Exp Biol Med* 130(1), pp. 305-310. doi: 10.3181/00379727-130-33543

Shundo, C., Zhang, H., Nakanishi, T. and Osaka, T. 2012. Cytotoxicity evaluation of magnetite (Fe3O4) nanoparticles in mouse embryonic stem cells. *Colloids and Surfaces B: Biointerfaces* 97, pp. 221-225. doi: https://doi.org/10.1016/j.colsurfb.2012.04.003

Siddiqi, N. J., Abdelhalim, M. A. K., El-Ansary, A. K., Alhomida, A. S. and Ong, W. Y. 2012. Identification of potential biomarkers of gold nanoparticle toxicity in rat brains. *Journal of neuroinflammation* 9, pp. 123-123. doi: 10.1186/1742-2094-9-123

Simonetti, R. B. M., L. S.; Streit Jr, D. P.; Oberst, E. R. 2016. Zebrafish (*Danio rerio*): Ethics in animal experimentation. *IOSR-JAVS* 9(7), pp. 106-110. doi: 10.9790/2380-090701106110

Singh, M., Barman, A. S., Devi, A. L., Devi, A. G. and Pandey, P. K. 2019. Iron mediated hematological, oxidative and histological alterations in freshwater fish Labeo rohita. *Ecotoxicol Environ Saf* 170, pp. 87-97. doi: 10.1016/j.ecoenv.2018.11.129

Singh, N. et al. 2012. The role of iron redox state in the genotoxicity of ultrafine superparamagnetic iron oxide nanoparticles. *Biomaterials* 33(1), pp. 163-170. doi: https://doi.org/10.1016/j.biomaterials.2011.09.087

Skjolding, L. M., Ašmonaitė, G., Jølck, R. I., Andresen, T. L., Selck, H., Baun, A. and Sturve, J. 2017. An assessment of the importance of exposure routes to the uptake and internal localisation of fluorescent nanoparticles in zebrafish (Danio rerio), using light sheet microscopy. *Nanotoxicology* 11(3), pp. 351-359. doi: 10.1080/17435390.2017.1306128

Smith, A. M. and Dragunow, M. 2014. The human side of microglia. *Trends in Neurosciences* 37(3), pp. 125-135. doi: https://doi.org/10.1016/j.tins.2013.12.001

Smith, A. M. et al. 2013. M-CSF increases proliferation and phagocytosis while modulating receptor and transcription factor expression in adult human microglia. *Journal of neuroinflammation* 10(1), p. 859. doi: 10.1186/1742-2094-10-85

Snitsarev, V. A., McNulty, T. J. and Taylor, C. W. 1996. Endogenous heavy metal ions perturb fura-2 measurements of basal and hormone-evoked Ca2+ signals. *Biophysical Journal* 71(2), pp. 1048-1056. doi: 10.1016/S0006-3495(96)79305-0

Solé-Domènech, S., Rojas, A. V., Maisuradze, G. G., Scheraga, H. A., Lobel, P. and Maxfield, F. R. 2018. Lysosomal enzyme tripeptidyl peptidase 1 destabilizes fibrillar Aβ by multiple endoproteolytic cleavages within the β-sheet domain. *Proceedings of the National Academy of Sciences* 115(7), pp. 1493-1498. doi: 10.1073/pnas.1719808115

Song, W., Popp, L., Yang, J., Kumar, A., Gangoli, V. S. and Segatori, L. 2015. The autophagic response to polystyrene nanoparticles is mediated by transcription factor EB and depends on surface charge. *Journal of Nanobiotechnology* 13(1), p. 87. doi: 10.1186/s12951-015-0149-6

Song, W., Soo Lee, S., Savini, M., Popp, L., Colvin, V. L. and Segatori, L. 2014. Ceria Nanoparticles Stabilized by Organic Surface Coatings Activate the Lysosome-Autophagy System and Enhance Autophagic Clearance. *ACS Nano* 8(10), pp. 10328-10342. doi: 10.1021/nn505073u

Sonnack, L. et al. 2015. Effects of metal exposure on motor neuron development, neuromasts and the escape response of zebrafish embryos. *Neurotoxicology and Teratology* 50, pp. 33-42. doi: https://doi.org/10.1016/j.ntt.2015.05.006

Sorbi, S., Forleo, P., Tedde, A., Cellini, E., Ciantelli, M., Bagnoli, S. and Nacmias, B. 2001. Genetic risk factors in familial Alzheimer's disease. *Mech Ageing Dev* 122(16), pp. 1951-1960.

Spence, R. and Smith, C. 2006. Mating preference of female zebrafish, Danio rerio, in relation to male dominance. *Behavioral Ecology* 17(5), pp. 779-783. doi: 10.1093/beheco/arl016

Srai, S. K. S., Bomford, A. and McArdle, H. J. 2002. Iron transport across cell membranes: molecular understanding of duodenal and placental iron uptake. *Best Practice & Research Clinical Haematology* 15(2), pp. 243-259. doi: https://doi.org/10.1053/beha.2002.0003

Srimuruganandam, B. and Shiva Nagendra, S. M. 2012. Application of positive matrix factorization in characterization of PM10 and PM2.5 emission sources at urban roadside. *Chemosphere* 88(1), pp. 120-130. doi: https://doi.org/10.1016/j.chemosphere.2012.02.083

Srivastava, J., Barber, D. L. and Jacobson, M. P. 2007. Intracellular pH sensors: design principles and functional significance. *Physiology (Bethesda)* 22, pp. 30-39. doi: 10.1152/physiol.00035.2006

Stafoggia, M. et al. 2014. Long-term exposure to ambient air pollution and incidence of cerebrovascular events: results from 11 European cohorts within the ESCAPE project. *Environmental health perspectives* 122(9), pp. 919-925. doi: 10.1289/ehp.1307301

Stefanatos, R. and Sanz, A. 2018. The role of mitochondrial ROS in the aging brain. *FEBS Letters* 592(5), pp. 743-758. doi: https://doi.org/10.1002/1873-3468.12902

Stern, S. T., Adiseshaiah, P. P. and Crist, R. M. 2012. Autophagy and lysosomal dysfunction as emerging mechanisms of nanomaterial toxicity. *Particle and fibre toxicology* 9, pp. 20-20. doi: 10.1186/1743-8977-9-20

Strähle, U. et al. 2012. Zebrafish embryos as an alternative to animal experiments--a commentary on the definition of the onset of protected life stages in animal welfare regulations. *Reprod Toxicol* 33(2), pp. 128-132. doi: 10.1016/j.reprotox.2011.06.121

Streit, W. J., Braak, H., Xue, Q. S. and Bechmann, I. 2009. Dystrophic (senescent) rather than activated microglial cells are associated with tau pathology and likely precede neurodegeneration in Alzheimer's disease. *Acta Neuropathol* 118(4), pp. 475-485. doi: 10.1007/s00401-009-0556-6

Streit, W. J. and Xue, Q. S. 2010. The Brain's Aging Immune System. *Aging Dis* 1(3), pp. 254-261.

Su, C. et al. 2017. Which metal represents the greatest risk to freshwater ecosystem in bohai region of china? *Ecosystem Health and Sustainability* 3(2), p. e01260. doi: 10.1002/ehs2.1260

Subramanian, M., Miaskowski, A., Jenkins, S. I., Lim, J. and Dobson, J. 2018. Remote manipulation of magnetic nanoparticles using magnetic field gradient to promote cancer cell death. *bioRxiv*, p. 317115. doi: 10.1101/317115

Suhel, A., Abdul Rahim, N., Abdul Rahman, M. R. and Bin Ahmad, K. A. 2021. Engine's behaviour on magnetite nanoparticles as additive and hydrogen addition of chicken fat methyl ester fuelled DICI engine: A dual fuel approach. *International Journal of Hydrogen Energy* 46(27), pp. 14824-14843. doi: https://doi.org/10.1016/j.ijhydene.2021.01.219

Sun, L., Hua, Y., Vergarajauregui, S., Diab, H. I. and Puertollano, R. 2015. Novel Role of TRPML2 in the Regulation of the Innate Immune Response. *Journal of immunology (Baltimore, Md. : 1950)* 195(10), pp. 4922-4932. doi: 10.4049/jimmunol.1500163

Swanson, J. A. 2008. Shaping cups into phagosomes and macropinosomes. *Nature reviews. Molecular cell biology* 9(8), pp. 639-649. doi: 10.1038/nrm2447

Sweeney, M. D., Sagare, A. P. and Zlokovic, B. V. 2018. Blood-brain barrier breakdown in Alzheimer disease and other neurodegenerative disorders. *Nat Rev Neurol* 14(3), pp. 133-150. doi: 10.1038/nrneurol.2017.188

Sztiller-Sikorska, M., Jakubowska, J., Wozniak, M., Stasiak, M. and Czyz, M. 2009. A non-apoptotic function of caspase-3 in pharmacologically-induced differentiation of K562 cells. *British journal of pharmacology* 157(8), pp. 1451-1462. doi: 10.1111/j.1476-5381.2009.00333.x

Tabuchi, M., Yoshimori, T., Yamaguchi, K., Yoshida, T. and Kishi, F. 2000. Human NRAMP2/DMT1, Which Mediates Iron Transport across Endosomal Membranes, Is Localized to Late Endosomes and Lysosomes in HEp-2 Cells *. *Journal of Biological Chemistry* 275(29), pp. 22220-22228. doi: 10.1074/jbc.M001478200

Taha, M., Quental, M. V., FA, E. S., Capela, E. V., Freire, M. G., Ventura, S. P. M. and Coutinho, J. A. P. 2017. Good's Buffer Ionic Liquids as Relevant Phase-Forming Components of Self-Buffered Aqueous Biphasic Systems. *J Chem Technol Biotechnol* 92(9), pp. 2287-2299. doi: 10.1002/jctb.5222

Takahashi, M., Shibata, M. and Niki, E. 2001. Estimation of lipid peroxidation of live cells using a fluorescent probe, Diphenyl-1-pyrenylphosphine. *Free Radical Biology and Medicine* 31(2), pp. 164-174. doi: https://doi.org/10.1016/S0891-5849(01)00575-5

Takuma, K. et al. 2009. RAGE-mediated signaling contributes to intraneuronal transport of amyloid-beta and neuronal dysfunction. *Proc Natl Acad Sci U S A* 106(47), pp. 20021-20026. doi: 10.1073/pnas.0905686106

Tang, T. et al. 2020. The role of lysosomes in cancer development and progression. *Cell & Bioscience* 10(1), p. 131. doi: 10.1186/s13578-020-00489-x

Tanzi, R. E. et al. 1992. Assessment of amyloid β-protein precursor gene mutations in a large set of familial and sporadic Alzheimer disease cases. *Am J Hum Genet* 51(2), pp. 273-282.

Tassa, C., Shaw, S. Y. and Weissleder, R. 2011. Dextran-coated iron oxide nanoparticles: a versatile platform for targeted molecular imaging, molecular diagnostics, and therapy. *Accounts of chemical research* 44(10), pp. 842-852. doi: 10.1021/ar200084x

Taylor, A. C. 1962. Responses of cells to pH changes in the medium. *J Cell Biol* 15, pp. 201-209. doi: 10.1083/jcb.15.2.201

Taylor, M. J., Perrais, D. and Merrifield, C. J. 2011. A high precision survey of the molecular dynamics of mammalian clathrin-mediated endocytosis. *PLoS biology* 9(3), pp. e1000604-e1000604. doi: 10.1371/journal.pbio.1000604

te Vruchte, D. et al. 2004. Accumulation of glycosphingolipids in Niemann-Pick C disease disrupts endosomal transport. *J Biol Chem* 279(25), pp. 26167-26175. doi: 10.1074/jbc.M311591200

Teja, A. S. and Koh, P.-Y. 2009. Synthesis, properties, and applications of magnetic iron oxide nanoparticles. *Progress in Crystal Growth and Characterization of Materials* 55(1), pp. 22-45. doi: https://doi.org/10.1016/j.pcrysgrow.2008.08.003

Tenopoulou, M., Kurz, T., Doulias, P.-T., Galaris, D. and Brunk, U. T. 2007. Does the calcein-AM method assay the total cellular 'labile iron pool' or only a fraction of it? *The Biochemical journal* 403(2), pp. 261-266. doi: 10.1042/BJ20061840

Thelen, A. M. and Zoncu, R. 2017. Emerging Roles for the Lysosome in Lipid Metabolism. *Trends in Cell Biology* 27(11), pp. 833-850. doi: 10.1016/j.tcb.2017.07.006

Thomsen, L. B. et al. 2013. Uptake and Transport of Superparamagnetic Iron Oxide Nanoparticles through Human Brain Capillary Endothelial Cells. *ACS Chemical Neuroscience* 4(10), pp. 1352-1360. doi: 10.1021/cn400093z

Tipping, E. 1981. Adsorption by goethite (α-FeOOH) of humic substances from three different lakes. *Chemical Geology* 33(1), pp. 81-89. doi: https://doi.org/10.1016/0009-2541(81)90086-3

Tishchenko, P. Y. 2000. Standardization of pH measurements based on the ion interaction approach *Russian Chemical Bulletin* 49(4), pp. 680-684.

Toblli, E. J., Cao, G., Oliveri, L. and Angerosa, M. 2011. Assessment of the extent of oxidative stress induced by intravenous ferumoxytol, ferric carboxymaltose, iron sucrose and iron dextran in a nonclinical model. *Arzneimittelforschung* 61(07), pp. 399-410.

Todd, J. J. 2005. URBAN AIR QUALITY. *Environment Design Guide*, pp. 1-8.

Tol, M. et al. 2018. HEPES activates a MiT/TFE-dependent lysosomal-autophagic gene network in cultured cells: A call for caution. *Autophagy* 14(3), pp. 437-449. doi: 10.1080/15548627.2017.1419118

Toyokuni, S. 1996. Iron-induced carcinogenesis: the role of redox regulation. *Free Radic Biol Med* 20(4), pp. 553-566. doi: 10.1016/0891-5849(95)02111-6

Ueno, M., Fujita, Y., Tanaka, T., Nakamura, Y., Kikuta, J., Ishii, M. and Yamashita, T. 2013. Layer V cortical neurons require microglial support for survival during postnatal development. *Nat Neurosci* 16(5), pp. 543-551. doi: 10.1038/nn.3358

Unterweger, H. et al. 2018. Dextran-coated superparamagnetic iron oxide nanoparticles for magnetic resonance imaging: evaluation of size-dependent imaging properties, storage stability and safety. *Int J Nanomedicine* 13, pp. 1899-1915. doi: 10.2147/ijn.S156528

Uzhytchak, M. et al. 2020. Iron Oxide Nanoparticle-Induced Autophagic Flux Is Regulated by Interplay between p53-mTOR Axis and Bcl-2 Signaling in Hepatic Cells. *Cells* 9(4), doi: 10.3390/cells9041015

Vakili-Ghartavol, R., Momtazi-Borojeni, A. A., Vakili-Ghartavol, Z., Aiyelabegan, H. T., Jaafari, M. R., Rezayat, S. M. and Arbabi Bidgoli, S. 2020. Toxicity assessment of superparamagnetic iron oxide nanoparticles in different tissues. *Artificial Cells, Nanomedicine, and Biotechnology* 48(1), pp. 443-451. doi: 10.1080/21691401.2019.1709855

Valavanidis, A., Fiotakis, K. and Vlachogianni, T. 2008. Airborne Particulate Matter and Human Health: Toxicological Assessment and Importance of Size and Composition of Particles for Oxidative Damage and Carcinogenic Mechanisms. *Journal of Environmental Science and Health, Part C* 26(4), pp. 339-362. doi: 10.1080/10590500802494538

Van Acker, Z. P., Bretou, M. and Annaert, W. 2019. Endo-lysosomal dysregulations and late-onset Alzheimer's disease: impact of genetic risk factors. *Molecular Neurodegeneration* 14(1), pp. 20-20. doi: 10.1186/s13024-019-0323-7

van den Bos, R., Mes, W., Galligani, P., Heil, A., Zethof, J., Flik, G. and Gorissen, M. 2017. Further characterisation of differences between TL and AB zebrafish (Danio rerio): Gene expression, physiology and behaviour at day 5 of the larval stage. *PLoS ONE* 12(4), p. e0175420. doi: 10.1371/journal.pone.0175420

van der Kant, R. and Neefjes, J. 2014. Small regulators, major consequences – Ca2+ and cholesterol at the endosome–ER interface. *Journal of Cell Science* 127(5), pp. 929-938. doi: 10.1242/jcs.137539

Vangijzegem, T., Stanicki, D. and Laurent, S. 2019. Magnetic iron oxide nanoparticles for drug delivery: applications and characteristics. *Expert Opinion on Drug Delivery* 16(1), pp. 69-78. doi: 10.1080/17425247.2019.1554647

Vaughan, D. W. and Peters, A. 1974. Neuroglial cells in the cerebral cortex of rats from young adulthood to old age: An electron microscope study. *Journal of Neurocytology* 3(4), pp. 405-429. doi: 10.1007/BF01098730

Vayenas, D. V., Repanti, M., Vassilopoulos, A. and Papanastasiou, D. A. 1998. Influence of iron overload on manganese, zinc, and copper concentration in rat tissues in vivo: study of liver, spleen, and brain. *International Journal of Clinical and Laboratory Research* 28(3), pp. 183-186. doi: 10.1007/s005990050041

Vega-Rubin-de-Celis, S., Peña-Llopis, S., Konda, M. and Brugarolas, J. 2017. Multistep regulation of TFEB by MTORC1. *Autophagy* 13(3), pp. 464-472. doi: 10.1080/15548627.2016.1271514

Verdery, R. B., Nist, C., Fujimoto, W. Y., Wight, T. N. and Glomset, J. A. 1981. Reversible ultrastructural changes in human fibroblasts grown in hepes buffered MCDB-104 supplemented with human serum. *In Vitro* 17(11), pp. 956-964. doi: 10.1007/BF02618420

Vikesland, P. J., Rebodos, R. L., Bottero, J. Y., Rose, J. and Masion, A. 2016. Aggregation and sedimentation of magnetite nanoparticle clusters. *Environmental Science: Nano* 3(3), pp. 567-577. doi: 10.1039/C5EN00155B

Vilhardt, F. 2005. Microglia: phagocyte and glia cell. *Int J Biochem Cell Biol* 37(1), pp. 17-21. doi: 10.1016/j.biocel.2004.06.010

Voinov, M. A., Sosa Pagán, J. O., Morrison, E., Smirnova, T. I. and Smirnov, A. I. 2011. Surface-mediated production of hydroxyl radicals as a mechanism of iron oxide nanoparticle biotoxicity. *J Am Chem Soc* 133(1), pp. 35-41. doi: 10.1021/ja104683w

von Bartheld, C. S., Bahney, J. and Herculano-Houzel, S. 2016. The search for true numbers of neurons and glial cells in the human brain: A review of 150 years of cell counting. *The Journal of comparative neurology* 524(18), pp. 3865-3895. doi: 10.1002/cne.24040

von der Heyden, B., Roychoudhury, A. and Myneni, S. 2019. Iron-Rich Nanoparticles in Natural Aquatic Environments. *Minerals* 9(5), doi: 10.3390/min9050287

Vuori, K.-M. 1995. Direct and indirect effects of iron on river ecosystems. *Annales Zoologici Fennici* 32(3), pp. 317-329.

Wager, K., Zdebik, A. A., Fu, S., Cooper, J. D., Harvey, R. J. and Russell, C. 2016. Neurodegeneration and Epilepsy in a Zebrafish Model of CLN3 Disease (Batten Disease). *PLoS ONE* 11(6), p. e0157365. doi: 10.1371/journal.pone.0157365

Walker, M. 2015. *Improved techniques for isolation of pure cellular organelles with magnetic ferrofluid.* Cardiff University.

Walker, M. W. and Lloyd-Evans, E. 2015. A rapid method for the preparation of ultrapure, functional lysosomes using functionalized superparamagnetic iron oxide nanoparticles. *Methods Cell Biol* 126, pp. 21-43. doi: 10.1016/bs.mcb.2014.10.019

Waller-Evans, H. and Lloyd-Evans, E. 2015. Regulation of TRPML1 function. *Biochemical Society Transactions* 43(3), pp. 442-446. doi: 10.1042/bst20140311

Wang, C., Zhang, H., Chen, B., Yin, H. and Wang, W. 2011a. Study of the enhanced anticancer efficacy of gambogic acid on Capan-1 pancreatic cancer cells when mediated via magnetic Fe3O4 nanoparticles. *International journal of nanomedicine* 6, pp. 1929-1935. doi: 10.2147/IJN.S24707

Wang, J., Ma, T., Ma, D., Li, H., Hua, L., He, Q. and Deng, X. 2021a. The Impact of Air Pollution on Neurodegenerative Diseases. *Ther Drug Monit* 43(1), pp. 69-78. doi: 10.1097/ftd.0000000000000818

Wang, L., Min, Y., Xu, D., Yu, F., Zhou, W. and Cuschieri, A. 2014. Membrane lipid peroxidation by the peroxidase-like activity of magnetite nanoparticles. *Chemical Communications* 50(76), pp. 11147-11150. doi: 10.1039/C4CC03082F

Wang, Q., Zhou, L., Qiu, L., Lu, D., Wu, Y. and Zhang, X.-B. 2015. An efficient ratiometric fluorescent probe for tracking dynamic changes in lysosomal pH. *Analyst* 140(16), pp. 5563-5569. doi: 10.1039/C5AN00683J

Wang, R., Wang, J., Hassan, A., Lee, C.-H., Xie, X.-S. and Li, X. 2021b. Molecular basis of V-ATPase inhibition by bafilomycin A1. *Nature Communications* 12(1), p. 1782. doi: 10.1038/s41467-021-22111-5

Wang, T. et al. 2018. Copper supplementation reverses dietary iron overload-induced pathologies in mice. *The Journal of nutritional biochemistry* 59, pp. 56-63. doi: 10.1016/j.jnutbio.2018.05.006

Wang, Y., Dave, R. N. and Pfeffer, R. 2004. Polymer coating/encapsulation of nanoparticles using a supercritical anti-solvent process. *The Journal of Supercritical Fluids* 28(1), pp. 85-99. doi: https://doi.org/10.1016/S0896-8446(03)00011-1

Wang, Y. et al. 2011b. Microglial activation, recruitment and phagocytosis as linked phenomena in ferric oxide nanoparticle exposure. *Toxicology Letters* 205(1), pp. 26-37. doi: https://doi.org/10.1016/j.toxlet.2011.05.001

Wen, D., Song, P., Zhang, K. and Qian, J. 2019. Thermal oxidation of iron nanoparticles and its implication for chemical-looping combustion - Wen - 2011 - Journal of Chemical Technology & Biotechnology - Wiley Online Library. *Chemical Technology and Biotechnology* 86(3), pp. 375-380. doi: 10.1002/jctb.2526

Weuve, J., Puett, R. C., Schwartz, J., Yanosky, J. D., Laden, F. and Grodstein, F. 2012. Exposure to particulate air pollution and cognitive decline in older women. *Archives of internal medicine* 172(3), pp. 219-227. doi: 10.1001/archinternmed.2011.683

WFD. 2014. Water Framework Directive implementation in England and Wales: new and updated standards to protect the water environment. In: Affairs, D.f.E.F.a.R. ed. https://assets.publishing.service.gov.uk/government/uploads/system/uploads/attachment_data/file/307788/river-basin-planning-standards.pdf: Welsh Government.

WHO. 2018. *Ambient (outdoor) air pollution*. World health organisation fact sheets: Available at: https://www.who.int/news-room/fact-sheets/detail/ambient-(outdoor)-air-quality-and-health#:~:text=%22WHO%20air%20quality%20guidelines%22%20estimate%20that%20reducing%20annual,would%20otherwise%20be%2C%20due%20to%20PM%20exposures%20 [Accessed: 12/07/].

Wiley, D. S., Redfield, S. E. and Zon, L. I. 2017. Chemical screening in zebrafish for novel biological and therapeutic discovery. *Methods Cell Biol* 138, pp. 651-679. doi: 10.1016/bs.mcb.2016.10.004

Wilke, S., Krausze, J. and Büssow, K. 2012. Crystal structure of the conserved domain of the DC lysosomal associated membrane protein: implications for the lysosomal glycocalyx. *BMC Biology* 10(1), p. 62. doi: 10.1186/1741-7007-10-62

Wilker, E. H. et al. 2015. Long-term exposure to fine particulate matter, residential proximity to major roads and measures of brain structure. *Stroke* 46(5), pp. 1161-1166. doi: 10.1161/strokeaha.114.008348

Williamson, J., Goldman, J. and Marder, K. S. 2009. Genetic aspects of Alzheimer disease. *Neurologist* 15(2), pp. 80-86. doi: 10.1097/NRL.0b013e318187e76b

Williamson, J. D. and Cox, P. 1968. Use of a new buffer in the culture of animal cells. *J Gen Virol* 2(2), pp. 309-312. doi: 10.1099/0022-1317-2-2-309

Wilmes, A. et al. 2017. Towards optimisation of induced pluripotent cell culture: Extracellular acidification results in growth arrest of iPSC prior to nutrient exhaustion. *Toxicol In Vitro* 45(Pt 3), pp. 445-454. doi: 10.1016/j.tiv.2017.07.023

Wolfe, D. M., Lee, J. H., Kumar, A., Lee, S., Orenstein, S. J. and Nixon, R. A. 2013. Autophagy failure in Alzheimer's disease and the role of defective lysosomal acidification. *Eur J Neurosci* 37(12), pp. 1949-1961. doi: 10.1111/ejn.12169

Wong, Y. C., Ysselstein, D. and Krainc, D. 2018. Mitochondria-lysosome contacts regulate mitochondrial fission via RAB7 GTP hydrolysis. *Nature* 554(7692), pp. 382-386. doi: 10.1038/nature25486

Woodward, T., Kay, T. and Rucklidge, M. 2015. Fetal bradycardia following maternal administration of low-molecular-weight intravenous iron. *Int J Obstet Anesth* 24(2), pp. 196-197. doi: 10.1016/j.ijoa.2015.01.008

Wu, H.-Y., Chung, M.-C., Wang, C.-C., Huang, C.-H., Liang, H.-J. and Jan, T.-R. 2013a. Iron oxide nanoparticles suppress the production of IL-1beta via the secretory lysosomal pathway in murine microglial cells. *Particle and fibre toxicology* 10, pp. 46-46. doi: 10.1186/1743-8977-10-46

Wu, J., Ding, T. and Sun, J. 2013b. Neurotoxic potential of iron oxide nanoparticles in the rat brain striatum and hippocampus. *NeuroToxicology* 34, pp. 243-253. doi: https://doi.org/10.1016/j.neuro.2012.09.006

Wu, K.-C., Liou, H.-H., Kao, Y.-H., Lee, C.-Y. and Lin, C.-J. 2017a. The critical role of Nramp1 in degrading α-synuclein oligomers in microglia under iron overload condition. *Neurobiology of Disease* 104, pp. 61-72. doi: https://doi.org/10.1016/j.nbd.2017.05.001

Wu, Q. et al. 2017b. Iron oxide nanoparticles and induced autophagy in human monocytes. *International journal of nanomedicine* 12, pp. 3993-4005. doi: 10.2147/IJN.S135189

Wu, Y., Huang, P. and Dong, X.-P. 2021. Lysosomal Calcium Channels in Autophagy and Cancer. *Cancers* 13(6), p. 1299.

Xie, J., Shen, Z., Anraku, Y., Kataoka, K. and Chen, X. 2019. Nanomaterial-based blood-brain-barrier (BBB) crossing strategies. *Biomaterials* 224, p. 119491. doi: https://doi.org/10.1016/j.biomaterials.2019.119491

Yamamoto, D. and Suzuki, N. 1987. Blockage of chloride channels by HEPES buffer. *Proc R Soc Lond B Biol Sci* 230(1258), pp. 93-100. doi: 10.1098/rspb.1987.0011

Yang, D.-S. et al. 2014. Defective macroautophagic turnover of brain lipids in the TgCRND8 Alzheimer mouse model: prevention by correcting lysosomal proteolytic deficits. *Brain* 137(12), pp. 3300-3318. doi: 10.1093/brain/awu278

Yang, Y., Wang, H., Kouadir, M., Song, H. and Shi, F. 2019. Recent advances in the mechanisms of NLRP3 inflammasome activation and its inhibitors. *Cell Death & Disease* 10(2), p. 128. doi: 10.1038/s41419-019-1413-8

Yauger, Y. J., Bermudez, S., Moritz, K. E., Glaser, E., Stoica, B. and Byrnes, K. R. 2019. Iron accentuated reactive oxygen species release by NADPH oxidase in activated microglia contributes to oxidative stress in vitro. *Journal of neuroinflammation* 16(1), p. 41. doi: 10.1186/s12974-019-1430-7

Yiannopoulou, K. and Papageorgiou, S. 2013. Current and future treatments for Alzheimer's disease. *Ther Adv Neurol Disord* 6(1), pp. 19-33. doi: 10.1177/1756285612461679

Ying, J.-F., Lu, Z.-B., Fu, L.-Q., Tong, Y., Wang, Z., Li, W.-F. and Mou, X.-Z. 2021. The role of iron homeostasis and iron-mediated ROS in cancer. *American journal of cancer research* 11(5), pp. 1895-1912.

Ylä-Anttila, P., Vihinen, H., Jokitalo, E. and Eskelinen, E. L. 2009. 3D tomography reveals connections between the phagophore and endoplasmic reticulum. *Autophagy* 5(8), pp. 1180-1185. doi: 10.4161/auto.5.8.10274

Yu, M., Huang, S., Yu, K. J. and Clyne, A. M. 2012. Dextran and polymer polyethylene glycol (PEG) coating reduce both 5 and 30 nm iron oxide nanoparticle cytotoxicity in 2D and 3D cell culture. *International journal of molecular sciences* 13(5), pp. 5554-5570. doi: 10.3390/ijms13055554

Yu, Z., Li, Q., Wang, J., Yu, Y., Wang, Y., Zhou, Q. and Li, P. 2020. Reactive Oxygen Species-Related Nanoparticle Toxicity in the Biomedical Field. *Nanoscale research letters* 15(1), pp. 115-115. doi: 10.1186/s11671-020-03344-7

Zanetti, O., Solerte, S. and Cantoni, F. 2009. Life expectancy in Alzheimer's disease (AD). *Archives of Gerontology and Geriatrics* 49, pp. 237-243. doi: 10.1016/j.archger.2009.09.035

Zhang, R. et al. 2013. In vivo cardiac reprogramming contributes to zebrafish heart regeneration. *Nature* 498(7455), pp. 497-501. doi: 10.1038/nature12322

Zhang, T. and Peterson, R. T. 2020. Modeling Lysosomal Storage Diseases in the Zebrafish. *Front Mol Biosci* 7, p. 82. doi: 10.3389/fmolb.2020.00082

Zhang, T. G., Zhang, Y. L., Zhou, Q. Q., Wang, X. H. and Zhan, L. S. 2020a. Impairment of mitochondrial dynamics involved in iron oxide nanoparticle-induced dysfunction of dendritic cells was alleviated by autophagy inhibitor 3-methyladenine. *J Appl Toxicol* 40(5), pp. 631-642. doi: 10.1002/jat.3933

Zhang, W., Li, X., Wang, S., Chen, Y. and Liu, H. 2020b. Regulation of TFEB activity and its potential as a therapeutic target against kidney diseases. *Cell Death Discovery* 6(1), p. 32. doi: 10.1038/s41420-020-0265-4

Zhang, X. et al. 2016a. Iron Oxide Nanoparticles Induce Autophagosome Accumulation through Multiple Mechanisms: Lysosome Impairment, Mitochondrial Damage, and ER Stress. *Molecular Pharmaceutics* 13(7), pp. 2578-2587. doi: 10.1021/acs.molpharmaceut.6b00405

Zhang, Y.-Q., Dringen, R., Petters, C., Rastedt, W., Köser, J., Filser, J. and Stolte, S. 2016b. Toxicity of dimercaptosuccinate-coated and un-functionalized magnetic iron oxide nanoparticles towards aquatic organisms. *Environmental Science: Nano* 3(4), pp. 754-767. doi: 10.1039/C5EN00222B

Zhang, Y. et al. 2016c. Purification and Characterization of Progenitor and Mature Human Astrocytes Reveals Transcriptional and Functional Differences with Mouse. *Neuron* 89(1), pp. 37-53. doi: 10.1016/j.neuron.2015.11.013

Zhao, Y., Sun, X., Zhang, G., Trewyn, B. G., Slowing, I. I. and Lin, V. S. Y. 2011. Interaction of Mesoporous Silica Nanoparticles with Human Red Blood Cell Membranes: Size and Surface Effects. *ACS Nano* 5(2), pp. 1366-1375. doi: 10.1021/nn103077k

Zhou, Y. and Levy, J. I. 2007. Factors influencing the spatial extent of mobile source air pollution impacts: a meta-analysis. *BMC public health* 7, pp. 89-89. doi: 10.1186/1471-2458-7-89

Zhu, J., Zhou, L. and XingWu, F. 2006. Tracking neural stem cells in patients with brain trauma. *N Engl J Med* 355(22), pp. 2376-2378. doi: 10.1056/NEJMc055304

Zhu, M. et al. 2016. Pro-Resolving Lipid Mediators Improve Neuronal Survival and Increase Aβ42 Phagocytosis. *Mol Neurobiol* 53(4), pp. 2733-2749. doi: 10.1007/s12035-015-9544-0

Zhu, X., Tian, S. and Cai, Z. 2012. Toxicity Assessment of Iron Oxide Nanoparticles in Zebrafish (Danio rerio) Early Life Stages. *PLoS ONE* 7(9), p. e46286. doi: 10.1371/journal.pone.0046286

Zhu, X., Zhou, J. and Cai, Z. 2011. TiO2 Nanoparticles in the Marine Environment: Impact on the Toxicity of Tributyltin to Abalone (Haliotis diversicolor supertexta) Embryos. *Environmental Science & Technology* 45(8), pp. 3753-3758. doi: 10.1021/es103779h

Zhu, Y., Hinds, W. C., Kim, S., Shen, S. and Sioutas, C. 2002. Study of ultrafine particles near a major highway with heavy-duty diesel traffic. *Atmospheric Environment* 36(27), pp. 4323-4335. doi: https://doi.org/10.1016/S1352-2310(02)00354-0

Zigler, J. S., Jr., Lepe-Zuniga, J. L., Vistica, B. and Gery, I. 1985. Analysis of the cytotoxic effects of light-exposed HEPES-containing culture medium. *In Vitro Cell Dev Biol* 21(5), pp. 282-287. doi: 10.1007/BF02620943